

Intramolecular Conflict: Conformation
and Self-Assembly of Architecturally
Complex Macromolecules in Solution

Thesis by
Paul Pirogovsky

In Partial Fulfillment of the Requirements for the
degree of
Doctor of Philosophy



CALIFORNIA INSTITUTE OF TECHNOLOGY

Pasadena, California

2014

(Defended Nov 1st, 2013)

© 2014
Paul Pirogovsky
All Rights Reserved

ACKNOWLEDGEMENTS

I am grateful to all of the people who have contributed to the completion of this thesis either by furthering the work detailed within or by supporting me during the process. First of all I would like to thank my advisor Julie Kornfield for taking me under her wing and keeping me inspired during all of the years that it took to complete this work. Her enthusiasm and insight helped me to look past the failures and to see opportunities and always helped me to see the beautiful science hidden behind all of the dirty glassware. I would also like to thank Zhen-Gang Wang for being my first mentor at Caltech and for continuing to support me even when I was struggling and unsure of what to do next. I am grateful to Milo Koretsky and Skip Rochefort who let me muddle about in their labs as an undergraduate and thereby gave me my first taste of research. I appreciate the time and energy put in by the members of my committee (Professors Mark Davis, David Tirrell and Zhen-Gang Wang) in reviewing my thesis.

Throughout my time at Caltech I have always been amazed at just how helpful people can be. Mike Roy made a lot of parts for my half-baked designs and more importantly was always happy to teach me how to do it myself next time. Rick Gerhardt is amazing with glassware and never made me feel too badly about having broken a Schlenk line. Everyone on the second floor of Spalding has been nice and willing to go out of their way to help. Suresh Gupta kept the computers crunching numbers and securely storing data and was instrumental in setting up the Kornfield lab cluster. Marcy Fowler and later Andrea Arias kept track of the craziness that is the Kornfield lab calendar and made travel a breeze. Kathy Bubash and Karen Baumgartner were always there to discuss the meaning of life and also make sure that forms made it to the right place and things actually got done.

The best part of a lab is always the people and it was a pleasure to work with the awesome folks in the Kornfield lab. I enjoyed the many interesting and in-depth conversations that I had with Matthew Mattson and Loddie Foose, both kind and thoughtful people even if their political views fall on opposite ends of the spectrum. Nothing brings people closer than sleepless nights spent together surrounded by giant machinery running neutron and x-ray

experiments. I will always happily remember the scattering trips with my brothers and sisters in arms: Zuli Kurji, Rohan Hule, Artemis Ailianou, Joey Kim and Boyu Li. It's been fun hanging out and complaining about life with Amy Fu, with whom I feel comfortable talking about pretty much everything. Jeremy Wei was always there to help out with anything in the lab, kept us all safe, and taught me the little that I know about synthetic procedures. Brad Olsen is a nice guy, a fantastic role model, and the most talented person with whom I have had the privilege of working. I am really grateful to have spent my grad school years surrounded by great people, as it really made the time fly.

Many of the experiments described in this thesis were conducted at various national laboratory facilities. I would like to acknowledge the Department of Energy (DOE) and Department of Commerce for supporting the facilities of Argonne National Laboratory (ANL), Lawrence Berkeley National Laboratory (LBNL), the National Institute of Standards and Technology (NIST), Los Alamos National Laboratory (LANL) and Oak Ridge National Laboratory (ORNL). I am grateful for the opportunity to learn about experimental techniques and data analysis provided by the DOE in the form of the National School of X-ray and Neutron Scattering. It was awesome to get a chance to learn from the leading experts in the field. Some of those same experts later helped me with the experiments. They designed, built and supported the scattering instruments at the national laboratory facility and help even the most demanding and difficult of users. I would like to thank Boualem Hammouda, John Barker, Lionel Porcar, Cedric Gagnon, Jeff Kryzwon, Kim Tomasi, Rex Hjelm, Monika Hartl, Ken Littrell, Lilin He, Kathy Bailey, John Ankner, Jim Browning and Candice Halbert for all of their help in making the scattering happen.

I am grateful to my family for being supportive and for always being there to help or just to lend an ear. Michael and Karen accepted me into their family and made me feel loved whenever we saw each other. Megan and Dane are the siblings that I never had. My parents Peter and Nina inspired me to go into science and provided the financial, intellectual and emotional support that I needed to get to the end of this journey. My grandfather Oleg and grandmother Sylvia were always there to share tales of research in a very different environment and were happy to listen to me talk about my work while feeding me as much

as I could possibly eat. Without family, life is empty, and thanks to you mine has always been full.

Finally I want to thank the wonderful lady who came with me to Southern California and agreed to be my wife. Mallory is wonderful, smart, sweet, and snarky and has always made me smile, even when absolutely nothing was working. We also got to share the PhD experience, and she led the way, becoming the first Dr. Pirogovsky of our generation.

It's been grand, so long, and thanks for all the fish.

ABSTRACT

The solution behavior of linear polymer chains is well understood, having been the subject of intense study throughout the previous century. As plastics have become ubiquitous in everyday life, polymer science has grown into a major field of study. The conformation of a polymer in solution depends on the molecular architecture and its interactions with the surroundings. Developments in synthetic techniques have led to the creation of precision-tailored polymeric materials with varied topologies and functionalities. In order to design materials with the desired properties, it is imperative to understand the relationships between polymer architecture and their conformation and behavior. To meet that need, this thesis investigates the conformation and self-assembly of three architecturally complex macromolecular systems with rich and varied behaviors driven by the resolution of intramolecular conflicts. First we describe the development of a robust and facile synthetic approach to reproducible bottlebrush polymers (Chapter 2). The method was used to produce homologous series of bottlebrush polymers with polynorbornene backbones, which revealed the effect of side-chain and backbone length on the overall conformation in both good and theta solvent conditions (Chapter 3). The side-chain conformation was obtained from a series of SANS experiments and determined to be indistinguishable from the behavior of free linear polymer chains. Using deuterium-labeled bottlebrushes, we were able for the first time to directly observe the backbone conformation of a bottlebrush polymer which showed self-avoiding walk behavior. Secondly, a series of SANS experiments was conducted on a homologous series of Side Group Liquid Crystalline Polymers (SGLCPs) in a perdeuterated small molecule liquid crystal (5CB). Monodomain, aligned, dilute samples of SGLCP-*b*-PS block copolymers were seen to self-assemble into complex micellar structures with mutually orthogonally oriented anisotropies at

different length scales (Chapter 4). Finally, we present the results from the first scattering experiments on a set of fuel-soluble, associating telechelic polymers. We observed the formation of supramolecular aggregates in dilute ($\leq 0.5\text{wt}\%$) solutions of telechelic polymers and determined that the choice of solvent has a significant effect on the strength of association and the size of the supramolecules (Chapter 5). A method was developed for the direct estimation of supramolecular aggregation number from SANS data. The insight into structure-property relationships obtained from this work will enable the more targeted development of these molecular architectures for their respective applications.

TABLE OF CONTENTS

Acknowledgements	iii
Abstract.....	vi
Table of Contents	viii
List of Figures.....	x
List of Tables.....	xii
List of Schemes	xiii
Chapter 1: Introduction	
1.1 Intramolecular Conflict	I-1
1.2 Polymer Chains in Solution	I-3
1.3 Experimental Characterization of Polymers	I-12
1.4 Architecturally Complex Macromolecules.....	I-17
References.....	I-21
Chapter 2: Robust and Modular Synthesis of Bottlebrush Polymers	
2.1 Introduction.....	II-1
2.2 Experimental.....	II-6
2.3 Results and Discussion.....	II-21
2.4 Conclusions.....	II-35
References.....	II-36
Chapter 3: Dilute Solution Properties of Bottlebrush Polymers	
3.1 Introduction.....	III-1
3.2 Experimental.....	III-8
3.3 Results and Discussion.....	III-18
3.4 Conclusions.....	III-50
References.....	III-54
Chapter 4: Side-Group Liquid Crystalline Polymers in Small Molecule LC	
4.1 Introduction.....	IV-1
4.2 Experimental.....	IV-7
4.3 Results.....	IV-18
4.4 Discussion.....	IV-33
4.5 Conclusions.....	IV-51
References.....	IV-53
Chapter 5: Self-Assembly of Complementary Telechelic Polymers	
5.1 Introduction.....	V-1
5.2 Experimental.....	V-8
5.3 Results.....	V-14
5.4 Discussion.....	V-23
5.5 Conclusions and Suggested Future Experiments.....	V-30
References.....	V-32

Appendix A: Modeling of Particle Envelopment in a Biomimetic Membrane	
A.1 Introduction.....	A-1
A.2 Model and Methods.....	A-4
A.3 Results and Discussion.....	A-15
A.4 Model and Methods.....	A-26
References.....	A-27

LIST OF FIGURES

<i>Figure</i>	<i>Page</i>
1.1 Molecular weight distributions.....	I-3
1.2 Schematic of a freely jointed chain.....	I-5
1.3 Schematic of a freely rotating chain.....	I-7
1.4 Effect of solvent quality on conformation.....	I-9
1.5 Concentration regimes for polymer solutions.....	I-11
1.6 Scattering function of a polymer coil.....	I-15
2.1 Synthetic approaches to making bottlebrush polymers.....	II-2
2.2 GPC traces for PS, dPS and PtBA macromonomers.....	II-22
2.3 GPC traces for bottlebrushes with PS side-chains.....	II-25
2.4 GPC traces for bottlebrushes with dPS side-chains.....	II-28
2.5 GPC traces for bottlebrushes with PtBA side-chains.....	II-29
2.6 GPC traces for linear polynorbornenes.....	II-32
2.7 Titration curves for poly(acrylic acid) bottlebrushes.....	II-34
3.1 Schematic of bottlebrush polymer with length scales.....	III-2
3.2 R_g of PS, dPS and PtBA bottlebrushes by MALLS/GPC.....	III-19
3.3 $R_g(N)$ for linear polynorbornene.....	III-23
3.4 Aspect ratio vs R_g/R_h for prolate spheroid and cylinder.....	III-26
3.5 1D SANS of PS bottlebrushes in good and theta solvent.....	III-31
3.6 1D SANS of PtBA bottlebrushes in toluene.....	III-35
3.7 R_g from SANS for all bottlebrushes.....	III-38
3.8 1D SANS of dPS-25 bottlebrushes and linear polynorbornene.....	III-40
3.9 1D SANS of dPS-25 bottlebrushes in mixed THF.....	III-42
3.10 1D SANS of 820-dPS-65 in dTHF.....	III-43
3.11 1D SANS of poly(acrylic acid) bottlebrushes.....	III-47
4.1 Chemical structures of SGLCP- <i>b</i> -PS diblock copolymers.....	IV-8
4.2 2D SANS of SGLCP homopolymers in nematic and isotropic 5CB.....	IV-18
4.3 1D SANS sector averages for 1wt% and 5wt% homopolymer.....	IV-20
4.4 1D SANS sector averages for all homopolymers at 1wt%.....	IV-22
4.5 2D SANS for nematic SGLCP- <i>b</i> -PS diblocks.....	IV-26

4.6 1D SANS sector averages for nematic diblocks and homopolymers	IV-27
4.7 1D SANS for isotropic diblocks and homopolymers	IV-29
4.8 TEM micrographs for SGLCP- <i>b</i> -PS in 5CB	IV-31
4.9 1D SANS sector averages of nematic SGLCP- <i>b</i> -PS individually	IV-34
4.10 Schematic illustration of plausible self-assembled structures	IV-39
4.11 Scattering pattern generated with ellipsoid model	IV-48
4.12 Scattering pattern generated with random walk model	IV-49
5.1 Schematic of self-association in telechelic polymers	V-6
5.2 Schematic of complementary pairwise association in telechelic polymers ..	V-6
5.3 Chemical structure of telechelic polymers	V-9
5.4 Schematic of hydrogen bonding between TetraAcid and TetraBase	V-10
5.5 1D SANS for 400kPB polymers in dodecane and toluene	V-14
5.6 1D SANS for 300kPB polymers at 0.1wt% and 0.3wt% in cyclohexane ..	V-16
5.7 R_g vs M_w from MALLS for diTetraEster ended polybutadiene in THF	V-19
5.8 1D SANS for different M_w of ester and acid polymers at 0.1wt% in THF	V-20
5.9 R_g from SANS (Figure 5.8) compared to R_g from MALLS (Figure 5.7) ...	V-21
5.10 1D SANS for 200kPB with varied number of acid groups in THF	V-22
5.11 Excess scattering for mix of acid and base polymers in cyclohexane	V-29
A.1 Schematic of particle-membrane interaction	A-6
A.2 Sketch of free energy as a function of the reaction coordinate	A-13
A.3 Minimum free energy F as function of the separation	A-15
A.4 F and θ of the locally stable wrapped state	A-18
A.5 Barriers to adhesion (ΔF_a) and dehesion (ΔF_d) as functions of L	A-21
A.6 Force explicit free energy G as a function of separation L	A-24
A.7 Barrier to dehesion in force explicit free energy (ΔG)	A-25

LIST OF TABLES

<i>Table</i>	<i>Page</i>
2.1 Results of GPC characterization of macromonomers.....	II-23
2.2 MALLS/GPC of polystyrene bottlebrushes.....	II-26
2.3 MALLS/GPC of deuterated polystyrene bottlebrushes.....	II-28
2.4 MALLS/GPC of poly(tert-butyl acrylate) bottlebrushes.....	II-30
2.5 MALLS/GPC of linear polynorbornene	II-32
3.1 Characteristics of bottlebrush polymers with polynorbornene backbones..	III-9
3.2 Molecular weight and extent of hydrolysis for PAA bottlebrushes	III-10
3.3 Molecular weight and polydispersity of linear polynorbornenes	III-10
3.4 MALLS and DLS results for PS, dPS and PtBA bottlebrushes	III-21
3.5 R_g and R_{CS} for PNB- <i>g</i> -PS bottlebrushes in good and theta solvent	III-34
3.6 R_g and R_{CS} for PNB- <i>g</i> -PtBA bottlebrushes in good solvent.....	III-36
3.7 R_g and ν for bottlebrush backbones and linear polynorbornene.....	III-41
3.8 Hydrodynamic radii from DLS for PNB- <i>g</i> -PAA at varied pH	III-46
3.9 R_{CS} for PNB- <i>g</i> -PAA at varied pH	III-48
4.1 Composition and M_w of SGLCPs	IV-9
4.2 Aspect ratios for homopolymers in nematic phase.....	IV-21
4.3 Results from polymer excluded volume fit to SANS in Figure 4.4	IV-24
4.4 Results from polymer excluded volume fit for isotropic SGLCP- <i>g</i> -PS....	IV-30
4.5 Sizes of objects from stained and unstained TEM of SGLCP- <i>g</i> -PS	IV-32
4.6 R_g from SANS for nematic SGLCP- <i>b</i> -PS diblocks at 1wt% in 5CB.....	IV-45
5.1 Characteristics of associating polymers from MALLS/GPC	V-10
5.2 R_g from SANS of 400kPB ester and base in dodecane and toluene.....	V-15
5.3 R_g from SANS of 3400kPB ester and base in cyclohexane	V-18
5.4 R_g from SANS for varied M_w of ester and acid at 0.1wt% in THF.....	V-21
5.5 R_g from SANS for 200kPB acid with varied number of stickers in THF ..	V-22
5.6 Estimated C^* for PB in a variety of deuterated solvents.....	V-26

LIST OF SCHEMES

<i>Scheme</i>	<i>Page</i>
2.1 Synthesis of norbornene-alkyne	II-7
2.2 Atom Transfer Radical Polymerization	II-9
2.3 Conversion of polymer end-group from bromine to azide	II-12
2.4 Click coupling of norbornene-alkyne to azido terminated polymer.....	II-14
2.5 Ring opening metathesis polymerization of macromonomer.....	II-17
2.6 Removal of tert-butyl protecting group from poly(tert-butyl acrylate).....	II-19
2.7 Ring opening metathesis polymerization of norbornene	II-20

Chapter 1

Introduction

1.1 Intramolecular Conflict

Nature is driven by conflict, with competing forces in delicate balance on a microscopic level. Every molecule is held together by electrostatic forces and is simultaneously and constantly pulled and pushed by thermal fluctuations. However, most relevant properties of nature and matter are macroscopic properties which depend on the combined behavior of a multitude of constituent molecules. Even for some of the largest known molecules (10^7 kg/mol) at a low concentration (0.1wt%) in a very small sample volume (1 μ L) there are 10^{11} molecules contributing to a single macroscopic measurement, a number greater than the total population of the Earth[1]. Thus, the only way to learn about molecular behavior is from the macroscopic consequences on experimentally measurable quantities.

Experimental measurements (with rare exceptions such as femto-second spectroscopy[2]) are slow and coarse when compared to molecular timescales. Ensemble-averages that are interrogated by most spectroscopic, scattering, rheological, and other measurements probe material characteristics at or near equilibrium[3]. Therefore, thermodynamics can teach us a great deal about the states that are amenable to thorough experimental characterization. By the combined first and second laws of thermodynamics, systems are described by a free energy; $G = H - TS$ where H is enthalpy, T is temperature and S is entropy[3]. Equilibrium can be defined as a state that minimizes G and is a balance between minimizing enthalpy and maximizing entropy. The entropic contribution maximizes the number of different conformations that contribute to

the ensemble-average while enthalpic considerations make certain conformations more likely to occur than others.

The conformation of a polymer in solution depends on the molecular architecture (substituents of the polymer chain, length, and topology) and interactions with the environment (the solvent, other polymer chains, and external fields). An ordinary linear polymer coil has a conformation that maximizes the configurational entropy constrained by the favorability of interactions with the solvent. Changing the solvent conditions and/or the chain composition controls the stiffness of a polymer chain and can lead to compact or expanded conformations. Polymer chains can be made sensitive to external fields (e.g. electric, magnetic, flow or nematic) and take on anisotropic, oriented coil conformations. Having inhomogeneous polymers with incompatible domains (or associating groups) results in the formation of self-assembled structures composed of multiple polymer chains. Such changes can have very useful effects, changing the rheological, optical, or other properties of the solution. However, we cannot directly characterize the myriad conformations in solution. Macroscopic measurements allow us to deduce the consequences of architectural and functional changes on polymer conformation and self-assembly.

Each chapter of this thesis is written as a standalone study of a specific architecturally complex macromolecular system (described in section 1.4). The historical and scientific context for each is described within the introduction to that particular chapter. It is, however, presumed that the reader is familiar with many of the concepts and techniques of polymer physics. The goal of this chapter is to introduce the basic ideas and concepts encountered throughout the rest of the work. Although by no means

exhaustive, it is hoped that this brief review of polymer physics will make the work accessible to a more general audience.

1.2 Polymer Chains in Solution

Polymers are molecules composed of a large number of repeating units (known as monomers). Their very large molecular weight (as high as 10,000,000g/mol) has led them to be referred to as macromolecules. The mass of a polymer chain M is equal to the product of the number of repeat units (N) and the mass of one monomer. Synthetic polymers are polydisperse, having a distribution of chains with different molecular weights (Figure 1.1).

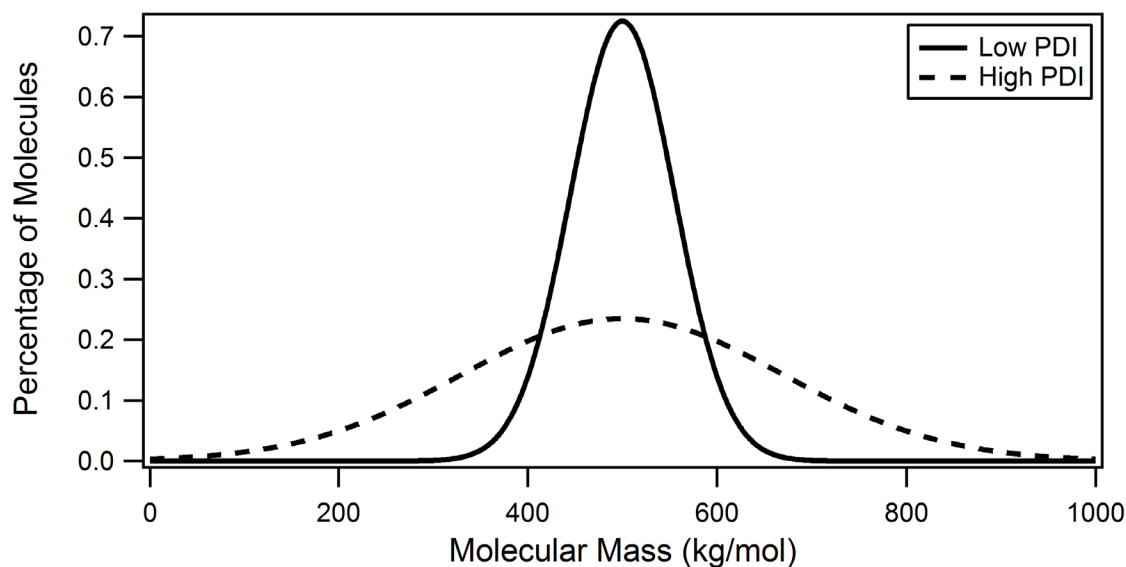


Figure 1.1: Molecular weight distributions. These are Gaussian distributions corresponding to the same mean M_n with PDI=1.01 (solid line) and PDI=1.1 (dashed line).

The molecular weight of a polymer is typically described by one of two typically used averages[4]: the number average M_n and the weight average M_w . These are defined

in Equations 1.1 and 1.2, respectively, where P_i is the probability of an individual chain having molecular weight M_i ,

$$M_n = \sum_i P_i M_i \quad (1.1)$$

$$M_w = \frac{\sum_i P_i M_i^2}{\sum_i P_i M_i} \quad (1.2)$$

Since M_i is a positive quantity, M_w is always greater than M_n with longer chains contributing more to the average. For symmetric monomodal (single peak) distributions such as that in Figure 1.1, the M_n is near the peak while the M_w is to the right of the peak. A commonly used measure of the narrowness of the distribution is the polydispersity index $PDI = M_w/M_n$ which is 1 for a monodisperse ideal polymer and 2 for a polymer prepared by free radical polymerization[5].

Even for a perfectly monodisperse linear polymer in dilute solution, the size of the molecule is polydisperse due to the multiplicity of conformations that the molecule can adopt. The instantaneous conformation of a given polymer is the spatial configuration of its constituent atoms in space described by a set of vectors \mathbf{r}_i . A typical polymer is a linear chain of N atoms separated by their equilibrium bond length (b), with the bond angle and orientation being determined by the precise chemical nature of the polymer backbone.

The simplest model for a linear polymer chain is a three-dimensional random walk with step length b , known as the freely jointed chain[6]. One such walk is shown in Figure 1.2 along with the characteristic length scale, the end-to-end distance R_{e-e} .

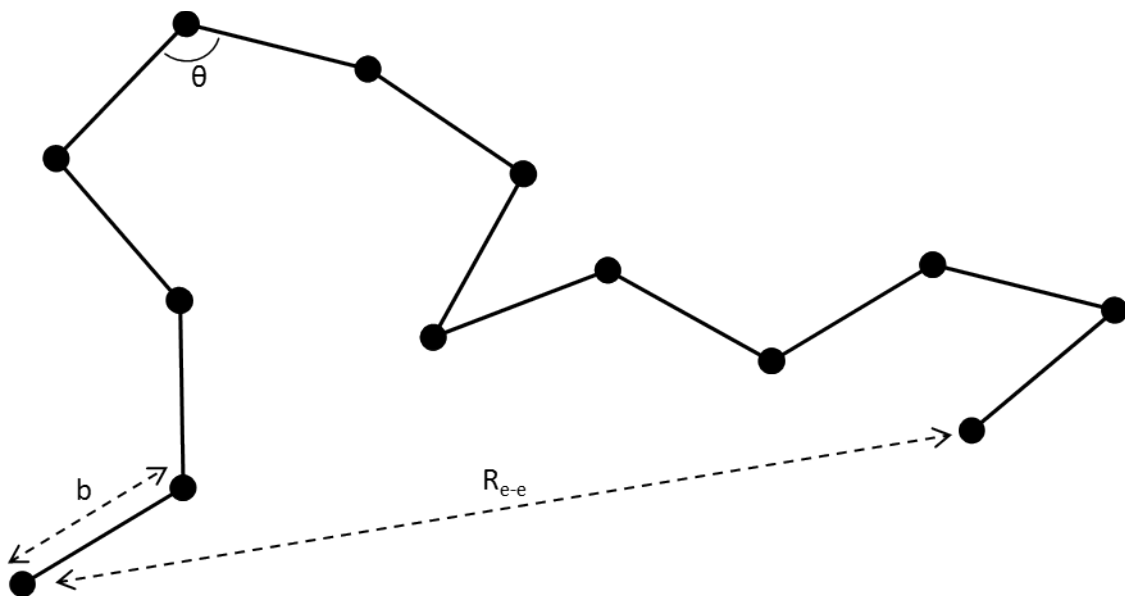


Figure 1.2: Schematic of a freely jointed chain. The model is a random walk of step length b , resulting in an end-to-end distance R_{e-e} and having no restrictions on the bond angle θ between adjacent segments.

In this simple model, all conformations are possible, including the fully extended conformation in which $R_{e-e} = Nb = L$ (the contour length of the chain). At any given moment, a single chain might have any allowable conformation. Most experimental measurements provide averages over an ensemble (a mental collection of all the possible configurations of the system[7]). For example, most experimental methods that interrogate a molecular radius R_{e-e} (e.g. static light scattering and dynamic light scattering) actually measure an average value

$$\langle R_{e-e} \rangle = \frac{\sum_i n_i R_{e-e,i}}{\sum_i n_i} \quad (1.3)$$

where n_i is the number of chains in the ensemble having conformations with radius $R_{e-e,i}$. Although characterizing the conformation of an individual polymer chain in solution is

impossible, an ensemble of freely jointed chains follows a simple scaling relationship derived by Lord Rayleigh for random flights

$$\sqrt{\langle R_{e-e}^2 \rangle} = bN^{1/2} \quad (1.4)$$

This result for the root mean square R_{e-e} (unless otherwise noted radii are always the absolute expectation value $R = \langle R^2 \rangle^{1/2}$) shows that 3D random walks are fractal objects. That is, the relationship between their mass and their pervaded volume has the form $V \sim R^3 \sim M^{3/d}$, where the fractal dimension d is a measure of compactness. A rigid rod, a freely jointed chain, and a sphere have fractal dimension $d = 1, 2$ and 3 , respectively.

An actual polymer chain is composed of covalently linked atoms, which have specific bond distances and angles, a detail that is not captured by the freely jointed chain. A more sophisticated model for a polymer is the freely rotating chain (Figure 1.3), in which the angle θ between adjacent segments is fixed to a particular value (e.g. the carbon-carbon bond angle of 109°). From basic geometry we know that in such a chain the dot product of two successive segments is $\langle \mathbf{r}_i \cdot \mathbf{r}_{i+1} \rangle = b^2 \cos \theta$. This relationship defines the degree of correlation between adjacent segments and leads to the following decay in the orientational correlation between two segments with increasing separation (j segments) along the chain $\langle \mathbf{r}_i \cdot \mathbf{r}_{i+j} \rangle = b^2 (\cos \theta)^j$. Assuming that the number of segments (N) is large, this can be used to derive the end-to-end distance[6]

$$R_{e-e} \equiv \sqrt{\langle R_{e-e}^2 \rangle} = \left(\frac{1 + \cos \theta}{1 - \cos \theta} \right)^{1/2} bN^{1/2} \quad (1.5)$$

The addition of a fixed bond angle does not alter the scaling of R_{e-e} with N , but it indicates that for the freely rotating chain the random walk step length is no longer equal to the length of an individual segment. Regardless of the precise chemical nature of the backbone a polymer chain can be treated as a freely jointed chain in the limit of large N with $R_{e-e} = C_{\infty}^{1/2} b N^{1/2}$ where C_{∞} is the “characteristic ratio”. The physical interpretation of C_{∞} is the number of repeat units that must be lumped together to produce a “super bond” that has orientation uncorrelated with adjacent “super bonds” in the equivalent freely jointed chain (Figure 1.3). This leads to the definition of an equivalent segment length, the Kuhn segment[6], $l_k = C_{\infty} b$ such that $R_{e-e} = l_k N_k^{1/2}$ where the number of Kuhn segments $N_k = N/C_{\infty}$.

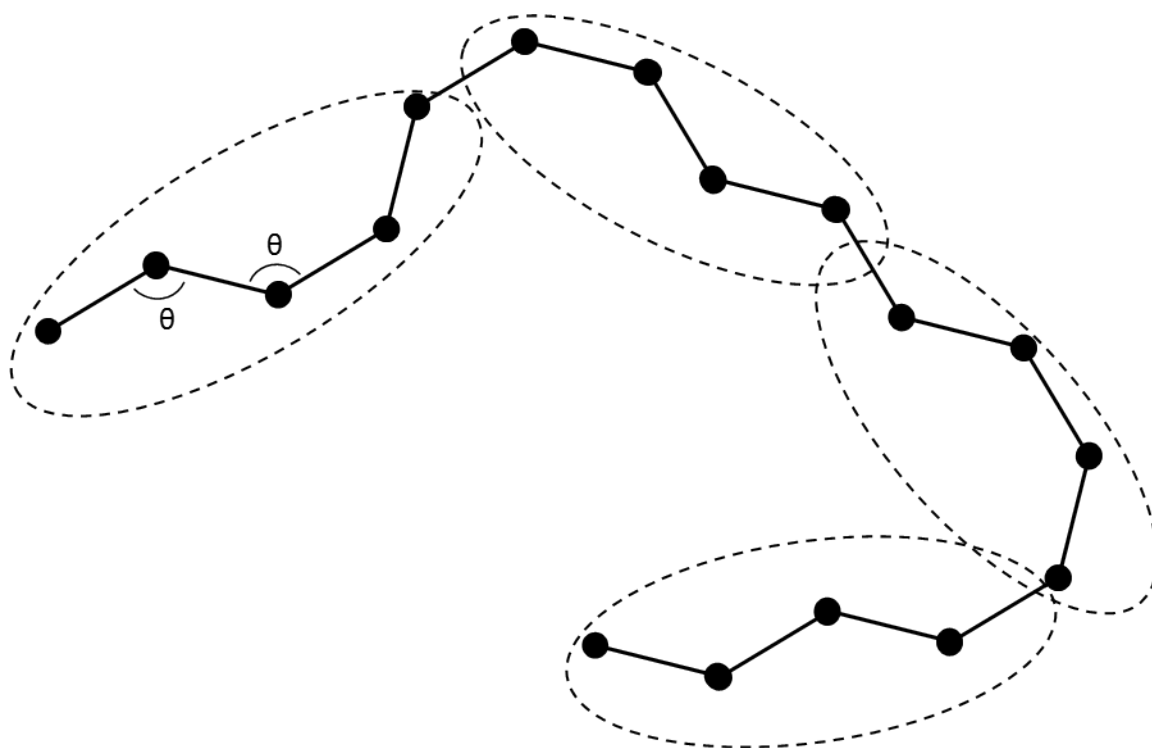


Figure 1.3: Schematic of a freely rotating chain. The angle between adjacent segments is fixed at a value of θ . The dashed ellipses show the Kuhn segments (four actual segments) that make the chain equivalent to a freely jointed chain made up of fewer, longer segments.

The magnitude of C_∞ is an indication of the local chain “stiffness” and is governed by monomer level structure. The length plays an important role in determining the stiffness/flexibility of the whole polymer chain. When $L \leq l_k$ the polymer behaves like a rigid rod with $R_{e-e} = L$. For chains with $L \gg l_k$ the freely jointed chain model holds and $R_{e-e} = l_k N_k^{1/2}$. Polymer chains that fall between these two limiting regimes must be treated by more sophisticated approaches such as the wormlike chain model[8]

$$R_{e-e}^2 = l_k^2 N_k - \left(\frac{l_k^2}{2}\right) (1 - e^{-2N_k}) \quad (1.6)$$

This model is appropriate for stiff polymeric systems (large C_∞) such as DNA but also captures both the rodlike and flexible coil polymer regimes in the limits of small and large N_k , respectively.

The end to end distance is straightforward to calculate, but is difficult to determine experimentally. It is also ill defined for polymers that are not simply linear, having branches or loops[6]. A more useful measure of the coil dimension is the radius of gyration

$$R_g \equiv \left(\frac{1}{N} \sum_{i=1}^N (\mathbf{R}_i - \mathbf{R}_{cm})^2 \right)^{1/2} \quad (1.7)$$

where \mathbf{R}_i is the position of an individual monomer and \mathbf{R}_{cm} is the position of the coil’s center of mass. R_g has the same scaling with N as R_{e-e} and is related to it by $R_{e-e} =$

$D \times R_g$, with D a constant and equal to $\sqrt{6}$ for a linear polymer chain[6]. The R_g is a meaningful measure of size, as it is the average distance of polymer segments from the center of the coil.

The interaction of the polymer and solvent plays an important role in determining the conformation (Figure 1.4). Solvent quality is related to the favorability of the solvent-polymer interaction as compared to the polymer-polymer interaction. In a “good solvent” the polymer-solvent interactions are more favorable and each polymer segment is surrounded by solvent molecules. This forbids conformations in which polymer segments cross[9], an effect known as excluded volume interaction. In a “theta solvent” polymer-polymer and polymer-solvent interactions are equivalent and the polymer follows unperturbed random walk statistics. In a “poor solvent” the polymer-solvent interactions are significantly less favorable than polymer self-interactions and solubility is limited.

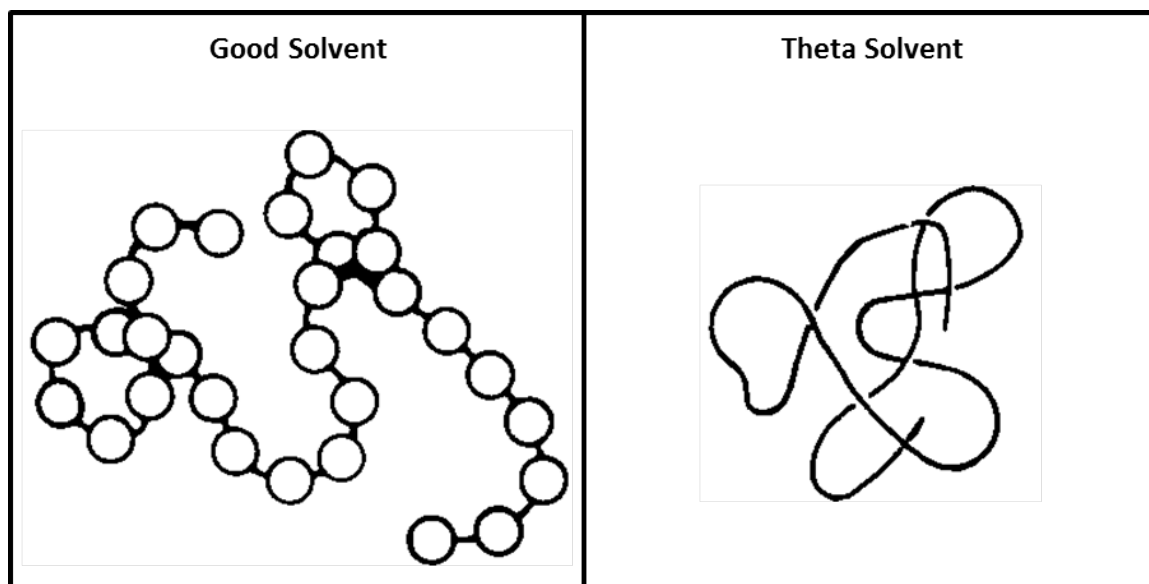


Figure 1.4: Effect of solvent quality on conformation. Identical polymer chains have a more expanded conformation in good solvent conditions (left) than in theta solvent conditions (right) due to excluded volume interactions. [Adapted from [9]]

The scaling relationship of Equation 1.4 can be generalized to $R_g \sim N^\nu$ where $\nu=0.5$ and $\nu \sim 0.6$ for theta and good solvent, respectively[6]. The subsequent arguments all remain valid with the exponent ν instead of $1/2$ in all of the equations. Solvent quality is temperature dependent and ideal theta conditions for a polymer-solvent pair occur at a particular temperature. For the case of polystyrene in cyclohexane the theta temperature is 34.5°C[4].

All of the preceding discussion applies to isolated polymer coils, corresponding to a very dilute solution. The volume pervaded by a polymer coil in solution is mostly solvent, with the density of segments $\rho \sim M^{1-3\nu}$ being much lower than the bulk polymer. For example, the pervaded volume of a polystyrene coil with $M_w=1000\text{kg/mol}$ in tetrahydrofuran (a good solvent) is only 0.4% polymer by mass. Thus, even at low absolute mass fractions of polymer in solution, the coils can overlap, leading to perturbed conformations. The overlap concentration C^* is defined as the concentration at which $V_{\text{sample}} = n_{\text{coil}} \times V_{\text{coil}}$ where V_{sample} is the total volume, n_{coil} is the number of polymer chains and V_{coil} is the pervaded volume of an individual polymer chain. This concentration can be very low for high molecular weight polymer. For example, the polystyrene mentioned above has C^* of approximately 0.1wt%. Thus polymer solutions have a semi-dilute concentration regime (Figure 1.5), for which $C^* < C \ll 100\text{wt}\%$.

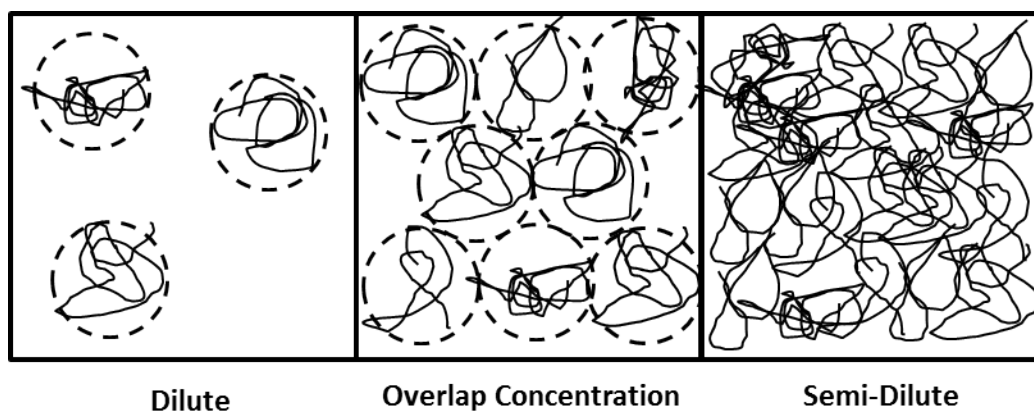


Figure 1.5: Concentration regimes for polymer solutions. In the dilute regime ($C < C^*$, left) the polymer coils are far apart and independent. At the overlap concentration ($C = C^*$, center) the volume of polymer coils is equal to the sample volume and the coils come into contact. In the semi-dilute regime ($C > C^*$, right) the polymer chains are overlapping and no longer distinguishable.

In the semi-dilute regime, the individual polymer chains overlap. This has a significant impact on rheological behavior, with the solution becoming much more viscous[4]. It also makes it impossible to distinguish individual polymer coils and to measure properties such as the R_g .

In this work we are interested in the effect of molecular architecture on the solution conformation of more complex macromolecules. This is done primarily through comparison to the behavior expected of a linear polymer chain in dilute solution. Linear chains are expected to have $R_g = D_\infty \times M_w^\nu$ where ν is the scaling (0.5 for theta solvent and 0.6 for good solvent) and D_∞ is a prefactor that is related to the chain stiffness. More complex macromolecules may follow similar scaling relationships, with different values of D_∞ and ν , or they may deviate from the simple power law behavior described here. The nature of these deviations provides insight into the relationship between architecture and conformation.

1.3 Experimental Characterization of Polymers

The M_w and PDI of a polymer sample are typically determined using Gel Permeation Chromatography (GPC), in which columns separate polymers by the size exclusion principle (largest comes out first)[4]. In the simplest variant, a differential refractometer (RI) detects changes in the refractive index of the eluent (Δn) which is proportional to the concentration of polymer through the constant (dn/dc) that depends on the polymer and solvent types. Using previously characterized monodisperse standards, a calibration curve $M_w(t)$ is obtained at the same instrumental configuration and used to convert the $C(t)$ data to $C(M_w)$ resulting in a plot similar to Figure 1.1. Obtaining reliable measurements by this method requires having high quality standards that are identical in topology and chemistry to the unknown polymer and span the relevant molecular weight range.

Using a Multi Angle Laser Light Scattering (MALLS) detector in series with the RI detector allows for the absolute determination of M_w without the use of standards[10]. For a given M_w fraction of polymer, the corresponding R_g is obtained from the angular dependence of the light scattering intensity. For objects that are small relative to the wavelength of light, the intensity of scattered light as a function of scattering angle is approximately:

$$\frac{R_\theta}{Kc} = M_w \left(1 - \left(\frac{16\pi^2}{3\lambda^2} \right) \right) \langle R_g \rangle^2 \sin^2 \left(\frac{\theta}{2} \right) \quad (1.8)$$

where R_θ is the Rayleigh ratio (directly proportional to the ratio of scattered intensity at angle θ to the incident intensity), K is an optical constant, c is the concentration, and λ is the laser wavelength[11]. A commonly used method (the Zimm method[11]) of obtaining

the M_w and R_g from experimental data is to plot Kc/R_θ vs $\sin^2(\theta/2)$ and fit the inverse of Equation 1.8

$$\frac{Kc}{R_\theta} = \frac{1}{M_w} + \frac{16\pi^2}{3\lambda^2} \frac{1}{M_w} \langle R_g \rangle^2 \sin^2\left(\frac{\theta}{2}\right) \quad (1.9)$$

Using this method, the M_w is obtained from the intercept and R_g from the slope of the line with concentration provided by the RI detector. Equation 1.8 is independent of the shape of polymer coils and can be used to characterize polymers of any architecture. Taking advantage of the separation by size, MALLS/GPC is able to directly provide $R_g(M_w)$ for polymers with sufficiently large R_g ($\geq 15\text{nm}$).

Scattering techniques are useful in obtaining more detailed information about polymer conformation. Small angle x-ray and neutron scattering techniques use much shorter wavelengths ($1 < \lambda(\text{\AA}) < 20$) and can probe features with length scales of 1 to 1000nm[12]. X-ray scattering derives its contrast from differences in electron density (proportional to the atomic number) between the polymer and the solvent. Typical polymers are composed primarily of carbon and hydrogen, as are most organic solvents, resulting in poor contrast for dilute solution samples[12]. Contrast in neutron scattering is derived from nuclear properties and has a strong dependence on the isotope with hydrogen and deuterium (^2H) having a very large difference in scattering length density (SLD, related to the scattering cross-section)[13]. The use of deuterated solvents with ordinary polymers provides strong contrast and allows high quality data to be obtained even from very dilute (0.1wt%) samples.

Unlike the light scattering described by Equation 1.8, which assumed that the polymer coil was much smaller than the wavelength of light, small angle neutron scattering (SANS) depends on the details of the structure. In an experiment, a collimated

beam of neutrons is directed at a sample and the scattered intensity is recorded as a function of scattering angle. The difference between these is the scattering vector \mathbf{q} which has magnitude

$$|\mathbf{q}| = q = \frac{4\pi}{\lambda} \sin\left(\frac{\theta}{2}\right) \quad (1.10)$$

where λ is the neutron wavelength and θ is the angle between the source and the detector. Higher magnitudes of q correspond to larger length scales, and for scattering from a pure crystal with spacing d the relationship is $q = 2\pi/d$. For purely elastic scattering from a set of N scatterers (such as the segments of a polymer chain) with SLD b_i and position \mathbf{r}_i , the scattering intensity $I(\mathbf{q})$ can be written

$$I(\mathbf{q}) = \sum_{i=1}^N \sum_{j=1}^N b_i b_j \langle e^{i\mathbf{q} \cdot (\mathbf{r}_i - \mathbf{r}_j)} \rangle \quad (1.11)$$

The right hand side of the scattering function (Equation 1.11) is often written as the product of two terms: the form factor $P(\mathbf{q})$ and the structure factor $S(\mathbf{q})$ with $I(\mathbf{q})=P(\mathbf{q})S(\mathbf{q})$. The form factor captures the scattering from a single polymer coil and the structure factor captures the inter-coil scattering. In the absence of long-range interactions, polymer coils in dilute solution are uncorrelated. Thus for dilute samples we can assume that $S(\mathbf{q}) = 1$ and that $I(\mathbf{q}) = P(\mathbf{q})$. Since it is not possible to invert Equation 1.11, the typical approach to analyzing SANS data is to propose model functions $P(\mathbf{q})$ with a few adjustable parameters and then fit these to experimental data. Structure factors $P(\mathbf{q})$ have been calculated for many simple objects (e.g. spheres, cylinders, micelles,...)[13].

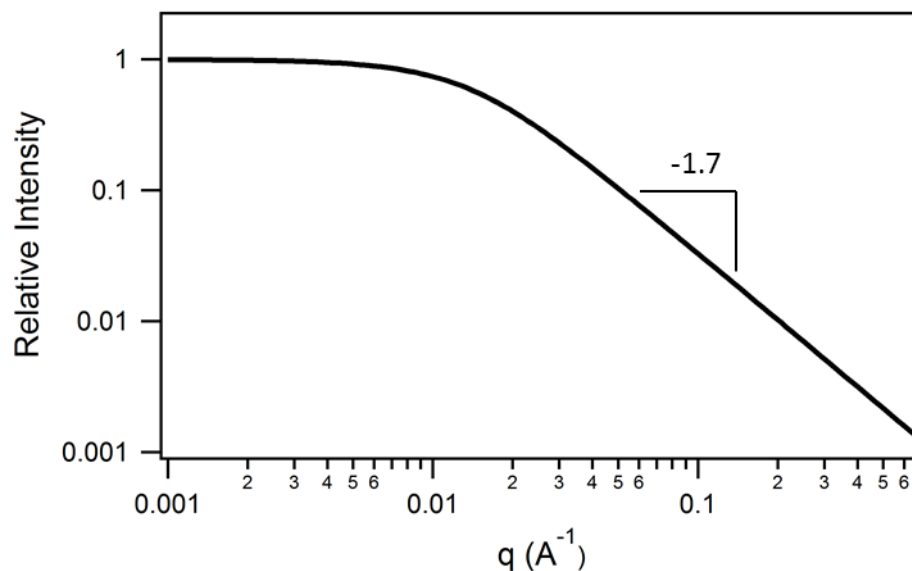


Figure 1.6: Scattering function of a polymer coil. This was calculated using the polymer excluded volume scattering function[14] in the IGOR Pro macros written by Steven Kline[15]. The particular coil used has $R_g=10\text{nm}$ and $\nu=0.6$.

The scattering function $P(q)$ for a polymer coil of $R_g=10\text{nm}$ in good solvent ($\nu=0.6$) (Figure 1.6) captures the main scattering features of a fractal object. At higher q (corresponding to length scales smaller than R_g) the scattering has power law behavior $I \sim q^{-m}$ known as Porod scattering[13] where $m = d = 1/\nu = 1/0.6 = 1.7$ is the mass fractal dimension. This is an extremely useful property, as it allows the scaling for a polymer coil to be measured directly. Moving to lower q corresponding to length scales larger than R_g , the scattering reaches a nearly q independent plateau corresponding to scattering from the whole coil. The position of the transition between the two behaviors and the slope of the plateau can be used to determine the R_g of the polymer coil. This mass fractal behavior of scattering from a polymer coil has been generalized to other mass fractal objects with $1 < d < 4$ by Beaucage[16, 17] and Hammouda[18]. Both the polymer specific and the general form factors are used in this work to obtain length scales and scaling laws for more complex polymeric structures.

Dynamic Light Scattering (DLS) measures the scattering from a small sample volume at very short intervals and determines the correlation of scattering intensity fluctuations with time[4]. The scattering intensity is due mainly to the local concentration fluctuations caused by Brownian motion. The rate of decay of correlation provides information about the relative motion of the polymer coils (or other particles). Through very fast acquisition of intensity data (<1 μ s per measurement), a normalized time autocorrelation function is obtained[19]

$$g^{(2)}(\tau) = \frac{\langle I(t)I(t + \tau) \rangle}{\langle I(t) \rangle^2} \quad (1.12)$$

where $I(t)$ is the intensity at time t , $I(t+\tau)$ is the intensity at time $t+\tau$, and the brackets indicate an average over t . Equation 1.12 can be transformed, through the Siegert relation, into the form $g^{(2)}(\tau) = B + \beta[g^{(1)}(\tau)]^2$ where B is the background intensity (close to 1), β is an instrumental constant, and $g^{(1)}(\tau)$ is the first order autocorrelation function[20]. For the simplest system (monodisperse spherical particles in very dilute solution) there is only one correlation time, τ , and the correlation function decays exponentially[20] $g^{(1)}(\tau) = \exp(-\Gamma\tau)$, with decay rate $\Gamma = Dq^2$ where D is the diffusion coefficient and q is the scattering vector defined in Equation 1.10. The diffusion coefficient can then be related to the particle radius using the Stokes-Einstein equation[21]

$$D = \frac{kT}{6\pi\eta R_h} \quad (1.13)$$

where k is the Boltzmann constant, η is the solvent viscosity, T is the temperature, and R_h is the hydrodynamic radius. For polydisperse systems (such as polymers in solution) $g^{(1)}(\tau)$ cannot be represented as a single exponential. In this case the method of cumulants[22] can be used to obtain the average decay rate $\bar{\Gamma}$ through a power series expansion method. This can then be used to determine the average diffusion coefficient and the average R_h . R_h is only equal to the actual radius for solid spherical particles. In all other cases it is an equivalent radius, corresponding to the size of sphere that would diffuse at the rate observed for the material of interest.

The hydrodynamic radius is another useful measure of the conformation of a polymer coil. It is the relevant size for separation by GPC columns and is an indication of the effect that a polymer will have on the viscosity of a solution. The ratio of the two characteristic radii (R_g/R_h) can be used to study the compactness of a particle. For a solid spherical particle the R_h is equal to the radius while R_g is smaller than the sphere, giving $R_g/R_h \sim 0.8$. Using published experimental data for polystyrene[23], we estimate $R_g/R_h \sim 1.3$ and 1.4 for a 100kg/mol linear polymer in theta solvent and good solvent, respectively. Thus the R_g/R_h ratio is related to the scaling exponent ν , which is $1/3$, $1/2$, and $3/5$ for a solid sphere, a polymer in theta solvent, and a polymer in good solvent, respectively.

1.4 Architecturally Complex Macromolecules

The solution behavior of linear polymer chains is well understood, having been the subject of intense study throughout the previous century. As plastics became ubiquitous in everyday life, polymer science grew into a major field of study. The work of many brilliant chemists and physicists (including several Nobel Laureates) has laid the

foundation for understanding more advanced polymeric materials. Developments in synthetic techniques have led to the creation of precision tailored polymeric materials with varied topology and functionalities.

In order to design materials with the desired properties, it is imperative to understand the relationships between polymer architecture and their conformation and behavior. In this work, we use the techniques developed for the characterization of linear polymers to investigate the conformation and self-assembly of macromolecules with rich and varied behaviors driven by the resolution of intramolecular conflicts. The work within this thesis is divided into sections, each focusing on a different type of macromolecule.

1.4.1 Bottlebrush Polymers (Chapters 2 and 3)

Bottlebrush polymers have polymeric side-chains covalently linked to every backbone repeat unit. The competition between the conformational freedom of the side-chains and the backbone is resolved by a conformational compromise. The backbone becomes extended, giving up some configurational entropy, and allowing the side-chains to retain essentially unperturbed conformations. The conformation of a bottlebrush polymer in solution is determined largely by the length and chemical composition of the side-chains (as long as the backbone is longer than the side-chains with a cylindrical, rather than spherical, composition).

In Chapter 2 we describe the development of a robust and facile synthetic approach to bottlebrush polymers, improving upon an approach developed by previous work in the Kornfield lab. This method is then used to synthesize a homologous series of bottlebrush polymers, systematically varying the side-chain and backbone length. We

take advantage of the modular synthetic approach to make matched sets of bottlebrushes with regular and deuterated side-chains (providing contrast matching for SANS experiments). A series of bottlebrushes with poly(tert-butyl acrylate) side chains are deprotected, resulting in water soluble bottlebrushes with poly(acrylic acid) side-chains.

In Chapter 3 we use a variety of scattering methods (MALLS, DLS and SANS) to study the conformation of bottlebrush polymers in solution. The effects of side-chain and backbone length on the conformation are studied in both good and theta solvent conditions. The side-chain conformation is obtained from a series of SANS experiments and is determined to be indistinguishable from the behavior of free linear polymer chains. Using the deuterium labeled bottlebrushes, we are able for the first time to directly observe the conformation of the backbone of a bottlebrush polymer.

1.4.2 Side-Group Liquid Crystalline Polymers in Liquid Crystalline Solvent (Chapter 4)

Side-Group Liquid Crystalline Polymers have mesogens, resembling small molecule liquid crystals (LCs), covalently linked to a flexible backbone. They combine the entropic flexibility of a linear polymer with the anisotropic optical and electromagnetic properties of small molecule liquid crystal. When dissolved in a small molecule LC, SGLCPs take on either oblate or prolate ellipsoid conformations, with the aspect ratio and orientation determined by the nature of the side-group.

In Chapter 5 we describe a series of SANS experiments on a homologous series of SGLCPs in deuterated small molecule liquid crystal. The samples are aligned and monodomain, allowing the orientation and anisotropy of the polymer coils to be measured. A series of block copolymers, having SGLCP blocks covalently linked to a

linear polystyrene block, are studied under the same conditions. They are determined to self-assemble into complex micellar structures with mutually orthogonally oriented anisotropies at different length scales.

1.4.3 Complementary Associating Polymers for Mist Control Kerosene (Chapter 5)

Complementary associating polymers have long linear backbones with associative groups at both ends. Using complementary end groups A and B (with each chain having either A or B end-groups) results in the formation of linear and cyclic supramolecules of much higher molecular weight than the individual chains. This molecular design has been developed in the Kornfield lab in order to combine mist suppression and resistance to shear degradation, needed for the development of fire safer fuels. A series of polymers with varied backbone molecular weight and end-group types has been synthesized in the Kornfield lab. In Chapter 5 we present the results from the first scattering experiments allowing direct characterization of the conformation and self-assembly of fuel soluble pairwise complementary associating telechelic polymers.

1.4.4 Theoretical Study of Membrane Particle Interaction (Appendix A)

Vesicle membranes are composed of a bilayer of surfactant molecules self-assembled into a spherical shell. Although they are not linear polymeric structures, they are also macromolecules with non-covalent interactions holding together the constituent molecules of the structure. Appendix A describes purely theoretical work conducted under the supervision of Zhen-Gang Wang during my first year at Caltech. The work described is the calculation of the energy barriers involved in the adhesion of a vesicle

membrane to a spherical particle. Using a simple, elastic model of the membrane, we evaluate the contribution of the curvature free energy to the adhesion barrier.

References

1. Cohen, J.E., *Human population: the next half century*. science, 2003. **302**(5648): p. 1172-1175.
2. Khundkar, L.R. and A.H. Zewail, *Ultrafast molecular reaction dynamics in real-time: progress over a decade*. Annual Review of Physical Chemistry, 1990. **41**: p. 15-60.
3. Callen, H.B., *Thermodynamics and an introduction to thermostatistics*. 2nd ed. 1985, New York: Wiley. xvi, 493 p.
4. Sperling, L.H., *Introduction to physical polymer science*. 4th ed. 2006, Hoboken, N.J.: Wiley. xxx, 845 p.
5. Odian, G.G., *Principles of polymerization*. 4th ed. 2004, Hoboken, N.J.: Wiley-Interscience. xxiv, 812 p.
6. Rubinstein, M. and R.H. Colby, *Polymer physics*. 2003, Oxford ; New York: Oxford University Press. xi, 440 p.
7. Hill, T.L., *An introduction to statistical thermodynamics*. 1986, New York: Dover Publications. xiv, 508 p.
8. Norisuye, T., *Semiflexible polymers in dilute solution*. Progress in polymer science, 1993. **18**(3): p. 543-584.
9. Flory, P., *Spatial Configuration of Macromolecular Chains*, in *Nobel Lecture* 1974.
10. Wyatt, P.J., *Light scattering and the absolute characterization of macromolecules*. Analytica chimica acta, 1993. **272**(1): p. 1-40.
11. Andersson, M., B. Wittgren, and K.-G. Wahlund, *Accuracy in Multiangle Light Scattering Measurements for Molar Mass and Radius Estimations. Model Calculations and Experiments*. Analytical Chemistry, 2003. **75**(16): p. 4279-4291.
12. Roe, R.J., *Methods of X-ray and neutron scattering in polymer science*. Topics in polymer science. 2000, New York: Oxford University Press. xiv, 331 p.
13. Higgins, J.S. and H. Benoît, *Polymers and neutron scattering*. 1994: Clarendon Press Oxford.
14. Hammouda, B., *SANS from homogeneous polymer mixtures: a unified overview*, in *Polymer Characteristics*. 1993, Springer. p. 87-133.
15. Kline, S.R., *Reduction and analysis of SANS and USANS data using IGOR Pro*. Journal of applied crystallography, 2006. **39**(6): p. 895-900.
16. Beaucage, G., *Approximations leading to a unified exponential/power-law approach to small-angle scattering*. Journal of Applied Crystallography, 1995. **28**(6): p. 717-728.
17. Beaucage, G., *Small-angle scattering from polymeric mass fractals of arbitrary mass-fractal dimension*. Journal of Applied Crystallography, 1996. **29**(2): p. 134-146.
18. Hammouda, B., *A new Guinier-Porod model*. Journal of Applied Crystallography, 2010. **43**(4): p. 716-719.
19. Berne, B.J. and R. Pecora, *Dynamic light scattering : with applications to chemistry, biology, and physics*. Dover ed. 2000, Mineola, N.Y.: Dover Publications. vii, 376 p.
20. Frisken, B.J., *Revisiting the method of cumulants for the analysis of dynamic light-scattering data*. Applied Optics, 2001. **40**(24): p. 4087-4091.

21. Deen, W.M., *Analysis of transport phenomena*. Topics in chemical engineering. 1998, New York: Oxford University Press. xix, 597 p.
22. Koppel, D.E., *Analysis of Macromolecular Polydispersity in Intensity Correlation Spectroscopy: The Method of Cumulants*. The Journal of Chemical Physics, 1972. **57**(11): p. 4814-4820.
23. Fetters, L., et al., *Molecular weight dependence of hydrodynamic and thermodynamic properties for well-defined linear polymers in solution*. Journal of physical and chemical reference data, 1994. **23**(4): p. 619-640.

*Chapter 2***Robust and Modular Synthesis of Bottlebrush Polymers****2.1 Introduction**

Bottlebrush polymers (also referred to as cylindrical polymer brushes, poly(macromonomers) or molecular brushes) consist of polymeric side chains densely grafted to a flexible backbone[1, 2]. The interplay between excluded volume interactions among the side chains and the inherent entropic flexibility of the backbone leads to a fascinating range of conformations and self-assembled structures in solution[3], the solid state[4, 5], and on surfaces[6]. Their behavioral diversity has led to a strong interest on both the theoretical [7-9] and experimental [10-12] fronts. Significant controversy remains as to the dependence of the conformation in solution upon the many relevant parameters (side-chain length[13], side-chain chemistry[14], backbone length[12], the grafting density[15], and the solvent quality[16]) and much of the work in the field is fragmented. Studies of matched sets of bottlebrushes independently varying the relevant parameters would help to resolve some of the discrepancies seen in the data. However, the synthesis of bottlebrush polymers with precise control over the size and architecture remains challenging.

Three synthetic approaches have been used to prepare bottlebrush polymers (Figure 2.1): “grafting-from”, “grafting-to”, and “grafting-through”[1, 2]. In grafting-from, a backbone containing many initiating sites is prepared and serves as the macroinitiator for the polymerization of monomers [15, 17-23]. In grafting-to, backbones and side-chains are prepared separately and then coupled together [24-29]. Grafting-through involves the polymerization of appropriately end-functionalized polymers

(referred to as macromonomers)[30-38]. All three have been of interest to polymer chemists due to the challenge presented by the high degree of crowding and extremely large molecular masses of bottlebrush polymers.

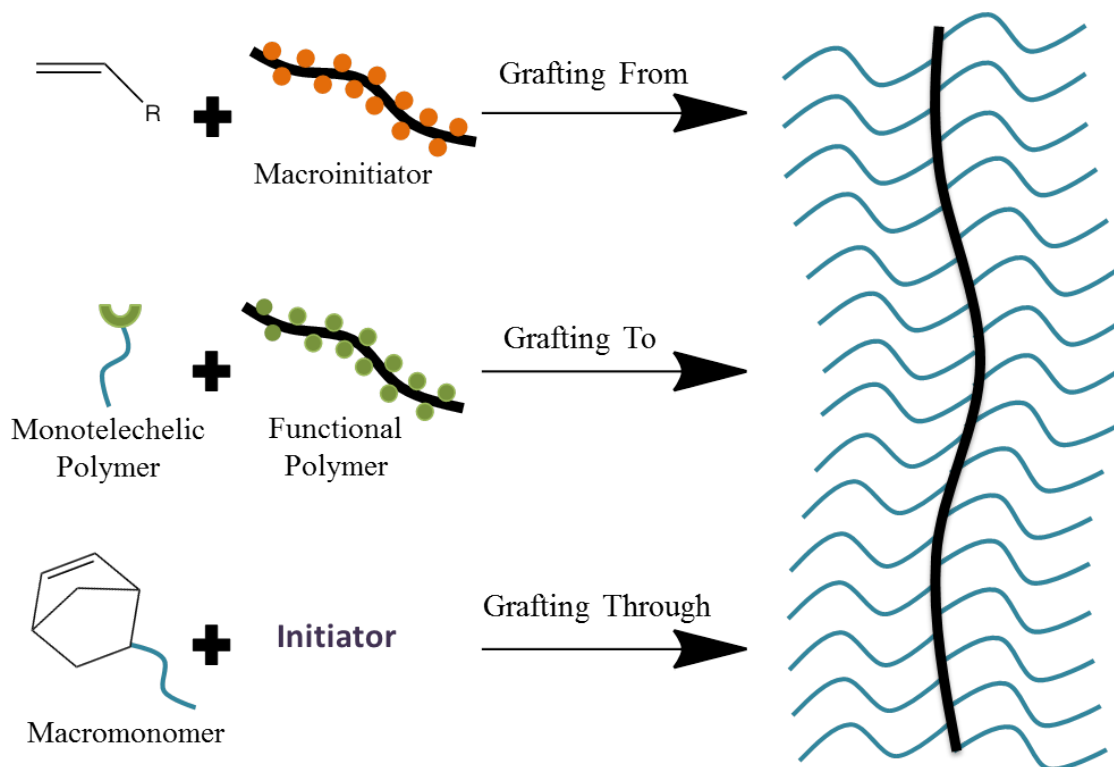


Figure 2.1: Synthetic approaches to making bottlebrush polymers. The top is “grafting-from” in which a backbone containing initiation sites is used as the macro-initiator for polymerization, growing the side-chains *in situ*. The middle is “grafting-to” in which end-functionalized side chains are grafted to a backbone having complementary functionality (e.g. azide-alkyne or thiol-ene click chemistries). The bottom and preferred method is “grafting-through”, also known as the macromonomer approach, where end functionalized polymer chains are used as the monomers in a polymerization.

The grafting-from method has been the most frequently used and is generally able to achieve the highest molecular masses of any method (up to 6.4×10^7 g/mol), but it is generally not possible to definitively characterize the length and polydispersity of the side chains independent of the backbone. Additionally, the effect of local segment density on the rate of propagation leads to the possibility of systematic non-uniformity in the side-chain lengths (e.g. having short arms next to long ones). The grafting density is also

uncertain, as it is extremely difficult to determine the percentage of initiating sites involved in polymerization and the initiation efficiency may be limited[39]. Grafting-to provides the advantage of being able to characterize both the backbone and the side-chains independently, but the degree of conversion is often limited and strongly dependent upon the length and composition of side-chains[1], and the presence of residual unreacted side-chains can cause complications.

For those interested in the physics of bottlebrush polymers, the grafting-through or poly(macromonomer) approach presents the best balance of control and achievable molecular weight. The length and polydispersity of the side-chains are well characterized and precisely matched for a series of bottlebrushes of different backbone lengths grown from a given batch of macromonomer. The grafting density is precisely determined and uniform with every backbone monomer carrying a side-chain. The overall molecular weight and polydispersity of each batch of bottlebrushes is all that remains to be determined and are readily characterized.

All three approaches have seen a resurgence of interest with the development of polymerization methods (Atom Transfer Radical Polymerization(ATRP)[40] and Ring Opening Metathesis Polymerization(ROMP) with Grubbs catalyst[41, 42]) that offer more tolerance of functional groups and less stringent purification requirements than anionic polymerization, while retaining precise control over the molecular weight and polydispersity[43]. The combination of ATRP,ROMP and highly efficient “click” coupling chemistry [44, 45] allows for the synthesis of precisely defined bottlebrush polymers[33]. Our goal was to use and refine this synthetic procedure to allow for the

modular and facile synthesis of matched sets of bottlebrush polymers with varied side-chain chemistries, side-chain lengths, and overall molecular weight.

The chosen approach, following Xia et al.[33], was to first synthesize an alkyne functionalized exo-norbornene (much higher reactivity than endo[46]). This allows for azide-alkyne “click” chemistry to be used to couple this polymerizable moiety to any azide functionalized side-chain. ATRP is used to create monodisperse polymers with terminal bromine functionality which can then be easily and quantitatively converted into an azide. Subsequently this is coupled to the exo-norbornene through the use of “click” chemistry, resulting in a stable and easily polymerized macromonomer.

It was observed that the purity of the macromonomer was critical to the success of the subsequent ROMP and some impurities could not be removed by precipitation. Thus a chromatographic purification method was developed that took advantage of the large difference in molecular weight between the desired macromonomer and small molecule contaminants, along with a gradient solvent system, resulting in highly pure macromonomers. This straightforward and fast purification method dramatically increased the subsequent conversion in ROMP of macromonomers with conversion >94% in all cases and >98% in most. The high purity of the resulting bottlebrushes is vital to obtaining reliable measurements of physical properties, which may be influenced by the presence of short polymer chains.

Prior literature shows that polymer backbones with side-chains length (N_s) of less than ~20 repeat units do not show the stiff and expanded conformation characteristic of bottlebrushes[37]. When the length of the backbone (N_b) is less than or equal to N_s , the molecule resembles a star polymer (with spherical symmetry)[47]. The N_b should be

greater than N_s in order for the molecules to have a flexible cylindrical conformation. Both in previous literature and our attempts, it was determined that $N_s \sim 100$ and $N_b \sim 1000$ represent the attainable limits. Thus the sizes chosen for the molecules in this work had $20 < N_s < 100$ and $200 < N_b < 1200$.

The functional group tolerance of the Grubbs 2nd generation catalyst allows for the use of any of the monomers compatible with ATRP in the synthesis of the macromonomers. In order to compare our results to previous work[3, 37] and have a good understanding of the side-chain polymers, polystyrene was used as a side-chain material. The availability of perdeuterated styrene (styrene-d8) allowed the synthesis of deuterium labeled macromonomers, providing contrast for neutron scattering and NMR experiments and allowing the backbone conformation to be studied. We also used tert-butyl acrylate in the synthesis of macromonomers, allowing for the study of matched pairs of neutral and polyelectrolyte bottlebrushes by transforming the neutral bottlebrushes into polyelectrolytes through removal of the tert-butyl protecting groups.

Here we report the successful synthesis of matched series of bottlebrush polymers with polystyrene (PS), deuterated polystyrene (dPS), and poly(tert-butyl acrylate) side-chains by the grafting-through of macromonomers. Two side-chain lengths and several backbone lengths were prepared for each macromonomer type with all lengths being reasonably well-matched, allowing for comparison. The resulting bottlebrush polymers were subsequently characterized by Gel Permeation Chromatography (GPC) with Multi Angle Laser Light Scattering, enabling the molecular weight and radius of gyration to be determined. The resulting bottlebrush materials reached molecular weights pushing the boundaries of sizes previously achieved while maintaining excellent conversion of

macromonomer and low polydispersity. The reaction procedure is repeatable, reliably controlled, and modular, allowing for facile synthesis of model polymers for bottlebrush studies.

2.2 Experimental

2.2.1 Materials

Styrene and 10-undecyn-1-ol (98%) were purchased from TCI America. Styrene-d₈ was purchased from Polymer Source. Deuterated Chloroform (CDCl₃) w/o TMS was purchased from Cambridge Isotope Laboratories. Tetrahydrofuran (THF, ACS grade, manufactured by EMD), Hexanes (ACS Grade, manufactured by BDH), Ethyl Acetate (HPLC grade, manufactured by J.T. Baker) and Dichloromethane (DCM, ACS Grade, manufactured by J.T. Baker) were purchased from VWR. N-(3-Dimethylaminopropyl)-N'-ethylcarbodiimide hydrochloride (EDC, >99%) was purchased from ProteoChem. Exo-5-Norbornene-2-Methanol (97%) was purchased from Frinton Laboratories. All other chemical reagents were purchased from Sigma Aldrich and used as received.

2.2.2 Characterization Methods

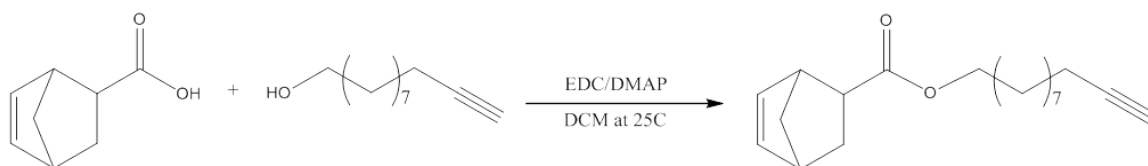
¹H NMR spectra were taken in CDCl₃ on a 500MHz Varian Inova spectrometer using a 2 second relaxation delay and taking either 32 or 64 scans. Samples were prepared by weighing out 5-10mg of sample into a scintillation vial, adding 0.7-1mL of CDCl₃ and either shaking until homogeneous for small-molecules or placing on wrist action shaker for 30 minutes for polymer samples.

Gel Permeation Chromatography was used to determine molecular weight and polydispersity for polymers. The system used a multi detector configuration, combining a

Wyatt DAWN EOS Multi-Angle Light Scattering detector ($\lambda=690\text{nm}$) with a Waters 410 differential refractometer ($\lambda=930\text{nm}$) connected in series to obtain detailed information about the polymers[48]. Chromatographic separation was achieved by using four Agilent PLgel columns (pore sizes $10^3, 10^4, 10^5$, and 10^6 Å) connected in series to provide separation over a molecular weight range of 500 to 10,000,000 g/mol. Degassed THF at 35°C and a flow rate of $0.9\text{mL}/\text{min}$ was used as the mobile phase. The time for complete elution through all four columns was about 50 minutes. Samples were prepared by dissolving 5.0mg of polymer in 1.00mL of THF and filtering the solution through a $0.45\mu\text{m}$ PTFE membrane syringe filter immediately before injection. Data was analyzed using Wyatt Astra Software (version 5.3.4) and dn/dc determined by the 100% mass recovery method. This method returned the molecular weight (M_w) and polydispersity (PDI) for a polymer sample and also used a proprietary method based on the Berry fitting formula[49] to obtain the radius of gyration (R_g).

Thin Layer Chromatography (TLC) was done using J.T. Baker silica gel IB-F plastic backed plates. The results were visualized in two ways: fluorescent compounds were revealed under short wave UV light while all others were seen by developing the plate using an iodine vapor chamber. The iodine reacts with most compounds, resulting in yellow spots on the plate.

2.2.3 Synthesis of Alkyne terminated Norbornene



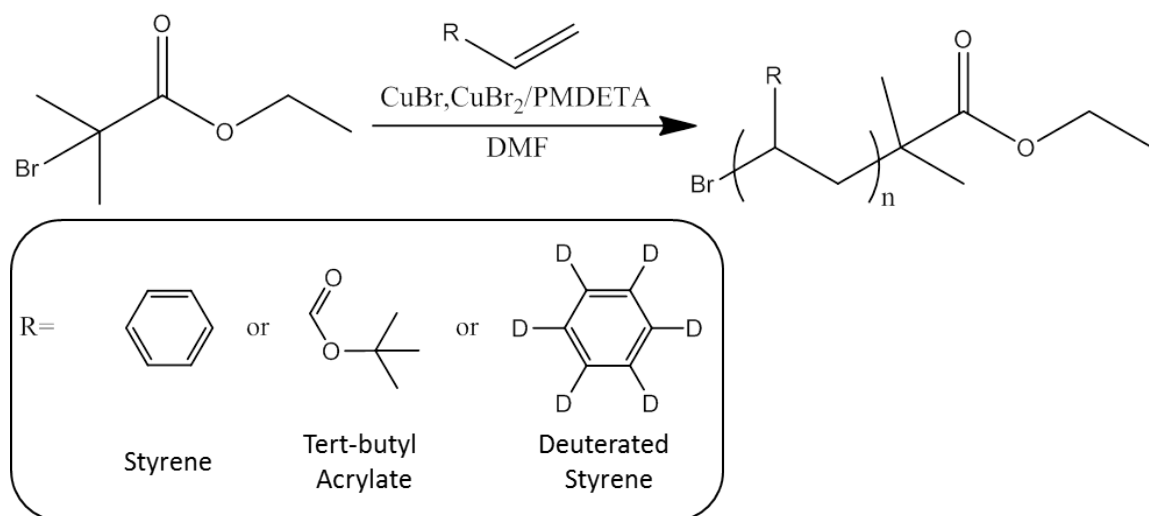
Scheme 2.1: Synthesis of “clickable” norbornene-alkyne.

A 250mL round bottom flask was charged with a PTFE coated stirbar, oven dried, and allowed to cool to room temperature. Exo-5-Norbornene-2-carboxylic acid (3.75g) was added to the flask, along with 1.05 molar equivalents of 10-Undecyn-1-ol (5g) and Dichloromethane (125mL). One third of a molar equivalent (1.09g) of 4-(Dimethylamino)pyridine (DMAP) was added to the flask, which was placed in an ice water bath on a magnetic stirrer and allowed to stir until all solids were completely dissolved. At this time 1.25 molar equivalents (6.6g) of N-(3-Dimethylaminopropyl)-N'-ethylcarbodiimide hydrochloride (EDC) were slowly added to the flask while keeping the solution at 0°C and vigorously stirring. The flask was capped with a rubber septum and purged with Argon (Ar) for 10 minutes. The water bath temperature was set to 25°C and the solution left to stir overnight.

The reaction mixture was transferred to a 500mL separatory funnel along with 200mL of DI water. This was shaken vigorously, allowed to settle, and the cloudy aqueous top layer was discarded. This washing process was repeated three times to remove the water soluble urea and excess EDC. The organic phase was then washed with 200mL of 1M hydrochloric acid to remove residual DMAP and lastly with 200mL of brine (saturated NaCl solution) in order to remove water from the organic phase. The organic phase was collected into an Erlenmeyer flask containing NaSO₄. The brine was extracted twice with 50mL of DCM which was combined with the organic phase. The organic phase was allowed to dry for one hour, swirling occasionally. After filtering to remove solid NaSO₄ it was rotovapped down to a clear, yellow oil. TLC using 30:70 ethyl acetate/hexanes as the eluent showed two spots: one with high mobility corresponding to the product and another with low mobility containing residual reactants.

The crude product (8.6g) was purified by flash chromatography using silica gel as the static phase and 10:90 ethyl acetate:hexanes as the mobile phase. 30mL fractions were collected in test tubes (20 fractions for a total of 600mL). Fractions were tested by TLC and fractions 9 through 16 were found to contain product. Interestingly these also showed something like condensation or “legs”, with droplets beading up on the walls above the meniscus. These fractions were combined and rotovapped down to a clear oil which was placed under high vacuum at room temperature overnight, resulting in 6.9 grams of pure product (88% yield). A reddish band remained at the top of the silica gel similar in color to the 5-norbornene-2-carboxylic acid as it was supplied. This indicates that some unknown impurity was present in the acid starting material, but removed by the column. The density of the pure norbornene-alkyne was determined to be 0.97g/mL by weighing a 100uL sample as measured out by a 100uL precision syringe.

2.2.4 Typical ATRP procedure for tert-butyl acrylate, styrene, and deuterated styrene



Scheme 2.2: Atom Transfer Radical Polymerization of styrene, tert-butyl acrylate, and styrene-d₈

The batch sizes ranged from 2g to 20g and the monomer to initiator ratios were varied from 80:1 to 300:1 to achieve the desired N_s ; therefore the procedure is presented in terms of molar ratios relative to the initiator and noting differences between the different monomer types. The percentage of chains retaining their bromine functionality falls off rapidly at higher conversion percentages[50], resulting in chains that cannot be functionalized. This was avoided by selecting monomer/catalyst ratios that would result in higher than desired molecular weight and terminating at conversions below 70%. It has been shown that using a reducing agent to regenerate the halide species as in ARGET ATRP greatly improves the retention of functionality[51]. Since the ligand itself can be used as a reducing agent for this purpose[52] an excess of the nitrogen-based ligand, PMDETA, was used.

The monomer was removed from the refrigerator, allowed to come to room temperature, and 1.5 times the amount needed was passed through a column of activated basic alumina to remove the inhibitor. For the deuterated styrene a miniature column was used, made by placing a small wad of glass wool into a Pasteur pipette. An oven dried Schlenk flask was charged with an egg shaped PTFE stirbar and the desired volume of monomer was added to the flask using a disposable syringe. Anhydrous DMF (0.2 equivalents by volume) was added using another disposable syringe. The initiator, Ethyl α -Bromoisobutyrate (eBiB), was added by precision syringe. The ligand, Pentamethyldiethylenetriamine (PMDETA), was added by precision syringe volumetrically measuring out 0.4 molar equivalents to the eBiB. The reactor was sealed with a septum and was degassed by three Freeze-Pump-Thaw cycles using an LN_2 (liquid

nitrogen) bath to freeze the solution and a heat gun to thaw it, pumping down the vessel to 100mTorr and refilling the reactor with argon after each thaw.

The frozen solution was pumped down again. The flask was removed from the LN₂ bath (to avoid freezing argon) and the septum removed with argon flowing. The solid copper catalysts (CuBr and CuBr₂ using 0.2 and 0.02 molar equivalents to eBiB) were added and the septum replaced. The flask was again lowered into LN₂ and the head space was pumped down to 100mTorr and subsequently filled with argon, repeating this procedure three times. While under vacuum the solution was thawed. The flask was filled with argon and disconnected from the Schlenk line.

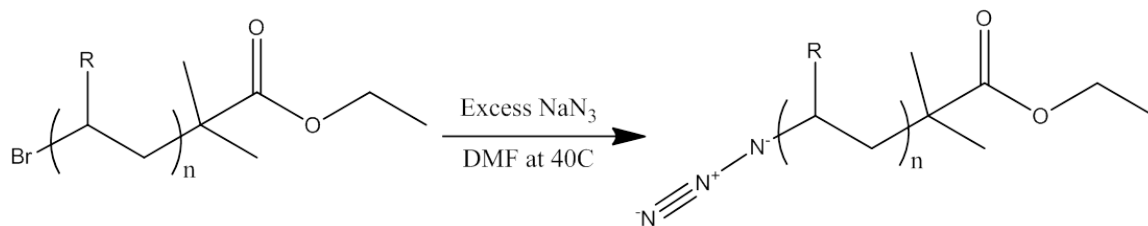
The flask was placed into an oil bath on a magnetic stir plate and was reacted, stirring vigorously, at either 65°C (tert-butyl acrylate) or 95°C (styrene and styrene-d₈) until the target conversion was reached (typically between 6 and 32 hours). The flask was removed from the oil bath and the reaction quenched by plunging the flask into LN₂. The viscous reaction mixture was diluted with a volume of THF approximately equal to the reaction volume and passed through a column of neutral alumina, continuing to flow through THF until the outflow became very rapid indicating complete elution of the polymer. Afterwards the packing material had a dark blue band at the very top and a lighter blue color spreading through the packing caused by the retained copper. If insufficient column length was used for the catalyst loading, the blue color would extend all the way to the bottom and the solution retained a greenish color that was removed by a second column.

The resulting colorless polymer solution was reduced in volume by rotary evaporation to a viscosity that was just able to be transferred by a pipette. This was

precipitated by pipetting the solution into a large volume (200mL for a 2g batch of polymer) of vigorously stirred solvent. The solvent was a good solvent for the monomer and a poor solvent for the polymer, with MeOH used for PS and 20:80 H₂O:MeOH mixture used for PtBA.

The styrene based polymers precipitated cleanly into a white powder that was collected by vacuum filtration, transferred into a glass vial and placed under high vacuum overnight to dry. The PtBA was near/above its glass transition and was swollen, having a gooey consistency. It tended to stick to PTFE stirbars, necessitating the use of glass stirbars (problematic due to their frequent breakage under the aggressive stirring used for precipitation). The solid was carefully collected out of the precipitating solvent using a metal spatula and scraped into a large jar. When placed into the vacuum oven, the polymer foamed and expanded to many times its original size. Once dry the polymer was glassy and the brittle foam was crushed into powder for easier handling.

2.2.5 Conversion of Terminal Bromine to Azide

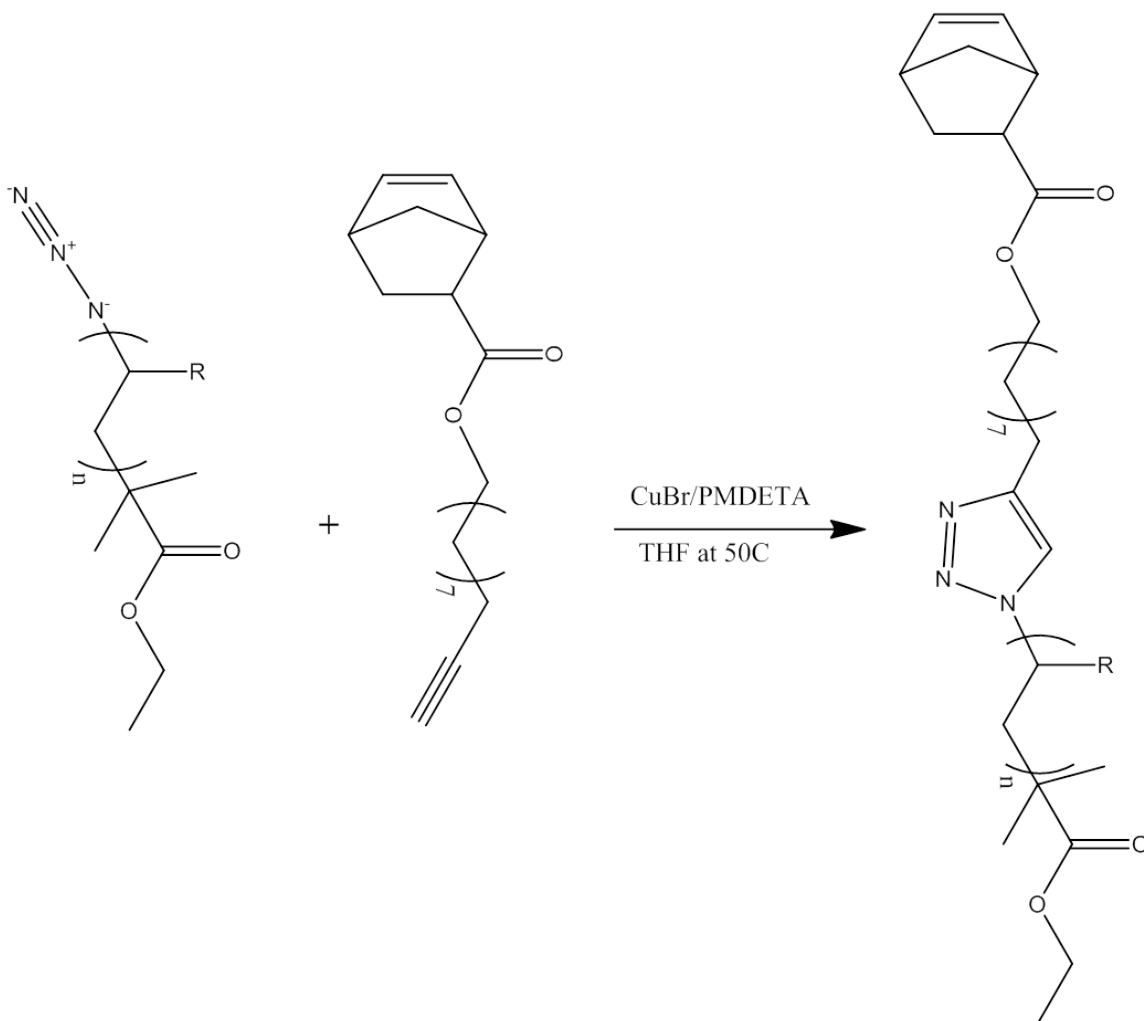


Scheme 2.3: Conversion of bromine terminated polymer to azido-terminated polymer

The polymer from section 2.2.4 was dissolved in sufficient DMF to bring the concentration to approximately 0.1g/mL. This was transferred into a round bottom flask with a PTFE stirbar and NaN₃ (10 equivalents to the end-group) was added to the flask. The flask was stirred at 40°C overnight. The reaction mixture appeared opaque and

yellowish and once stirring was turned off, a whitish precipitate (presumed to be a mixture of NaBr and NaN₃) settled on the bottom of the flask. DCM was added to the flask and swirled until homogeneous, resulting in further precipitation. The liquid was then poured into a separatory funnel containing a mixture of deionized water and ice and shaken thoroughly (the mixing is highly exothermic). The reaction vessel was rinsed with DCM several times into the separatory funnel. The aqueous phase was discarded and the organic phase washed with water three more times, followed by 1M HCl and finally brine. Upon shaking the mixture appeared foamy (most likely due to the polymeric nature of the product) and was allowed to settle for several hours, resulting in three layers: clear organic layer at the bottom, a clear aqueous layer at the top, and a thin, opaque, foamy band between them indicating incomplete separation. The clear organic layer was collected, dried over NaSO₄, filtered, and solvent transferred to THF (rotovapping the solution to a very thick liquid and adding THF, repeating the cycle three times). This was used as the starting point for the subsequent click reaction.

2.2.6 Click coupling of azido terminated polymer to norbornene-alkyne



Scheme 2.4: “Clicking” the Norbornene-Alkyne to the azido terminated polymer. The R group is the pendant group of the monomer type (styrene, styrene-d8, or tert-butyl acrylate) as seen in Scheme 2.2.

The azido-terminated polymer solution from the previous step was transferred into a Schlenk flask charged with a PTFE stirbar. Norbornene-alkyne was added volumetrically to the flask (one molar equivalent to the end-group of polymer assuming 100% recovery in the previous step) using a precision syringe. PMDETA (0.2 equivalents to norbornene-alkyne) was added to the flask by precision syringe. The flask was sealed

with a septum and degassed by three freeze-pump-thaw cycles. Solid CuBr (1 equivalent to PMDETA) was added by the procedure used in section 2.2.4.

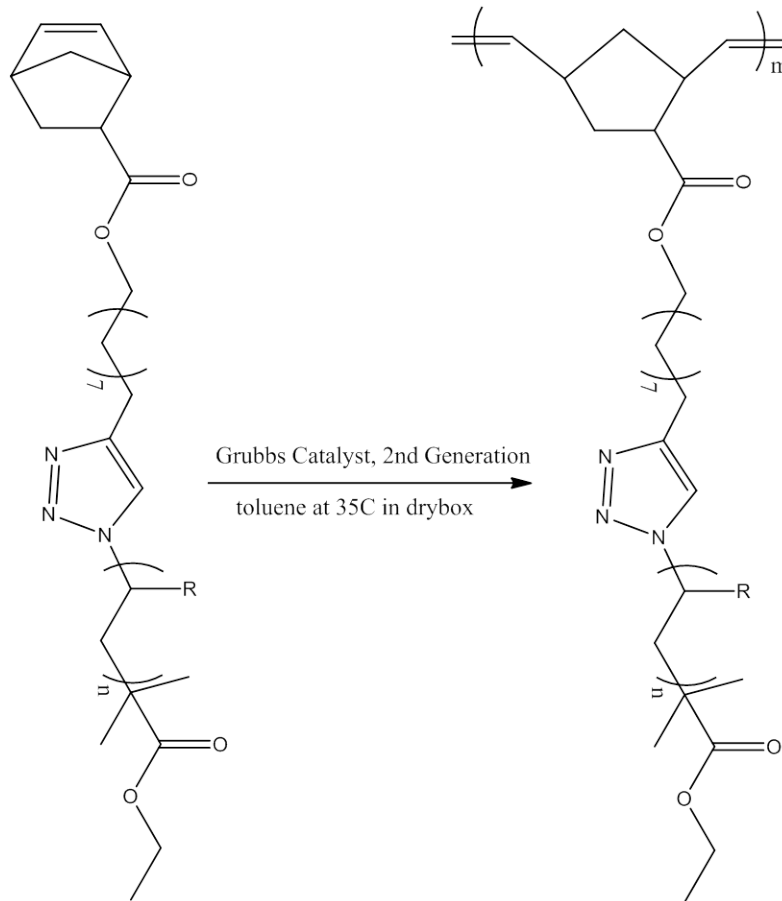
The flask was stirred at 50°C overnight, allowed to cool to room temperature, and the reaction mixture was passed through a column of neutral alumina to remove the copper catalyst. The column was flushed with excess THF for maximum polymer recovery and the resulting clear solution was rotovapped down to a thick yellowish liquid. The resulting polymer solution was precipitated in the manner described in section 2.2.4. Both the recovered solid polymer and the solvent used for precipitation were yellow. Repeated precipitation (up to five times) reduced the intensity of the color but was not able to remove it completely.

2.2.7 Purification of Macromonomers

TLC of the norbornene terminated polymer (macromonomer), using 20:80 ethyl acetate/hexanes and developed using iodine vapor, showed multiple spots. There were several closely grouped spots near the solvent front and a broad band of polymer lower on the plate. Attempts to separate the spots using regular flash chromatography were unsuccessful due to the spread of the spots, so a gradient method was developed. The mobile phases used for the PtBA were ethyl acetate/hexanes, while those used for PS and dPS were hexanes/DCM/methanol because polystyrene precipitates out of solvent mixtures that have more than 80% hexanes by volume. The procedure was to first wet pack a 1.5 inch wide, 24 inch long silica gel column using nonpolar solvent and load the polymer by dissolving it in the least polar solvent mixture possible (10:90 ethyl acetate:hexane for PtBA and 25:75 hexane:DCM for PS and dPS) and loading it onto the

column. The crude product appeared as a deep yellow band at the top of the packing material. A large volume of the less polar solvent was run through the column using argon pressure to force it down and collecting 250mL fractions. The yellow band split into a more rapidly eluting, thin, reddish band and a slow moving, broad, yellow band. After all traces of yellow color were gone from the packing material and at least 100mL of eluent had been colorless, the solvent was switched to a more polar mixture (30:70 ethyl acetate:hexanes for PtBA and 5:95 methanol:DCM for PS and dPS). A large volume had to be used (up to 3 liters) collecting 500mL fractions and testing by TLC to ensure all polymer had eluted from the column. A light brownish band remained at the top of the packing material. All of the fractions were then tested by TLC using 30:70 ethyl acetate:hexanes and developed using iodine vapor. The polymer spot appeared after one or two fractions in the more polar solvent and then persisted for a large elution volume. Polymer containing fractions were combined and the solvent exchanged to THF. The polymer was precipitated and dried as described in section 2.2.4 resulting in white or slightly off-white powder for all polymers.

2.2.8 ROMP of Macromonomers

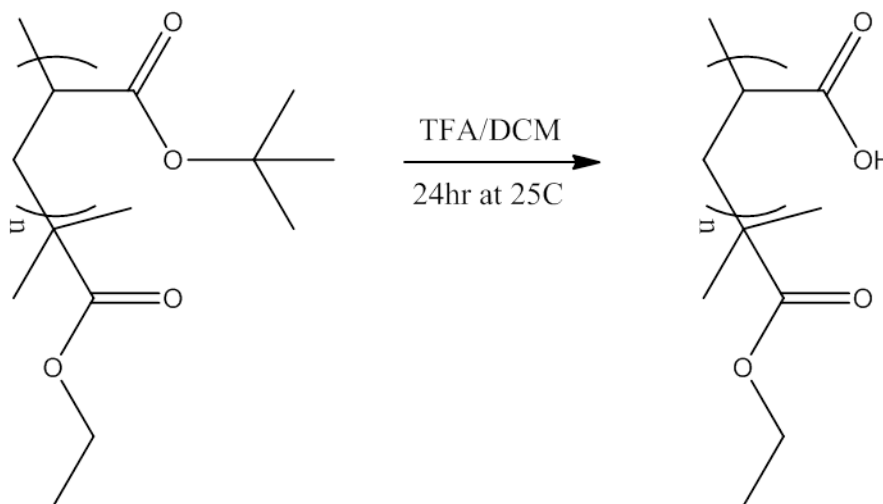


Scheme 2.5: Ring Opening Metathesis Polymerization of Macromonomer

Although N_b was not equal to the monomer/catalyst ratio, the M/C ratio provided reliable control over the N_b of the resulting brush. Thus a typical procedure is described in terms of molar ratios. An oven dried 7mL glass vial was charged with an oven-dried stir bar and macromonomer (200mg) was weighed directly into the vial. Grubbs catalyst (2nd generation) (2mg) was weighed out into a 2mL glass vial which was sealed with a septum cap. The two vials were transferred into an MBRAUN drybox (N_2 atmosphere with $<0.1\text{ppm } O_2$ and $<0.1\text{ppm } H_2O$) by placing the 7mL vial into the antechamber with the cap slightly loosened and piercing the septum of the smaller 2mL vial with a thin

needle to avoid loss of the fine catalyst powder. The antechamber was pumped down to 150mTorr and refilled with N₂, repeating this process three times. Toluene (anhydrous 99.8%) was added to the 7mL vial in a ratio of 1mL/100mg polymer. The vial was capped and shaken aggressively until the polymer was dissolved and placed in a temperature controlled block set to 35°C with magnetic stirring. Precisely 1mL of toluene was injected into the vial containing catalyst, shaken to ensure complete mixing, and a volume of this solution (appropriate to the M/C ratio) was injected into the polymer vial. This was capped and left to stir for 6 hours and was subsequently terminated by injecting approximately 200µL of ethyl vinyl ether and then removed from the drybox. The toluene was evaporated by blowing N₂ gas through a needle and THF (1mL/100mg) was added to the vial which was then capped and placed on a wrist action shaker for 1 hour. The polymer was then precipitated in a manner identical to that described in section 2.2.4, resulting in white powder for polystyrene based bottlebrushes and an off-white foamy solid for the poly(tert-butyl acrylate) based ones.

2.2.9 Hydrolysis of poly(tert-butyl acrylate) into poly(acrylic acid)

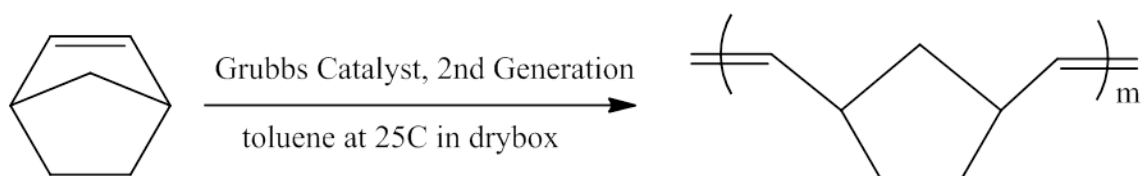


Scheme 2.6: Removal of the tert-butyl protecting group from poly(tert-butyl acrylate). The carbon at the top of the presented structure would be connected through the linker to the polynorbornene backbone in the case of a bottlebrush polymer.

A method for hydrolyzing the tert-butyl ester without breaking the ester linkage between the backbone and the side-chains was based on procedures reported in the literature [17, 22, 53]. Polynorbornene-*g*-PtBA bottlebrush polymer (150mg) was weighed out into a 7mL vial and a stirbar was added. DCM (2mL) was added to the vial and this was stirred until the polymer was completely dissolved. Trifluoroacetic acid (2mL, 20x excess) was added to the vial and this was capped with a PTFE lined cap and left to stir overnight. The solution took on a tan color and became thick and gel-like. The acid and DCM were evaporated by argon gas flow over the course of several hours and THF (4mL) was added to the vial, which was capped and placed on the shaker overnight (solvation was difficult due to the marginal solubility of the PNB-*g*-PtBA). The polymer solution was precipitated into hexanes (50mL) and the resulting powder was collected by filtration, transferred into a vial, and dried in a vacuum oven at 35°C overnight. The resulting polymer was a white powder soluble in water but not in most organic solvents.

The extent of deprotection was determined through titration. PNB-*g*-PAA (9.9mg) was dissolved in double distilled water (9.9mL) by shaking overnight. A solution of NaOH in double distilled water of approximately 0.33mmol/mL was prepared and then normalized by titration with 2M HCl using a Fischer Scientific AB15 pH meter. The polymer solution was titrated with the normalized NaOH solution up to pH ≥ 12 . The resulting pH as a function of added moles of NaOH was used to determine the concentration of acid groups and therefore the conversion.

2.2.10 Making bare backbones by ROMP of norbornene



Scheme 2.7: Ring Opening Metathesis Polymerization of norbornene.

To serve as a control for the graft polymers, a series of polynorbornenes were synthesized and characterized. The following is the synthesis procedure for all three. Bicyclo[2.2.1]hept-2-ene (norbornene, 0.5g, 5.3mmol) was placed into each of three 20mL glass scintillation vials charged with a magnetic PTFE coated stirbar. Three 2mL vials with septum caps were weighed and then Dichloro[1,3-bis(2,4,6-trimethylphenyl)-2-imidazolidinylidene](benzylidene)bis(3-bromopyridine)ruthenium(II), referred to as Grubbs 3, was weighed out into each to have monomer-to-catalyst ratios of 250,500 and 1000 (18.8mg, 9.5mg, and 5.1mg respectively). All of the vials were passed into the glovebox used for all of the ROMP reactions, cycling the antechamber three times. 11mL of toluene was added to each of the vials containing norbornene and these were capped

and shaken until homogeneous. These were then placed into a temperature controlled stirring block set to 25°C under vigorous stirring. Toluene (1mL) was added to each of the small vials containing catalyst and these were capped and shaken until the solution became a homogeneous green color. The contents of the three catalyst vials were rapidly injected into the monomer vials using a syringe. The addition of the catalyst solution caused rapid thickening of the reaction mixture and bubbles were evolved in all three vials. The vials were allowed to stir for 30 minutes to ensure complete conversion and 1mL of ethyl vinyl ether was added to each vial. These were removed from the glovebox, precipitated into methanol, and collected by filtration. The resulting stringy, elastic, off-white polymers were transferred into vials and dried under vacuum at 45°C overnight.

2.3 Results and Discussion

2.3.1 Macromonomers

A series of macromonomers suitable for ROMP were obtained by synthesizing bromine terminated polymers through Atom Transfer Radical Polymerization (ATRP) (Scheme 2.2), converting the end group to an azide (Scheme 2.3) and coupling it to an alkyne functionalized norbornene (Scheme 2.4). Gel Permeation Chromatography (GPC) (Figure 2.2) showed that the resulting materials have narrow, monomodal molecular weight distributions.

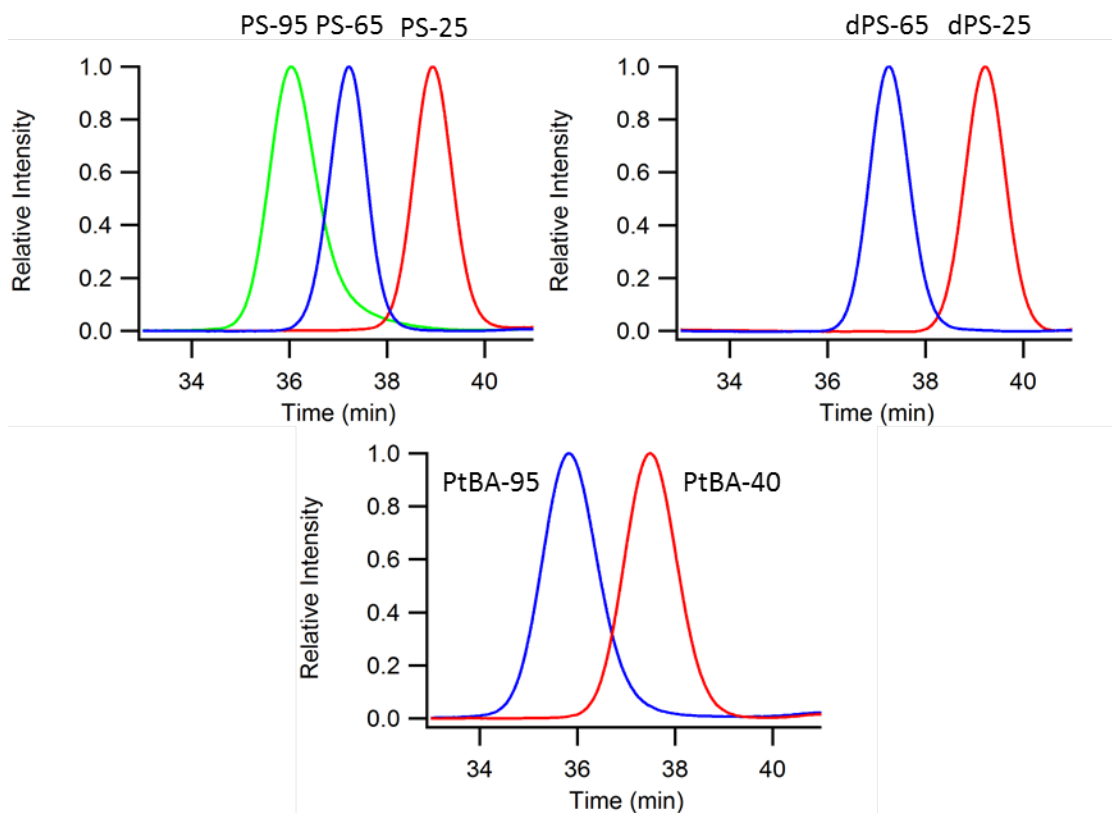


Figure 2.2: Gel Permeation Chromatograms for polystyrene (upper left) , polystyrene-d8 (upper right) and poly(tert-butyl acrylate) (lower center) based macromonomers. The intensity shown is differential refractivity data with the highest observed intensity normalized to 1. Note that the macromonomer names are shown next to their corresponding traces and are formed as P-X where P is the polymer type (PS,dPS,PtBA) and X is the number of repeat units rounded to the nearest five.

For each monomer type, several molecular weights of macromonomer were prepared in order to facilitate comparison between both side-chain chemistry and degree of polymerization. The three monomers (styrene, styrene-d8, and tert-butyl acrylate) all resulted in macromonomers with low PDI and a high degree of functionalization, summarized in Table 2.1. N_s (the number of repeat units) was calculated by subtracting the mass of the norbornene and linker (0.3kg/mol) from the M_w and dividing this by the monomer mass and rounding to the nearest whole number.

Table 2.1: Results of GPC characterization of macromonomers.

Name	Monomer	Repeat Units	dn/dc (mL/g)	Mw (kg/mol)	PDI (Mw/Mn)
PS-25	styrene	27	0.177	3.0	1.05
PS-65	styrene	63	0.185	6.6	1.01
PS-95	styrene	97	0.185	10.0	1.04
dPS-25	styrene-d8	27	0.150	3.2	1.08
dPS-65	styrene-d8	65	0.162	7.3	1.02
PtBA-40	tBA	39	0.058	5.3	1.05
PtBA-95	tBA	94	0.061	12.3	1.04

To obtain a compromise between the polydispersity (PDI) which decreases with increasing conversion[43] and retained bromine functionality which also decreases[50], reaction conditions were set up with the targeted molecular weight reached at 65% conversion. Attempts at kinetic monitoring by taking aliquots of the reaction in progress were unsuccessful, as it was observed that the reaction rate appeared to become slower as samples were taken, probably due to trace oxygen that is inevitably introduced whenever the septum of the reaction vessel is pierced. Thus, the time at which to terminate the reaction was determined by setting up and running several reactions at each set of conditions and then interpolating the appropriate time to be used for the final polymerization. This method was successful, resulting in matched sets of monodisperse macromonomers having PDI < 1.1 (Table 2.1).

An interesting observation is that the temperature turned out to be a very important parameter for the polymerization, with the optimal temperatures found to be 95°C for styrene/styrene-d8 and 65°C for tert-butyl acrylate. GPC traces became bimodal for polymers synthesized at temperatures as little as 10°C above the optimum, showing a high molecular weight shoulder consistent with chain-chain termination. The reaction

profiles were consistent with the linear kinetics expected of ATRP[54], allowing the reaction time for a given conversion to be reliably predicted. The reaction kinetics were similar for deuterated and ordinary styrene, although the reaction rate was about 15% slower for the deuterated monomer. Several test reactions confirmed the vital role of the DMF solvent in supporting a controlled polymerization. It was found that reducing the amount of DMF resulted in broader molecular weight distributions.

For the conversion of the ATRP based polymers into macromonomers, a norbornene with alkyne functionality was “clicked” onto the azide terminated polymer chain (Scheme 2.3 and Scheme 2.4). Both endo/exo mixtures and pure exo norbornene were tested and the expected higher conversion in ROMP was seen for the exo-norbornene, in accord with prior literature[46, 55]. An alkyl spacer was used at the norbornene in order to further reduce the steric congestion at the norbornene[33]. After the functionalization and repeated precipitation, the resulting macromonomers were generally yellow solids (powder for the PS/dPS, and a foamy solid for the PtBA). The color was determined to be due to a small molecule impurity that could be separated from the polymer by flash chromatography using a gradient solvent system specific to the monomer type. The very large difference in mobility between the polymer and small molecules makes it possible to achieve very high purity, with all of the post column macromonomers being white in color. The isolated impurity is seen to be deeply colored (reddish yellow) with multiple TLC spots and a large number of NMR peaks, suggesting the presence of multiple compounds. Identification of the impurities would require further work, such as LCMS.

The column purification was determined to be essential, with repeated precipitation achieving insufficient purity. This is demonstrated by the results for PS-65 in ROMP using a monomer to catalyst ratio of 400:1. Using the light yellow PS-65 after three precipitations resulted in a conversion of only 44%, while the white, post column PS-65 reached >99% conversion under the same conditions (Table 2.2).

2.3.2 Polystyrene Bottlebrushes

Using ROMP with Grubbs 2nd generation catalyst[42], the polystyrene based macromonomers were polymerized into well-defined bottlebrush polymers that showed monomodal molecular weight distributions. Up to the largest molecules in the present study, elution followed the expected “largest molecules come out first” rule, showing the suitability of the selected column system for the bottlebrushes studied. The GPC traces (Figure 2.3) show that bottlebrush polymers peaks start at elution times of 22-25 minutes, which is later than ordinary linear polymers of equivalent molecular weight, consistent with their relatively small hydrodynamic radii (see chapter 3).

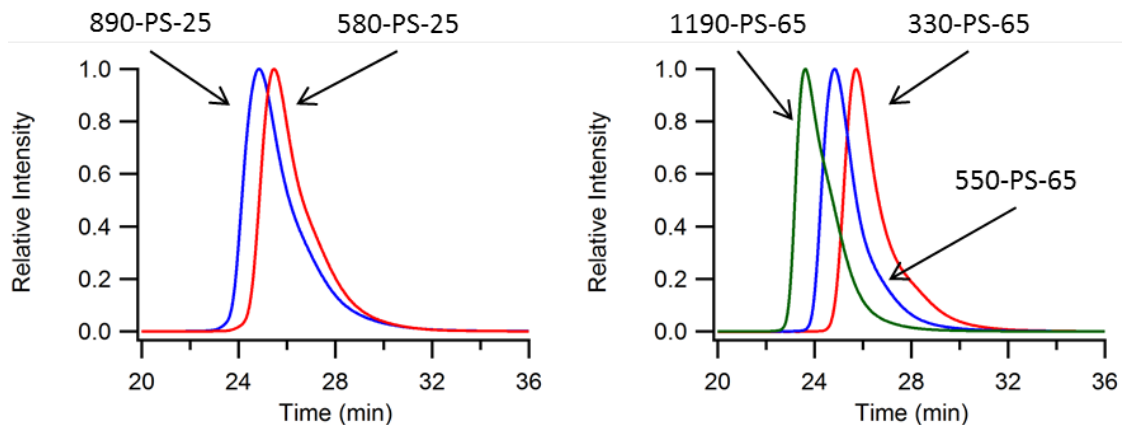


Figure 2.3: Gel Permeation Chromatograms for selected bottlebrushes based on polystyrene macromonomers. Both plots show the 90° light scattering detector intensity normalized to a maximum intensity of 1. The plot on the left shows bottlebrushes based on the shorter macromonomer (25 repeat units) and the plot on the right shows those based on the longer (65 repeat units) macromonomer.

The resulting bottlebrush polymers were characterized by GPC/MALLS in order to obtain the M_w , PDI, and R_g (Table 2.2). The difference in elution characteristics between linear and bottlebrush polymers seen in the literature[15] and confirmed by comparison to polystyrene confirms that the use of light scattering in combination with differential refractometry in GPC is the most reliable method for determining the polymer characteristics[56]. N_b was calculated by dividing the brush M_w by the M_w of the appropriate macromonomer. Conversion was based on the relative area under the peaks in the RI trace corresponding to the bottlebrush and the macromonomer.

Table 2.2: MALLS/GPC derived characteristics of polystyrene bottlebrushes.

Name	Repeat Units	M/C ratio	Conversion (%)	dn/dc (mL/g)	Mw (kg/mol)	PDI (Mn/Mw)	Rg (nm)
570-PS-25	575	200	98.8	0.177	1724	1.12	36.4
580-PS-25	582	200	99.5	0.170	1745	1.22	34.8
890-PS-25	893	400	99.6	0.167	2680	1.19	45.9
330-PS-65	325	200	99	0.182	2148	1.16	31.1
550-PS-65	550	400	99.1	0.186	3633	1.15	45.1
1190-PS-65	1193	800	99.2	0.171	7871	1.13	69.3

For the two sets of bottlebrush polymers ($N_s=25$ and $N_s=65$) a series of backbone lengths was successfully synthesized. The initial goal was to have the longest backbones have on the order of 10^3 backbone repeat units (each with a grafted side-chain) and then to have lengths of $\frac{1}{2}$ and $\frac{1}{4}$ that of the longest backbone in order to study the effect of backbone length. This was intended to be controlled by the macromonomer/catalyst ratio and was generally successful as molecular weight trended monotonically with the M/C ratio. In all cases N_b of the brushes appeared to be higher than expected, as has been seen for similar systems in the literature[30, 33]. A comparison of 570-PS-65 and 580-PS-65

indicates that this effect is repeatable and thus it should be possible for the desired N_b to be achieved by adjusting the M/C ratio to compensate. The larger than expected molecular weight is consistent with the high rate of propagation relative to the rate of initiation of Grubbs 2nd generation catalyst[57, 58]. The polymerization was well controlled and nearly complete in all cases with PDI < 1.25 and conversion of about 99%.

The overall molecular weight of the largest bottlebrush 1190-PS-65 at 8×10^6 g/mol is near the upper limit achieved for bottlebrush polymers by grafting through [30]. In addition to the polymers presented in Table 2.2, the ROMP of PS-95 was attempted under identical conditions to those used for the other macromonomers. This was unsuccessful, as the highest N_b achieved was ~ 20 . There appears to be a threshold side-chain molecular weight for polystyrene macromonomers above which the attainable N_b drops off precipitously.

2.3.3 Deuterated Polystyrene Bottlebrushes

A set of bottlebrushes of backbone and side-chain lengths matching those of the polystyrene bottlebrushes but with deuterium labeled side-chains was synthesized from dPS-25 and dPS-65. The resulting bottlebrushes (Table 2.3) also had monomodal molecular weight distributions (Figure 2.4). The elution times mirrored those of the regular polystyrene bottlebrushes (Figure 2.3).

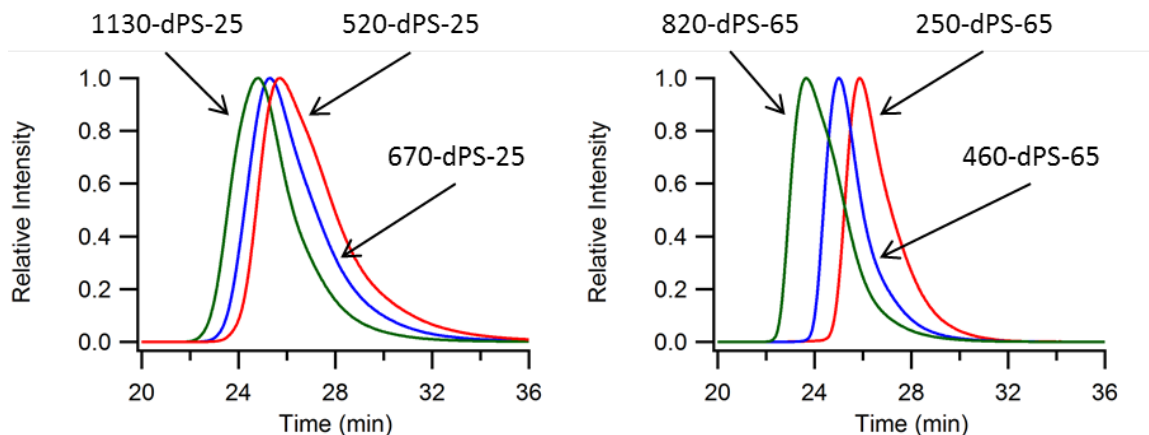


Figure 2.4: GPC traces of light scattering intensity from 90° detector normalized to a maximum intensity of 1 for bottlebrushes based on deuterated polystyrene. The left plot shows bottlebrushes based on the shorter macromonomer (25 repeat units) and the right plot shows those based on the longer macromonomer (65 repeat units).

Only a selected subset of the bottlebrush traces are shown in Figure 2.4 because the remaining two brushes (540-dPS-25 and 780-dPS-25) overlap significantly with the traces of 520-dPS-25 and 670-dPS-25, respectively, and are similar in appearance to those shown.

Table 2.3: MALLS/GPC derived characteristics of deuterated polystyrene bottlebrushes.

Name	Repeat Units	M/C ratio	Conversion (%)	dn/dc (mL/g)	Mw (kg/mol)	PDI (Mn/Mw)	Rg (nm)
520-dPS-25	520	200	99.5	0.158	1663	1.13	39.1
540-dPS-25	536	200	99.5	0.157	1714	1.09	39.3
670-dPS-25	667	400	99.4	0.161	2133	1.19	45.6
780-dPS-25	782	400	>99.9	0.158	2501	1.17	49
1130-dPS-25	1125	800	>99.9	0.154	3600	1.22	58.1
250-dPS-65	251	200	98.5	0.172	1835	1.36	27.2
460-dPS-65	457	400	99.5	0.167	3336	1.29	40.4
820-dPS-65	817	800	97.9	0.186	5965	1.43	64.4

The bottlebrushes based on dPS-25 and dPS-65 generally mirror the trends seen for those based on PS-25 and PS-65. The molecular weights are proportional to the M/C,

but exceed it in most cases. It is interesting to note, however, that it appears that for dPS-65, N_b is remarkably similar to the M/C for all of the backbone lengths. For bottlebrushes with both PS (Table 2.2) and dPS (Table 2.3) side-chains, longer macromonomers more closely track the monomer/catalyst ratio. It has been suggested that the crowding of the side-chains near the backbone reduces the rate of propagation while not significantly affecting the rate of initiation[30] and thereby allows a greater percentage of the catalyst to initiate. The bottlebrushes based on dPS-25 achieved conversions of >99% in all cases with $PDI < 1.25$. For the longer macromonomer, dPS-65, the conversions remain high (>97%); however, the PDI increases to ≥ 1.3 .

2.3.4 Poly(*tert*-Butyl Acrylate) Bottlebrushes

A set of bottlebrushes was synthesized based upon the poly(*tert*-butyl acrylate) macromonomers with $N_s=40$ and $N_s=95$ and using the same range of M/C ratios used with PS and dPS macromonomers. Both macromonomers resulted in bottlebrushes with high conversion and monomodal GPC traces (Figure 2.5).

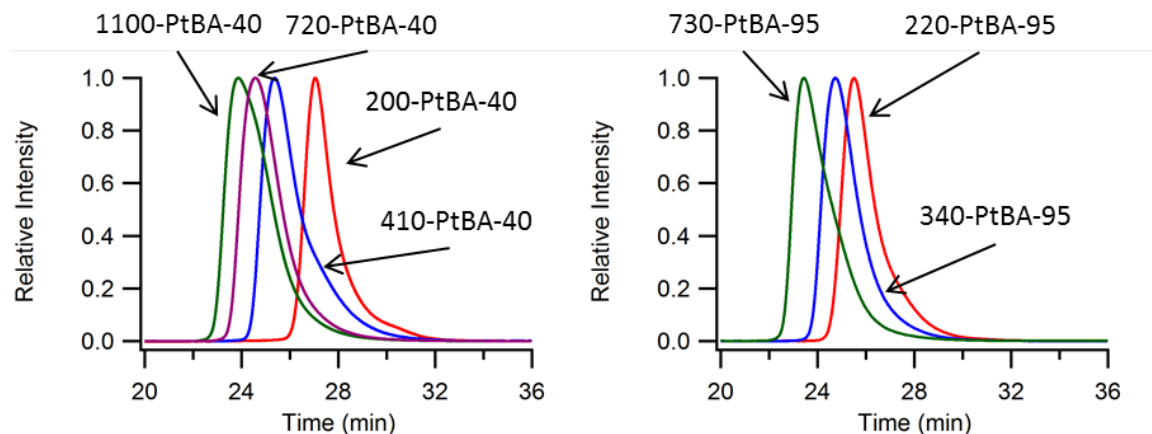


Figure 2.5: GPC traces of light scattering intensity from 90° detector normalized to a maximum intensity of 1 for bottlebrushes based on *tert*-butyl acrylate. The left plot shows bottlebrushes based on the shorter macromonomer (40 repeat units) and the right plot shows those based on the longer macromonomer (90 repeat units).

Interestingly, N_b values for PtBA brushes (Table 2.4) were almost entirely in accord with the M/C ratios (excepting 720-PtBA-40 and 1100-PtBA-40). This may be due to the effect of longer side-chains on the chain transfer of catalyst described in the previous section. The PtBA based bottlebrushes are the largest molecules synthesized in this work, with 733-PtBA-95 achieving $M_w \sim 9 \times 10^6$ g/mol. This appears to be nearing the upper limit for the chemistry methods described, as the conversions achieved for these are markedly lower than for the other bottlebrushes, dropping to a low of 94.4% for 730-PtBA-95, although the PDI values remain reasonably good with $PDI < 1.3$ for all of the PtBA based bottlebrushes. The lower conversion would also explain the fact that $N_b < M/C$ for 340-PtBA-95 and 730-PtBA-95 with the catalyst lifetime being shorter than the time needed to consume all of the macromonomer. The residual macromonomer in the PtBA-95 samples could be removed by repeated precipitation, preparative GPC, or fractionation due to the much greater molecular mass of the bottlebrush polymers.

Table 2.4: MALLS/GPC derived characteristics of tert-butyl acrylate bottlebrushes.

Name	Repeat Units	M/C ratio	Conversion (%)	dn/dc (mL/g)	Mw (kg/mol)	PDI (Mn/Mw)	Rg (nm)
200-PtBA-40	204	200	97.8	0.058	1081	1.14	18.7
410-PtBA-40	414	400	97.8	0.060	2194	1.26	34.5
720-PtBA-40	722	500	97.5	0.059	3829	1.22	48.8
1100-PtBA-40	1098	800	96.8	0.056	5817	1.28	61.2
140-PtBA-95	136	100	97.1	0.056	1670	1.38	19.5
220-PtBA-95	220	200	96.1	0.056	2710	1.28	29.9
340-PtBA-95	343	400	95.5	0.059	4214	1.27	43.3
730-PtBA-95	733	800	94.4	0.058	9021	1.29	71.6

It is also interesting that the upper limit of length for macromonomer appears to depend on the chemical nature of the side-chain. It was possible to achieve N_b of 730 for

PtBA-95 while PS-95 was restricted to $N_b \sim 20$. This may be due to the flexibility or size of the polymer in solution affecting the steric hindrance of macromonomer addition.

ROMP of very large monomers is highly sensitive to the choice and purity of solvent. The reaction conditions used to make 410-PtBA-40 were replicated using solvents that had been previously used for ROMP of macromonomers in the literature THF[33] and DCM[17, 30]. The results were markedly worse than achieved in toluene with conversion in THF $\sim 30\%$ and in DCM $\sim 23\%$. The effect cannot be attributed to the dependence of reaction rate upon the solvent quality for the macromonomers, as all three are good solvents. The low conversion is most probably due to poisoning of the catalyst by the inhibitors present in DCM and THF. Although both solvents were purchased at the highest purity available from Sigma-Aldrich, they were used as received and contained inhibitors. While in most cases the concentration of inhibitor is much lower than the reagents, the catalyst concentration was ~ 50 ppm, which is comparable to the concentrations of inhibitors typically used. In order to conclusively determine the effect of solvent upon the reaction it would be necessary to purify the solvents by distillation. Since commercially available toluene works very well, it seems like the optimal solvent choice.

2.3.5 Polynorbornene Linear Polymers

To isolate the effect of the grafted side-chains on a bottlebrush polymer, it is instructive to study the corresponding bare backbone. The availability of research-grade polynorbornene is limited and the literature on its behavior in solution is sparse. For these reasons we synthesized a series of polynorbornenes of different molecular weights to use as controls in the study of bottlebrush polymer conformations in solution.

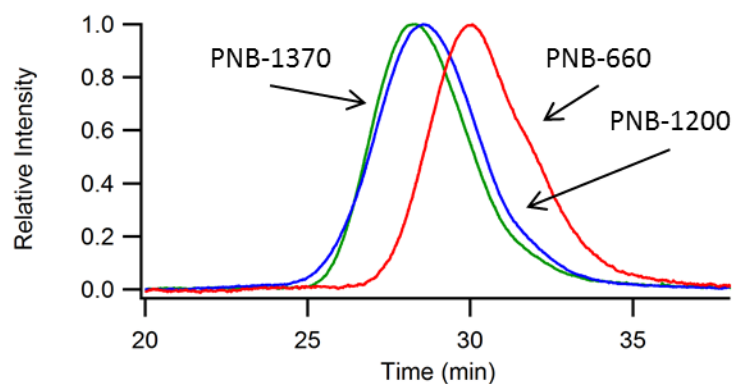


Figure 2.6: GPC traces of light scattering intensity from 90° detector for three different molecular weights of polynorbornene normalized to the maximum intensity for each trace.

The distributions (Figure 2.6) are monomodal, but are broader than those for bottlebrush polymers of similar N_b . The three polynorbornenes were synthesized using a procedure identical to that used to polymerize the macromonomers, although the concentration was reduced by a factor of 10. The reaction rate was extremely rapid, with the solution viscosity increasing dramatically and immediately upon addition of the catalyst solution. In all cases the conversion of monomer was complete and the resulting polymer was off-white and rubbery (very unlike the bottlebrushes).

Table 2.5: MALLS/GPC derived characteristics of the polynorbornenes used to study ungrafted backbones.

Name	Repeat Units	M/C ratio	dn/dc (mL/g)	Mw (kg/mol)	PDI (Mn/Mw)	Rg (nm)
PNB-660	662	250	0.125	62	1.35	-
PNB-1200	1202	500	0.125	113	1.57	16.2
PNB-1370	1365	1000	0.125	129	1.4	17.8

The intent had been to have N_b similar to those of the bottlebrushes and thus similar M/C ratios were used. The N_b of the resulting polymers (Table 2.5) increased monotonically with the M/C ratio but deviated significantly from it. The molecular weight distribution was broader than that of bottlebrush polymers, with PNB-660 and PNB-1370 having PDI~1.4 and PNB-1200 much worse at PDI~1.6. The broader peaks support the idea that the presence of the side-chains makes the ROMP of macromonomers more controlled by slowing the rate of propagation relative to the rate of initiation. However, PNB-660 and PNB-1370 are similar in N_b and PDI to some of the bottlebrush samples and are suitable for use as controls.

2.3.6 Poly Acrylic Acid Bottlebrushes by Hydrolysis of PtBA Bottlebrushes

Using the procedure described in section 2.2.6, a portion of each of the bottlebrushes based on PtBA-95 (Table 2.4) was converted into poly(acrylic acid). This was accomplished by removing the tert-butyl protecting groups from the side-chains using trifluoroacetic acid. In order to determine the degree of conversion to acrylic acid, the brushes were titrated with NaOH and the pH recorded (Figure 2.7). After the deprotection procedure the brushes were soluble in water and were insoluble in most organic solvents (e.g. dichloromethane, chloroform, hexanes...). The solid brushes appeared to be much more crystalline and were a brilliant white, with many of the samples forming hard clumps when precipitated. Due to the incompatibility with THF (mobile phase for GPC), it was not possible to determine the molecular weight and polydispersity of the PAA brushes. Since we used a very gentle deprotection procedure, we consider it safe to assume that the overall structure of the bottlebrushes is unaffected

with the only change in molecular weight being due to the loss of the tert-butyl protecting groups.

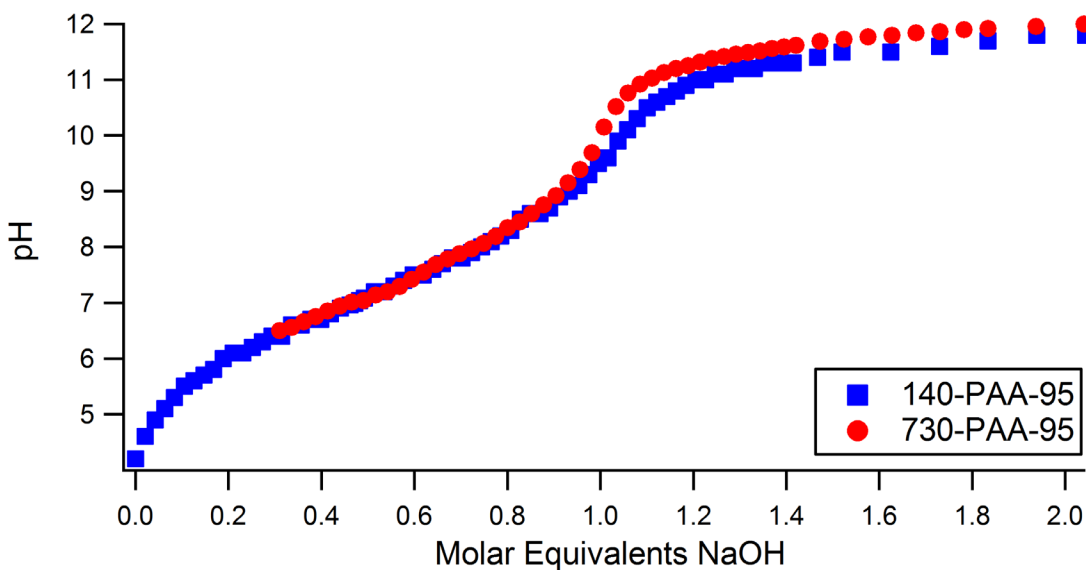


Figure 2.7: Titration curves showing pH as a function of added NaOH for 140-PAA-95 (blue squares) and 730-PAA-95 (red circles). The molar equivalents of NaOH are calculated taking into account the percentage of deprotection (81% for 140-PAA-95 and 90% for 730-PAA-95).

The extent of deprotection was estimated from the pH data using equation 2.1 with $[PAA]$, the molar concentration of carboxylic acid groups in the solution being titrated, calculated as (fraction deprotected) \times (concentration of bottlebrush).

$$pH \approx 14 + \log([NaOH] - [PAA]) \quad (2.1)$$

The pH curve predicted by this equation was compared to the experimental data for the high pH plateau region ($pH > 11$) and extent of deprotection giving the best correspondence was taken to be correct. Using this method it was determined that the percentages of tert-butyl groups removed were 81% and 90% for 140-PAA-95 and 730-

PAA-95 respectively. Although limited amounts of material did not permit the testing of 220-PAA-95 and 340-PAA-95 it is assumed that their PAA content is similar.

The titration curves (Figure 2.7) agree with those seen for linear poly(acrylic-acid) for which the acidity decreases with increasing deprotonation[59]. This effect of the pKa increasing for each subsequent proton removed is what gives rise to the gradually increasing pH and not very sharp rise in pH near the equivalence point. In the range $6 < \text{pH} < 9$ the dependence on pH on added NaOH is linear, acting like an ideal buffer solution. The conformation of PAA also changes dramatically in this region of pH, and the PAA-95 based bottlebrushes provide a set of materials suitable for study of the influence of polyelectrolyte side-chains on bottlebrush conformation.

2.5 Conclusions

Homologous series of bottlebrush polymers were synthesized using a robust and efficient method, refined from previously published procedures combining ATRP, azide-alkyne click chemistry, and ROMP. The resulting bottlebrush polymers reach $N_s \sim 100$ and $N_b > 1000$, comparable to the largest values previously reported in the literature. The development of a macromonomer purification procedure utilizing flash chromatography using a gradient solvent system allowed for the facile and efficient purification of macromonomer, resulting in greater conversion than had been previously observed in this type of system[33].

By simplifying macromonomer purification and thereby improving the repeatability and conversion in the ROMP of macromonomers, the protocol described here enabled bottlebrushes with systematic and reproducible N_b (Tables 2.2, 2.3, and 2.4) to be made from polystyrene macromonomers with $N_s = 25$ and 65. The procedure was not

affected significantly by deuterium labeling and allowed for matched pairs (same N_b and N_s) of bottlebrushes with PS and dPS side-chains. This provided the necessary contrast labeling for neutron scattering experiments to isolate the conformation of the backbone in a bottlebrush polymer and compare it to the overall object conformation (Chapter 3). Another series of bottlebrushes were made using tert-butyl acrylate as the side chain monomer, and this was seen to reach even higher side-chain lengths of 40 and 95 repeat units and similar backbone lengths to the polystyrene bottlebrushes; This allows for study of the effect of side-chain chemistry and flexibility upon the bottlebrush behavior. Through the hydrolysis of the tert-butyl ester it was also possible to transform the PtBA based brushes into ones with poly(acrylic acid) side-chains with >80% deprotection. This allows for the effect of pH and salt concentration upon a bottlebrush polymer to be examined using a series of thoroughly characterized polymers.

The development of this robust, modular, and accessible synthetic method also opens up opportunities for the creation of more complex bottlebrush structures (e.g. polypeptide, block copolymer, or multivalent side-chains). Such bottlebrushes have been predicted to have very complex internal structures[60, 61] and the availability of the materials will enable experimental validation of theory to begin.

References

1. Sheiko, S.S., B.S. Sumerlin, and K. Matyjaszewski, *Cylindrical molecular brushes: Synthesis, characterization, and properties*. Progress in Polymer Science, 2008. **33**(7): p. 759-785.
2. Zhang, M. and A.H. Müller, *Cylindrical polymer brushes*. Journal of Polymer Science Part A: Polymer Chemistry, 2005. **43**(16): p. 3461-3481.
3. Rathgeber, S., et al., *Bottle-brush macromolecules in solution: Comparison between results obtained from scattering experiments and computer simulations*. Polymer, 2006. **47**(20): p. 7318-7327.
4. Zhang, B., et al., *Synthesis and solid state structures of macromolecular cylindrical brushes with varying side chain length*. Polymer, 2004. **45**(12): p. 4009-4015.

5. Rzayev, J., *Synthesis of polystyrene– polylactide bottlebrush block copolymers and their melt self-assembly into large domain nanostructures*. *Macromolecules*, 2009. **42**(6): p. 2135-2141.
6. Li, X., et al., *Surface Properties of Bottlebrush Polymer Thin Films*. *Macromolecules*, 2012. **45**(17): p. 7118-7127.
7. Feuz, L., et al., *Bending rigidity and induced persistence length of molecular bottle brushes: a self-consistent-field theory*. *Macromolecules*, 2005. **38**(21): p. 8891-8901.
8. Hsu, H.-P., W. Paul, and K. Binder, *Structure of bottle-brush polymers in solution: A Monte Carlo test of models for the scattering function*. *The Journal of chemical physics*, 2008. **129**(20): p. 204904-204904-11.
9. Hsu, H.-P., et al., *Characteristic length scales and radial monomer density profiles of molecular bottle-brushes: Simulation and experiment*. *Macromolecules*, 2010. **43**(3): p. 1592-1601.
10. Auriemma, F., et al., *Small Angle X-Ray Scattering Investigation of Norbornene-Terminated Syndiotactic Polypropylene and Corresponding Comb-Like Poly (macromonomer)*. *The Journal of Physical Chemistry B*, 2013.
11. Grigoriadis, C., et al., *Dynamic Homogeneity by Architectural Design–Bottlebrush Polymers*. *Macromolecular Chemistry and Physics*, 2012. **213**(13): p. 1311-1320.
12. Rathgeber, S., et al., *On the shape of bottle-brush macromolecules: Systematic variation of architectural parameters*. *The Journal of chemical physics*, 2005. **122**: p. 124904.
13. Zhang, B., et al., *Conformation of cylindrical brushes in solution: effect of side chain length*. *Macromolecules*, 2006. **39**(24): p. 8440-8450.
14. Xia, Y., et al., *Efficient synthesis of narrowly dispersed brush copolymers and study of their assemblies: The importance of side chain arrangement*. *Journal of the American Chemical Society*, 2009. **131**(51): p. 18525-18532.
15. Bak, J.M., et al., *Molecular brushes with extreme grafted side chain densities*. *Polymer*, 2012. **53**(16): p. 3462-3468.
16. Hokajo, T., et al., *Solution Properties of Polymacromonomers Consisting of Polystyrene V. Effect of Side Chain Length on Chain Stiffness*. *Polymer journal*, 2001. **33**(6): p. 481-485.
17. Kriegel, R.M., W.S. Rees, and M. Weck, *Synthesis and hydrolysis of poly (norbornene)/poly (acrylic acid) graft copolymers synthesized via a combination of atom-transfer radical polymerization and ring-opening metathesis polymerization*. *Macromolecules*, 2004. **37**(17): p. 6644-6649.
18. Grigoriadis, C., et al., *Dynamic Homogeneity by Architectural Design - Bottlebrush Polymers*. *Macromolecular Chemistry and Physics*, 2012. **213**(13): p. 1311-1320.
19. Beers, K.L., et al., *The synthesis of densely grafted copolymers by atom transfer radical polymerization*. *Macromolecules*, 1998. **31**(26): p. 9413-9415.
20. Chen, X. and N. Ayres, *Synthesis of low grafting density molecular brush from a poly (N-alkyl urea peptoid) backbone*. *Journal of Polymer Science Part A: Polymer Chemistry*, 2011. **49**(14): p. 3030-3037.
21. Cheng, C., E. Khoshdel, and K.L. Wooley, *ATRP from a norbornenyl-functionalized initiator: Balancing of complementary reactivity for the preparation of α -norbornenyl macromonomers/ ω -haloalkyl macroinitiators*. *Macromolecules*, 2005. **38**(23): p. 9455-9465.
22. Cheng, G., et al., *Amphiphilic cylindrical core-shell brushes via a “grafting from” process using ATRP*. *Macromolecules*, 2001. **34**(20): p. 6883-6888.
23. Runge, M.B., S. Dutta, and N.B. Bowden, *Synthesis of comb block copolymers by ROMP, ATRP, and ROP and their assembly in the solid state*. *Macromolecules*, 2006. **39**(2): p. 498-508.

24. Dag, A., et al., *Block-brush copolymers via ROMP and sequential double click reaction strategy*. Journal of Polymer Science Part A: Polymer Chemistry, 2011. **49**(4): p. 886-892.
25. Deffieux, A. and M. Schappacher, *Synthesis and characterization of star and comb polystyrenes using isometric poly (chloroethyl vinyl ether) oligomers as reactive backbone*. Macromolecules, 1999. **32**(6): p. 1797-1802.
26. Gao, H. and K. Matyjaszewski, *Synthesis of molecular brushes by "grafting onto" method: combination of ATRP and click reactions*. Journal of the American Chemical Society, 2007. **129**(20): p. 6633-6639.
27. Oussadi, K., V. Montembault, and L. Fontaine, *Synthesis of poly (oxyethylene phosphate)-g-poly (ethylene oxide) via the "grafting onto" approach by "click" chemistry*. Journal of Polymer Science Part A: Polymer Chemistry, 2011. **49**(23): p. 5124-5128.
28. Schappacher, M. and A. Deffieux, *New comblike copolymers of controlled structure and dimensions obtained by grafting by polystyryllithium onto poly (chloroethyl vinyl ether) chains*. Macromolecular Chemistry and Physics, 1997. **198**(12): p. 3953-3961.
29. Schappacher, M. and A. Deffieux, *From combs to comb-g-comb centipedes*. Macromolecules, 2005. **38**(17): p. 7209-7213.
30. Jha, S., S. Dutta, and N.B. Bowden, *Synthesis of ultralarge molecular weight bottlebrush polymers using Grubbs' catalysts*. Macromolecules, 2004. **37**(12): p. 4365-4374.
31. Johnson, J.A., et al., *Core-clickable PEG-branch-azide bivalent-bottle-brush polymers by ROMP: grafting-through and clicking-to*. Journal of the American Chemical Society, 2010. **133**(3): p. 559-566.
32. Li, A., et al., *One-pot, facile synthesis of well-defined molecular brush copolymers by a tandem RAFT and ROMP, "Grafting-through" strategy*. Journal of Polymer Science Part A: Polymer Chemistry, 2012. **50**(9): p. 1681-1688.
33. Xia, Y., J.A. Kornfield, and R.H. Grubbs, *Efficient synthesis of narrowly dispersed brush polymers via living ring-opening metathesis polymerization of macromonomers*. Macromolecules, 2009. **42**(11): p. 3761-3766.
34. Ito, K. and S. Kawaguchi, *Poly (macromonomers): homo-and copolymerization*, in *Branched Polymers I*. 1999, Springer. p. 129-178.
35. Tsukahara, Y., et al., *Study on the radical polymerization behavior of macromonomers*. Macromolecules, 1989. **22**(4): p. 1546-1552.
36. Tsukahara, Y., et al., *Radical polymerization behavior of macromonomers. 2. Comparison of styrene macromonomers having a methacryloyl end group and a vinylbenzyl end group*. Macromolecules, 1990. **23**(25): p. 5201-5208.
37. Wintermantel, M., et al., *Molecular bottlebrushes*. Macromolecules, 1996. **29**(3): p. 978-983.
38. Yamada, K., et al., *Atom transfer radical polymerization of poly (vinyl ether) macromonomers*. Macromolecules, 1999. **32**(2): p. 290-293.
39. Sumerlin, B.S., D. Neugebauer, and K. Matyjaszewski, *Initiation efficiency in the synthesis of molecular brushes by grafting from via atom transfer radical polymerization*. Macromolecules, 2005. **38**(3): p. 702-708.
40. Matyjaszewski, K. and J. Xia, *Atom transfer radical polymerization*. Chemical Reviews, 2001. **101**(9): p. 2921-2990.
41. Choi, T.L. and R.H. Grubbs, *Controlled Living Ring-Opening-Metathesis Polymerization by a Fast-Initiating Ruthenium Catalyst*. Angewandte Chemie, 2003. **115**(15): p. 1785-1788.
42. Scholl, M., et al., *Synthesis and Activity of a New Generation of Ruthenium-Based Olefin Metathesis Catalysts Coordinated with 1, 3-Dimesityl-4, 5-dihydroimidazol-2-ylidene Ligands* §. Organic Letters, 1999. **1**(6): p. 953-956.

43. Odian, G.G., *Principles of polymerization*. 4th ed. 2004, Hoboken, N.J.: Wiley-Interscience. xxiv, 812 p.
44. Fournier, D., R. Hoogenboom, and U.S. Schubert, *Clicking polymers: a straightforward approach to novel macromolecular architectures*. Chemical Society Reviews, 2007. **36**(8): p. 1369-1380.
45. Kolb, H.C., M. Finn, and K.B. Sharpless, *Click chemistry: diverse chemical function from a few good reactions*. Angewandte Chemie International Edition, 2001. **40**(11): p. 2004-2021.
46. Pollino, J.M., L.P. Stubbs, and M. Weck, *Living ROMP of exo-norbornene esters possessing PdII SCS pincer complexes or diaminopyridines*. Macromolecules, 2003. **36**(7): p. 2230-2234.
47. Pesek, S.L., et al., *Small-Angle Neutron Scattering Analysis of Bottlebrush Polymers Prepared via Grafting-Through Polymerization*. Macromolecules, 2013.
48. Wyatt, P.J., *Light scattering and the absolute characterization of macromolecules*. Analytica chimica acta, 1993. **272**(1): p. 1-40.
49. Berry, G., *Thermodynamic and Conformational Properties of Polystyrene. I. Light-Scattering Studies on Dilute Solutions of Linear Polystyrenes*. The Journal of Chemical Physics, 1966. **44**: p. 4550.
50. Lutz, J.F. and K. Matyjaszewski, *Nuclear magnetic resonance monitoring of chain-end functionality in the atom transfer radical polymerization of styrene*. Journal of Polymer Science Part A: Polymer Chemistry, 2005. **43**(4): p. 897-910.
51. Jakubowski, W., et al., *Polystyrene with Improved Chain-End Functionality and Higher Molecular Weight by ARGET ATRP*. Macromolecular Chemistry and Physics, 2008. **209**(1): p. 32-39.
52. Kwak, Y. and K. Matyjaszewski, *ARGET ATRP of methyl methacrylate in the presence of nitrogen-based ligands as reducing agents*. Polymer International, 2009. **58**(3): p. 242-247.
53. Zhang, M., et al., *Amphiphilic cylindrical brushes with poly (acrylic acid) core and poly (< i > n < / i > -butyl acrylate) shell and narrow length distribution*. Polymer, 2003. **44**(5): p. 1449-1458.
54. Davis, K.A. and K. Matyjaszewski, *Atom transfer radical polymerization of tert-butyl acrylate and preparation of block copolymers*. Macromolecules, 2000. **33**(11): p. 4039-4047.
55. Asrar, J., *Metathesis polymerization of N-phenylnorbornenedicarboximide*. Macromolecules, 1992. **25**(20): p. 5150-5156.
56. Andersson, M., B. Wittgren, and K.-G. Wahlund, *Accuracy in multiangle light scattering measurements for molar mass and radius estimations. Model calculations and experiments*. Analytical chemistry, 2003. **75**(16): p. 4279-4291.
57. Love, J.A., et al., *Synthesis, structure, and activity of enhanced initiators for olefin metathesis*. Journal of the American Chemical Society, 2003. **125**(33): p. 10103-10109.
58. Sanford, M.S., J.A. Love, and R.H. Grubbs, *Mechanism and activity of ruthenium olefin metathesis catalysts*. Journal of the American Chemical Society, 2001. **123**(27): p. 6543-6554.
59. Borukhov, I., et al., *Polyelectrolyte titration: theory and experiment*. The Journal of Physical Chemistry B, 2000. **104**(47): p. 11027-11034.
60. Erukhimovich, I., et al., *Mesophase formation in two-component cylindrical bottlebrush polymers*. The Journal of chemical physics, 2011. **134**(5): p. 054906-054906-22.
61. Theodorakis, P.E., W. Paul, and K. Binder, *Interplay between Chain Collapse and Microphase Separation in Bottle-Brush Polymers with Two Types of Side Chains*. Macromolecules, 2010. **43**(11): p. 5137-5148.

Chapter 3

Dilute Solution Properties of Bottlebrush Polymers with Polynorbornene Backbones

3.1 Introduction

Bottlebrush polymers, also referred to as polymacromonomers or molecular brushes, are polymers in which polymeric side-chains are densely grafted to a flexible backbone[1, 2]. Their conformation is determined by the competition of the excluded volume interactions between the side-chains and the configurational entropy of the backbone. It is a conflict that the side-chains win by sheer force of numbers, as it is much less costly in terms of free energy for the backbone to become somewhat extended and allow the side-chains to retain an almost unperturbed conformation[3]. This results in significant effective stiffness of the overall cylindrical brush, controlled by the detailed molecular structure.

The molecular architecture is described by a few key parameters: the number of monomer units of the backbone (N_b) and of the side-chains (N_s) and the density of grafting (σ , defined as the number of side-chains per backbone monomer). Additionally, the side-chain chemistry (i.e. the monomer unit of the side-chains) and the backbone chemistry (i.e. the monomer unit of the backbone) determine the intrinsic stiffness, compatibility, and solvent affinity of the bottlebrush components. The choice of backbone monomer also has important consequences due to the length of the monomer unit, l_b . In order to compare two bottlebrush polymers with different backbone monomer units N_b and σ must be rescaled appropriately. When comparing results from two different types of bottlebrushes with l_b (our material) and l'_b (comparison) we consider

the renormalized $\sigma' = \sigma l'_b/l_b$ and $N'_b = N_b l_b/l'_b$. For the comparison relevant to the current work we compare polynorbornene backbones with $l_b = 0.5\text{nm}$ to vinyl type backbones with $l'_b = 0.25\text{nm}$. Having been synthesized by the poly(macromonomer) method (see Chapter 2 for synthetic details) our bottlebrushes have $\sigma = 1$ with $\sigma' = 0.5$ and $N'_b = 2N_b$.

Bottlebrush polymers have a hierarchical structure in solution with their overall conformation having a number of relevant length scales[4]. A schematic of a bottlebrush polymer in solution is shown in Figure 3.1.

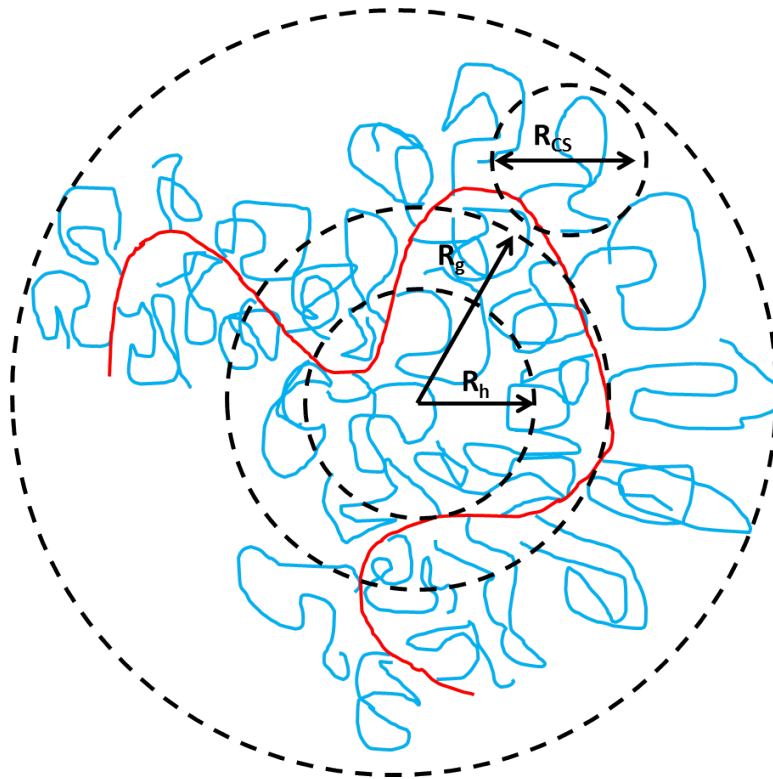


Figure 3.1: Schematic of a bottlebrush polymer in solution illustrating the relevant length scales. The red curve is the backbone and its length, L , is the contour length. The blue curves are the densely grafted side-chains with their relevant length scale being R_{CS} shown as the small circle in the upper right corner and corresponding to the approximate radial size perpendicular to the backbone. The three experimentally relevant length scales of the bottlebrush are illustrated by the three centered circles. From smallest to largest these are the hydrodynamic radius R_h , the radius of gyration R_g and the end to end distance.

The bottlebrush polymer conformation is shown with the backbone contour in red and the side-chains in blue. The backbone contour length cannot be measured directly and is often approximated as the fully extended length ($N_b l_b$)[5, 6]. A set of experimentally relevant length scales is shown as dashed circles. The shortest length scale is the approximate cross-section radius of the flexible cylinder perpendicular to the backbone contour. This is shown as the small circle in the upper right hand corner, labeled R_{CS} , and is related to the side-chain size[7]. The innermost of the centered circles corresponds to R_h , which is the hydrodynamic radius of the bottlebrush molecule. This is the hard sphere radius that corresponds to the observed diffusivity of the molecule and is obtained from Dynamic Light Scattering (DLS). A larger length scale is the radius of gyration, R_g , which is the weight averaged radius of the molecule. This is the size that is obtained from Multi Angle Laser Light Scattering (MALLS) and Small Angle Neutron Scattering (SANS). The largest circle represents the pervaded volume of the coil and corresponds to the end-to-end distance of the molecule R_{e-e} . The end-to-end distance cannot be measured directly in solution and is estimated indirectly from the overlap concentration as described in Section 3.3.2. The relative sizes of the three centered circles in Figure 3.1 are consistent with our experimental results, while the side-chain length scale is enlarged to show detail.

The flexible cylinder shape of a bottlebrush polymer with side-chains nearly overlapping all around the backbone contour leads to unique polymer structure. The R_g of a bottlebrush polymer is much larger than a linear polymer with N (the number of monomer units) equal to N_b , but is much smaller than a linear polymer of equal molecular weight leading to an order of magnitude higher segment density within the pervaded

volume. Along the backbone contour the density is much higher (approximately 1/6 of the density of a solid polymer particle). Thus bottlebrush polymers resemble unimolecular nanoparticles that are inherently soluble and indefinitely stable in solution. Their R_h and solution viscosity is much lower than a linear polymer of equal molecular weight, allowing for highly concentrated solutions to be easily processed. The unique structural features have led to significant interest in their solution properties and the structure property relations.

Synthetically there are three approaches to bottlebrush polymers: grafting-from (side-chains grown from initiator sites on a specially designed backbone), grafting-to (end-functionalized side-chains coupled to a complementary functionalized backbone), and grafting-through (using end-functionalized side-chains as macromonomers in a polymerization process). Of these, only grafting-through allows for all of the key structural parameters (N_s , N_b , and σ) to be precisely determined. Early experimental work on bottlebrush properties[5, 6, 8-15] used materials synthesized through a combination of techniques: anionic polymerization was used to make macromonomers compatible with radical polymerization and these were then polymerized by thermally initiated free radical polymerization. This resulted in batches of bottlebrushes with $\sigma=1$ and precisely controlled N_s with low polydispersity, but very broad distributions of N_b . Through tedious fractionation procedures very small amounts of more narrowly distributed materials were isolated and these were thoroughly characterized by a combination of various scattering techniques (DLS, MALLS, SAXS) and viscometry.

Multiple studies [5, 6, 10] in both good and theta solvents show $R_g(N_b)$ behavior that can reasonably be described by the wormlike chain model[16] used to represent the

behavior of semi-flexible polymers. Introducing corrections for the polydispersity of N_b [14], the excluded volume of the cylindrical brush[5] and the effect of the side-chains near the ends of the backbone[11, 13] it was also possible to fit the viscosity[12] and R_h [11] data to a wormlike chain model. However, cross sectional dimeters (d_h) obtained from viscosity measurements were not consistent with those determined by DLS[9], indicating that understanding of bottlebrush hydrodynamics is incomplete. More recently, small angle x-ray scattering has been used to directly determine the cross-sectional radius (RCS)[8, 15, 17, 18]. These studies have led to a qualitatively consistent picture of bottlebrushes as having an extended overall conformation with an effective Kuhn segment length (l_k) one or two orders of magnitude greater than a linear polymer, and a cross sectional region of high segment density surrounding the backbone contour. However, quantitative agreement about the scaling of $R_g(N_b, N_s)$, $R_h(N_b, N_s)$, and $l_k(N_s)$ has not been reached due to discrepancies between various experimental results.

Theoretical scaling arguments by Fredrickson[19] predicted a nearly quadratic dependence of the Kuhn segment length on N_s and a fully extended backbone conformation for $N_s > 60$. Experimental results have shown l_k independent of N_s [20], l_k varying linearly with N_s [5, 10, 12], and l_k having a stronger than linear dependence on N_s [6]. The absolute R_g values determined for bottlebrushes with polystyrene side-chains and similar values of N_s and N_b varied by more than 50% between reports on bottlebrushes with a poly(methyl acrylate) backbone[6] and polystyrene backbone[5].

Significant controversy also remains in regards to the conformation of side-chains and the degree to which they are perturbed from their free conformation. The conformation of the side-chains was theoretically predicted to scale as a 2D Self-

Avoiding Walk (SAW) with scaling $RCS \sim N_s^{0.75}$ [21-23], but recent simulations do not support this scaling, instead predicting a 3D SAW in good solvent with $RCS \sim N_s^{0.6}$ [3, 4, 24, 25]. Experimentally determined side-chain conformations have spanned the range of predictions with both unperturbed [10, 12] and fully extended conformations [13] reported in the literature. The general conclusion is that all of the experimentally and computationally accessible bottlebrushes have not reached the asymptotic N_s and N_b range treated by scaling theories. Adding to the complexity are simulation results that suggest that the classic definition of a persistence length does not apply to bottlebrush polymers [26] and that the backbone conformations are not smooth curves consistent with the wormlike chain model [24].

Development of improved polymerization methods has led to a resurgence of interest in bottlebrush polymers. In particular, Controlled Radical Polymerization (CRP) and Ring Opening Metathesis Polymerization (ROMP) have been used in combination to synthesize a wide variety of bottlebrush polymers with varied side-chain composition, N_s and N_b (see Chapter 2 for more information on bottlebrush synthesis). Most recent literature reports have focused on bottlebrushes prepared by the ROMP polymerization of norbornene terminated macromonomers [27-36], resulting in polynorbornene backbones with a variety of side-chain chemistries. Characterization has been primarily done by Atomic Force Microscopy of thin films with results not relevant to solution behavior due to the very different forces in play for bottlebrushes adsorbed on surfaces [37-39]. Some work has been done on linear rheological properties [40], the segmental relaxation has been studied by Electron Paramagnetic Resonance [41], and there have been several reports on SANS of bottlebrushes with polynorbornene backbones [42-44] (limited to

small N_b and N_s). To date no comprehensive study of their solution properties as a function of N_b , N_s and side-chain chemistry has been reported.

In the present work we describe a thorough characterization of an extensive series of bottlebrush polymers with polynorbornene backbones and four different side-chain chemistries (polystyrene, deuterated polystyrene, poly-tert butyl acrylate, and poly(acrylic acid)), synthesized as described in Chapter 2. Both N_b and N_s were systematically varied with low polydispersity of the side-chains ($PDI < 1.1$) and bottlebrushes ($PDI < 1.3$). The R_g , R_h and RCS were determined through a series of Multi Angle Light Scattering, Dynamic Light Scattering, and Small Angle Neutron Scattering experiments on solutions of the bottlebrush polymers. The apparent Kuhn segment length l_k was obtained by fitting the wormlike chain expression for $R_g(N_b)$. For the polystyrene side-chain bottlebrushes, both good (THF) and theta (cyclohexane) solvent conditions were used to examine the effect of solvent quality on the side-chain conformation. The results were then compared to published data on bottlebrushes with PS and PMA backbones in order to connect the work on polynorbornene-based bottlebrushes to previous experiments.

In addition, the level of control achieved in Chapter 2 was used to prepare matched bottlebrushes with deuterated polystyrene side-chains to isolate the scattering due to the backbone, and for the first time, directly observe the backbone conformation of a bottlebrush polymer. The effect of concentration was examined and incipient liquid crystalline order was evident with as little as 5wt% polymer. In this contrast matched solvent system, inter-backbone correlation provided a clear indication of ordering. For

1wt% solutions the backbone scattering was qualitatively the same as the of a linear polynorbornene, suggesting that the backbone conformation is a 3D self-avoiding walk.

Finally, bottlebrushes with poly(tert-butyl) acrylate side-chains were characterized in good solvent conditions. Using the same polynorbornene backbones (nearly identical N_b) as the polystyrene side-chain bottlebrushes allowed for the effect of the side-chain chemistry to be observed. Subsequently the characterized bottlebrushes with PtBA side-chains were converted into PAA side-chains through the removal of the tert-butyl protecting groups (see chapter 2). SANS and DLS experiments were performed on aqueous solutions of these polyelectrolyte bottlebrushes, varying pH and salt concentration. This provided insight into the effect of dramatic conformational changes of the side-chains on the overall bottlebrush conformation.

3.2 Experimental

3.2.1 Materials

Perdeuterated solvents used in SANS experiments (cyclohexane-d₁₂, tetrahydrofuran-d₈, toluene-d₈ and deuterium oxide) were purchased from Cambridge Isotope Laboratories. Boric acid (H₃BO₃, ACS reagent), glacial acetic acid (CH₃COOH, ACS reagent), phosphoric acid (H₃PO₄, 85% solution), and sodium deuteroxide (NaOD, 40wt% in D₂O) were purchased from Sigma Aldrich. Tetrahydrofuran (THF), cyclohexane, toluene, and sodium hydroxide were purchased at ACS reagent grade from Sigma Aldrich.

Cuvettes used for dynamic light scattering of samples in organic solvents were Starna Cells 23-G-10 glass square cells with 10mm path length and PTFE stopper. For

aqueous samples Eppendorf UVette plastic disposable cuvettes with a 10mm path length were used. Hellma cylindrical quartz “banjo” cells with 2mm path length (120-QS-2) were used for SANS experiments at NIST and ones with 5mm path length (120-QS-5) used for SANS experiments at ORNL.

A series of bottlebrush polymers with varying backbone lengths were synthesized by ROMP from six different norbornene terminated macromonomers: two lengths each of polystyrene (PS), deuterated polystyrene (dPS) and poly(tert-butyl acrylate) (PtBA). Synthesis and characterization by MALLS/GPC of the bottlebrush polymer samples are described in Chapter 2 and the sample characteristics are shown in Table 3.1.

Table 3.1: Characteristics of bottlebrush polymers with polynorbornene backbones by MALLS/GPC.

Name	Bottlebrush M _w (kg/mol)	Bottlebrush PDI	Side-Chain Type	Side-Chain Mw (kg/mol)	Side-Chain PDI
570-PS-25	1724	1.12	PS	3	1.05
580-PS-25	1745	1.22			
890-PS-25	2680	1.19			
330-PS-65	2148	1.16	PS	6.6	1.01
550-PS-65	3633	1.15			
1190-PS-65	7871	1.13			
520-dPS-25	1663	1.13	dPS	3.2	1.08
540-dPS-25	1714	1.09			
670-dPS-25	2133	1.19			
780-dPS-25	2501	1.17			
1130-dPS-25	3600	1.22			
250-dPS-65	1835	1.36	dPS	7.3	1.02
460-dPS-65	3336	1.29			
820-dPS-65	5965	1.43			
200-PtBA-40	1081	1.14	PtBA	5.3	1.05
410-PtBA-40	2194	1.26			
720-PtBA-40	3829	1.22			
1100-PtBA-40	5817	1.28			
140-PtBA-95	1670	1.38	PtBA	12.3	1.04
220-PtBA-95	2710	1.28			
340-PtBA-95	4214	1.27			
730-PtBA-95	9021	1.29			

The naming convention is [backbone repeat units]-[side-chain chemistry]-[side-chain repeat units] with the side-chain number rounded to the nearest five and the backbone rounded to the nearest ten. A portion of each of the brushes based on PtBA-95 was hydrolyzed using CF_3COOH (trifluoroacetic acid) as described in Chapter 2, and the extent of conversion determined by titration. The resulting brushes are shown in Table 3.2.

Table 3.2: Molecular weight and extent of hydrolysis for Poly(acrylic acid) based bottlebrushes.

Name	Bottlebrush M_w (kg/mol)	Side-Chain M_w (kg/mol)	Extend of Hydrolysis (%)
140-PAA-95	1093	8	81
220-PAA-95	1715	7.8	86 (a)
340-PAA-95	2667	7.8	
730-PAA-95	5556	7.6	90

a.) 140-PAA-95 and 730-PAA-95 were titrated and the extent of hydrolysis for the other two brushes taken to be the mean.

As a direct comparison to the densely grafted bottlebrush polymers, a series of linear polynorbornenes of approximately equivalent number of monomer units were synthesized and characterized (Chapter 2). Their molecular weights and polydispersities are summarized in Table 3.3. The naming follows that of macromonomers: [polymer type]-[number of repeat units].

Table 3.3: Molecular weight and polydispersity of linear polynorbornenes.

Name	Repeat Units	M_w (kg/mol)	PDI (M_n/M_w)
PNB-660	662	62	1.35
PNB-1200	1202	113	1.57
PNB-1370	1365	129	1.4

For the study of the PAA-95 based series of bottlebrushes, we prepared buffer solutions at three pH values (5, 7, and 9) and two salt concentrations (0.1M and 1.0M). A single universal buffer was used in order to have the same composition of salts in all of the samples. The Britton-Robinson buffer[45] , composed of a mixture of boric, phosphoric, and acetic acids, is linearly adjustable over the pH range of interest.

A deuterated 0.2M buffer solution was prepared by adding boric acid (74.3mg, 1.20mmol), glacial acetic acid (68.7 μ L, 1.20mmol), and phosphoric acid (82.1 μ L, 1.20mmol) to a glass vial containing 30.0mL of deuterium oxide (D₂O). This was split into three portions by pipetting 10mL of the solution into each of three new glass vials. A 0.2M sodium deuterioxide solution was prepared by diluting 40% NaOD (266 μ L, 4.00mmol) with 20.0mL of D₂O. The three acid solutions were then each brought to the desired pH by adding NaOD solution until the pH (as determined by pH paper) had reached 5, 7, and 9 respectively for the three solutions. The amount of sodium deuterioxide that had to be added in order to reach the desired pH was greater than indicated[45], and this is most likely due to the difference in acidity between hydroxyl and deuterioxyl groups. Identical buffer solutions were prepared using ordinary NaOH and H₂O for dynamic light scattering experiments, and in this case the amount of NaOH needed to reach the desired pH was in accord with the literature. The finished buffer solutions were each split into two equal portions, diluting one to 0.1M concentration and adding sodium chloride to the other to reach 1M salt concentration.

3.2.2 Multi Angle Laser Light Scattering with Gel Permeation Chromatography

Multi Angle Laser Light Scattering (MALLS) was used in conjunction with Gel Permeation Chromatography (GPC) to determine the molecular weight and radius of

gyration (R_g) of the polymers[46]. Our system used a Wyatt DAWN EOS multi angle laser light scattering detector ($\lambda=690\text{nm}$) with a Waters 410 differential refractometer (RI) ($\lambda=930\text{nm}$) connected in series. Chromatographic separation by the size exclusion principle (largest comes out first) was achieved by using four Agilent PLgel columns (pore sizes $10^3, 10^4, 10^5$, and 10^6 Å) connected in series. Degassed THF was used as the mobile phase with a temperature of 35°C and a flowrate of $0.9\text{mL}/\text{min}$. The time for complete elution through the system was 50 minutes and MALLS and RI data were recorded at 5Hz. Samples were prepared by dissolving 5mg of polymer in 1mL of THF and filtering the solution through a $0.45\mu\text{m}$ PTFE membrane syringe filter immediately before injection. An injection volume of $20\mu\text{L}$ was used.

The data was analyzed using Wyatt Astra Software (version 5.3.4) using the Berry fitting formula[47] (more accurate than Zimm for larger polymers[48]) to obtain the radius of gyration (R_g) and weight average molecular weight (M_w) for each time point. In addition to obtaining an average molecular weight and size for each polymer sample injected, it was also possible to measure $R_g(M_w)$ for a range of values around the average. Continuous data acquisition during the elution process effectively provides the data for a large number of finely separated fractions. Despite the low concentrations of polymer in the fractions, the high molecular weight of the polymers combined with the sensitivity of the light scattering detectors provided high accuracy size and molecular weight data, particularly for the larger molecular weight fractions. This method allows a small number of polymer samples to be used to accurately map out the R_g vs M_w behavior as has been demonstrated in the literature[6].

3.2.3 Dynamic Light Scattering

Dynamic Light Scattering experiments were performed using a Brookhaven Instrument Company ZetaPALS instrument with an integrated laser light source ($\lambda = 632.8\text{nm}$) and integrated digital correlator. The 90° detector position was used and the integrated electronic dust filter used to reject sudden spikes in the signal intensity. Samples were loaded into 10mm path length cuvettes and the intensity optimized for each sample using the integrated software. The instrument provided integrated temperature control, and after setting the temperature the sample was allowed to equilibrate for 10 minutes. The resulting correlation function was analyzed by the method of cumulants[49, 50] using a cubic fit to obtain an average value for the diffusivity. The Stokes-Einstein relation (equation 3.1), where K_B is the Boltzmann constant, D is the diffusivity and η is the viscosity of the solvent, relates the diffusivity to an effective hydrodynamic radius R_h .

$$D = \frac{K_B T}{6\pi\eta R_h} \quad (3.1)$$

The R_h was recorded for each of five data acquisition runs of 2 minutes each and the results subsequently averaged to obtain an R_h for each sample. The data acquisition and calculation of R_h was done in the Brookhaven Instrument Company 9kdlsw32 software (version 3.55).

Samples were prepared as solutions of approximately 0.5mg/mL concentration (the results are not concentration dependent as long as the sample is dilute). This was done by weighing out polymer into a new 4mL vial and adding the appropriate solvent (buffer for PAA based bottlebrushes, THF as the good solvent for PS and dPS bottlebrushes, cyclohexane as the theta solvent for PS bottlebrushes, and toluene for the

PtBA bottlebrushes) and placing the sealed vial on a wrist action shaker. For hydrophobic polymer samples (PNB and both PS and PtBA bottlebrushes) the polymers dissolved within a few minutes, while the PAA based brushes were left on the shaker overnight. Once homogeneous, the sample solutions were filtered through a 0.45 μm PTFE membrane syringe filter into either a brand new disposable cuvette (aqueous samples) or a thoroughly cleaned (rinsed three times with organic solvent, soaked overnight in detergent solution, rinsed with double distilled water and then ethanol) and vacuum oven dried glass cuvette (samples in organic solvents). These were immediately capped to prevent any additional dust contamination.

3.2.4 Small Angle Neutron Scattering at NIST

SANS experiments were performed at the NIST Center for Neutron Research at the National Institute of Standards and Technology in Gaithersburg, MD on the 30m cold neutron SANS instrument on beamline NG-3[51] using the refractive lenses to improve the signal quality at low- q [52]. Sample solutions in 2mm path length quartz banjo cells were placed in aluminum holders and into a sample changer (temperature controlled using recirculating water bath). Two-dimensional scattering patterns were taken at each of three configurations:

- 1) 6 \AA neutrons, 7 neutron guides, and 1.3m sample-to-detector distance (SDD).
- 2) 6 \AA neutrons, 5 guides, and 4m SDD.
- 3) 8.4 \AA neutrons, 0 guides, and 13m SDD with lenses focusing the neutron beam.

This resulted in an overall scattering vector range of ($0.0015 < q(\text{\AA}^{-1}) < 0.4$) where $q = (4\pi/\lambda)\sin(\theta/2)$. The raw data was corrected for background electronic noise and neutron radiation, detector pixel sensitivity, and empty cell scattering and subsequently

normalized by the incident neutron flux using NIST provided software[53] resulting in absolute, coherent scattering intensity.

The 2D scattering patterns were radially averaged and data from the three detector distances combined into one $I(q)$ curve spanning the entire available q -range. The data for cells containing only solvent was processed in the same way in order to obtain $I_{\text{solvent}}(q)$. The background solvent scattering was subtracted from the sample data using the following equation:

$$I_{\text{sample}}(q) = I(q) - C \times I_{\text{solvent}}(q) \quad (3.2)$$

The constant C was chosen so that at $q > 0.3 \text{ \AA}^{-1}$ (where the scattering is independent of structure and of q) the residual intensity would correspond to the expected residual incoherent scattering due to the sample. For an unlabeled polymer in perdeuterated solvent at 1wt% this corresponds to 5% of the original scattering intensity, giving values for C that are close to 1.0 but vary slightly ($\pm 10\%$), possibly due to the variation in path length between individual cells.

Four different solvents were used for the scattering experiments: perdeuterated tetrahydrofuran (dTHF), mixed deuterated and ordinary tetrahydrofuran (mTHF, 54.8% deuterium content), perdeuterated toluene, and deuterated cyclohexane (96% deuterium content). The tetrahydrofuran is a good solvent for polystyrene and the toluene is a good solvent for poly(*tert*-butyl acrylate). Cyclohexane (at 34.5°C) is a theta solvent for polystyrene. The different amounts of deuteration were used as a means of adjusting the scattering contrast with the cyclohexane deuteration percentage (96%) chosen to make the Scattering Length Density(SLD)[54] approximately equal to that of dTHF (6.4×10^{-6}

\AA^{-2}). The mTHF (54.8% deuterated) was chosen to have its SLD ($3.57 \times 10^{-6} \text{\AA}^{-2}$) be halfway between that of the polynorbornene backbone ($0.73 \times 10^{-6} \text{\AA}^{-2}$) and the dPS side-chains ($6.4 \times 10^{-6} \text{\AA}^{-2}$). When used as a solvent for bottlebrushes with deuterated side-chains this should provide equal scattering contrast for the backbone and the side-chains.

Samples were prepared in all cases by weighing out the appropriate amount of polymer (1wt% for 0.75ml taking into account the density of the solvent) into new 2mL glass vials with PTFE lined caps. Solvent (0.750mL) was added by precision syringe and the vial was placed on a shaker to mix for 1 hour. Samples were then transported to the neutron scattering facility in the sealed vials. Solutions of bottlebrushes with polystyrene side-chains in cyclohexane appeared cloudy at room temperature and were placed on a temperature controlled shaker set to 50°C and then kept in an oven at 40°C to ensure that the polymer would be fully solvated. Sample solutions were filtered through a 0.45 μm PTFE membrane syringe filter into the 2mm path length banjo cells (0.56mL volume). The cyclohexane based samples were transported to the NG-3 SANS instrument in a temperature controlled box set to 40°C and placed directly into the sample changer preset to 40°C.

3.2.5 Small Angle Neutron Scattering at ORNL

SANS experiments at the High Flux Isotope Reactor (HFIR) at Oak Ridge National Laboratory (ORNL) were performed using the 40m GP-SANS instrument on beamline CG-2[55]. The newly upgraded 1m x 1m linear position sensitive ^3He detector was used for these experiments[56]. Sample solutions in 5mm path length quartz banjo cells were secured in brass holders and placed into a twelve position sample changer with

Peltier based temperature control. Two-dimensional scattering patterns were taken at each of three configurations:

- 1) 4.72Å neutrons, 7 neutron guides, and 0.3m sample-to-detector distance (SDD).
- 2) 4.72Å neutrons, 5 guides, and 6m SDD.
- 3) 12Å neutrons, 0 guides, and an 18.5m SDD.

This resulted in an overall scattering vector range of ($0.0012 < q(\text{Å}^{-1}) < 0.8$) where $q = (4\pi/\lambda)\sin(\theta/2)$. The raw 2D data were corrected for background electronic noise and neutron radiation, detector tube geometry, pixel sensitivity, and empty cell scattering. The data was normalized by the incident neutron flux and open beam transmission using macros in IGOR Pro developed by Dr. Ken Littrell, resulting in the absolute, coherent scattering intensity. The 2D data was radially averaged and the data from the three detector distances combined into an $I(q)$ curve spanning the entire available q -range using NIST provided software[53]. The solvent background was subtracted in the manner described in section 3.2.4.

The solvents used were tetrahydrofuran (for linear polynorbornene) and buffer solutions at pH 5, pH 7, and pH 9 (for PNB-g-PAA bottlebrushes). The samples were prepared by weighing out the polymer into a 4mL vial and adding the appropriate solvent (1.50mL), sealing the vial with a PTFE lined cap and placing the vial on a shaker overnight. The pH values of the aqueous bottlebrush solutions were tested and found to be lower than that of the original buffer solution due to the addition of a significant amount of acid. Sodium deuteroxide solution (1M) was added to bring the pH to the desired value as measured using pH paper. Solutions were filtered through a 0.45µm PTFE membrane syringe filter into the 5mm banjo cells (1.4mL volume).

3.3 Results and Discussion

3.3.1 Hydrodynamic and Gyration Radii of Bottlebrushes in Good Solvent

Results

Multi Angle Laser Light Scattering (MALLS) in combination with GPC was successful in determining the relationship between the Radius of Gyration (R_g) and the weight average molecular weight (M_w) for bottlebrush polymers. In order to facilitate comparison between bottlebrushes with different side chains this is represented as a function of N_b . The THF used as an eluent in the GPC system is a good solvent for polystyrene, poly(tert-butyl acrylate), and polynorbornene. The chromatographic separation by the GPC columns fractionates the polymer sample and also ensures that the concentration of sample in the MALLS flow cell is very low ($<0.05\text{mg/mL} \cong 0.006\text{ wt\%}$) ensuring that the radius measured is in the dilute regime. Due to the fractionation effect, radii for a range of N_b values around the average were obtained for each bottlebrush polymer sample. Results from bottlebrushes based on the same macromonomer were combined to obtain $R_g(N_b)$ over a large range of N_b values for all of the brushes in Table 3.1 and are plotted in Figure 3.2.

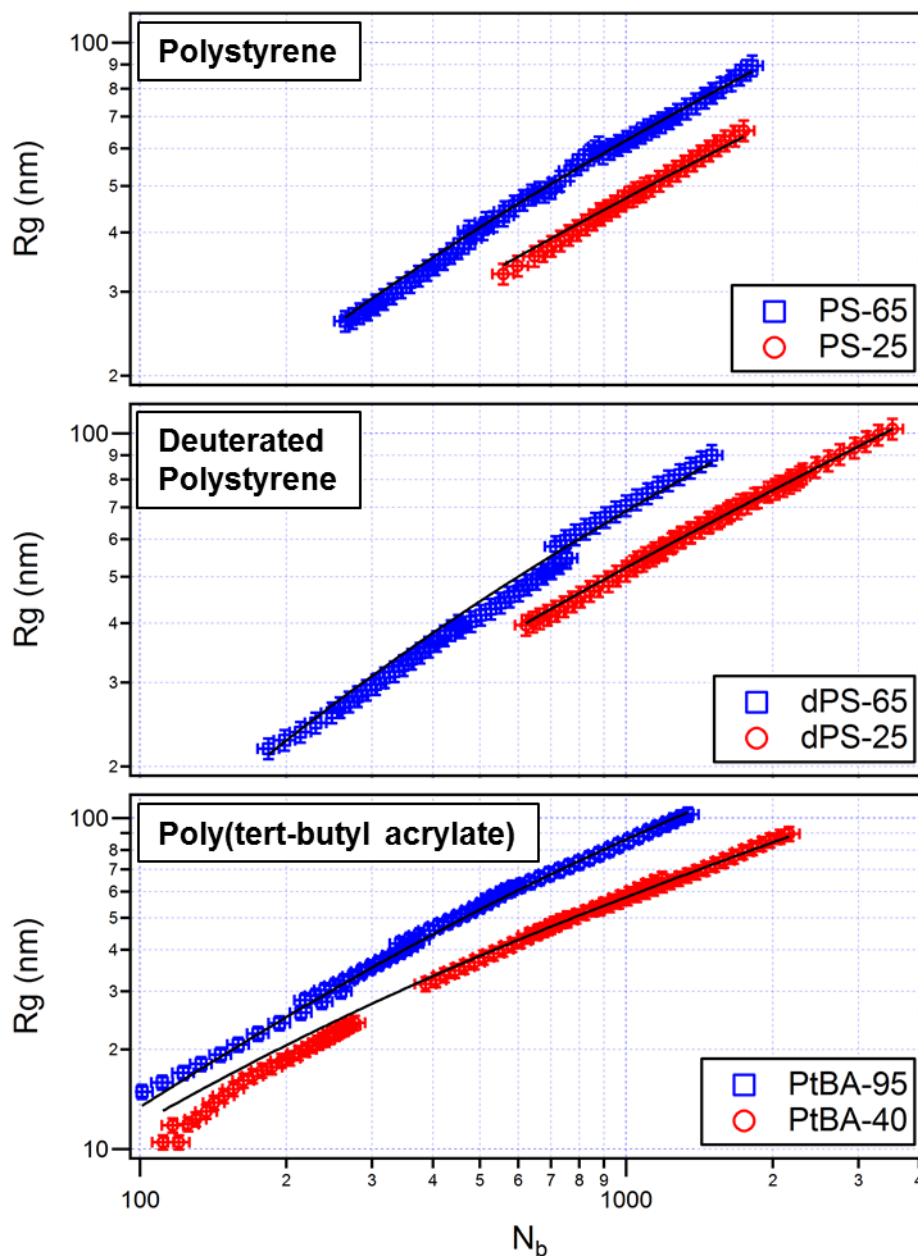


Figure 3.2: MALLS/GPC determined $R_g(N_b)$ for all bottlebrush polymers in THF. The three plots correspond to the three different side chain types (from top to bottom): polystyrene, deuterated polystyrene and poly(tert-butyl acrylate). In each plot the blue squares correspond to the shorter side chain length and the red circles correspond to the longer side chain length. The solid black lines are the wormlike chain model fits for each bottlebrush family.

The $R_g(N_b)$ curves (log-log) do not follow a simple power law ($R_g \sim N_b^\nu$) as would be expected for a linear polymer in good solvent[7] and observed for polynorbornene which has $R_g = 0.197 N^{0.611}$ (Figure 3.3). This is expected and has been

previously established for bottlebrush polymers which are stiffened by the steric repulsion between their side-chains and have $R_g(N_b)$ behavior better described by the Kratky-Porod wormlike chains[7]. In such polymer chains the orientation of segments is correlated with that of their neighbors for a distance along the backbone contour characterized as the persistence length. The physical interpretation of the persistence length is controversial for bottlebrush polymers, as the inter-segmental correlation depends on the distance from the chain ends[26]. We therefore avoid drawing conclusions about the local chain stiffness from the l_k obtained by fitting. For an ideal wormlike chain with L (the backbone contour length) and l_k (the Kuhn segment length for an infinitely long chain), the radius of gyration has the analytical form (first derived by Benoit and Doty[57]):

$$\langle R_g^2 \rangle = \frac{l_k L}{6} - \frac{l_k^2}{4} + \frac{l_k^3}{4L} - \left(\frac{l_k^4}{8L^2} \right) \left(1 - e^{-2L/l_k} \right) \quad (3.3)$$

The model is valid for both stiff and flexible polymer chains, and the two limiting behaviors can be derived by setting $(L / l_k) \sim 1$ and $(L / l_k) \gg 1$ with corresponding $\nu=1$ and $\nu=0.5$ [16], respectively. For the bottlebrush polymers the changing power law with $0.5 < \nu < 1$ confirms that the materials are in the intermediate semi-flexible regime. This model was a reasonable fit to the experimental data for all N_b of bottlebrushes with polystyrene and deuterated polystyrene side-chains, but deviates from the data for $N_b < 200$ for the bottlebrushes based on PtBA-40 where ν is close to 1. The contour length L was estimated by assuming a length per monomer of 0.5nm (based on the carbon bond lengths and angles) and this provided a reasonable fit to the experimental results for all bottlebrushes. The results of this fit are shown along with the calculated

contour length, the local average scaling exponent for each bottlebrush derived from a power law fit and the hydrodynamic radius R_h obtained from DLS in Table 3.4.

Table 3.4: MALLS and DLS results for PS, dPS and PtBA bottlebrushes.

Polymer	R_g (nm)	R_h (nm)	R_g/R_h	Scaling Exponent	Contour Length (nm)	wormlike l_k (nm)
570-PS-25	36.4	25.9	1.41	0.61	288	29
890-PS-25	45.9	30.9	1.49	0.60	447	
330-PS-65	31.1	25.5	1.22	0.69	163	55
550-PS-65	45.1	33.1	1.36	0.66	275	
1190-PS-65	69.3	42.5	1.63	0.59	597	
520-dPS-25	39.1	26.3	1.49	0.57	260	37
670-dPS-25	45.6	31.4	1.45	0.56	334	
1130-dPS-25	58.1	35.9	1.62	0.52	563	
250-dPS-65	27.2	-	-	0.72	126	69
460-dPS-65	40.4	-	-	0.67	229	
820-dPS-65	64.4	-	-	0.59	409	
200-PtBA-40	18.7	13.5	1.39	0.79	102	45
410-PtBA-40	34.5	22.3	1.55	0.68	207	
720-PtBA-40	48.8	-	-	0.62	361	
1100-PtBA-40	61.2	32.6	1.88	0.59	549	
220-PtBA-95	29.9	24.4	1.23	0.76	110	127
340-PtBA-95	43.3	30.9	1.40	0.71	172	
730-PtBA-96	71.6	39.5	1.81	0.62	367	

The l_k values show a clear correlation with the side chain length, increasing with N_s in accord with all previous literature on bottlebrush polymers except for the results of Rathgeber et al[20]. These values are an order of magnitude greater than the 3.4nm measured for a linear polynorbornene, confirming the importance of the side-chains in expanding the conformation. The l_k values are larger for the deuterated polystyrene than the unlabeled equivalent. The ratio of $l_k(N_s=65)$ to $l_k(N_s=25)$ is approximately the same for the regular and the deuterated polystyrene (1.8), which is lower than the ratio of the

side-chain lengths (2.6). For the PtBA the ratio of l_k (2.8) is greater than the ratio of side-chain lengths (2.1). There is not sufficient data to conclude whether this is due to differences between the poly(tert-butyl acrylate) and polystyrene side chains or is a consequence of a dependence on the N_s which are larger for the PtBA brushes.

The hydrodynamic radii are smaller than the radii of gyration for all bottlebrushes studied, as expected for polymeric materials[7] and consistent with previous work on bottlebrushes. The hydrodynamic radius increases with increasing side-chain and backbone length, although the dependence of the R_h on backbone length is weaker than would be expected for a linear polymer in good or theta solvent with $R_h \sim N_b^\nu$ having $\nu < 0.5$. The R_g/R_h values (which are a measure of compactness) increase with increasing N_b , but are smaller for a brush with equal N_b and shorter side-chains. These observations are consistent with the picture of a bottlebrush polymer as a wormlike chain with the diameter proportional to the side-chain length. Although for a linear polymer the R_g/R_h ratio is expected to plateau at about 1.4 as N_b becomes large, in bottlebrushes the ratio continues to increase with N_b . No evidence of a plateau in R_g/R_h is seen for our bottlebrushes, nor has one been reported in the literature.

The scaling derived from fitting a power law $R_g \sim N_b^\nu$ to local regions of the $R_g(N_b)$ becomes smaller with increasing backbone length as expected for a wormlike chain[16]. For most of the bottlebrushes (based on macromonomers PS-25, PS-65, dPS-65, PtBA-40 and PtBA-95) this appears to be approaching the value for a polymer with excluded volume of $\nu=0.6$. However for dPS-25 it appears to be approaching $\nu=0.5$ as predicted for an infinitely long wormlike chain. The scaling exponent reported for 200-

PtBA-40 corresponds to $N_b > 170$, above the break in the $R_g(N_b)$ curve (Figure 3.2) for smaller values of N_b , the scaling exponent is consistent with rodlike behavior.

Discussion

The bottlebrush polymers have R_g several times larger than the corresponding linear polynorbornene (PNB), shown in Figure 3.3. As an example, the R_g of 730-PtBA-95 ($N_b=730$ with PtBA side-chains and $N_s=95$) is 72nm, while the R_g for a linear PNB with $N=730$ is 11nm, an almost sevenfold increase.

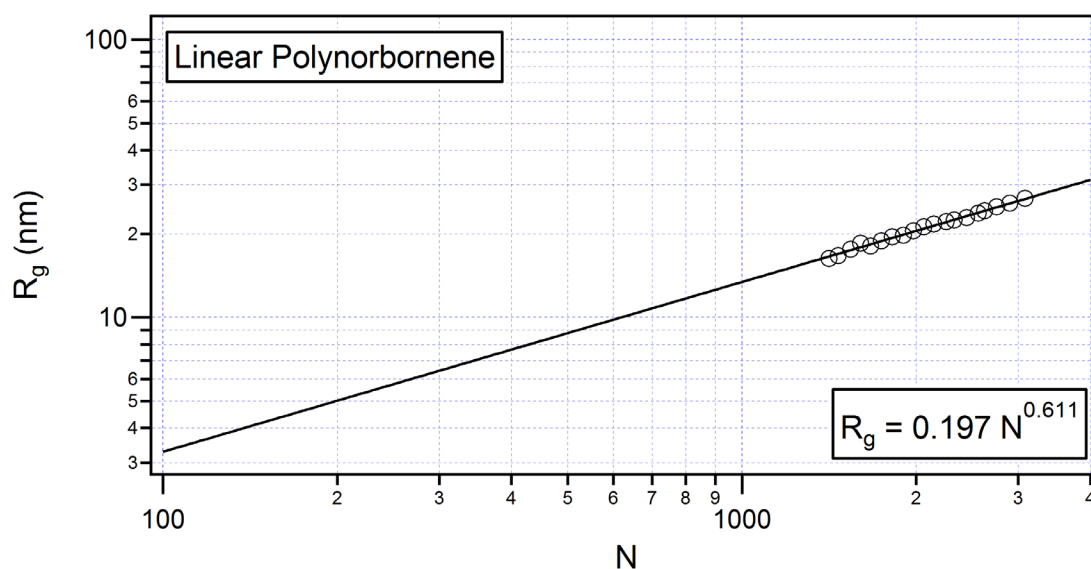


Figure 3.3: Radius of gyration as a function of N for linear polynorbornene in THF. The measured R_g (open circles) were determined by MALLS/GPC of PNB-1370 with the data limited to larger N by the limitation of reliable light scattering size determination to $R_g \geq 15$ nm. This data was then extrapolated to lower N values, assuming the power law behavior to hold over the range of interest.

Only a very small increase in size can be explained by the extra distance spanned by the side-chains themselves and thus most of the effect is due to a stiffening and stretching of the backbone (and consequently the brush as a whole) as is confirmed by the strong dependence of the R_g on N_b . Since the overall contour length is the same for linear

and grafted polynorbornene this supports the conclusion that the densely grafted side-chains stiffen the bottlebrush, resulting in a much longer effective Kuhn segment l_k .

The conformation of the backbone itself has not been experimentally observed and it is unclear whether it behaves like a semi-flexible wormlike chain. Lattice Monte Carlo simulation results on bottlebrushes of $N_b < 300$ suggest that the backbone is stiffened significantly by side-chains, becoming semi-flexible for all side-chain lengths used in our experiments ($N_s \geq 20$)[4]. It was also determined, however, that the persistence length is ill-defined and the local stiffness is not uniform along the backbone[26]. The apparent rigidity is greater at the middle of a bottlebrush and appears to grow monotonically with N_b , which clearly renders the ordinary interpretation of the wormlike persistence length meaningless. Taking into consideration these caveats, the wormlike chain model does offer a satisfactory model of overall bottlebrush conformation and can be used to estimate and compare their stiffness.

The unperturbed wormlike chain model has been used by Schmidt and coworkers to determine the persistence lengths of bottlebrushes in good solvent[6]. Later work by Schmidt and coworkers[13, 14, 58] and also by Nakamura and coworkers[5, 9-12, 59-61] has incorporated further refinements: the change in contour length due to the side-chains near the end[11, 62] (important for $N_b \sim N_s$), incorporation of polydispersity[13, 14], and of excluded volume interactions[5, 12]. The quality of the fit is improved by these modifications, but only very moderately in the intermediate range of N_b ($200 < N_b < 2000$) where all of our bottlebrushes fall. These corrections all introduce further parameters into the model that must be determined experimentally or found in the literature as they cannot all be determined uniquely from the experimental R_g and R_h

data. Calculating the R_h for a wormlike chain introduces another parameter, the diameter of the chain. The three parameters of the resulting model (d , L , l_k) could not be determined by fitting given the paucity of R_h data. Attempts to use the l_k and L determined from $R_g(N_b)$ to model the $R_h(N_b)$ were also unsuccessful. The Yamakawa-Fujii[63] and Norisuye-Motowaka-Fujita[64] models for the translational diffusion of wormlike chains have been used to describe DLS results for bottlebrush polymers. Neither model provided a good fit to our $R_h(N_b)$ data while using the l_k obtained from fitting equation 3.3 to the $R_g(N_b)$ data.

The shapes of the bottlebrushes can be characterized qualitatively by comparison to previously measured bottlebrush polymers and theoretically calculated R_g/R_h values for cylinders and prolate spheroids. The hydrodynamic radii as a function of the aspect ratio (length/radius) have been derived for prolate spheroids[65] as well as for cylinders with aspect ratios between 4 and 40[66, 67]. Using these results, the R_g/R_h ratios were calculated for cylinders and prolate spheroids over a range of aspect ratios. The data was interpolated by polynomial and is shown in Figure 3.4.

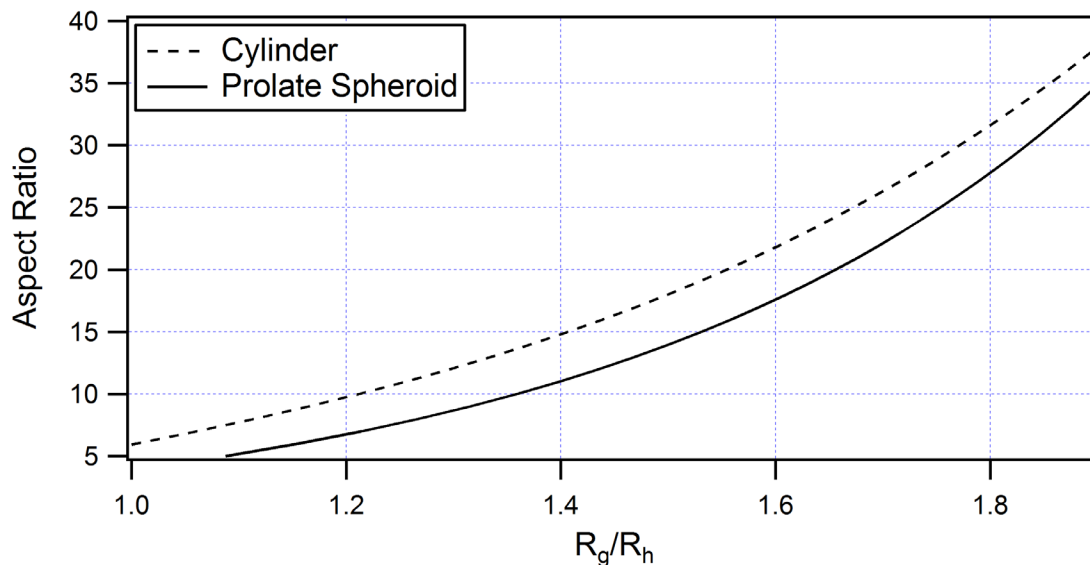


Figure 3.4: Aspect ratio of a prolate spheroid (solid line) and a cylinder (dashed line) as a function of the apparent ratio of the radius of gyration to the hydrodynamic radius. The curves were generated by calculating the R_g and R_h for cylindrical and prolate spheroidal hard particles for a number of values within the plotted range and then interpolating the data. The aspect ratio is defined as primary/secondary axes for the prolate spheroid and as length/radius for the cylinder.

It is immediately evident that the ratio is indeed a strong indication of anisotropy as it monotonically increases with the aspect ratio for both cylinders and prolate spheroids. The cylinder has a higher aspect ratio for a given R_g/R_h value than the prolate spheroid, which more closely resembles a typical polymer coil. We can start by assuming that the overall length of the bottlebrush in solution is proportional to N_b and that the radius is proportional to N_s . This is consistent with the observed increase in R_g/R_h with the N_b for a series of brushes with identical side-chain chemistry and N_s . Decreasing the side-chain length has the effect of increasing R_g/R_h consistent with increasing the aspect ratio. The prolate spheroid aspect ratio corresponding to the observed R_g/R_h values lead to aspect ratios ranging from 7 to 35 which seem somewhat high.

The hydrodynamic radius of a polymeric ellipsoid without hard boundaries cannot be calculated analytically and does not have a readily available approximate form. It is,

however, reasonable to expect that the R_g/R_h value at any given aspect ratio will be higher by considering the difference between a hard sphere ($R_g/R_h = 0.8$) and a polymer coil in good solvent ($R_g/R_h = 1.4$). The shift in values will be much less dramatic for a bottlebrush polymer due to the much greater segmental density of side-chains around the backbone contour. Although the exact aspect ratios cannot be interpreted physically, the trends observed in the model are consistent with our experimental results.

From these considerations we can conclude that the bottlebrushes take on extended conformations in solution which become more extended as N_b is increased. The observed R_g/R_h values are consistent with the bottlebrushes having local segmental density near the backbone that is higher than that for a linear polymer. The effect of the side-chain length is less clear, as making the side-chains shorter serves to increase the aspect ratio, but also reduces the crowding, leading to more flexible structure. Resolving the role of these two effects requires further investigation.

The series of bottlebrush polymers investigated show behavior that is qualitatively consistent with that observed for bottlebrushes made using radical polymerization of vinyl terminated macromonomers. Quantitatively some differences are expected due to the change in effective grafting density ($\sigma \neq \sigma'$), resulting from the change in monomer structure and the contour length per monomer (0.25nm for radical polymerization and 0.5nm for ROMP). Since the repeat unit length is different, it is not correct to compare results for bottlebrushes of the same N_b . Instead we can consider our bottlebrushes to have N'_b of about double their N_b , with a side-chain grafted at every other repeat unit of the backbone ($\sigma' = 0.5$).

Comparing the R_g for the PS-65 base brushes to the F65 series of Nakamura[10], both having polystyrene side-chains with 65 repeat units, we get good agreement between R_g values by offsetting the N_b values of our bottlebrushes by 1.7 instead of 2. This confirms that our bottlebrushes are less stiff due to the reduction in grafting density, but that the effect is not dramatic. There was no data available for comparison with the PS-25 based brushes, but comparing to data for F33[5] ($N_s = 33$) we see that the effective N_b shift factor is about 1.5, which may be lower than the 1.7 seen for PS-65 because of the mismatch in side-chain length between F33 and PS-25. The l_k values reported for F33[5] and F65[10] are 36nm and 75nm respectively, slightly higher than those for PS-25 (29nm) and PS-65 (55nm). Comparing to the results of Wintermantel[6] is more difficult due to lack of identical side-chain lengths. The only reasonable match is our PS-25 to their PS29 ($N_s=29$) for which their N_b (165,212 and 1019) are not well-matched to ours (570,890). By plotting their data on a log-log plot along with ours we can get an estimate of the shift factor by adjusting the N_b shift for our data until all points (our and theirs) are collinear. The resulting shift factor is approximately 1, indicating that their brushes are much more extended than ours as their ratio of overall size to contour length is double that of our materials. Their bottlebrushes are also stiffer, having an l_k of 89nm, which is three times our measured value. The R_g/R_h values were commensurately higher. Their bottlebrush with $N_s=29$ and $N_b=1019$ had an $R_g/R_h=2.08$, larger than our observed maximum of 1.9 and much greater than the 1.5 of 890-PS-25.

The origin of the difference between the results of Wintermantel and Nakamura is unknown. It may be a solvent effect, as Nakamura used toluene while our group and Wintermantel both used THF. While both are good solvents, polystyrene takes on a more

expanded conformation in THF. The other possibility is the role of the backbone chemistry. While all side-chains were polystyrene, three different backbones were used: polymethylacrylate (Wintermantel), polystyrene (Nakamura), and polynorbornene (this work).

It appears that the lower effective grafting density of ROMP based bottlebrushes somewhat reduces their size, stiffness, and degree of anisotropy when compared to bottlebrushes prepared by radical polymerization. However, the magnitude of this effect is unclear due to the broad range of results reported in the literature. It is also important to note that polynorbornene based bottlebrushes have greater R_g for a given molecular weight since the mass per monomer is very similar but the contour length per monomer is doubled.

3.3.2 SANS of Unlabeled Bottlebrushes – Side-Chains in Good and Theta Solvents

Results

Small Angle Neutron Scattering patterns were obtained for 1wt% solutions of polystyrene based bottlebrushes in both THF (a good solvent) and cyclohexane (a theta solvent). Scattering was done at 25°C for samples in THF and at 40°C for samples in cyclohexane. While the theta temperature for linear polystyrene is 34.5°C, bottlebrush solutions in cyclohexane became cloudy at 38°C and thus the testing was conducted at 40°C to ensure that the solutions were homogeneous. Based on prior work on bottlebrush polymers in cyclohexane the effect of the temperature change on size is less than that seen for linear polystyrene[5] and should be minimal for the small (<5°C) change. Scattering patterns with very good statistics were obtained in less than 1.5 hours on

beamline NG-3 at NIST. Reduced, radially averaged scattering patterns with the solvent background subtracted are shown in Figure 3.5.

All of the scattering patterns in Figure 3.5 have a two-plateau shape corresponding to two-length scales of interest. Starting from high q (0.42 \AA^{-1}) there is a region of incoherent scattering that is indistinguishable from the solvent background until $q \cong 3 \text{ \AA}^{-1}$ where there is Porod-like scattering[54] corresponding to the monomer level structure of the side-side chains. This reaches a plateau in the region $0.06 \text{ \AA}^{-1} < q < 0.15 \text{ \AA}^{-1}$ corresponding to length scales of 4 to 10 nm and consistent with the overall dimensions of the side-chains. The position of the plateau moves to lower q (larger length scales) for longer side-chain lengths and moves to higher q (shorter length scale) when changing the solvent quality from good to theta. This is consistent with the interpretation of this plateau as corresponding to the side-chains.

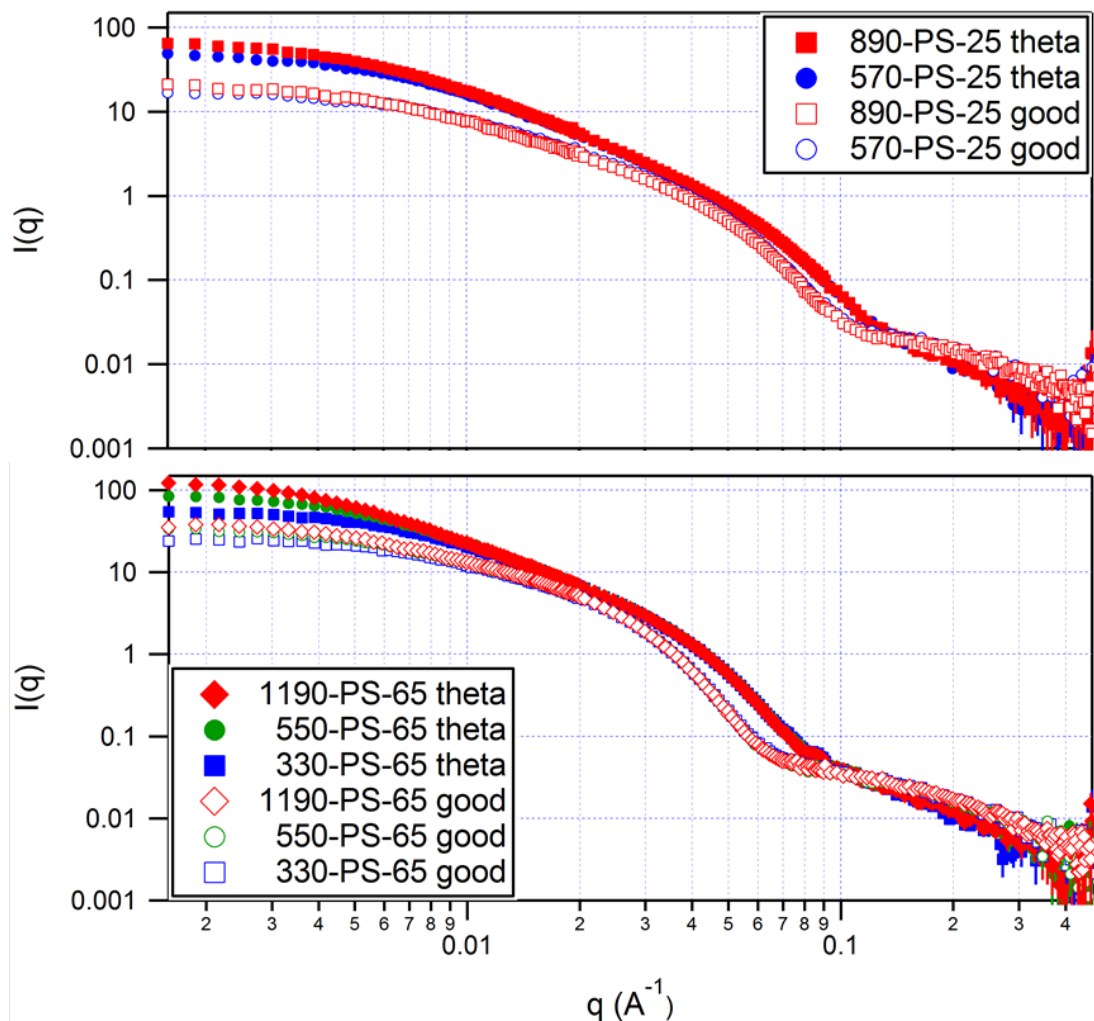


Figure 3.5: Radially averaged SANS patterns (taken on NG-3 at NIST) for 1wt% solutions of bottlebrushes with polystyrene side chains ($N_s = 25$ top and $N_s = 65$ bottom). The filled symbols correspond to samples in THF (good solvent) while the empty symbols correspond to samples in cyclohexane (theta solvent).

Moving to lower q there is a steep rise in the scattering intensity with power law increases $I(q) \sim q^{-m}$ of $3 < m < 4$, corresponding to surface fractal scattering[68]. This is interpreted to be the q region corresponding to the outer surface of the bottlebrush perpendicular to the backbone contour, with the exact q position dependent on the location of the high q plateau. After the steep surface scattering there is a sloping region with what appears to be power law scattering in the mass fractal range $1 < m < 2$ most

probably corresponding to the correlation between side-chain blobs (or semi-flexible cylindrical segments) along the backbone. At the lowest accessible q values $q < 0.006 \text{ \AA}^{-1}$ the scattering levels off into a plateau corresponding to the overall length scale of the object. The scattering patterns for a series of bottlebrushes with the same side-chains but varying backbone length are identical at high and mid q and separate at low q , with the longest backbone polymers having higher intensity (corresponding to more scattering centers per object) and plateauing at lower q corresponding to larger length scales.

The overall shape, two-plateau character, and shift of the q positions of the two plateaus is in qualitative agreement to scattering patterns obtained from Monte Carlo simulations[3, 4]. SANS experiments conducted on bottlebrushes prepared by grafting through[20, 69] and on shorter backbone bottlebrushes ($N_b \leq 300$) prepared by grafting through[42] showed qualitatively similar profiles. Based on the Monte Carlo simulations, a scattering function $I(q)$ has been derived for bottlebrushes in solution[69]. This, however, is a complicated expression with many parameters that makes significant *a priori* assumptions about the structure of the bottlebrushes in an attempt to directly determine the persistence length, side-chain scaling, side-chain radius, and overall size from the SANS pattern.

Instead we used a more general fitting approach to determine just the length scales relevant to the bottlebrush while assuming only that the bottlebrushes are fractal (polymeric) objects. The empirical Beaucage scattering function[70, 71] has been used to approximate the scattering from many different systems including random coils and ellipsoidal particles. It is a generalization of the scattering from polymer coils to a broader range of fractal behaviors and is particularly well-suited to polymeric systems

with multiple length scales of interest. In the expression for the scattering intensity shown below, $R_{g,i}$ is a radius of gyration corresponding to the plateau region, the P_i is the fractal (or Porod) scaling corresponding to the i^{th} length scale. The two prefactors G_i and B_i are lumped scale parameters for the Guinier and fractal scattering terms incorporating the number of scatterers per coil, the local density, the concentration, the contrast factor, and other physical parameters.

$$I(q) = Bkgd + \sum_{i=1}^2 G_i \exp\left(-\frac{q^2 R_{g,i}^2}{3}\right) + \frac{B_i \left[\text{erf}\left(\frac{q R_{g,i}}{\sqrt{6}}\right) \right]^{3P_i}}{q^{P_i}} \quad (3.4)$$

We used the two-level Beaucage model in order to determine both the overall and radial (perpendicular to the backbone contour) sizes of the bottlebrushes. The fitting was done by guessing values for the length scales of the features based on the q value of the plateau regions and the power laws by the slope of the scattering curve at q values near the onset of the plateau. This captured the shape of the scattering curve (the positions of the plateaus and the slopes of the upturns) as well as the more complicated models described in the literature[69]. The values of the remaining parameters were then determined by nonlinear least squares fitting in Igor Pro, after which point all of the parameters were further refined by nonlinear least squares fitting. The resulting length scales R_{CS} corresponding to the higher q plateau and R_g corresponding to the lower q plateau are shown in Table 3.5 along with R_h values determined by Dynamic Light Scattering (DLS).

Table 3.5: Cross-sectional and overall object radii for PNB-g-PS bottlebrushes in good(THF) and theta(cyclohexane) solvent determined by fitting the Beaucage scattering function $I(q)$ to SANS patterns in Figure 3.5.

Polymer	Good Solvent			Theta Solvent		
	R_{CS} (nm)	R_g (nm)	R_h (nm) ^(a)	R_{CS} (nm)	R_g (nm)	R_h (nm) ^(a)
570-PS-25	4.3	18.0	25.9	3.3	20.6	19.3
890-PS-25	4.1	21.0	30.9	3.3	24.7	22.3
330-PS-65	7.1	21.6	25.5	5.3	20.7	20.3
550-PS-65	7.1	25.2	33.1	5.3	26.4	26.3
1190-PS-65	7.1	28.8	42.5	5.3	34.0	35.0

^(a) R_h values were obtained by DLS and are taken from Table 3.4.

The side-chain length scales R_{CS} show the expected behavior being proportional to N_s and smaller in theta solvent than in good solvent. R_{CS} appears to be independent of N_b , confirming the identification of the higher q length scale with the side-chains. While there is not data available for bottlebrushes with identical side-chain lengths, measured R_{CS} values are in line with those reported in the literature for other bottlebrushes. For polystyrene bottlebrushes prepared by grafting from, Rathgeber[20] reported R_{CS} in good solvent of 4.2nm and 6.3nm for N_s of 24 and 54, respectively. The hydrodynamic radii of the bottlebrushes appear to be proportional to R_{CS} with the average ratio $R_{h,good}/R_{h,theta}$ (1.3) equal to the average ratio $R_{CS,good}/R_{CS,theta}$ (also 1.3). The exact scaling of the R_h with side-chain dimensions would require more data points to discern. A very interesting and unexpected result is the larger values for apparent R_g in theta solvent conditions than in good solvent as seen for all except 330-PS-65. The R_g values determined by SANS are also much smaller than those determined by MALLS and shown in Table 3.4, with the effect being more pronounced for bottlebrushes with longer backbones.

SANS patterns for 1wt% solutions of bottlebrushes with poly(tert-butyl acrylate) side-chains in toluene at 25°C were also acquired at NIST. The radially averaged and

solvent subtracted absolute $I(q)$ for several N_b and two side-chain lengths ($N_s=40$ and $N_s=95$) are shown in Figure 3.6. There is no well-documented theta solvent for PtBA, so all scattering was conducted in good solvent conditions.

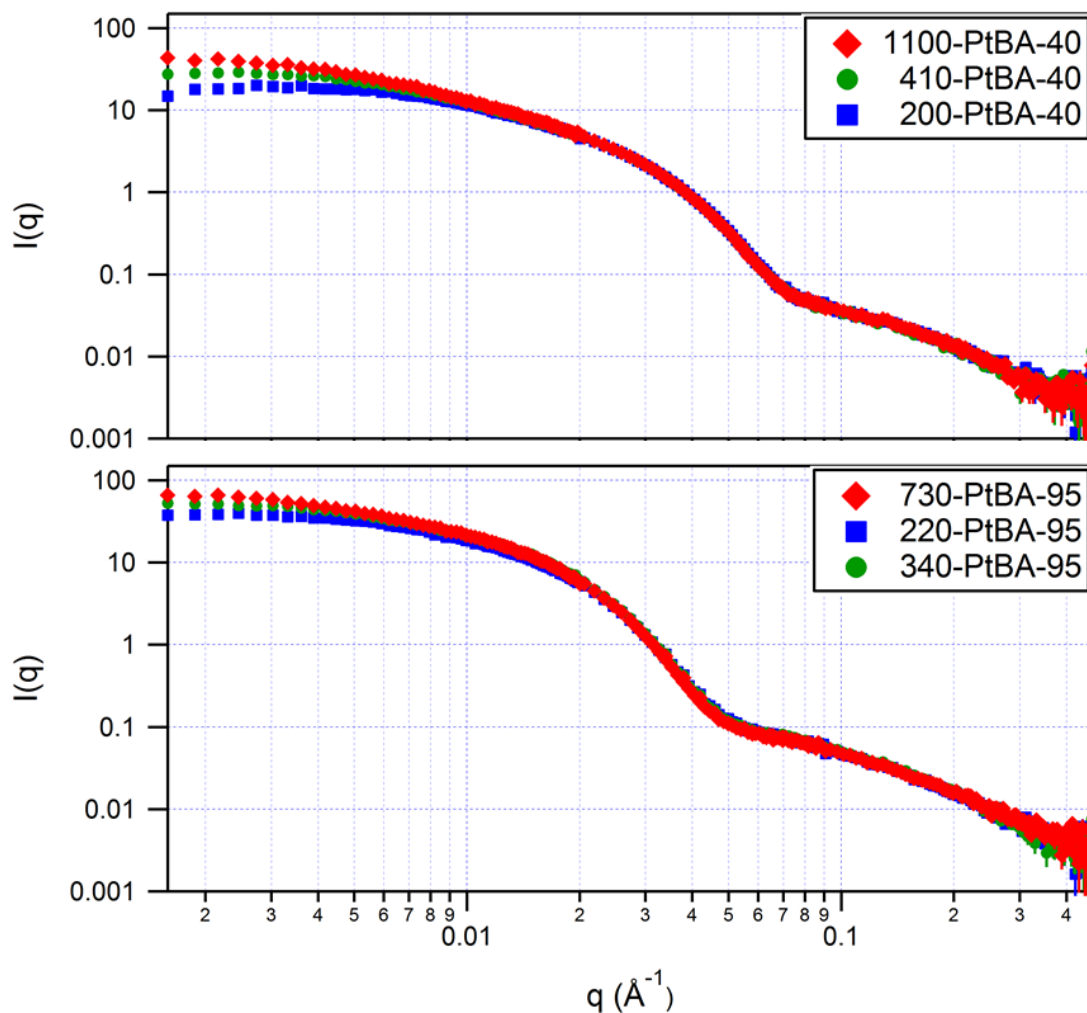


Figure 3.6: Radially averaged SANS patterns (taken on NG-3 at NIST) for 1wt% solutions of bottlebrushes with poly(tert-butyl acrylate) side-chains ($N_s=40$ top and $N_s=95$ bottom). All samples were in toluene, a good solvent.

The scattering patterns show the same qualitative features as were observed for bottlebrushes with polystyrene side-chains. There are two plateaus corresponding to the side-chain length scale (high q) and the overall object size (low q). The scattering patterns for bottlebrushes based on the same macromonomer overlap at high and mid q

and then separate at low q , with higher low q intensity observed for bottlebrushes with longer backbones. Good fits were obtained using the same two-level Beaucage model used for the polystyrene bottlebrushes. These are summarized in Table 3.6.

Table 3.6: Cross-sectional and overall object radii for PNB-*g*-PtBA bottlebrushes in good solvent determined by fitting the Beaucage scattering function $I(q)$ to SANS patterns in Figure 3.6.

Polymer	R_{CS} (nm)	R_g (nm)
200-PtBA-40	6.1	17.0
410-PtBA-40	6.1	22.5
1100-PtBA-40	6.2	28.6
220-PtBA-95	9.7	23.5
340-PtBA-95	9.9	28.0
730-PtBA-95	10.0	35.3

R_{CS} values for the PtBA bottlebrushes are of a similar order of magnitude to the PS results with the size for PtBA-40 falling between PS-25 and PS-65 and PtBA-95 having the largest R_{CS} . The behavior of bottlebrushes with PtBA side-chains in good solvent is very similar to the behavior of ones with PS side-chains with the overall R_g determined by SANS significantly smaller than measured by MALLS.

Discussion

In order to establish a consistent picture of the bottlebrushes in solution it is first necessary to resolve the disagreement between the R_g determined by SANS and that determined by MALLS. Given the consistent scaling and good agreement with the previous literature, we conclude that the MALLS R_g values are correct and endeavor to determine the origin of the SANS results. Observing the weak dependence of the R_g on the backbone length ($R_g \sim N_b^\nu$, $\nu < 0.4$) we conclude that the 1wt% solutions must be in the semi-dilute regime[7]. In this case the observed R_g would actually be the approximate

entanglement or blob length scale rather than the size of a single molecule. Overlap occurs when the volume available to each coil in solution is less than the pervaded volume of the coil and therefore the mean center-to-center distance (R_{c-c}) is less than R_{coil} . R_{c-c} can be estimated using the following equation:

$$R_{c-c} = \left(\frac{3}{4\pi} \times \frac{Volume}{\# \text{ of coils}} \right)^{1/3} \cong 3.414 \left(\frac{M_w}{\rho_{solvent}} \right)^{1/3} \quad (3.5)$$

In this expression R_{c-c} is the mean center-to-center distance in nm, M_w is that of the bottlebrush in g/mol and $\rho_{solvent}$ is the density of the solvent in g/mL. The numerical prefactor (3.414) accounts for the unit conversions and the 1wt% concentration used in the experiments. In order to compare this expression to the SANS data we have plotted all of the R_g values (both good and theta solvent) from Table 3.5 and Table 3.6 against $(M_w/\rho_{solvent})^{1/3}$ in Figure 3.7.

It is evident from the linear fit in Figure 3.7 that R_g data follow the scaling predicted by Equation 3.5 with 1190-PS-65 the only possible outlier. This is especially significant given that two different side-chain chemistries (PS and PtBA) and both good and theta solvent conditions were used. If R_g were approximately equal to R_{c-c} , the relationship would be linear with a slope of 3.414 (Equation 3.5). Instead, the linear fit (Figure 3.7) has a slope of 1.612. This indicates that above the overlap concentration R_g is approximately half of R_{c-c} and that another length scale (larger than R_g) determines overlap for bottlebrushes.

The linear fit shown on the plot fits the data but has a slope of 1.612, in contrast to the 3.414 that was estimated (a ratio of 0.47). This indicates that the R_g is significantly smaller than R_{c-c} at the overlap concentration and suggests that there is another length

scale for the bottlebrush that determines the overlap. It is probable that this is the end-to-end distance (R_{e-e}) of the bottlebrush polymer, which is 2.13 times the R_g .

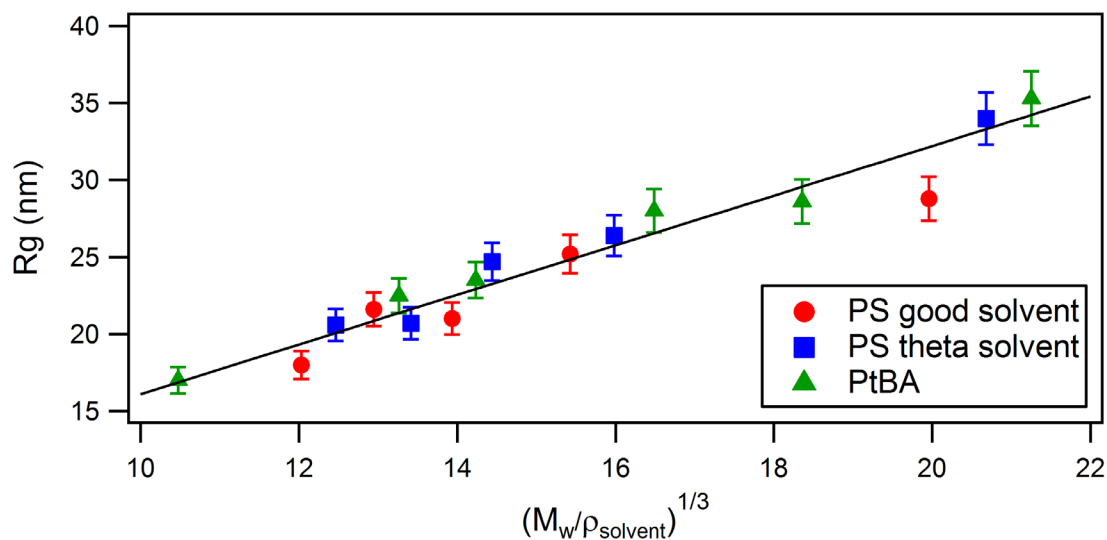


Figure 3.7: Radii of gyration determined from SANS for all brushes in Table 3.5 and Table 3.6 plotted as a function of the cube root of the molecular weight divided by the density of the solvent. At a constant mass fraction of polymer, this is proportional to the radius of the spherical volume available to each polymer molecule. The solid line is a linear fit to the data ($R^2 = 0.94$).

Thus SANS experiments were inadvertently conducted in the semi-dilute regime for the bottlebrushes and the apparent R_g values do not correspond to the overall sizes of the bottlebrushes. The 1wt% concentration used had been estimated to be below the overlap concentration by estimating the overlap concentration using equation 3.5 and setting R_{c-c} equal to the R_g determined by MALLS. This result indicates that for bottlebrushes of similar N_s and N_b scattering experiments must be conducted at very low concentrations ($<0.1\text{wt}\%$) to enable determination of the overall dimensions.

Although the bottlebrushes were above the overlap concentration, it is unlikely that interpenetration of the side-chains is present at 1wt%. The crowding around the backbone disfavors side-chain interpenetration, leading in some cases to lyotropic liquid

crystalline behavior in which the bottlebrushes have a parallel alignment in solution with spacing determined by the side-chain dimensions. These phenomena, however, are observed at much higher concentrations (5 to 16 wt%)[72-74]. Thus we can consider the R_{CS} for the side-chains to be the unperturbed side-chain dimensions.

The R_{CS} values in Table 3.5 are in remarkably good agreement with end-to-end distances estimated for free polystyrene chains with $N=N_s$. Using empirically fitted equations for $R_g(M_w)$ [75] and converting from R_g to R_{e-e} [16] we calculate R_{e-e} for PS-25 to be 4.3nm in THF and 3.3nm in cyclohexane. For PS-65 the values are 7.2nm in THF and 5.3nm in cyclohexane. These values deviate from the R_{CS} determined for the corresponding bottlebrushes by less than the experimental uncertainty. This indicates that both the radii of the side-chains and the molecular weight dependence are the same as those of free polystyrene chains. Although data on the R_g of free PtBA chains was not available for comparison, the scaling of R_{CS} with N_s of $\nu \sim 0.6$ is consistent with that of a linear polymer chain in good solvent. From these results we can conclude that the side-chain conformation does not appear to be significantly distorted by being grafted to the backbone.

3.3.3 SANS with Perdeuterated Side-Chains – The Backbone Conformation

Results

In order to determine the conformation of the bottlebrush backbone, we used bottlebrushes with ordinary polynorbornene backbones and deuterated side-chains. SANS experiments were conducted in deuterated THF which has a neutron scattering length density that almost exactly matches dPS, leaving only the scattering contribution of the backbone. SANS experiments were conducted on 1wt% solutions of 670-dPS-25 and

1130-dPS-25 in dTHF with 0.3wt% solutions of linear polynorbornene with N=660 and N=1370 serving as the control. The resulting radially averaged and solvent subtracted scattering patterns are shown in Figure 3.8.

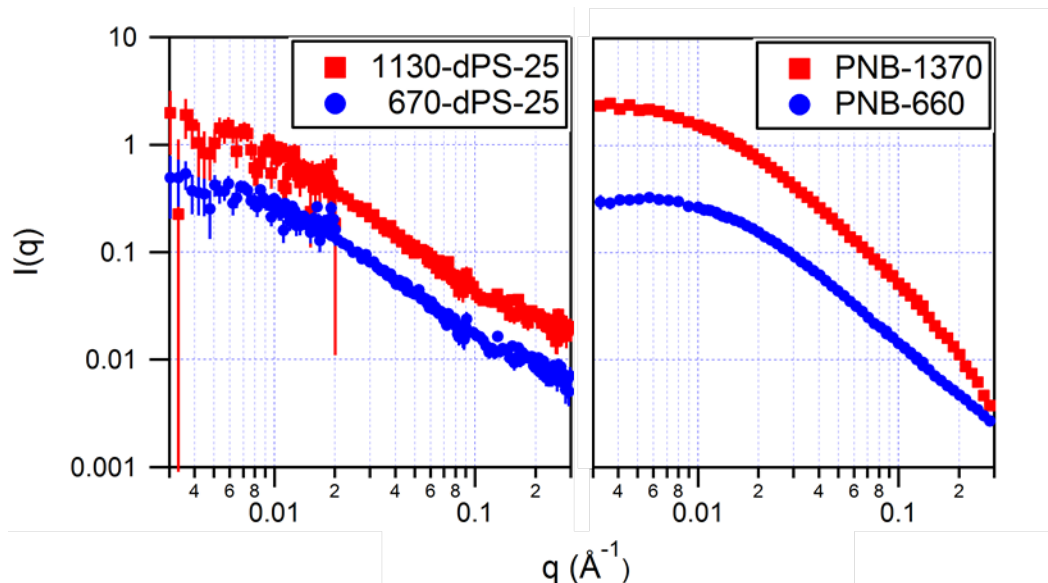


Figure 3.8: Radially averaged SANS patterns for PNB-g-dPS bottlebrushes (left, taken at NIST) and linear polynorbornene (right, taken at ORNL). All samples are in deuterated THF which is an almost exact contrast match for the deuterated polystyrene side chains, leaving only the scattering from the backbone for the brushes and providing good contrast for the linear PNB. The scattering curves for both the 1130-dPS-25 and PNB-1370 were offset for clarity (done by multiplying the intensity by 4.0).

Qualitatively the scattering curves $I(q)$ for the bottlebrush backbones are remarkably similar to those of linear polynorbornene. All of the curves in Figure 3.8 have power law scattering $I(q) \sim q^{-m}$ in the mid q region ($0.02\text{\AA}^{-1} < q < 0.1\text{\AA}^{-1}$) with a q independent plateau at lower q . This is the behavior expected of a linear polymer coil in dilute solution and is typically fitted using a generalization of the Debye scattering function[54] allowing for values of the power law other than the $m=2$ expected for a gaussian polymer. The resulting expression characterizes the scattering from polymers with scaling $\nu = 1/m$ [76]:

$$I(q) = \frac{1}{\nu U^{1/2\nu}} \gamma\left(\frac{1}{2\nu}, U\right) - \frac{1}{\nu U^{1/\nu}} \gamma\left(\frac{1}{\nu}, U\right) \quad (3.6)$$

Here $\gamma(x,U)$ is the incomplete gamma function and U is given by

$$U = \frac{q^2 R_g^2 (2\nu+1)(2\nu+2)}{6} \quad (3.7)$$

The expression is valid over the range $1/3 < \nu < 1$ but is most reliable in the excluded volume polymer region with $\nu \sim 0.6$. This model was fit to the data by setting the background to zero and then determining the rest of the parameters by nonlinear least squares fitting. The resulting R_g and ν values are presented in Table 3.7.

Table 3.7: Radii and scaling exponents for the backbones of bottlebrushes with deuterium labeled side-chains and linear polynorbornene obtained by fitting polymer excluded volume $I(q)$ to Figure 3.8.

Bottlebrush			Linear		
Polymer	R_g (nm)	Scaling	Polymer	R_g (nm)	Scaling
670-dPS-25	14.4	0.66	PNB-660	8.9	0.60
1130-dPS-25	15.6	0.64	PNB-1370	12.1	0.60

The polymer excluded volume expression perfectly characterizes the scattering of both the bottlebrush backbones and linear polynorbornene. The similar sizes and scaling exponents reinforce the similarity that was evident from inspection of the scattering curves. The scaling exponent ν for the backbones is slightly larger for the backbones than the linear polynorbornene, indicating that they are somewhat stretched. The R_g values for the bottlebrush polymer backbones are much smaller than those determined for the bottlebrushes by MALLS. This is consistent with the bottlebrushes being above the overlap concentration and the measured radius corresponding to R_{c-c} rather than the backbone R_g .

In order to determine the side-chain dimensions perpendicular to the backbone contour, SANS scattering patterns were taken for the same bottlebrushes (dPS-25) in a

partially deuterated THF solvent (described in section 3.2.4), providing equal contrast for the side-chains and the backbone. The resulting radially averaged and solvent subtracted scattering patterns are shown in Figure 3.9.

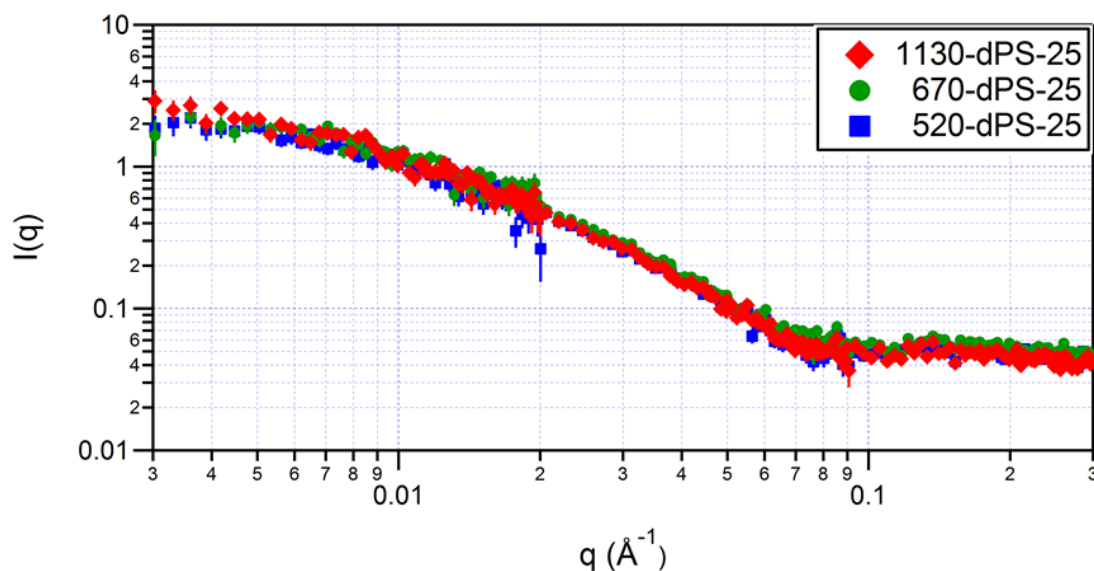


Figure 3.9: Radially averaged SANS patterns for PNB-g-PS bottlebrushes in a mixed THF solvent (54.8% deuterated) providing equal contrast for the backbone and the side-chains.

The scattering patterns are similar to those of ordinary unlabeled PS bottlebrushes in deuterated THF. The noise level is much greater due to the significant incoherent scattering caused by the greater hydrogen content of the solvent, drowning out much of the monomer level scattering at high q and obscuring the differences between the different N_b at low q . The cross-sectional size was determined to be $R_{CS} = 4.8\text{nm}$ using a Beaucage fitting function.

SANS experiments on 1wt% solutions of 820-dPS-65 were attempted, but the very low concentration of backbone (0.04wt%) resulted in unacceptably poor signal to noise ratios. It was not possible to acquire a usable pattern even after 3 hours of acquisition time. Raising the bottlebrush concentration to 5wt% allowed a pattern to be

acquired although the low- q region ($q < 0.01 \text{ \AA}^{-1}$) was still too noisy to use. A peak was observed in the scattering for a 5wt% solution that was not present at 1wt% and so the 1wt% data was subtracted from the 5wt% in order to isolate this feature, shown in Figure 3.10.

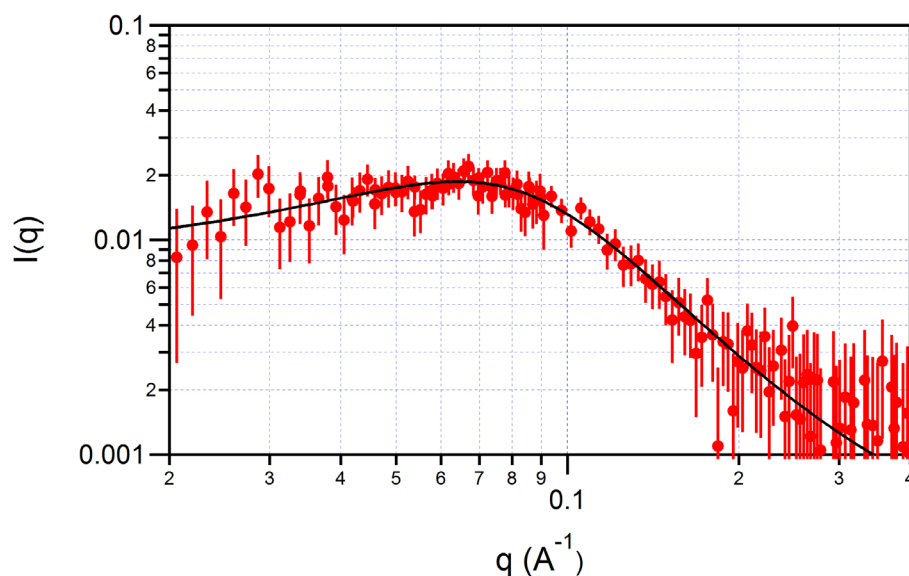


Figure 3.10: Radially averaged SANS pattern (taken at NIST) for 820-dPS-65 in deuterated THF (contrast matched to the side chains) isolating the scattering due to the backbone. This sample is at 5wt% concentration with a 1wt% sample used as the background (subtracted from the data). The solid black line is a Lorentzian fit to the peak which is centered on $q = 0.064 \text{ \AA}^{-1}$ corresponding to a length scale of 9.8nm.

At 5wt% the scattering for 820-dPS-25 shows a peak in the mid q range ($0.02 \text{ \AA}^{-1} < q < 0.2 \text{ \AA}^{-1}$). Fitting a Lorentzian to this peak allowed the center position to be determined as $q_{\text{peak}} = 0.064 \text{ \AA}^{-1}$, corresponding to a length scale of 9.8nm, which is of the same order of magnitude but somewhat larger than the side-chain size R_{CS} of PS-65 bottlebrushes (7.1nm).

Discussion

Small Angle Neutron Scattering patterns for the backbones of bottlebrush polymers are remarkably similar to those of linear polynorbornenes of $N \sim N_b$. The

intensity trends and the turnover from power law to q independent scattering is located at a similar position in q . The scaling exponent ν is lower for 1130-dPS-25 than for 670-dPS-25 and this drop of ν with N_b is consistent with a contour length $L > l_k$, but not yet at its asymptotic limit $L \gg l_k$. The l_k calculated from light scattering data for a linear polynorbornene is 3.4nm while that for dPS-25 based bottlebrushes is 37nm, meaning that the asymptotic limit of scaling is reached for a bottlebrush with N_b ten times greater than expected for PNB.

Based on this similarity between the linear polynorbornene and the bottlebrush backbone, we conclude that the backbone conformation is not significantly perturbed, although the Kuhn length l_k is presumed to be larger than that of PNB. The very low number of data points precludes the determination of l_k for the backbone without further scattering experiments on bottlebrushes with differing N_b . The R_g of the backbones may not be reliable due to the overlap issue discussed in section 3.3.2, which would explain the very small difference in R_g between 1130-dPS-25 and 670-dPS-25. Reducing the sample concentration and using samples with shorter backbones should resolve this issue.

Through the use of selective labeling we have been able to isolate the scattering from the backbone of a bottlebrush polymer. However, this proved to be possible only for relatively short side-chain lengths ($N_s < 65$) and required more than 2 hours of acquisition time per sample. Further study will require careful planning and may benefit from the use of sample cells with much longer path length (2mm path length cells were used in experiments at NIST).

Although it was not possible to obtain $I(q)$ over the entire range for 820-dPS-65, a very interesting feature was seen in the 5wt% scattering pattern, a peak corresponding to

a feature with a 9.8nm length scale. Since the side-chains are contrast matched to the solvent, this must be due to a backbone-backbone correlation length. Polymer mass fractals do not give rise to scattering peaks and this length scale is not explained by the overlap scaling shown in Figure 3.7. Thus we hypothesize that this peak is direct evidence of a lyotropic liquid crystalline phase with the 9.8nm corresponding to the characteristic intermolecular spacing. Lyotropic phases have been observed for bottlebrush polymers in solution [72-74], but to the best of our knowledge this is the first molecular level characterization of such a phase.

3.3.4. Bottlebrushes with Poly(Acrylic Acid) Side Chains

Results

Dynamic Light Scattering was used to determine hydrodynamic radii for bottlebrush polymers with polyelectrolyte side chains. The bottlebrushes used were obtained by the deprotection of previously characterized materials prepared from the PtBA-95 macromonomer. The PAA-95 bottlebrushes of all backbone lengths ($N_b = 140, 220, 340$ and 730) were tested as dilute ($<0.1\text{wt}\%$) solutions in aqueous buffers, with $\text{pH}=5$ and $\text{pH}=9$ corresponding to the extreme ends of the linear titration region for poly(acrylic acid) in which the degree of deprotonation of the acid groups is proportional to the pH . These buffers were prepared with no additional salts to an overall concentration of 0.1M and for comparison the R_h of 730-PAA-95 was determined in buffers with 1M salt concentration (achieved by adding NaCl) at both $\text{pH} 5$ and 9 . The resulting R_h values are summarized along with those of the parent PtBA-95 brushes in Table 3.8.

Table 3.8: Hydrodynamic radii obtained from DLS for PAA-95 based bottlebrushes in a series of buffer solutions with varying pH and salt concentration with the PtBA-95 based pre-polymer data for comparison.

Polymer	[Salt] (mol/L)	R_h (nm)		
		pH5	pH9	PtBA*
140-PAA-95	0.1	12.8	27.4	-
220-PAA-95	0.1	11.8	33.2	24.4
340-PAA-95	0.1	15.0	36.0	30.9
730-PAA-95	0.1	29.0	41.2	39.5
730-PAA-95	1	27.9	32.3	39.5

The R_h in pH 5 buffer is significantly smaller for all bottlebrushes than the R_h in pH 9 buffer with the results for the PtBA in good solvent falling in between the two. The difference between the R_h for the PAA brush at pH 9 and the corresponding PtBA brush in toluene becomes smaller with increasing N_b . Adding salt serves to shield the charges of the acid groups from each other and reduce the repulsion between them. For 730-PAA-95 at pH 5 the effect of the additional salt is minimal while at pH 9 the addition of NaCl serves to reduce the R_g by about 20%. Interestingly, it appears that at pH 9 with 1M salt, 730-PAA-95 has a smaller R_h than 730-PtBA-95 in toluene.

It has been previously established that the hydrodynamic radius is closely related to R_{CS} , the length scale of the side-chains perpendicular to the backbone contour. SANS experiments were conducted on 0.3 wt% solutions of 140-PAA-95 and 730-PAA-95 in deuterated buffers corresponding to those used for DLS. Radially averaged, solvent subtracted scattering patterns (obtained at ORNL) are shown in Figure 3.11.

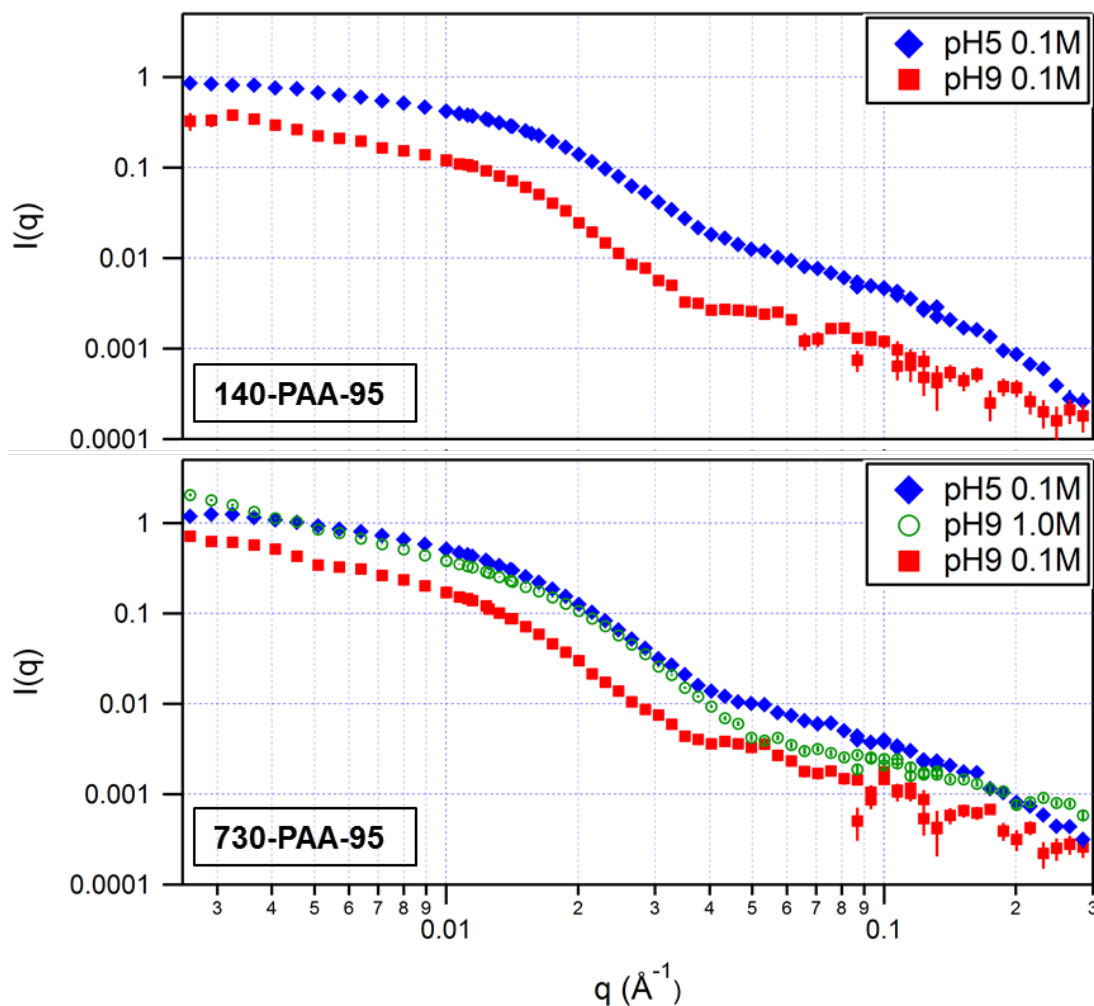


Figure 3.11: Radially averaged SANS patterns for two bottlebrushes with poly(acrylic acid) side-chains (140-PAA-95 top and 730-PAA-95 bottom) at 0.3wt% in aqueous buffers with varied pH and salt (NaCl) concentration. The red squares correspond to a basic condition (pH = 9) at the lowest accessible salt concentration (0.1M) with a large percentage of the acid groups deprotonated. The blue diamonds correspond to pH = 5 which is near the initial pKa of poly(acrylic acid). The open green circles correspond to pH = 9 with 1M salt concentration.

Scattering curves $I(q)$ for 140-PAA-95 and 730-PAA-95 show qualitatively similar features to those of the equivalent PtBA-95 based brushes. There is a mid q plateau corresponding to the side-chain dimensions, followed by steep rise due to the surface fractal scattering and finally either a plateau region (although for 730-PAA-95 at pH 9 and 1.0M salt, the scattering intensity continues rising at low q). For the samples in pH 9 buffer at 0.1M salt concentration the scattering appears to be more complex than

that observed for the other conditions, with multiple hump features indicating a hierarchical structure. For 730-PAA-95 these are seen at $q \sim 0.003\text{\AA}^{-1}$, $q \sim 0.006\text{\AA}^{-1}$, masked by the surface fractal scattering and then reappear at $q \sim 0.05\text{\AA}^{-1}$ and possibly $q \sim 0.1\text{\AA}^{-1}$, although higher q features are difficult to resolve due to the weak signal. The q locations of these features are multiples of each other, which suggests that they are the scattering harmonics of some structural length scale.

Determination of the overall length scale of the bottlebrushes was not possible due to the concentration being above the overlap concentration as determined in section 3.3.2. A two-level Beaucage scattering function was successfully fitted to the data using nonlinear least squares fitting of all parameters and the higher q ($q > 0.02\text{\AA}^{-1}$) length scales are reported in Table 3.9.

Table 3.9: Cross-sectional radius determined by fitting a Beaucage $I(q)$ to the SANS in Figure 3.11.

Sample	PAA in pH5 0.1M	PAA in pH9 0.1M	PAA in pH9 1M	ptBA in toluene
R_{CS} (nm)	11.1	14.1	9.0	9.9

The R_{CS} values shown in Table 3.9 are the averages of those obtained for 140-PAA-95 and 730-PAA-95 and are independent of the backbone length as was seen for PS and PtBA bottlebrushes in organic solvents. R_{CS} values are strongly dependent on the pH and the salt concentration. For 0.1M salt concentrations the R_{CS} increases by 27% going from pH5 to pH9, with the side-chains significantly more extended when in the charged state. Interestingly, adding salt leads to a significantly more compact conformation for the side-chains with R_{CS} 10% smaller than that for PtBA-95 in toluene.

Discussion

As is the case for free linear poly(acrylic acid), the side-chains grafted to a polynorbornene backbone undergo conformational transition with pH[77]. The side chain dimension R_{CS} is expanded by raising the pH and thereby increasing the charge of the side-chains and their repulsive interactions. Adding salt to shield the electrostatic interactions of the side-chains leads to a collapsed state in which the conformation is more compact than that for the equivalent PtBA side-chains in good solvent conditions. This is consistent with the weak scaling of PAA R_g with N_b for aqueous solutions at high salt concentrations, indicating that such solutions are similar to theta solvents[78]. In order to facilitate more quantitative conclusions, further study of a series of PAA side chain lengths will be needed.

The overall dimensions of a limited set of bottlebrushes with polyelectrolyte side-chains have been studied by Atomic Force Microscopy[79, 80] and by dynamic light scattering[81]. It was observed that their apparent size is significantly larger at pH 9 than at pH 5 as is the measured persistence length[81]. In the AFM studies it was observed that densely grafted bottlebrushes with PAA side-chains had fully extended backbone conformations at all pH values[79]. This is not consistent with our observed side chain dimensions for PAA-95 in pH 5 buffer, which are only marginally more extended than PtBA-95 in good solvent (10%). SANS patterns show a clear plateau at low q for both 140-PAA-95 and 730-PAA-95 at 0.1M salt concentrations and do not show a power law dependence of $I(q) \sim q^{-1}$ as would be expected for a fully extended cylindrical object[54]. The only sample showing power law scattering at low q is 730-PAA-95 at pH 9 with 1.0M salt concentration. We hypothesize that this is due to aggregation of the

bottlebrushes due to the hydrophobic interactions that become more dominant when electrostatic interactions are shielded[80].

We have established the feasibility of connecting the behavior of polyelectrolyte brushes to their ordinary hydrophobic analogues. We have also directly observed the change in the conformation of side-chain dimensions with pH and salt concentration. Future experiments on this family of materials, incorporating multi angle light scattering and SANS at lower concentrations, will enable the determination of persistence length and conformation in solution.

3.4 Conclusions

We determined the dilute solution size and conformation of a series of bottlebrush polymers synthesized by the polymerization of norbornenyl terminated macromonomers using a combination of Multi Angle Laser Light Scattering, Dynamic Light Scattering, and Small Angle Neutron Scattering. The synthetic approach described in Chapter 2 allowed us access to matched sets of materials independently varying the N_b , N_s , and the side-chain chemistry (consisting of PS or PtBA).

R_g as a function of N_b was measured in good solvent for bottlebrushes with two different lengths of polystyrene side chains ($N_s = 25$ and $N_s = 65$), using both ordinary and deuterated polystyrene. $R_g(N_b)$ was also obtained for bottlebrushes with two different lengths of PtBA side-chains ($N_s=40$ and $N_s=95$). Using the wormlike chain model we were able to obtain the Kuhn segment lengths (l_k) for the bottlebrushes, which successfully captures the $R_g(N_b)$ behavior of bottlebrush polymers. Compared to previous literature results on bottlebrushes synthesized by free radical polymerization (having approximately double the grafting density along the backbone contour) our brushes were

found to be less stiff, with lower l_k values for a given side-chain N_s . The magnitude of this effect cannot be determined by comparison to previous literature due to the significant disagreement among previously published results. The actual values of R_g determined for a given N_b were larger than those for more densely grafted bottlebrushes with equal N_s , consistent with the longer monomer of a polynorbornene backbone (0.5nm) than the vinyl type backbones of the bottlebrushes synthesized by radical polymerization (0.25nm). Data were made to match literature values by multiplying the N_b of our brushes by a shift factor for comparison to the literature values, expected to be 2.0 for brushes of equal stiffness. The actual values ranged from 1.7 to 1.0 when compared to various sets of data in the literature. Thus quantitative determination of the effect of grafting density requires further investigation.

Hydrodynamic radii for the bottlebrush polymers are much smaller than the radii of gyration. The R_h values are proportional to the side-chain dimensions and depend on the solvent quality being smaller in theta solvent than in good solvent. The ratios R_g/R_h are consistent with those reported in the literature and suggest extended conformations in solution. The trends in R_g/R_h with side-chain dimensions and backbone length are qualitatively explained by modeling the bottlebrush as a prolate spheroid although the predicated aspect ratios are higher than is reasonable. A more detailed hydrodynamic model, taking into account the segment density perpendicular to the backbone contour, should allow for a quantitative fit.

Small Angle Neutron Scattering revealed that 1wt% solutions of the bottlebrushes were in the semi-dilute regime. The overlap concentrations estimated on the basis of the R_g determined by MALLS were several times larger. The overlap concentration of

bottlebrush polymers is determined by a different length scale that is approximately 2 times larger than the R_g and is likely related to the end-to-end distance. Thus it was not possible to determine the overall size of the bottlebrushes by SANS. There was no evidence of a Holtzer plateau in the scattering function ($I(q) \sim q^{-1}$), indicating that the bottlebrushes do not behave like stiff rods and precluding the determination of a persistence length.

The Beaucage scattering function was used to obtain R_{CS} , the length scale of the side-chains perpendicular to the backbone contour. For polystyrene side-chains this was found to be in good agreement with the end-to-end distance expected for free PS of $N=N_s$. The scaling of R_{CS} with N_s was estimated to be similar to that of a polymer in good solvent, although more side-chain lengths are needed for a quantitative fit. All available evidence suggests that the side-chain behavior is not significantly perturbed from the behavior of free linear polymer chains. Most likely the stretching of the backbone (a slight loss of entropy) allows for the side chains to retain nearly unperturbed, coiled conformations (significant gain of entropy).

We have successfully conducted SANS experiments on bottlebrushes with solvent contrast matched to the side-chains isolating the scattering contribution of the backbone. SANS in this contrast matched condition was conducted for 1wt% solutions of 670-dPS-25 and 1130-dPS-25 as well as 5wt% solution of 820-dPS-65. The scattering for 670-dPS-25 and 1130-dPS-25 was compared to that of linear polynorbornenes with N similar to N_b (PNB-660 and PNB-1370) and was qualitatively identical, with scattering behavior described by the scattering function for a polymer with excluded volume. The fractal scaling derived for the backbones of the bottlebrushes was at $\nu=0.64$, only slightly larger

than the $\nu=0.6$ observed for the PNB. This suggests that the backbone is somewhat stiffened by the presence of the side-chains but retains similar behavior to its linear counterpart, showing no evidence of helical structure.

At 5wt% the backbone scattering of 820-dPS-65 shows a peak at 0.064\AA^{-1} corresponding to a length scale of 9.8nm. This indicates an ordered correlation between the backbones of adjacent bottlebrushes and is direct evidence of lyotropic ordering. Further study is necessary to identify the concentration and structural dependence of this lyotropic phase.

A preliminary investigation was conducted into the behavior of deprotected, poly(acrylic acid) bottlebrushes derived from the series based on the PtBA-95 macromonomer. Due to the lack of a MALLS system configured for aqueous solutions it was not possible to determine the R_g of the resulting polyelectrolyte brushes. DLS for solutions at pH5 and pH9 at 0.1M salt concentration and pH9 at 1.0M salt concentration showed that bottlebrush R_h has a strong dependence of the acidity and salt concentration. SANS showed the effect of solvent conditions on the side-chain dimensions, R_{CS} . At 0.1M salt concentration and pH9, both R_{CS} and R_h were significantly larger than those of the corresponding PtBA bottlebrush in toluene. Lowering the pH served to reduce the charge on the side-chains and led to a more compact conformation with lower R_{CS} and R_h . Adding salt shielded the electrostatic interactions among the side chains and led to more compact R_{CS} than that determined for the PtBA in toluene and may have resulted in aggregation (as determined from the low q slope of the SANS pattern). In order to determine the scaling relationships between N_s , N_b , and the radii of interest further

investigations on a series of polyelectrolyte bottlebrushes with varied side-chains lengths are recommended.

With the synthetic methods described in Chapter 2 we now have a robust and modular toolkit for making a variety of bottlebrush materials. The understanding of their structure-property relations gained from the physical studies described in this work will allow for more targeted design of materials for specific applications.

References

1. Sheiko, S.S., B.S. Sumerlin, and K. Matyjaszewski, *Cylindrical molecular brushes: Synthesis, characterization, and properties*. Progress in Polymer Science, 2008. **33**(7): p. 759-785.
2. Zhang, M. and A.H. Müller, *Cylindrical polymer brushes*. Journal of Polymer Science Part A: Polymer Chemistry, 2005. **43**(16): p. 3461-3481.
3. Hsu, H.-P., W. Paul, and K. Binder, *Structure of bottle-brush polymers in solution: A Monte Carlo test of models for the scattering function*. The Journal of chemical physics, 2008. **129**(20): p. 204904-204904-11.
4. Hsu, H.-P., et al., *Characteristic length scales and radial monomer density profiles of molecular bottle-brushes: Simulation and experiment*. Macromolecules, 2010. **43**(3): p. 1592-1601.
5. Terao, K., Y. Nakamura, and T. Norisuye, *Solution properties of polymacromonomers consisting of polystyrene. 2. Chain dimensions and stiffness in cyclohexane and toluene*. Macromolecules, 1999. **32**(3): p. 711-716.
6. Wintermantel, M., et al., *Molecular bottlebrushes*. Macromolecules, 1996. **29**(3): p. 978-983.
7. Rubinstein, M. and R.H. Colby, *Polymer physics*. 2003, Oxford ; New York: Oxford University Press. xi, 440 p.
8. Amitani, K., et al., *Small-angle X-ray scattering from polystyrene polymacromonomers in cyclohexane*. Polymer journal, 2005. **37**(4): p. 324-331.
9. Hokajo, T., et al., *Translational diffusion coefficient of polystyrene polymacromonomers. Dependence on side-chain length*. Polymer journal, 2005. **37**(7): p. 529-534.
10. Hokajo, T., et al., *Solution Properties of Polymacromonomers Consisting of Polystyrene V. Effect of Side Chain Length on Chain Stiffness*. Polymer journal, 2001. **33**(6): p. 481-485.
11. Terao, K., et al., *Solution properties of polymacromonomers consisting of polystyrene*. Polymer Bulletin, 2000. **44**(3): p. 309-316.
12. Terao, K., et al., *Solution properties of polymacromonomers consisting of polystyrene. 3. Viscosity behavior in cyclohexane and toluene*. Macromolecules, 1999. **32**(11): p. 3690-3694.
13. Fischer, K. and M. Schmidt, *Solvent-Induced Length Variation of Cylindrical Brushes*. Macromolecular rapid communications, 2001. **22**(10): p. 787-791.

14. Gerle, M., et al., *Main chain conformation and anomalous elution behavior of cylindrical brushes as revealed by GPC/MALLS, light scattering, and SFM*. *Macromolecules*, 1999. **32**(8): p. 2629-2637.
15. Wataoka, I., et al., *Structural characterization of polymacromonomer in solution by small-angle x-ray scattering*. *Polymer international*, 1997. **44**(3): p. 365-370.
16. Norisuye, T., *Semiflexible polymers in dilute solution*. *Progress in polymer science*, 1993. **18**(3): p. 543-584.
17. Nakamura, Y., *Small-angle X-ray scattering from polystyrene polymacromonomers with relatively short main chains*. *Applied Crystallography*, 2007.
18. Nakamura, Y., et al., *Synchrotron small-angle X-ray scattering from polystyrene polymacromonomers in toluene*. *Polymer Journal*, 2007. **39**(11): p. 1098-1104.
19. Fredrickson, G.H., *Surfactant-induced lyotropic behavior of flexible polymer solutions*. *Macromolecules*, 1993. **26**(11): p. 2825-2831.
20. Rathgeber, S., et al., *On the shape of bottle-brush macromolecules: Systematic variation of architectural parameters*. *The Journal of chemical physics*, 2005. **122**: p. 124904.
21. Ball, R., et al., *Polymers grafted to a convex surface*. *Macromolecules*, 1991. **24**(3): p. 693-703.
22. Li, H. and T.A. Witten, *Polymers grafted to convex surfaces: a variational approach*. *Macromolecules*, 1994. **27**(2): p. 449-457.
23. Denesyuk, N., *Conformational properties of bottle-brush polymers*. *Physical Review E*, 2003. **67**(5): p. 051803.
24. Hsu, H.P., W. Paul, and K. Binder, *Understanding the Multiple Length Scales Describing the Structure of Bottle-brush Polymers by Monte Carlo Simulation Methods*. *Macromolecular Theory and Simulations*, 2011. **20**(7): p. 510-525.
25. Theodorakis, P.E., et al., *Computer simulation of bottle-brush polymers with flexible backbone: Good solvent versus theta solvent conditions*. *The Journal of chemical physics*, 2011. **135**: p. 164903.
26. Hsu, H.-P., W. Paul, and K. Binder, *Standard definitions of persistence length do not describe the local "intrinsic" stiffness of real polymer chains*. *Macromolecules*, 2010. **43**(6): p. 3094-3102.
27. Anderson-Wile, A.M., et al., *Synthesis and Ring-Opening Metathesis Polymerization of Norbornene-Terminated Syndiotactic Polypropylene*. *Macromolecules*, 2012. **45**(19): p. 7863-7877.
28. Deshmukh, P., et al., *Hierarchically Self-Assembled Photonic Materials from Liquid Crystalline Random Brush Copolymers*. *Macromolecules*, 2013.
29. Johnson, J.A., et al., *Core-clickable PEG-branch-azide bivalent-bottle-brush polymers by ROMP: grafting-through and clicking-to*. *Journal of the American Chemical Society*, 2010. **133**(3): p. 559-566.
30. Johnson, J.A., et al., *Drug-loaded, bivalent-bottle-brush polymers by graft-through ROMP*. *Macromolecules*, 2010. **43**(24): p. 10326-10335.
31. Li, A., et al., *One-pot, facile synthesis of well-defined molecular brush copolymers by a tandem RAFT and ROMP, "Grafting-through" strategy*. *Journal of Polymer Science Part A: Polymer Chemistry*, 2012. **50**(9): p. 1681-1688.
32. Li, X., et al., *Surface Properties of Bottlebrush Polymer Thin Films*. *Macromolecules*, 2012. **45**(17): p. 7118-7127.
33. Li, Z., et al., *Facile syntheses of cylindrical molecular brushes by a sequential RAFT and ROMP "grafting-through" methodology*. *Journal of Polymer Science Part A: Polymer Chemistry*, 2009. **47**(20): p. 5557-5563.
34. Runge, M.B. and N.B. Bowden, *Synthesis of high molecular weight comb block copolymers and their assembly into ordered morphologies in the solid state*. *Journal of the American Chemical Society*, 2007. **129**(34): p. 10551-10560.

35. Xia, Y., J.A. Kornfield, and R.H. Grubbs, *Efficient synthesis of narrowly dispersed brush polymers via living ring-opening metathesis polymerization of macromonomers*. *Macromolecules*, 2009. **42**(11): p. 3761-3766.
36. Xia, Y., et al., *Efficient synthesis of narrowly dispersed brush copolymers and study of their assemblies: The importance of side chain arrangement*. *Journal of the American Chemical Society*, 2009. **131**(51): p. 18525-18532.
37. Hsu, H.-P., W. Paul, and K. Binder, *Conformational studies of bottle-brush polymers absorbed on a flat solid surface*. *The Journal of chemical physics*, 2010. **133**: p. 134902.
38. Park, I., et al., *Focusing bond tension in bottle-brush macromolecules during spreading*. *Journal of Materials Chemistry*, 2011. **21**(23): p. 8448-8453.
39. Park, I., et al., *Molecular tensile testing machines: breaking a specific covalent bond by adsorption-induced tension in brushlike macromolecules*. *Macromolecules*, 2009. **42**(6): p. 1805-1807.
40. Hu, M., et al., *Linear rheological response of a series of densely branched brush polymers*. *Macromolecules*, 2011. **44**(17): p. 6935-6943.
41. Xia, Y., et al., *EPR Study of Spin Labeled Brush Polymers in Organic Solvents*. *Journal of the American Chemical Society*, 2011. **133**(49): p. 19953-19959.
42. Duplessix, R. and V. Heroguez, *On the conformation and the structure of polymacromonomers*. *The European Physical Journal E*, 2004. **15**(1): p. 27-39.
43. Cheng, G., et al., *Conformation of oligo (ethylene glycol) grafted poly (norbornene) in solutions: A small angle neutron scattering study*. *European Polymer Journal*, 2008. **44**(9): p. 2859-2864.
44. Pesek, S.L., et al., *Small-Angle Neutron Scattering Analysis of Bottlebrush Polymers Prepared via Grafting-Through Polymerization*. *Macromolecules*, 2013.
45. Britton, H.T.S. and R.A. Robinson, *CXCVIII.—Universal buffer solutions and the dissociation constant of veronal*. *Journal of the Chemical Society (Resumed)*, 1931: p. 1456-1462.
46. Wyatt, P.J., *Light scattering and the absolute characterization of macromolecules*. *Analytica chimica acta*, 1993. **272**(1): p. 1-40.
47. Berry, G., *Thermodynamic and Conformational Properties of Polystyrene. I. Light-Scattering Studies on Dilute Solutions of Linear Polystyrenes*. *The Journal of Chemical Physics*, 1966. **44**: p. 4550.
48. Andersson, M., B. Wittgren, and K.-G. Wahlund, *Accuracy in Multiangle Light Scattering Measurements for Molar Mass and Radius Estimations. Model Calculations and Experiments*. *Analytical Chemistry*, 2003. **75**(16): p. 4279-4291.
49. Frisken, B.J., *Revisiting the method of cumulants for the analysis of dynamic light-scattering data*. *Applied Optics*, 2001. **40**(24): p. 4087-4091.
50. Koppel, D.E., *Analysis of Macromolecular Polydispersity in Intensity Correlation Spectroscopy: The Method of Cumulants*. *The Journal of Chemical Physics*, 1972. **57**(11): p. 4814-4820.
51. Glinka, C., et al., *The 30 m small-angle neutron scattering instruments at the National Institute of Standards and Technology*. *Journal of applied crystallography*, 1998. **31**(3): p. 430-445.
52. Choi, S.-M., et al., *Focusing cold neutrons with multiple biconcave lenses for small-angle neutron scattering*. *Journal of applied crystallography*, 2000. **33**(3): p. 793-796.
53. Kline, S.R., *Reduction and analysis of SANS and USANS data using IGOR Pro*. *Journal of applied crystallography*, 2006. **39**(6): p. 895-900.
54. Higgins, J.S. and H. Benoît, *Polymers and neutron scattering*. 1994: Clarendon Press Oxford.

55. Wignall, G.D., et al., *The 40 m general purpose small-angle neutron scattering instrument at Oak Ridge National Laboratory*. Journal of Applied Crystallography, 2012. **45**(5): p. 990-998.
56. Berry, K.D., et al., *Characterization of the neutron detector upgrade to the GP-SANS and Bio-SANS instruments at HFIR*. Nuclear Instruments and Methods in Physics Research Section A: Accelerators, Spectrometers, Detectors and Associated Equipment, 2012. **693**(0): p. 179-185.
57. Benoit, H. and P. Doty, *Light scattering from non-Gaussian chains*. The Journal of Physical Chemistry, 1953. **57**(9): p. 958-963.
58. Zhang, B., et al., *Conformation of cylindrical brushes in solution: effect of side chain length*. Macromolecules, 2006. **39**(24): p. 8440-8450.
59. Hatanaka, Y. and Y. Nakamura, *Dilute solution properties of polyacromonomer consisting of polybutadiene backbone and polystyrene side chains*. Polymer, 2013. **54**(5): p. 1538-1542.
60. Sugiyama, M., Y. Nakamura, and T. Norisuye, *Dilute-solution properties of polystyrene polyacromonomer having side chains of over 100 monomeric units*. Polymer journal, 2007. **40**(2): p. 109-115.
61. Tomoaki, Y. and N. Yo, *First Cumulant of Polyacromonomers Consisting of Polystyrene*. Macromolecules, 2009. **42**(13): p. 4918-4920.
62. Terao, K., et al., *Radius of Gyration of Polystyrene Combs and Centipedes in a θ Solvent*. Macromolecules, 2005. **38**(4): p. 1447-1450.
63. Yamakawa, H. and M. Fujii, *Translational friction coefficient of wormlike chains*. Macromolecules, 1973. **6**(3): p. 407-415.
64. Norisuye, T., M. Motowoka, and H. Fujita, *Wormlike chains near the rod limit: translational friction coefficient*. Macromolecules, 1979. **12**(2): p. 320-323.
65. Perrin, F., *Mouvement Brownien d'un ellipsoïde (II). Rotation libre et dépolarisation des fluorescences. Translation et diffusion de molécules ellipsoïdales*. J. phys. radium, 1936. **7**(1): p. 1-11.
66. Tirado, M.M. and J.G. de La Torre, *Translational friction coefficients of rigid, symmetric top macromolecules. Application to circular cylinders*. The Journal of Chemical Physics, 1979. **71**: p. 2581.
67. Tirado, M.M., C.L. Martinez, and J.G. de la Torre, *Comparison of theories for the translational and rotational diffusion coefficients of rod-like macromolecules. Application to short DNA fragments*. The Journal of chemical physics, 1984. **81**: p. 2047.
68. Hammouda, B., *A new Guinier-Porod model*. Journal of Applied Crystallography, 2010. **43**(4): p. 716-719.
69. Rathgeber, S., et al., *Bottle-brush macromolecules in solution: Comparison between results obtained from scattering experiments and computer simulations*. Polymer, 2006. **47**(20): p. 7318-7327.
70. Beaucage, G., *Approximations leading to a unified exponential/power-law approach to small-angle scattering*. Journal of Applied Crystallography, 1995. **28**(6): p. 717-728.
71. Beaucage, G., *Small-angle scattering from polymeric mass fractals of arbitrary mass-fractal dimension*. Journal of Applied Crystallography, 1996. **29**(2): p. 134-146.
72. Nakamura, Y., et al., *Lyotropic liquid crystal formation of polystyrene polyacromonomers in dichloromethane*. Polymer, 2008. **49**(22): p. 4877-4881.
73. Tsukahara, Y., et al., *Mesomorphic phase formation of poly (macromonomer) s of polystyrene macromonomers*. Polymers for Advanced Technologies, 2000. **11**(5): p. 210-218.
74. Wintermantel, M., et al., *Lyotropic phases formed by "molecular bottlebrushes"*. Angewandte Chemie International Edition in English, 1995. **34**(13-14): p. 1472-1474.

75. Fetters, L., et al., *Molecular weight dependence of hydrodynamic and thermodynamic properties for well-defined linear polymers in solution*. Journal of physical and chemical reference data, 1994. **23**(4): p. 619-640.
76. Hammouda, B., *SANS from homogeneous polymer mixtures: a unified overview*, in *Polymer Characteristics*. 1993, Springer. p. 87-133.
77. Laguecir, A., et al., *Size and pH effect on electrical and conformational behavior of poly (acrylic acid): Simulation and experiment*. European polymer journal, 2006. **42**(5): p. 1135-1144.
78. Reith, D., et al., *How does the chain extension of poly (acrylic acid) scale in aqueous solution? A combined study with light scattering and computer simulation*. The Journal of chemical physics, 2002. **116**: p. 9100.
79. Lee, H.-i., et al., *pH-induced conformational changes of loosely grafted molecular brushes containing poly (acrylic acid) side chains*. Polymer, 2008. **49**(25): p. 5490-5496.
80. Xu, Y., et al., *Manipulating cylindrical polyelectrolyte brushes on the nanoscale by counterions: collapse transition to helical structures*. Soft Matter, 2009. **5**(2): p. 379-384.
81. Kanemaru, E., et al., *Dimensions and viscosity behavior of polyelectrolyte brushes in aqueous sodium chloride. A polymacromonomer consisting of sodium poly (styrene sulfonate)*. Polymer, 2008. **49**(19): p. 4174-4179.

Chapter 4

Structure and Self-Assembly of Side-On and End-On Side-Group Liquid Crystalline Polymers in a Small Molecule Nematic Liquid Crystal Solvent

The polymers discussed in this chapter were originally synthesized by Rafael Verduzco (side-on) and Neal Scruggs (end-on) during their thesis work. Unstained TEM images were taken by Dr. Rohan Hule. Stained TEM was carried out by Zuleikha Kurji in the laboratory of Prof. Soo-Young Park at the Kyungpook National University in Daegu, Korea. The SANS experiments were proposed, designed, and executed in collaboration with Zuleikha Kurji, and Rohan Hule. Together we wrote the proposals for beamtime and travelled to the neutron sources, sharing the duties of performing the scattering experiments. We acknowledge the support of the National Institute of Standards and Technology, U.S. Department of Commerce, in providing the neutron research facilities used in this work.

4.1 Introduction

Liquid Crystals (LCs) are materials in which the component molecules have anisotropic shape and/or polarizability that drives the formation of mesophases with a degree of order intermediate between a crystalline solid (molecules occupy fixed positions in a lattice) and a liquid (having full orientational and positional symmetry). Specifically, anisotropic molecular structure in LCs leads to a coupling between their orientations that, even in the liquid state, produces long range orientational order along a preferred axis known as the director[1]. This yields a material that is a fluid with

anisotropic optical, rheological, and electro-magnetic properties and is of immense technological importance as the active switching element in Liquid Crystal Displays[2]. The simplest LC phase (the “nematic”) has only a preferred orientation and no positional order. The degree of orientational order is described by an order parameter $S = \frac{1}{2} \langle 3(\cos \theta)^2 - 1 \rangle$ where θ is the angle of an individual molecular axis relative to the director and the brackets indicate an averaging over all molecules[3]. The particular liquid crystal used in this study is 4,4'-cyanopentylbiphenyl (5CB), a long studied and well understood nematic liquid crystal. It is thermotropic, undergoing a first order phase transition at a well-defined nematic-to-isotropic transition temperature (T_{ni}) above which it is isotropic, like conventional liquids.

Side-Group Liquid Crystalline Polymers (SGLCPs) combine the flexibility of a random coil polymer with the anisotropic optical, rheological, and electro-magnetic properties of small molecule liquid crystals. This is achieved by covalently linking mesogenic side groups (typically resembling a small molecule liquid crystal in structure) to a flexible polymer backbone[4]. In contrast to isotropic coil polymers, the mesogenic side-groups make the polymer soluble in compatible small molecule LC solvents. When dissolved in a nematic small molecule LC, SGLCPs adopt anisotropic conformations: the orientation of the host couples to that of the polymer's mesogens and, through the spacers, to the backbone segments [5-7]. The shape of the polymer is driven by a compromise between maximizing the conformational entropy and minimizing the free energy of the mesogenic groups in the nematic field of the solvent. The polymer/solvent interaction depends strongly on three molecular features: the length and flexibility of the spacer between the mesogen and the backbone, the strength of coupling between the

mesogen and small molecule LC, and the geometry of mesogen attachment[4, 8]. Side groups attached with their long axis parallel to the backbone (side-on, Figure 4.1 right) cause the polymer backbone to orient preferentially along the director and adopt a prolate conformation[7, 9]. Conversely, mesogens attached with their long axis perpendicular to the backbone (end-on, Figure 4.1 left) tend to do the opposite, usually leading to a mildly oblate conformation with long axes oriented perpendicular to the director[5, 7]. Interestingly, the relative orientation of the backbone segments with respect to the pendant mesogenic groups can play a role determining the conformation of the polymer by penalizing perpendicular orientation and reinforcing parallel orientation, consistent with the much greater aspect ratios[10] observed[11] for side-on polymers.

The present study also examines diblock copolymers that link a coil-type polymer to an SGLCP. Diblock copolymers microphase separate in the melt, leading to a range of accessible morphologies determined by the chemical structure and relative length of the blocks[12]. Binary interaction between the blocks (A and B) is described by a Flory-Huggins interaction parameter χ_{AB} that characterizes the free-energy cost per unit of contact between the two blocks[13]. Placing the diblock copolymer in solution adds two more interaction parameters χ_{AS} and χ_{BS} for the solvent S and the A and B blocks, respectively. Their relative values or “selectivity” determine the partitioning of solvent between microdomains rich in A and those rich in B, which strongly influences the microstructure[14-18]. In a nonselective solvent ($\chi_{AS} = \chi_{BS}$) the two blocks are equally solvated and, to leading order, the self-assembled morphology will be determined by χ_{AB} as in the melt. In a strongly selective solvent ($\chi_{AS} \gg \chi_{BS}$) diblock copolymers organize into micelles, compact objects that sequester their A blocks into a highly concentrated

core and allow their B blocks to reach out into the solvent, forming a more solvated corona that surrounds the core.

Ordinary flexible coil polymers are not soluble in nematic LCs[19] due to the large entropic penalty imposed by the orientational order of the LC, but become soluble in compatible LCs above T_{ni} . For example, Polystyrene (PS) is soluble in 5CB above T_{ni} . In contrast, SGLCPs are able to change their orientational symmetry in concert with the small molecule LC and remain soluble both above and below the host's T_{ni} . Thus, a small molecule nematic is a solvent of switchable selectivity for a block copolymer composed of covalently linked SGLCP and coil blocks.

Previous work in the Kornfield lab has used polymer analogous synthesis to prepare matched pairs (having identical backbones) of end-on and side-on SGLCP homopolymers and matched pairs of end-on and side-on SGLCP-*b*-PS diblock copolymers. The method has been used to create sets of SGLCP-*b*-PS with varying polystyrene content (listed in Table 4.1).

Using mesogens that are readily soluble in 5CB for the side groups of the SGLCPs gives the present end-on and side-on SGLCP homopolymers solubility in 5CB, both ordinary and perdeuterated, at all concentrations. The phase behavior of ternary solutions of the present SGLCPs and PS in 5CB has been characterized both above and below T_{ni} [20]. SGLCP-*b*-PS block copolymers at semi-dilute concentrations in 5CB have been shown to undergo an abrupt change through the nematic-to-isotropic phase transition affecting both the morphological and rheological properties[21]. Rubbed alignment layers and a magnetic field (of moderate strength $B < 1$ Tesla) were used to orient the director, creating monodomain samples with a well-defined director orientation

(chosen to be along the horizontal axis and perpendicular to the beam in the present scattering experiments). Small Angle Neutron Scattering (SANS) on 5wt% solutions of side-on and end-on homopolymers in d5CB showed anisotropic patterns below the T_{ni} with the side-on SGLCP adopting strongly prolate conformation and the end-on SGLCP having a mildly oblate conformation[22]. The scattering patterns became isotropic above the nematic-to-isotropic phase transition temperature. The very weak molecular weight dependence of the scattering patterns led to the conclusion that these 5wt% solutions were in the semi-dilute regime.

In nematic 5CB, SGLCP-*b*-PS diblocks were seen to self-assemble into micelles with clear form and structure factors observed in the scattering patterns. However, prior SANS experiments on these diblocks were performed using unaligned, polydomain nematics, making it impossible to determine anything about the anisotropy or relative orientation of the micelles with respect to the director.

To better understand the solution behavior of these fascinating molecules, we have conducted a series of SANS and TEM experiments on dilute (1wt%) solutions of SGLCPs in 5CB. Scattering methods enable noninvasive study of the morphology of polymer solutions[23]. For measurements in nematic solvents, neutron scattering is particularly important, because light scattering is frustrated by director fluctuations (overwhelming the polymer scattering) and x-ray scattering suffers from a lack in contrast in electron density between the solvent and the polymer. SANS is ideal for the present system because it allows us to access the relevant length scales (1-100nm) and use isotopic labeling (i.e., replace some hydrogen with deuterium) to introduce contrast without significantly altering the species' chemistry or structure [24]. Specifically, the

Kornfield group synthesizes a deuterated analogue of 5CB [25] that gives strong contrast, yielding good SANS scattering patterns down to polymer concentrations as low as 0.5wt%. In combination with this inverse space technique, Transmission Electron Microscopy (TEM) is used as a complementary real space method, allowing the self-assembled morphologies to be thoroughly characterized.

Going beyond prior studies, the present experiments on corresponding pairs of end-on and side-on SGLCP homopolymers are performed in the dilute regime to expose the overall size and shape of the polymer coil. The resulting SANS patterns have revealed that the homopolymer SGLCPs are much larger than was previously thought (retrospectively confirming the need for low concentration). The aspect ratio of the coils accords with the anisotropic blob size seen in semidilute solution (although a change in aspect ratio with concentration might occur at high concentration [26]).

The present characterization of the coil-SGLCP diblock copolymer micelles is the first to provide SANS patterns for monodomain samples of dilute coil-SGLCP micelles (using alignment layers and magnetic field). The aligned solutions of SGLCP-*b*-PS diblocks showed a remarkably complicated scattering behavior (Figure 4.5) consistent with a hierarchical structure having mutually orthogonal anisotropic structures within the self-assembled object. Fitting of model independent functions and using the homologous series of scattering patterns to test plausibility of “toy models” led us to propose structures that have an anisotropic polystyrene core surrounded by an anisotropic corona of SGLCP with the overall object having an orientation perpendicular to that of the core.

4.2 Experimental

4.2.1 Materials

Square, ground and polished fused quartz slides were purchased from Technical Glass Products in Painesville, OH. Elvamide 8023R Nylon resin was provided free of charge by DuPont. NOA 65 UV curing adhesive was purchased directly from Norland Products. Peltier modules and the associated control electronics were purchased from TE Technology in Traverse City, Michigan. 4-pentylbiphenyl (>96%) was purchased from TCI America, deuterium oxide (99.8% D) was purchased from Cambridge Isotope Laboratories. Tetrahydrofuran (THF) (ACS grade, EMD), Hexanes (ACS Grade, BDH), Dichloromethane (DCM)(ACS Grade, EMD), and Ethyl Acetate (HPLC grade, J.T. Baker) were purchased from VWR. All other reagents were purchased from Sigma Aldrich and used as received. Materials such as steel shim stock, aluminum, plumbing fittings, springs, and hardware were purchased from McMaster Carr.

The SGLCP polymers studied in this chapter were synthesized using polymer analogous chemistry, functionalizing previously prepared 1,2-polybutadiene polymers by grafting on mesogenic side groups. Two homopolymer backbones of varying length were purchased from Polymer Source in Montreal, Canada. A series of four Polystyrene-b-1,2-Polybutadiene block copolymers were synthesized by David Uhrig of the Center for Nanophase Material Science at Oak Ridge National Laboratory. These were designed to have a uniform polybutadiene block length of approximately 1000 repeat units and polystyrene blocks varying in length from 400 to 1200 repeat units. Using vinyl functionalized mesogenic groups chosen to confer solubility in 5CB, matched pairs of polymers were prepared, using either a laterally attached butoxy-benzoate based mesogen

resulting in side-on SGLCP or a terminally attached cyanobiphenyl based mesogen resulting in end-on SGLCPs.

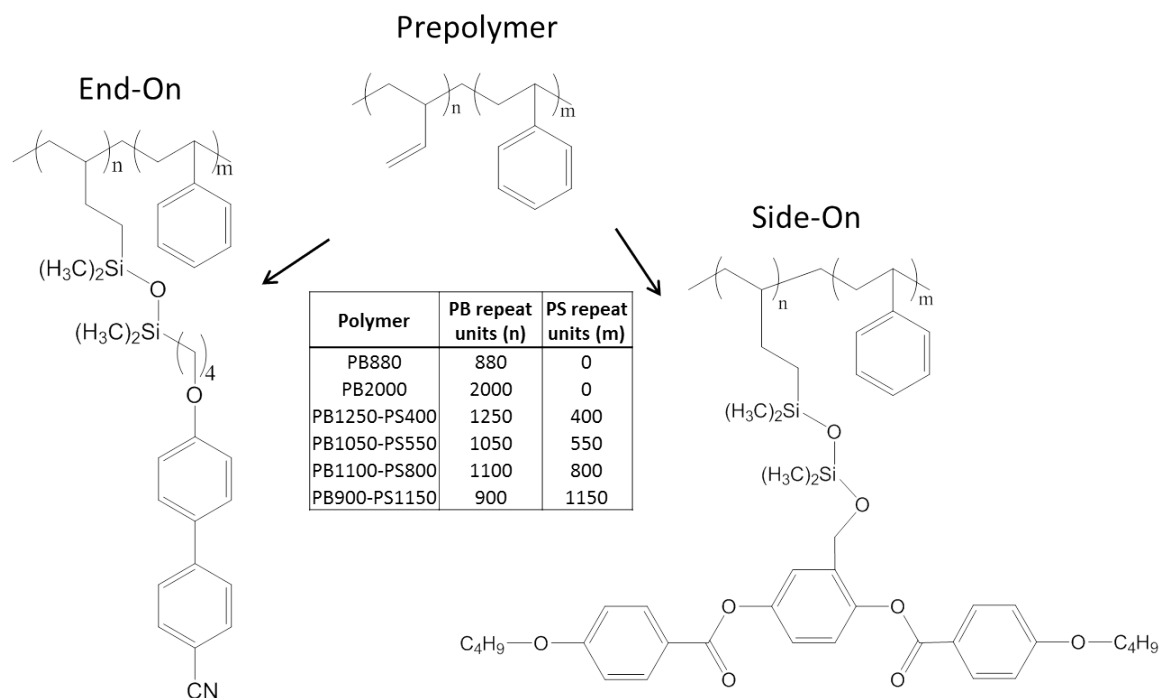


Figure 4.1: Chemical structures of the 1,2-Polybutadiene-*b*-Polystyrene prepolymers and the functionalized Side-Group Liquid Crystalline Polymers. The “End-On” polymer using a cyanobiphenyl based mesogen is shown on the left and the “Side-On” polymer using a butoxy-benzoate based mesogen is shown on the right. The degrees of polymerization of both blocks for all prepolymers used are shown in the central table.

The *SGLCP-b-PS* polymers were synthesized by Rafael Verduzco and Neal Scruggs during their graduate studies[22, 27]. They had also synthesized several batches of homopolymer SGLCPs and these were replenished by Zuleikha Kurji and myself as necessary. The polymers and their characteristics are listed in Table 4.1 below.

Table 4.1: Composition and molecular weight of SGLCPs studied in SANS experiments. Polymers above dashed line have cyanobiphenyl mesogens attached perpendicular to the backbone, while those below have butoxybenzoate mesogens attached parallel to the backbone. The names of the polymers follow the common scheme of LC(repeat units)-PS(repeat units).

Polymer Name	Molecular Weights (kg/mol)			fraction PS	PDI	SGLCP Block Composition (%)		
	PS block	SGLCP block	Combined			1,4-PB	1,2-PB	Mesogen
CB880	0	350	-	-	1.27	11	0	89
CB2000	0	762	-	-	1.11	4	6	90
CB1250-PS400	43	470	513	0.08	1.19	1	0	99
CB1050-PS550	59	390	449	0.13	1.11	3	15	82
CB1100-PS800	83	420	503	0.17	1.07	5	5	90
CB900-PS1150	121	320	441	0.27	1.05	1	22	77
BB880	0	497	-	-	1.15	11	7	82
BB2000	0	992	-	-	1.1	4	22	74
BB1250-PS400	43	592	635	0.07	1.37	1	21	78
BB1050-PS550	59	534	593	0.10	1.09	3	24	73
BB1100-PS800	83	620	703	0.12	1.13	5	9	86
BB900-PS1150	121	445	566	0.21	1.65	1	31	68

- a.) Determined by Gel Permeation Chromatography before and after mesogen attachment.
- b.) Determined by comparing area of ^1H NMR peaks due to backbone vinyl groups, double bonds, and the alkyl spacer of the mesogenic side-group.

4.2.2 Synthesis of Perdeuterated 4-pentyl-4'-cyanobiphenyl (d-5CB)

In order to provide contrast for the SANS studies, a perdeuterated analogue of 5CB was synthesized using improved methods based on previous work in the Kornfield laboratory[25, 28]. The d5CB has similar liquid crystalline properties to regular 5CB (but with a T_{ni} that is 7 to 10°C lower) but a dramatically different scattering length density due to the effect of the isotopic substitution[29].

4-pentylbiphenyl (50mL) was added to a PTFE lined 300mL PARR 4561 stirred pressure reactor with an internal thermocouple to monitor reaction temperature and heating with PID feedback control along with 800mg of carbon supported platinum catalyst and 150g of deuterium oxide. Aluminum foil (2cm²) was added to serve as an oxygen scavenger and extend the catalyst lifetime. The reactor vessel headspace was purged with N₂ gas at 60psig for 5 minutes and was then sealed and pressurized to 60psig

with N_2 . The reactor temperature was set to 205°C and the reaction was allowed to proceed with aggressive stirring for 3 days. At this point the reactor was allowed to cool and the D_2O was exchanged for fresh D_2O and an aliquot of the 4-pentylbiphenyl was taken. At this point another 100mg of catalyst was added to replace any dead catalyst and the reactor sealed, purged, repressurized, and set to react at 205°C for another 3 days. This process was continued for 3 or 4 cycles until a satisfactory level of deuteration ($>90\%$) was achieved.

Extent of deuteration was determined by preparing a sample of 50mg of the organic phase of the deuteration mixture and adding 5mg of pure anhydrous ethylene glycol, recording the exact mass of both and taking a ^1H NMR spectrum in CDCl_3 . The ethylene glycol peaks (3.46ppm and 3.65ppm) are used as an internal standard, with their area being compared to the 4-pentylbiphenyl proton peak area to determine the residual hydrogen content and therefore the degree of deuteration. This improved deuteration procedure produces about 50mL of d_{20} 4-pentylbiphenyl in 12 days as compared to the previous procedure producing about 10mL in about a month.

Subsequently the organic phase of the reaction mixture was separated from the aqueous phase, repeatedly filtered to remove the catalyst, and dried over MgSO_4 resulting in a clear yellowish liquid. For the next step deuterated 4-pentylbiphenyl (25g) was combined with FeBr_3 (0.94g) and anhydrous chloroform (50mL), resulting in a dark red solution. One equivalent of elemental bromine (5.25mL) was added dropwise at room temperature using an addition funnel and bubbling the resulting vapor through water to collect the corrosive HBr gas. The now greenish mixture was allowed to stir at room temperature, monitoring reaction progress by TLC, and reached completion after 3 hours,

turning purple. The solvent was almost completely evaporated by gas flow and then DI H₂O was added, resulting in a tan precipitate. The water was poured off and extracted with DCM three times. The DCM was then added back to the original flask, dissolving the precipitate, washed with H₂O, dried over MgSO₄, filtered, and the solvent evaporated under vacuum. This was recrystallized from hexanes, resulting in off-white solid 4-pentyl-4'-bromobiphenyl and was collected and vacuum dried overnight.

For the subsequent replacement of bromine by nitrile a palladium catalyst (Pd(TPP)₂) was generated *in situ* by combining Palladium(II)Acetate (325mg) and triphenyl phosphine on polymer support (1.75g) in 40mL of anhydrous toluene and stirring the mixture at 50°C for 30 minutes or until it turns red. At this point the deuterated 4-pentyl-4'-bromobiphenyl (1.8g), potassium cyanide (.4g), and tetramethylethylenediamine(160μL) were added to the reaction flask, which was purged with Ar, sealed, and stirred at 90°C for 3 days.

The product was extracted and purified by silica gel column using 1% ethyl acetate in hexanes as the eluent. Many fractions were collected and compared to the desired product by TLC with all matching fractions collected and combined. This was then further purified by repeated column chromatography, with fractions dried and tested for T_{ni} using polarized optical microscopy. The fractions with the highest T_{ni} were retained and combined.

4.2.3 Characterization Methods

Gel Permeation Chromatography was used to characterize the molecular weight and polydispersity of the SGLCPs. This was performed using a Waters GPC system with

THF at 35 °C eluting at a rate of 0.9 ml/minute serving as the mobile phase. The system was configured with four Agilent PLgel columns (pore sizes $10^3, 10^4, 10^5$, and 10^6 Å) connected in series to provide separation over a MW range of 500 to 10,000,000 g/mol. The time for complete elution through all four columns was 50 minutes. A Waters 410 differential refractometer was used to detect concentration as a function of time and the system was calibrated using monodisperse polystyrene standards. Samples were prepared by dissolving 5mg of polymer in 1mL of THF and filtering the sample through a $0.45\mu\text{m}$ PTFE membrane syringe filter immediately prior to injection.

Polarized Light Microscopy on a Zeiss Universal optical microscope equipped with crossed polarizers was used to determine the nematic-to-isotropic phase transition temperatures. Samples were prepared by placing a drop of material on a microscope slide and applying a coverslip to sandwich the material. This was placed on a Mettler FP82 temperature controlled stage and the temperature was ramped at 1°C per minute. The colorful, birefringent textures were observed in the nematic phase and their disappearance indicated the T_{ni} . Some samples had a biphasic window during which both nematic and isotropic regions were observed, and in these cases the T_{ni} was recorded as a range from the appearance of the first isotropic region to the disappearance of the last nematic one.

Proton (^1H) NMR spectra were taken using a Varian Inova 500 MHz spectrometer at room temperature. Samples were prepared as 5 to 20 mg/mL solutions in deuterated chloroform and scans were repeated 32 times with a relaxation delay of 2 seconds. NMR was used to determine the degree of functionalization for 1,2-PB by comparing the α -vinyl peak to that of the mesogen alkyl spacer[28].

Differential Scanning Calorimetric measurements were performed on a Perkin Elmer DSC-7 calorimeter with an enclosed sample area kept under dry N₂ gas. Samples were prepared by measuring out about 10mg of solution into an aluminum pan which was then hermetically sealed with an aluminum lid. The exact mass of the solution added was determined by weighing the empty and full pans on a precision (± 0.1 mg) balance. Temperature scans were performed at 10°C per minute, ramping from 20 to 100°C and back down, repeating until at least six consequent traces were indistinguishable by eye, at which point data was retained. The phase transition onset temperature and latent heat were calculated using Perkin-Elmer's Pyris® software (v3.04).

Unstained TEM was done using an FEI Technai-12 transmission electron microscope at an accelerating voltage of 120kV equipped with a Gatan CCD camera. Samples were prepared by dissolving polymer and 5CB in dichloromethane (DCM) and homogenizing on a shaker for at least 1 hour. Subsequently the volatile solvent was removed by drying at room temperature under vacuum for several days until no change in mass was observed. A small aliquot of solution was added to 300 mesh carbon coated copper grid and the excess blotted with Whatman filter paper, and the grids were allowed to equilibrate overnight before imaging. Images were quantitatively analyzed to extract morphological data using Image J software[30] from the National Institute of Health.

Stained TEM instrumentation and sample preparation is described in the thesis of Zuleikha Kurji.

4.2.4 Cell and Sample Preparation for SANS

Custom sample cells were made for the scattering experiments having alignment layers and a very small volume (69 μ L). One inch square fused and polished GE 124 quartz slides of 1mm thickness were cleaned by repeated rinsing with acetone and isopropanol, dried with N₂ gas, and were coated with a thin layer of DuPont Elvamide 8023R by spin coating at 3000rpm with a 0.5wt% solution of the nylon in methanol. This was aligned along one of the edges of the slide (marked with diamond scribe) by rubbing with an animal hair brush at least one hundred times in the direction parallel to the edge. Two such windows were used for each cell and were glued to a 1/32" thick aluminum shim with a 10mm circular hole in the middle and a slot for filling. The shim was 1.25" long in the direction of the filling slot, leaving some of the aluminum exposed for handling of the cell without touching the quartz surface. The gluing was done by applying a thin film of NOA65 liquid adhesive to both sides of the shim and then sandwiching this between the two windows, with the film on the inner side and the alignment direction perpendicular to the filling slot. This was clamped using binder clips on all four sides and was then cured using a Lesco Super Spot MkII UV curing source.

Samples were prepared by making stock solutions of polymer and the deuterated liquid crystals in THF using a precision balance and volumetric glassware. Precise amount of the solutions were then measured out into new 2mL glass vials using Hamilton Gastight syringes and mixed on a wrist action shaker for at least 30 minutes. These were then dried in a vacuum oven at room temperature for at least 1 day until the weight of the vial stopped changing.

4.2.5 Precision Temperature Controlled Sample Environment

In order to have fast and precise control over the temperature of our samples while scattering, I designed and built a custom sample environment. The previously available sample holders were based on recirculating fluid baths with a very large thermal mass and remote temperature measurement, resulting in large ($\pm 2^\circ\text{C}$) uncertainty in temperature settings. The phenomena of interest to us involve phase transitions and are extremely sensitive to temperature, making it imperative to have an uncertainty $\Delta T \leq 0.1^\circ\text{C}$. The sample holder is based on the TE Technologies CH-109-1.4-1.5 module that is 40mm by 40mm square with a 13mm diameter aperture at the center, and has a maximum $\Delta T = 70^\circ\text{C}$ and maximum power of 51 watts. Two such modules were glued using thermal transfer epoxy to aluminum heat sinks with 13mm apertures matching the openings in the Peltier modules. The heat sinks were hollow and had coolant circulated through them in order to maintain the reference side of the Peltier modules at a constant 25°C . One of the heat sinks was mounted to a base plate that had slots for mounting to an optical table, and the other was attached to it on sliding shafts with spring pressure used to hold the two Peltier modules in firm contact. On the inner face of the fixed Peltier, a small u-shaped aluminum shelf was glued below the opening in order to hold the sample cell in position and a precision $10\text{k}\Omega$ thermistor of 0.9mm diameter was glued next to this using thermal epoxy in order to measure the temperature as close to the sample as possible. The spring pressure served to establish as good of thermal contact between the Peltiers and the sample cell as is possible without the use of heat transfer compound.

Temperature was controlled using a bi-polar PID controller (TE Tech TC-36-25-RS232) in a home built enclosure incorporating a 24V power supply and a temperature

readout. The PID parameters were obtained using the classical tuning methods[31] and iteratively refined for response speed and minimal overshoot. The accuracy of the temperature readout was confirmed by comparing the reading on the thermistor to a calibrated thermocouple inserted into a sample cell. It was found that the temperature at the Peltier surface tracked the sample temperature with minimal offset and without observable time delay. The controller was connected directly to the SANS instruments and controlled through custom Labview code when running experiments. Testing showed good stability and speed of response in the range of -20°C to 70°C with precision of $\pm 0.05^{\circ}\text{C}$. In order to test the *in situ* phase behavior of liquid crystal samples I also built a holder for polarizing films that could be mounted on top of the sample environment to allow observation of the sample under crossed polarizers.

4.2.6 Small Angle Neutron Scattering

SANS experiments were performed at the NIST Center for Neutron Research at the National Institute of Standards and Technology in Gaithersburg, MD on the 30m NG-3 cold neutron instrument[32]. Samples were placed in previously described custom cells and the Peltier based sample environment was used for temperature control. The sample environment was placed between the poles of a water cooled electromagnet, providing a magnetic field of up to 0.9 Tesla. This breaks the symmetry of director orientation, resulting in a monodomain director field within nematic samples. Both the magnetic field and the rubbed alignment layers of the cell were oriented horizontally with the director orientation lying parallel to them and perpendicular to the neutron beam. Data was collected at several temperatures in both the nematic and isotropic phases.

Two-dimensional scattering patterns were taken at each of three sample-to-detector distances (1.3, 4.5, and either 11 or 9m) using monochromatic neutrons of $\lambda=6\text{\AA}$ wavelength resulting in an overall scattering vector range of $(0.004 < q (\text{\AA}^{-1}) < 0.3)$ where $q = (4\pi/\lambda)\sin(\theta/2)$. The raw data were corrected for background electronic noise and neutron radiation, detector pixel sensitivity, and empty cell scattering and the data was subsequently normalized by the incident neutron flux using NIST provided software[33] resulting in absolute, coherent scattering intensity.

The 2D scattering patterns were then sector averaged by combining all data having the same magnitude of q and lying within a sector of $\pm 10^\circ$ about the horizontal axis (parallel to the director) or the vertical axis (perpendicular to the director), keeping the left, right, top and bottom sectors separate. Data taken for a cell containing only the $d_{19}5CB$ was processed in the same manner, and this was subtracted sector by sector from the sample data in order to account for slight variations in scattering at different positions on the detector. Some flaring was observed around the bottom of the beamstop in some of the data and these were rejected. Finally the $I(q)$ curves for all three detector distances were combined, normalizing the intensity to the low- q data set (longest detector distance), resulting in final $I_{\text{par}}(q)$ and $I_{\text{perp}}(q)$ parallel and perpendicular to the director axis respectively.

4.3 Results

4.3.1 Homopolymer Conformation in Dilute Solution

Small angle neutron scattering patterns for mono-domain samples of both end-on (CB) and side-on (BB) homopolymers in d5CB at nematic temperatures (Figure 4.2) are anisotropic; the anisotropy disappears above the nematic-to-isotropic transition temperature (T_{ni}).

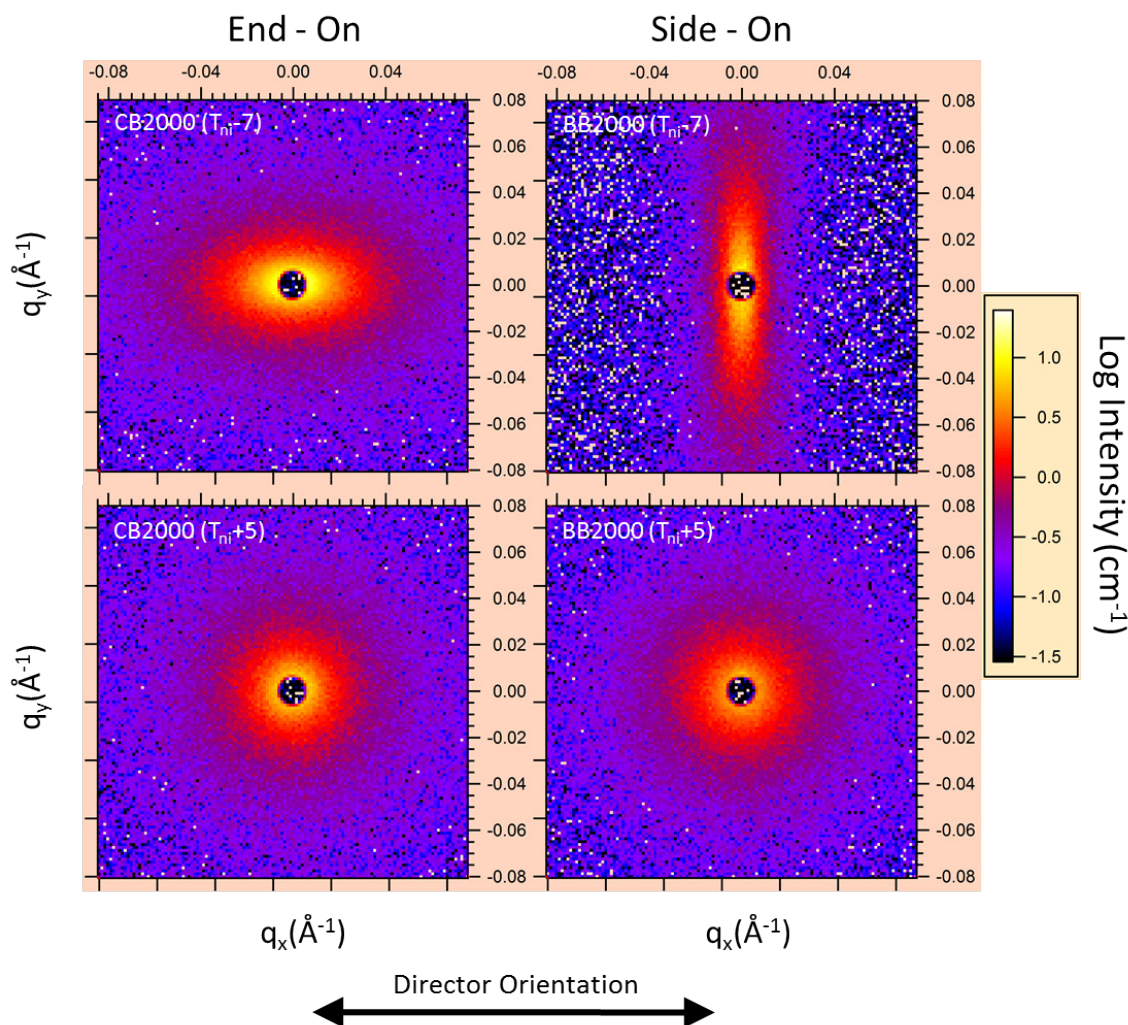


Figure 4.2: Two dimensional SANS patterns for End-On (left) and Side-On (right) homopolymers (structures shown in Figure 4.1) in d5CB both the nematic phase (top) and isotropic phase (bottom) using a sample to detector distance of 4m on beamline NG-3 (NIST). The top set of patterns is in the nematic phase 7°C below the nematic-isotropic phase transition and the bottom set of patterns is in the isotropic phase 5°C above the transition.

The nematic scattering patterns for the two mesogen attachment geometries are oriented orthogonally to each other, consistent with previously observed ellipsoidal conformations for SGLCPs in small molecule LCs[5, 7, 8]. Taking into account the rotational axis of symmetry about the nematic director, the end-on polymer coil is an oblate spheroid with its long axes perpendicular to the director and the side-on is a prolate spheroid with its long axis parallel to the director.

Sector averages parallel and perpendicular to the director for 1wt% solutions are compared to those for 5wt% solutions of the same polymers (Figure 4.3) by rescaling the intensity to account for the effects of concentration and path length. The q -dependence and relative magnitude of $I_{\text{par}}(q)$ and $I_{\text{perp}}(q)$ are indistinguishable at high q . In contrast, at low q ($<0.04\text{\AA}^{-1}$) the scattering in the direction of the polymer's short axis (I_{par} for CB and I_{perp} for BB) is significantly greater in the present 1wt% solutions than in the earlier 5wt% solutions. This change is consistent with the hypothesis that the 5wt% solutions are semidilute[22]. The scattering in the opposite direction was similar for the two concentrations, with a deviation visible only at the very lowest q values; this is consistent with the "blobs" in the semidilute solution having an anisotropic shape that is similar to that of the individual chains. The scattering patterns for 1.2wt% and 1.5wt% solutions are similar to the 1wt% data; therefore the 1wt% solutions are regarded as dilute. The scattering pattern of a 3wt% solution is intermediate between that of the 1.5% solution and that of the 5wt%, indicating that the overlap concentration between 1.5 and 3wt%.

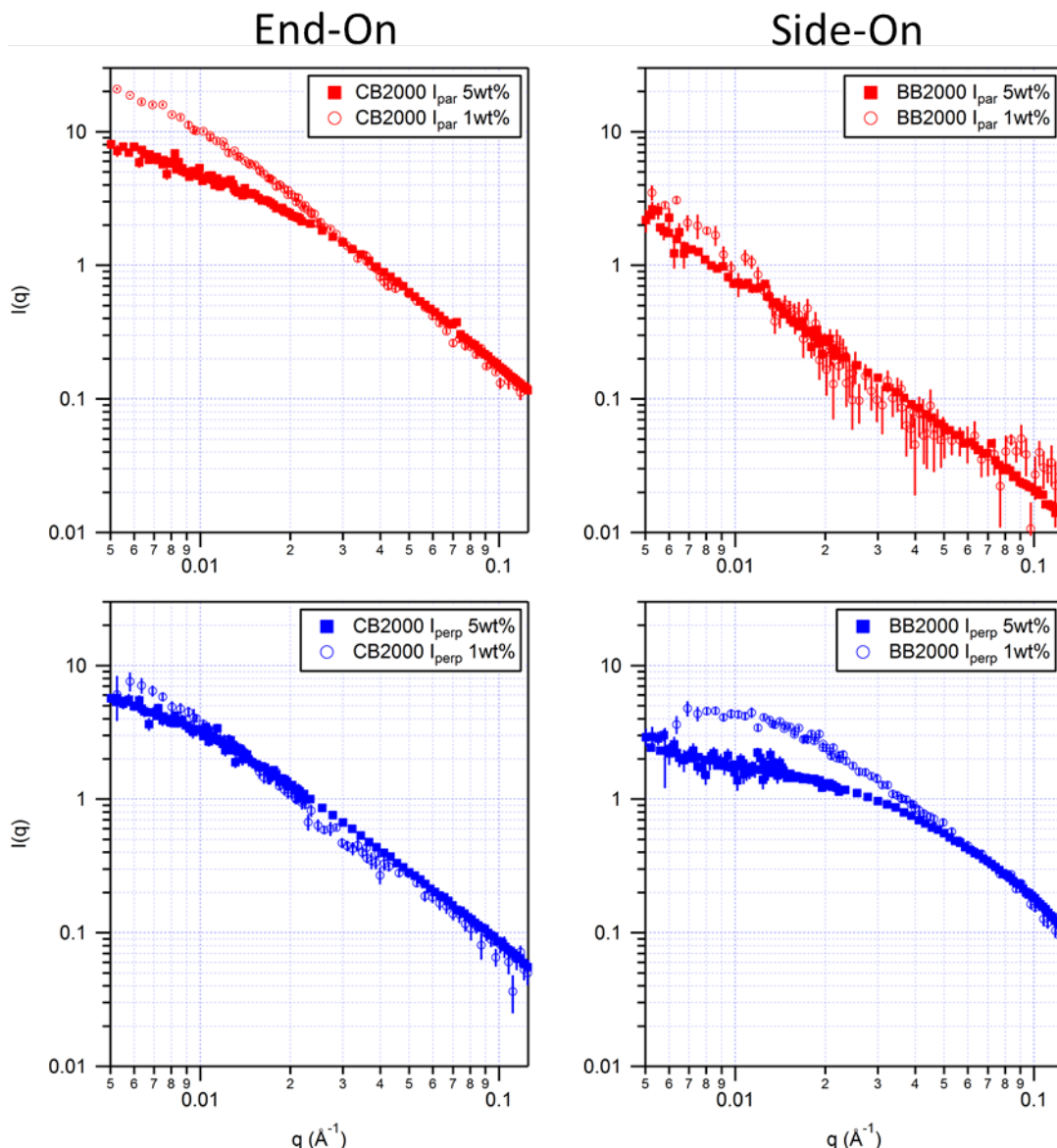


Figure 4.3: One dimensional sector averages along the director I_{par} (top) and perpendicular to it I_{perp} (bottom) from SANS patterns for solutions of End-On and Side-On polymers of 2000 DP at 1wt% and 5wt% in nematic d5CB at $T=T_{\text{ni}} - 7$. . The higher concentration data was obtained by Neal Scruggs and Rafael Verdusco[22] and is scaled to compensate for the higher concentration.

The conformational anisotropy is clearly visible in the sector averaged scattering patterns in the nematic phase at $T_{\text{ni}} - 7^{\circ}\text{C}$ (Figure 4.4): the side-on polymers scatter more strongly in the direction perpendicular to the nematic director and the end-on polymers have higher intensity scattering in the parallel direction. The side-on polymers are clearly

more anisotropic and their scattering has a greater difference in functional form between the parallel and perpendicular directions. Where data is available, the isotropic scattering ($T_{ni} + 5^{\circ}\text{C}$) falls between the two sector averages for the nematic phase and is closer in both form and magnitude to the sector corresponding to the short axis of the polymer (I_{par} for CB and I_{perp} for BB), consistent with the segment density distribution being more perturbed along the direction of greater stretching.

The aspect ratio of the coil was estimated by visually fitting an ellipse to an iso-intensity contour in the 2D scattering patterns (Table 4.2, 2D). A second estimate of $R_{\text{long}}/R_{\text{short}}$ (Table 4.2, right column) was found from 1D sector averages by comparing q_{par} and q_{perp} values for a given intensity in a region of q where the two curves are approximately parallel (i.e., using two points on an iso-intensity contour). The two methods generate similar aspect ratios ($\pm 30\%$) both for the mildly oblate end-on SGLCP and the strongly prolate side-on SGLCP. The aspect ratios appear to be independent of molecular weight to within the uncertainty inherent to the methodology and accord with the aspect ratios reported for semidilute solutions of these polymers[22].

Table 4.2: Aspect ratios estimated for homopolymers in the nematic phase: (center) by visually fitting an ellipse to iso-intensity contours in the 2D scattering patterns and (right) by comparing q -values corresponding to equal intensities for the sector averages parallel and perpendicular to the director.

Polymer	Aspect Ratio	
	2D	Sector Average
CB880	1.9	1.6
CB2000	1.4	1.5
BB880	3.3	4.5
BB2000	3.3	4.3

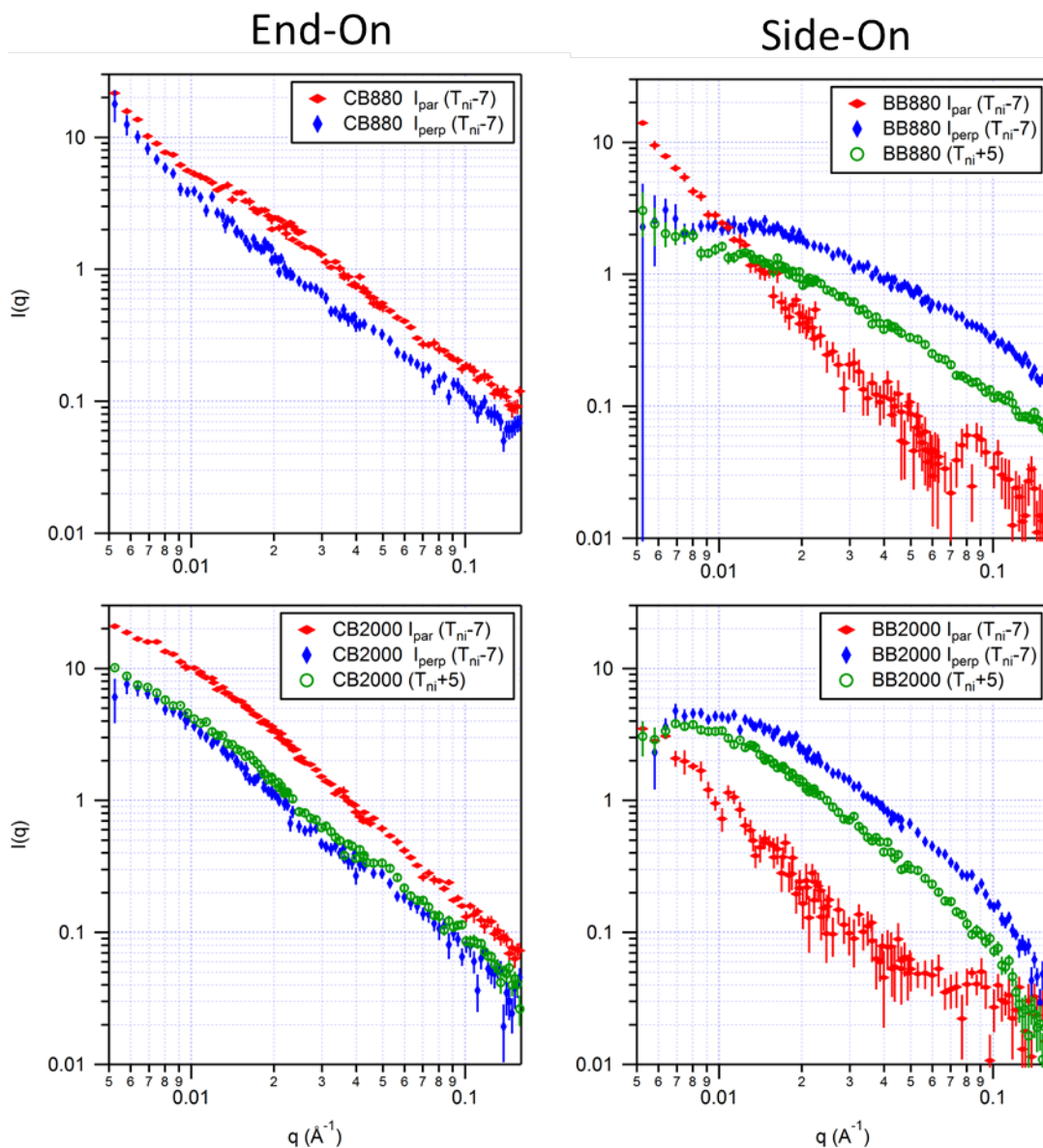


Figure 4.4: SANS intensity for parallel (red) and perpendicular (blue) sector averages for nematic solutions and circular average (green) for isotropic solutions at 1wt% in d5CB of both end-on (left) and side-on (right) SGLCPs having backbone DP=880 (top) and DP=2000 (bottom).

An upturn in intensity can be seen at low q in some of the scattering patterns (e.g. I_{par} of nematic CB880 and BB880 in Figure 4.4). This is not expected for polymer coils in the dilute regime, which should have scattering that is almost independent of q as q goes to zero. This sort of behavior has previously been observed in dilute solutions of PEO in

water[34, 35] and dilute solutions of SGLCP in isotropic solvent[36-38] and is generally attributed to interaction between the polymer coils. In the present systems, the feature was observed in less than half of the samples; when it was present, it would often be associated with the nematic phase (the feature would disappear upon heating to the isotropic phase). For most of the scattering data this effect was only seen at the lowest q -values, making it possible to fit a form factor (below) to the high- q data; however, when this feature was present, it precluded the use of a Guinier fit to estimate the overall size.

Polymer coils are fractal objects with the relationship between mass and radius for a polymer consisting of N segments and having radius R , described by $R \sim N^\nu$ where ν is the scaling exponent. The Debye function is frequently used to model the scattering from polymer coils[24] and assumes that $\nu=0.5$ (polymer in theta solvent or in the melt) resulting in $I(q) \sim q^{-m}$ where $m=1/\nu=2$. A similar scattering model function has been derived for a polymer with excluded volume (more expanded conformation) and scaling $\nu=1/m$ where m is the Porod exponent[39]. This is given by:

$$I(q) = \frac{1}{\nu U^{1/2\nu}} \gamma\left(\frac{1}{2\nu}, U\right) - \frac{1}{\nu U^{1/\nu}} \gamma\left(\frac{1}{\nu}, U\right) \quad (4.1)$$

Here $\gamma(x,U)$ is the incomplete gamma function and U is given by

$$U = \frac{q^2 R_g^2 (2\nu+1)(2\nu+2)}{6} \quad (4.2)$$

This model describes a flexible polymer chain with $1/3 < \nu < 1$, where the lower limit corresponds to a collapsed globule and the upper limit corresponds to a rigid rod. This functional form is most reliable for the excluded volume polymer region of $\nu \sim 0.6$. At intermediate values of q the scattering intensities for solutions of SGLCP in 5CB followed a power law scaling with $m < 2$ (i.e., $\nu > 0.5$). For end-on SGLCPs the slopes in

the power law portions of I_{par} and I_{perp} are seen to be similar; in the side-on SGLCPs I_{perp} sometimes has a shallower slope than I_{par} . Using the SANS analysis software in IGOR Pro developed by Steve Kline[33], equation 4.1 was fit to the sector averaged $I(q)$, setting the background to zero and neglecting the very noisy high q ($q > 0.15 \text{ \AA}^{-1}$) region corresponding to incoherent scattering with the other parameters allowed to float freely. Successful fits were obtained for all isotropic solutions and for the sector average that corresponds to the shorter axis of the ellipsoidal isointensity contours in the nematic phase, i.e., I_{par} for CB and I_{perp} for BB. (resulting R_g and ν values are in Table 4.3).

Table 4.3: Results obtained from fitting an excluded volume polymer scattering function to the scattering shown in Figure 4.4. Blank positions on the left for the nematic phase correspond to sectors for which this form factor was not a good fit. Data for CB880 in the isotropic phase was not available.

Polymer	Nematic Parallel		Nematic Perpendicular		Isotropic	
	R_g (nm)	scaling	R_g (nm)	scaling	R_g (nm)	scaling
CB880	15.8	0.59	-	0.63	-	-
CB2000	21.3	0.53	-	0.59	27.1	0.56
BB880	-	0.59	6.8	0.77	8.6	0.67
BB2000	-	0.53	9.6	0.56	13.2	0.56

It was not possible to obtain values for R_g for the long dimension of the ellipsoids in the nematic phase (I_{perp} for CB and I_{par} for BB) due to the lack of a plateau in the intensity at low q , with the power law scattering region extending out to the lowest available q . This indicates that the long axis of the ellipsoid is too large for the available q -range. In earlier studies, the apparent R_g was seen to be independent of the molecular weight[22] consistent with the hypothesis that the measured size and anisotropy were those of a “blob”[13] in the semidilute solution. Here, the R_g increases with molecular weight and the increase accords with the scaling exponents of $\nu \sim 0.6$ to within the experimental uncertainty. This is consistent with regarding the 1wt% solutions as dilute.

The minor radii of both end-on and side-on polymers in the nematic phase are seen to be slightly smaller than their isotropic radii, consistent with stretching of the polymer along the other axis. The scaling exponents obtained are consistent with behavior intermediate between a Gaussian chain ($\nu = 0.5$) and an excluded volume polymer ($\nu = 0.6$) with the exception of BB880 ($\nu=0.77$ perpendicular to the director). This anomalously high value may be related to the segment density profile in the direction of the very narrow dimension (6.8nm) of the coil, as this phenomenon is not observed for the longer BB2000.

4.3.2 SGLCP-*b*-PS Structure and Self-Assembly

2D scattering patterns of SGLCP-*b*-PS block copolymers in monodomain nematic d5CB have anisotropy at low q that is qualitatively similar to the corresponding homopolymer (oriented in the same direction) (Figure 4.5): the long axis of the overall object is oriented perpendicular to the nematic director for CB SGLCP-*b*-PS and parallel to it for BB SGLCP-*b*-PS. What is interesting and unexpected is the appearance of an oppositely oriented scattering feature at slightly larger q . Thus, it appears that on some intermediate length scales the self-assembled object has features that are opposite in orientation to the SGLCP coils and to the object as a whole (long axes perpendicular to the director for side-on polymers and parallel to the director for end-on polymers). With increasing polystyrene block length, the scattering patterns for polymers with approximately equal SGLCP block length show progressively stronger scattering in this orthogonally-oriented mid- q feature, while the feature near the beamstop shifts to smaller q , moving out of the observable range.

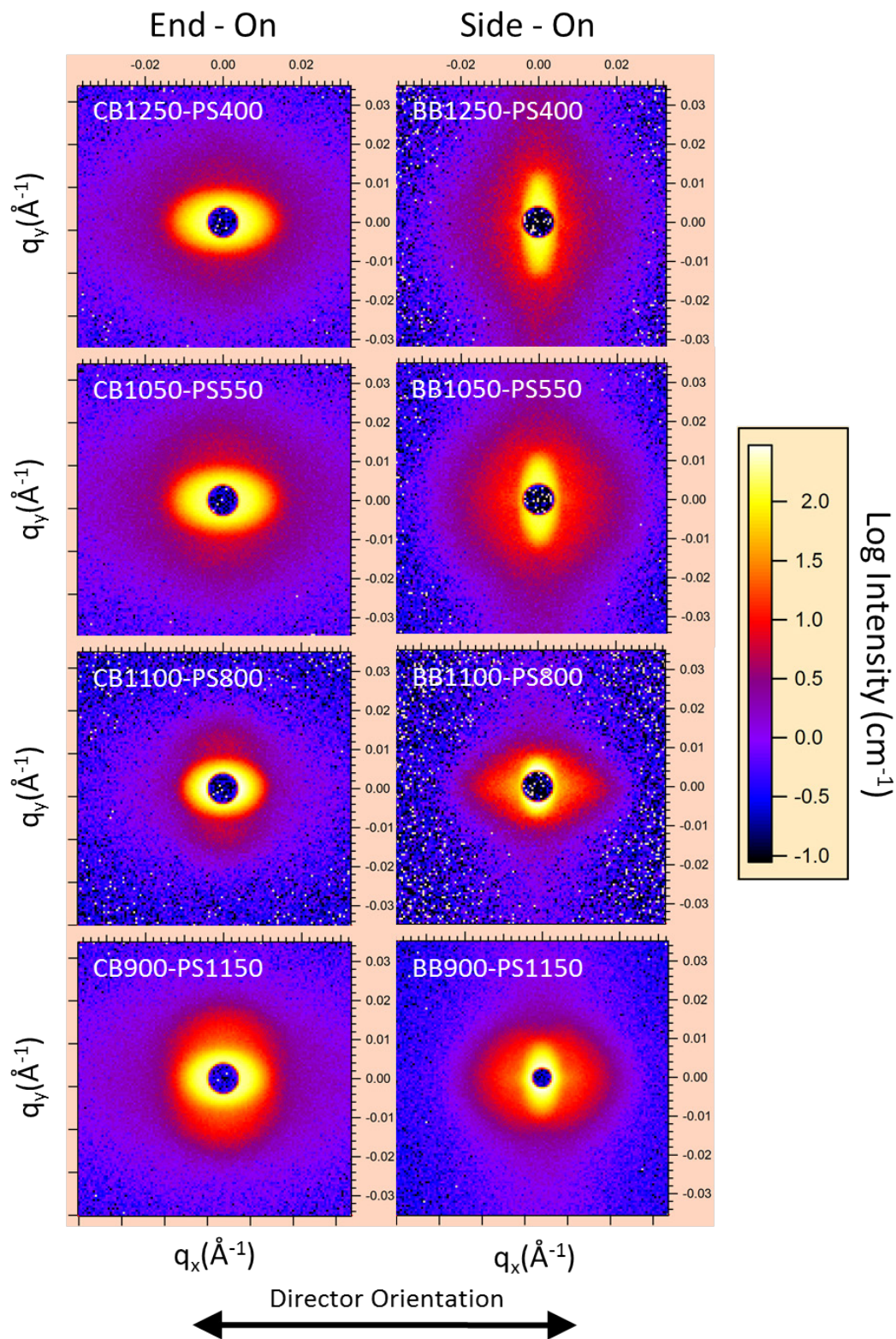


Figure 4.5: Two dimensional SANS patterns for SGLCP-*b*-PS block copolymers at 1wt% in nematic d5CB at $T = T_{ni} - 7^\circ\text{C}$ taken on beamline NG-3 at a sample-to-detector distance of 11 meters. Note that a smaller beam stop ($2''$) was used for BB900-PS1150 rather than the $3''$ used for all other samples.

Above the T_{ni} the scattering patterns become isotropic with dramatically lower intensity, consistent with both blocks becoming solvated in isotropic d5CB [20].

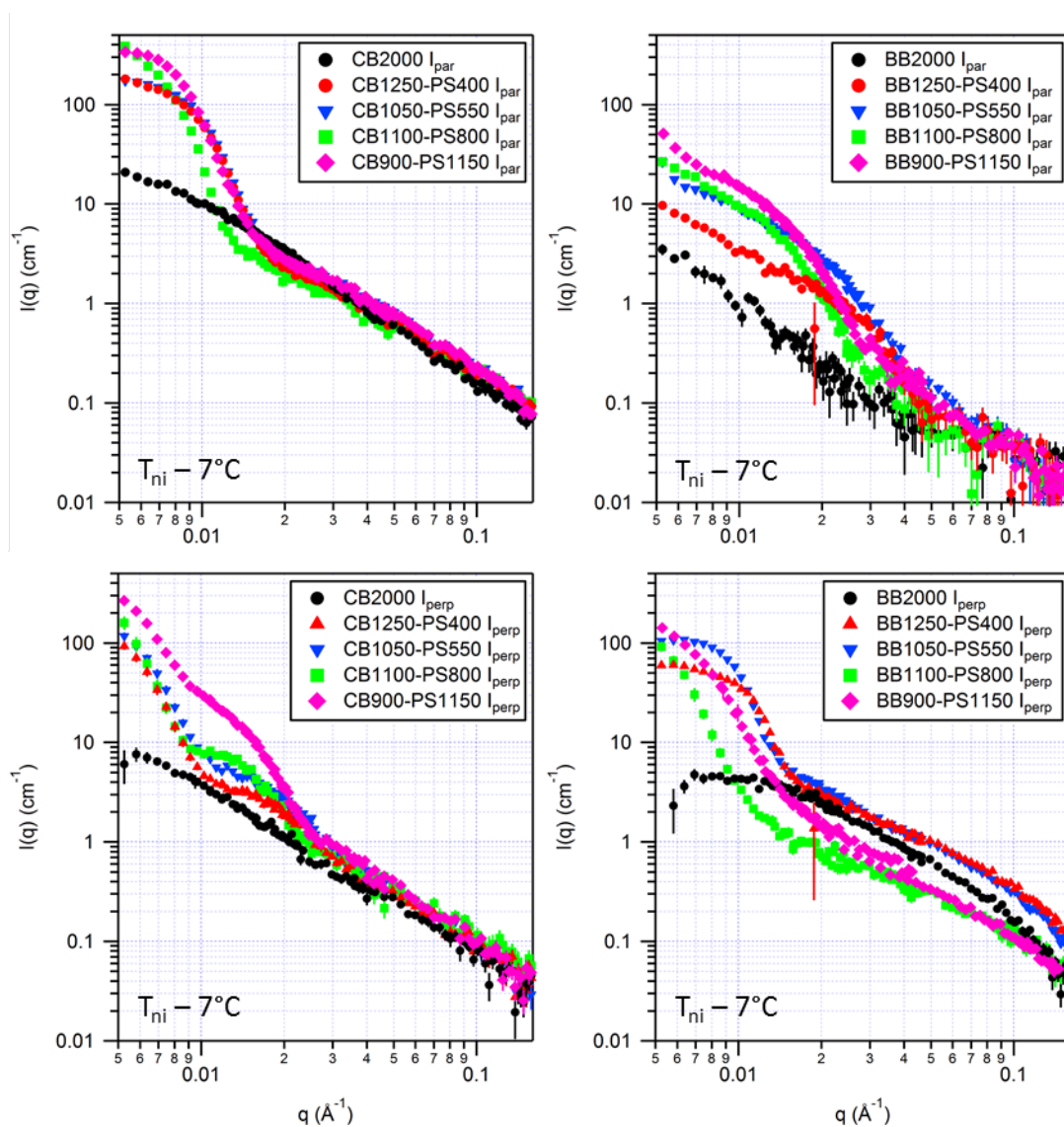


Figure 4.6: Sector averages parallel and perpendicular to the director taken from 2d SANS patterns for 1wt% solutions of SGLCPs in d5CB in the nematic phase. The end-on polymers are shown on the left hand side and side-on polymers on the right with the top images showing the sector parallel to the director and the bottom images showing the sector perpendicular to it. The homopolymer data (black circles) is the same as shown in Figure 4.3.

Sector averages of the scattering patterns parallel and perpendicular to the nematic director (Figure 4.6) show the multiple length scales of anisotropy quite clearly. In the end-on polymers (Figure 4.6 left) the scattering parallel to the director overlaps

with the scattering from a homopolymer at high q ($q > 0.3 \text{ \AA}^{-1}$) and then increases in intensity rapidly at mid q , beginning to plateau at the lowest available q values. The sector average perpendicular to the director also overlaps with the scattering from a homopolymer at high q ($q > 0.3 \text{ \AA}^{-1}$), but unlike I_{par} , the increase of intensity with decreasing q shows two distinct features. The scattering feature that appears at mid q ($0.01 \text{ \AA}^{-1} \leq q \leq 0.03 \text{ \AA}^{-1}$) becomes progressively more intense with increasing polystyrene block length. The side-on polymers (Figure 4.6 right) show interesting similarities and differences with respect to the end-on polymers.

Qualitatively, the shape of $I_{\text{perp}}(q)$ for BB SGLCP-*b*-PS resembles that of $I_{\text{par}}(q)$ for their CB SGLCP-*b*-PS counterparts. There is a suggestion at low- q that a second feature may be present in $I_{\text{par}}(q)$ of BB SGLCP-*b*-PS like the “double hump” character of $I_{\text{perp}}(q)$ for their CB SGLCP-*b*-PS counterparts. At high q , the BB SGLCP-*b*-PS inherit from the BB SGLCP homopolymers a much steeper q -dependence for $I_{\text{par}}(q)$ than for $I_{\text{perp}}(q)$, hence much weaker high- q scattering in the parallel sector than in the perpendicular one. Indeed, at high q , $I_{\text{par}}(q)$ for BB SGLCP-*b*-PS overlaps with the scattering from a BB SGLCP homopolymer. However, unlike the case for CB SGLCP-*b*-PS, the magnitude of the high- q scattering in the sector perpendicular to the director does not overlap that of the homopolymer (compare lower right of Figures 4.6 and 4.3): in the case of the shorter PS blocks, $I_{\text{perp}}(q)$ at high q is greater than expected based on the homopolymer, and in the case of the longer PS blocks it is less than $I_{\text{perp}}(q)$ at high q of the homopolymer.

Above the T_{ni} both BB and CB SGLCP-*b*-PS polymers have simple isotropic scattering patterns that resemble those of the corresponding homopolymer (i.e., an

excluded volume polymer) and vary weakly with polystyrene block length (Figure 4.7). This indicates that the solution is sufficiently dilute to have the Microphase Separation Temperature (MST) very near the T_{ni} for all of the present block lengths, consistent with earlier results that found a much greater concentration ($>5\text{wt}\%$) is required for segregation to persist above T_{ni} [22]. Consistent with having similar SGLCP backbone lengths (DP 1075 ± 175 , corresponding to $480\text{kg/mol} \pm 40\text{kg/mol}$ for CB and $620\text{kg/mol} \pm 60\text{kg/mol}$ for BB SGLCP-*b*-PS) and a small PS fraction (Table 4.1), there is only moderate variation in the isotropic-phase scattering patterns for the different molecular weights, indicating similar Porod exponents and overall coil sizes (

Table 4.4). The mid- q intensities for isotropic solutions of BB900-PS1150 and BB1100-PS800 overlap well but both are lower than those for BB1250-PS400 or BB1050-PS550; although this difference is much less than that observed in the nematic scattering perpendicular to the director, it is qualitatively similar.

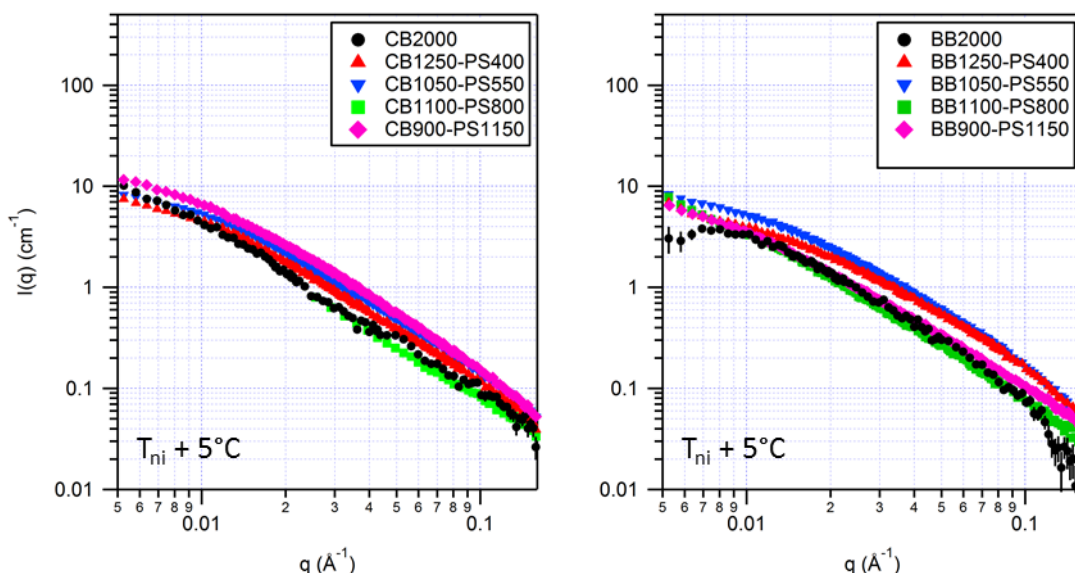


Figure 4.7: 1D scattering intensity for end-on (left) and side-on (right) SGLCP-*b*-PS polymers at 1wt% in d5CB above the T_{ni} . Scattering for the corresponding homopolymer is shown for comparison.

The scaling exponents for all of the block copolymers are very similar for both mesogen types and all polystyrene block lengths and are all ~ 0.6 , which is expected of an excluded volume polymer. This is somewhat unexpected for the side-on polymers given the more stretched exponent observed for the homopolymer. The observed R_g values appear to be essentially independent of the polystyrene block length for the end-on polymers, which is consistent with the very similar overall molecular weights for CB1250-PS400, CB1050-PS550, CB1100-PS800, and CB900-PS1150 (Table 4.1) which are $480\text{kg/mol} \pm 40\text{kg/mol}$. For the side-on polymers the variation in size is much more pronounced, with BB1100-PS800 and BB900-PS1150 having significantly larger radii than BB1250-PS400 and BB1050-PS550, although their molecular weights are not any more varied at $620\text{kg/mol} \pm 60\text{kg/mol}$. It is interesting to note that the division between small and large side-on diblocks corresponds to the intensity groupings observed in the 1D scattering patterns.

Table 4.4: Sizes obtained by fitting an excluded volume polymer form factor the $I(q)$ data for both End-On and Side-On polymers in the isotropic phase ($T_{ni}+5^\circ\text{C}$). Data for CB1100-PS800 was not available.

Polymer	Apparent Radius of Gyration (nm)	Scaling Exponent
CB1250-PS400	16.4	0.57
CB1050-PS550	15.2	0.57
CB1100-PS800	-	0.61
CB900-PS1150	16.0	0.56
BB1250-PS400	11.3	0.62
BB1050-PS550	12.7	0.58
BB1100-PS800	19.9	0.57
BB900-PS1150	19.2	0.61

Transmission Electron Micrographs of unstained dilute solutions of SGLCP-*b*-PS in 5CB show roughly circular objects with considerable polydispersity for both end-on (Figure 4.8,left) and side-on (Figure 4.8,right) block copolymers.

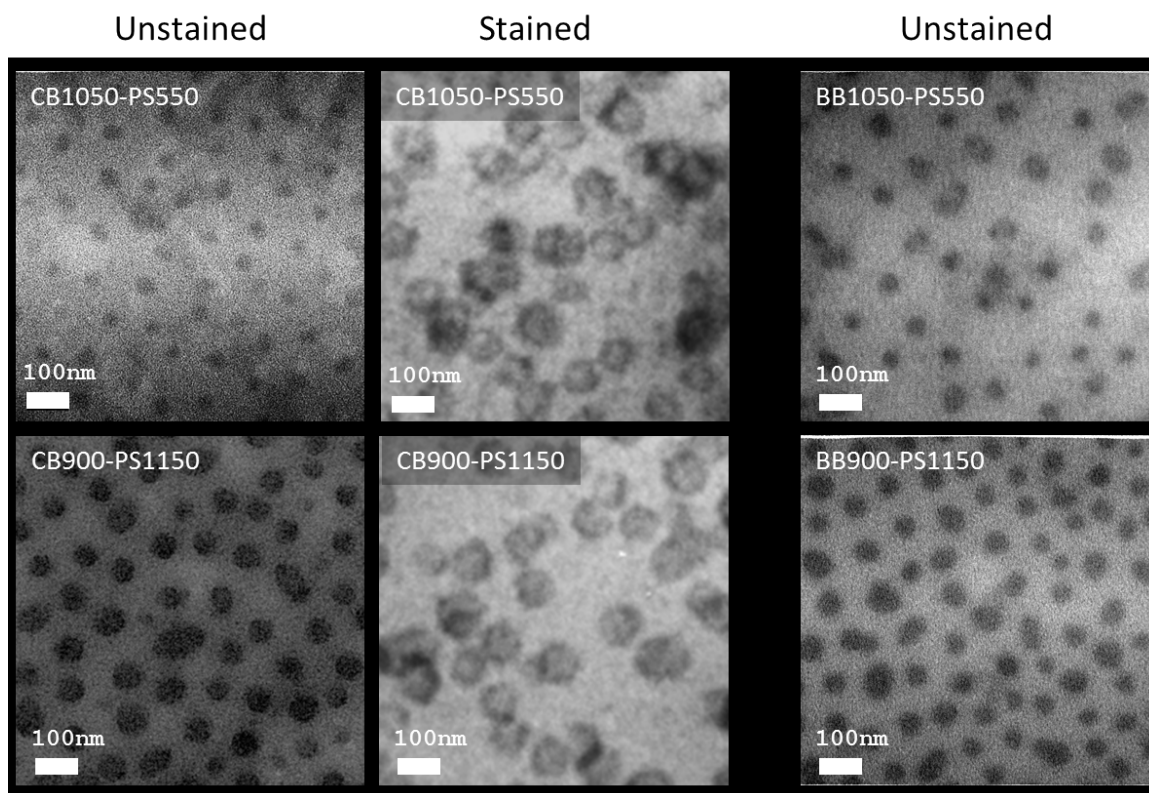


Figure 4.8: Transmission Electron Microscopy images of solutions of SGLCP-*b*-PS polymers in 5CB. The four images on the left are of end-on polymers while the two on the right are of the corresponding side-on polymers. The top images are for polystyrene block length of 550 repeat units and the bottom are for the longest PS block length of 1150 repeat units. Stained images were obtained using RuO₄ as the stain.

The focus and contrast were adequate for image analysis, simplified by the absence of any staining artifacts. The mean and standard deviation of the diameters of the objects seen in unstained TEM range from approximately 30-55nm and appear to increase with increasing PS length and are similar for end-on and side-on counterparts (Table 4.5).

Table 4.5: Diameters of the objects seen in TEM for SGLCP-*b*-PS in 5CB. These were obtained by using image J to quantitatively characterize a number of objects from each image to obtain average sizes. Attempts to stain solutions of side-on polymers were unsuccessful and it was not possible to obtain usable images for the unstained samples without a listed result.

Polymer	Unstained TEM Diameter(nm)	Stained TEM Diameter (nm)	
		Inner	Outer
CB1250-PS400	-		67±20
CB1050-PS550	28±5	47±7	102±13
CB1100-PS800	45±7	54±10	94±12
CB900-PS1150	49±8	57±9	93±9
BB1250-PS400	-	-	-
BB1050-PS550	46±6	-	-
BB1100-PS800	-	-	-
BB900-PS1150	55±7	-	-

TEM of end-on polymer samples stained with ruthenium tetroxide (RuO_4) show objects that are larger than those seen in the corresponding unstained images. Some of the objects seen in the stained images have lighter inner regions surrounded by a darker annulus. This is consistent with greater extent of staining in the SGLCP corona and thus the images are consistent with micelles composed of a polystyrene-rich core surrounded by a diffuse, SGLCP-rich corona. The stained TEM, for both CB1100-PS800 and CB900-PS1150 show inner diameters that agree with the diameter of the features seen in unstained TEM Table 4.5. The outer diameters are much larger, beyond the range of our SANS measurement: data were limited to $q > 0.005 \text{ \AA}^{-1}$, corresponding to structures smaller than 60nm. Interestingly, for each pair of end-on and side-on block copolymers with the same polystyrene block length (available for PS550 and PS1150), the core sizes determined by TEM are indistinguishable. This is consistent with the similarity in the q position of the upturns seen in the sector averages $I_{\text{par}}(q)$ for the CB SGLCP-*b*-PS and $I_{\text{perp}}(q)$ for its BB SGLCP-*b*-PS counterpart (Figure 4.6).

4.4 Discussion

4.4.1 Mutually Orthogonal Anisotropic Structures at Different Length Scales

The two-dimensional SANS patterns of both end-on and side-on SGLCP-coil block copolymers (Figure 4.5) clearly indicate mutually orthogonal anisotropic structures. On both the largest length scales (corresponding to $q < 0.01 \text{ \AA}^{-1}$) and the smallest length scales ($q > 0.02 \text{ \AA}^{-1}$) the orientation of anisotropy matches that of the corresponding homopolymer (Figure 4.2). An orthogonally oriented feature is evident at intermediate length scales ($0.01 \text{ \AA}^{-1} < q < 0.02 \text{ \AA}^{-1}$). Given the system's self-assembly into micelles with a PS-rich core and an SGLCP-rich corona, this suggests that both the core and the corona are anisotropic, but the orientations of their long axes appear to be *mutually orthogonal*.

Important features of the multi-scale anisotropic structure of the self-assembled objects are evident in the sector averages parallel and perpendicular to the director in the q -range ($q < 0.05 \text{ \AA}^{-1}$) that reveals the self-assembled structure, based on the observation that at larger q the scattering was insensitive to PS content ranging from 7% to 27% (Table 4.1) and, with the exception of vertical offsets in I_{perp} of BB SGLCP-*b*-PS, the scattering coincides with that of the corresponding SGLCP homopolymers ($q > \sim 0.05 \text{ \AA}^{-1}$ Figure 4.6). For each pair of polymers synthesized from the same prepolymer, there is a striking similarity between $I_{\text{par}}(q)$ of the CB and $I_{\text{perp}}(q)$ of the BB block copolymer (red symbols in the left and blue ones in the right column of Figure 4.9).

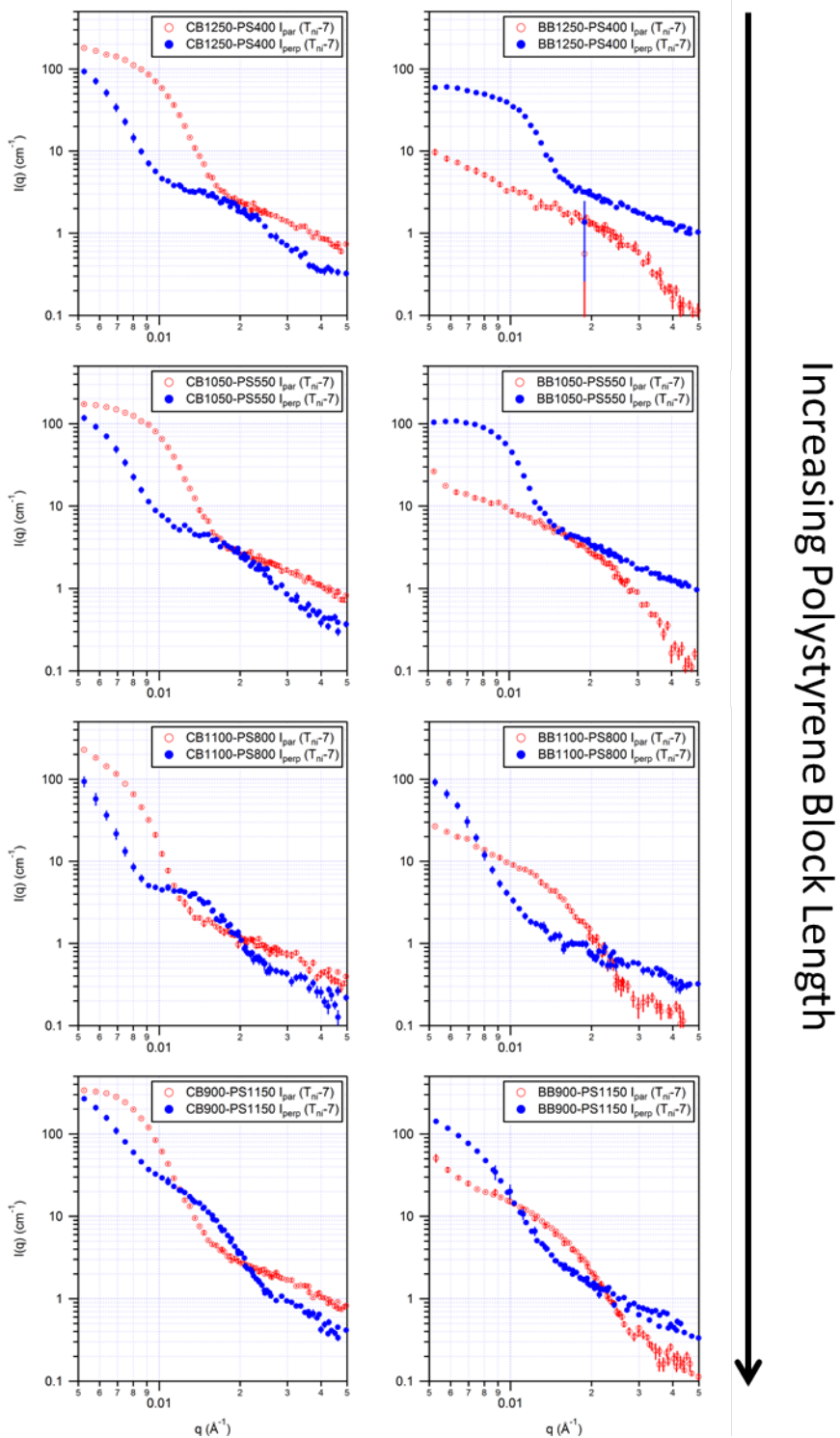


Figure 4.9: Sector averages both parallel and perpendicular to the director taken from 2D SANS patterns for all of the block copolymers in the nematic phase. The end-on and side-on polymers are on the left and right hand sides, respectively, with the polystyrene block length increasing from top to bottom.

All four polymers with PS400 and PS550 blocks show an abrupt rise in scattered intensity in $I_{\text{par}}(q)$ for CB and $I_{\text{perp}}(q)$ for BB as q decreases through 1.5\AA^{-1} and a “knee” as q decreases through 0.8\AA^{-1} . This feature changes with increasing PS block length similarly for both CB and BB SGLCP-*b*-PS: relative to the four polymers with PS400 and PS550, increasing the PS length to PS880 and PS1150 causes the feature in $I_{\text{par}}(q)$ of the CB and $I_{\text{perp}}(q)$ of the BB to increase in intensity and shift to lower q .

Relative to the single feature seen in $I_{\text{par}}(q)$ of the CB block copolymers, there are two features in $I_{\text{perp}}(q)$: one at higher q (ca. 0.25\AA^{-1}) and another at lower q (ca. 0.008\AA^{-1}). The lower q feature in $I_{\text{perp}}(q)$ of the CB micelles appears to correspond with the feature in $I_{\text{par}}(q)$ of their BB counterpart (the intensity rise at approximately 0.3\AA^{-1}). At the lowest q , $I_{\text{par}}(q)$ of BB micelles appears to roll off toward a knee, suggesting a low- q feature analogous to $I_{\text{perp}}(q)$ of the CB micelles may be present for the BB micelles at lower q than was accessible in the present study. We believe the mid- q features are due to the PS-rich core, which is anisotropic with a shorter dimension of 8-12nm and a longer one of 20-25nm with the long axis oriented perpendicular to the long axis of a corresponding homopolymer. Within each pair of homologous block copolymers, the magnitude of the rise in intensity in the mid- q features is greater for the CB micelles than for the BB counterpart, suggesting that the scattering contrast across the interface between the PS core and the surrounding corona is greater in the CB micelles than in the BB ones (i.e., the concentration of SGLCP in the corona is lower for CB than for BB).

Scattering data obtained for SGLCP-*b-d*PS polymers having a deuterium labeled polystyrene block and an SGLCP block resembling CB and contrast matched to the 5CB used as the solvent were observed to have an anisotropic core in aligned samples[40].

Although those polymers were much shorter (overall molecular weight $<20\text{kg/mol}$) than the present ones and had much higher PS content (roughly 60%), the presence of an anisotropic core is consistent with our scattering patterns. To our knowledge, orthogonal orientation of the overall object relative to the core has not been reported in the literature. Here we use our understanding of the materials from previous study of ternary phase behavior of SGLCP/PS/5CB to guide the construction of schematic diagrams of plausible structures that are in agreement with both the TEM and SANS data and accord with the homologous variations in the molecular structure of the polymers. The primary physical features expected of the core shell object are described in the following paragraphs.

The core is expected to have much higher polymer concentration than the corona. Prior literature on the ternary phase behavior of end-on SGLCP, PS and 5CB, shows that in the nematic phase ($T < T_{ni}$), 5CB preferentially solvates the SGLCP and partitions into 5CB rich, nematic SGLCP domains and 5CB poor, isotropic PS domains[20]. The fact that a very PS-rich isotropic phase coexists with a much lower concentration SGLCP nematic phase leads to the expectation that PS-SGLCP block copolymers assemble into objects that have concentrated, isotropic PS cores and semidilute SGLCP nematic coronas (in which the activity of 5CB is equal in the bulk nematic solvent, in the nematic SGLCP-containing corona and in the *isotropic* PS-rich core).

The shape of the corona is that which takes advantage of the spontaneous anisotropy of the SGLCPs to minimize crowding. By preferentially orienting the corona chains with their long axes orthogonal to the core-corona interface, the spontaneous anisotropy of the SGLCP serves as a “no-cost” stretching of the corona chains and allows a greater packing density without distorting the equilibrium conformation characteristic

of the SGLCP. In this preferred direction the thickness of the corona will be at least equal to the long dimension of the spontaneously anisotropic SGLCP, as this thickness is achieved without paying a penalty for stretching the SGLCP. Hence, the core should have more of its surface area tangent to the director for end-on (CB) and perpendicular to the director for side-on (BB).

The core must have at least one direction in which its radius is compatible with the size of the PS block (calculated to be 8-12nm for the PS blocks used in this study from literature for polystyrene homopolymers[41]). Given the relatively high concentration of polymer in the core ($\phi_{ps} > 0.50$) suggested by the ternary phase diagram[20], the disk-like core could avoid significant stretching of the PS by having a half-thickness of 8-12nm.

The longer dimension of the PS core can be deduced from the size of the circular features in unstained TEM (Figure 4.8) observed to have a radius of 20-25nm. Such a radius is too large to be compatible with the PS block lengths in this study and, therefore, must be orthogonal to the short axis of the core. The observed polydispersity in the size of the roughly circular features is consistent with a disk-like core in which the energy penalty for variations in the radius of the disk (the direction that can be increased without requiring stretching of the PS) is relatively low.

The shape and volume of the core is similar for side-on and end-on polymers of a given PS block length (i.e., made from the same prepolymer). Given that the concentration of SGLCP in the corona is low and, because of the spontaneous anisotropy of the SGLCP, the stretching penalty in the corona is also low. The interfacial tension between the core and corona is similar to that of a concentrated solution of PS in isotropic

5CB in contact with pure nematic 5CB. Consequently, the physics that governs the core area-volume ratio, composition, and thickness is insensitive to the length or type of the SGLCP block: the micelle core is expected to have similar size and shape for both CB and BB polymers having a given PS block length. Thus, increasing PS block length will increase the aggregation number and concentration of PS in the core similarly for both CB and BB SGLCP-*b*-PS.

An oblate spheroid represents a more favorable anisotropic core shape than a prolate one, for both end-on and side-on cases: the oblate shape affords greater area orthogonal to the long direction of the SGLCP (to take advantage of spontaneous stretching) while minimizing the area along the short axis of the SGLCP. Looking down the short axis of the oblate core can explain the circular features seen in the unstained TEM (Figure 4.8) that are too large to be spanned by the PS blocks lengths studied.

We speculate that the corona dimensions will take advantage of the spontaneous anisotropy of the backbone of the SGLCP (Figure 4.10). The corona will be thicker along the direction that is spontaneously elongated for a given SGLCP and thinner in the direction that is spontaneously thin for the SGLCP homopolymer. Consequently, we expect the oblate PS-rich core to orient such that most of its area is tangent to the director for CB SGLCP-*b*-PS (Figure 4.10, part A) and normal to the director for BB SGLCP-*b*-PS (Figure 4.10, part B). Over the small perimeter area of the disk-like core, the corona will have a thickness that is at least the short dimension of the anisotropic conformation that the corresponding SGLCP would adopt if it were free in solution (rather than tethered to a PS coil block). If the SGLCPs are not very crowded, these lower bounds for the corona thicknesses may be good approximations for the actual thicknesses.

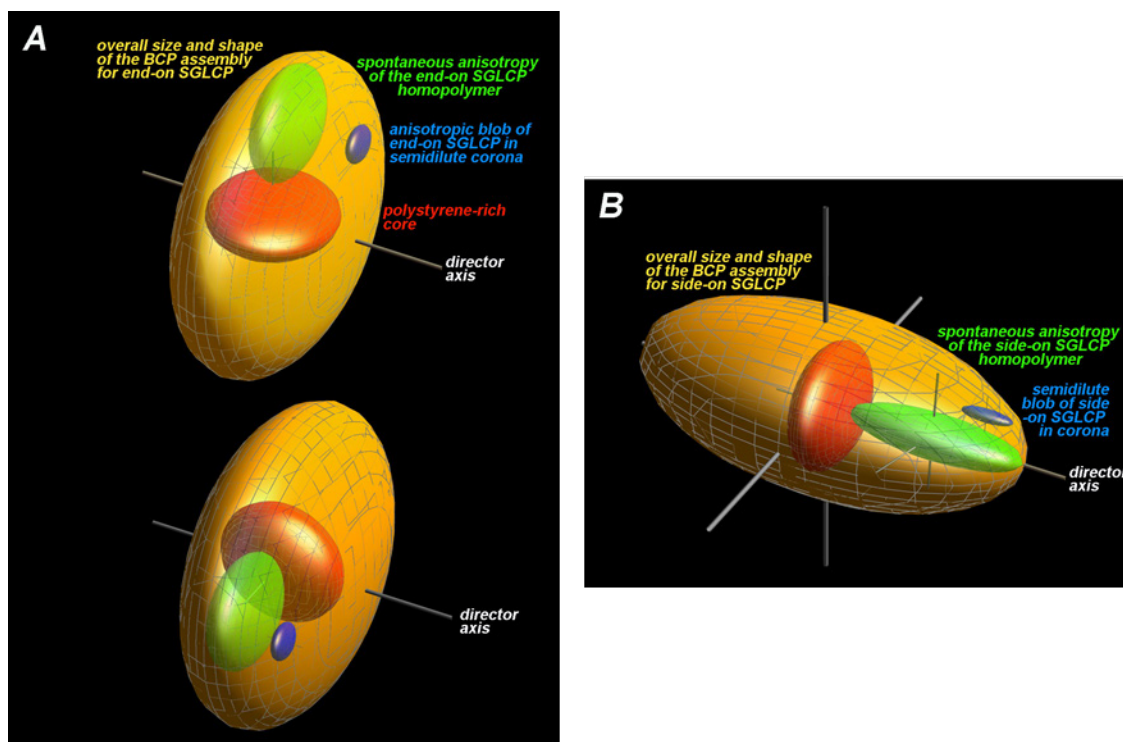


Figure 4.10: Schematic illustration of plausible self-assembled structures consistent with progression of mutually orthogonal structures at different length scales. The polystyrene rich core (red) is expected to have an oblate spheroidal shape. For a fixed PS block length, the core size and shape are expected to be similar in both end-on SGLCP-*b*-PS (A, left) and side-on SGLCP-*b*-PS (B, right). The anisotropic corona has a thicker dimension estimated to be equal to the long dimension of the corresponding SGLCP homopolymer (green). Due to the overlap among the corona chains, the corona is a semi-dilute solution with anisotropic blobs (purple). The colors of the overall assembly (yellow), core (red), and blobs (purple) correspond with the color of the corresponding features in the 2D SANS patterns (Figure 4.5).

The much higher concentration of polymer in the core than in the corona leads to high scattering contrast at the core-corona interface, hence intense scattering due to the core. This qualitative picture explains the similarity between $I_{\text{par}}(q)$ of CB and $I_{\text{perp}}(q)$ of BB (both reflecting the long dimension of the ellipsoidal core, 20-25nm) in the q -range dominated by the core. Indeed, moving from high q (small length scale) to low q (larger length scales) we see that the q -value ($\sim 0.015 \text{ \AA}^{-1}$) at which $I(q)$ deviates significantly from that of the homopolymer is indeed similar for both polymers (BB and CB) having an identical PS block length, and varies with PS block length in the same way for both

series of SGLCP-*b*-PS. The smaller dimension of the PS-rich core gives features that are at greater q -values (~ 0.02 - 0.04 \AA^{-1}) and are in the orthogonal direction for a given polymer. These are consistent with the expected length scale of the shorter core dimension and correspond to sensible aspect ratios. Rotational symmetry about the nematic director axis is inherent to the system. When the rotational axis of symmetry for the disk of the core is coincident with the director (side-on) the scattering reflects its actual size and aspect ratio. However, when the axis of rotational symmetry of the core is orthogonal to the director, the scattering pattern reflects an ensemble average over a cylindrically symmetric distribution (two representative orientations are shown in Figure 4.10A). Therefore, an equally anisotropic core would yield a less anisotropic scattering pattern in the end-on case than in the side-on case.

To gain insight into the dimensions to the corona structures, it is useful to consider the spontaneous conformational anisotropy of the two types of SGLCPs examined and the length scales expected for the SGLCP blocks in relation to the features observed in the SANS patterns.

4.4.2 Homopolymer Conformation in Dilute Solution

The present dilute solution data has enabled determination of the size and the scaling exponent for the whole chain (Table 4.3), revealing that the SGLCP homopolymers in the nematic phase are significantly larger and more stretched than their correlation blobs in the semi-dilute regime[7, 22]. The sense of orientation of the polymer backbone is determined by the geometry of side-group coupling with the mesogens, which preferentially orient along the director and force a compromise with the

inherent entropy of the backbone random walk. Thus, in the nematic phase the polymer coil becomes stretched, in the direction parallel to the nematic director for the side-on polymer and in the perpendicular direction for the end-on polymer.

The sizes for CB880 and CB2000 parallel to the nematic director at $T_{ni}-7^{\circ}\text{C}$ are 3.3 and 3.7 times larger than those previously measured, and those for BB880 and BB2000 perpendicular to the director are 2.2 and 3.2 times larger. The reason that the multiplier is lower for shorter polymers (especially BB880) is likely due to the fact that they are closer to the dilute regime at 5wt%, particularly for the narrow dimension of BB880 ($6.8\pm 0.3\text{nm}$).

As expected, the scaling exponents observed in the present dilute solutions agree with those observed in the semidilute solution at large q (within the semidilute blobs). In addition, the aspect ratios observed in dilute solution also agree with those seen in semidilute solution. It appears that the aspect ratio of the blob is approximately the same as that of the overall coil, perhaps due to the inherent asymmetry in the correlation along the backbone. The scaling exponents for all of the polymers are larger than expected for a Gaussian coil ($\nu > 0.5$), indicating that nematic 5CB is a good solvent for the SGLCPs.

Consistent with prior results, the anisotropy in chain conformation below the T_{ni} vanishes above the nematic-to-isotropic phase transition temperature[4]. Raising the temperature to $T_{ni}+5^{\circ}\text{C}$ removes the free energy benefit of mesogens orienting along the nematic director (which is no longer defined for the sample as a whole) and allows the backbone to dominate the conformation, leading to a spherically symmetric coil. The coil radius in the isotropic phase is 1.3 times the shorter radius (parallel to the nematic director for the end-on and perpendicular to the director for the side-on) in the nematic

phase. Nevertheless, the contraction along the long-axes of the nematic SGLCP is greater and the pervaded volume decreases substantially in the isotropic phase relative to the nematic phase; although the effect is mild for the end-on SGLCP (pervaded volume in isotropic 80% of that in the nematic phase), it is a dramatic effect for the side-on SGLCP (the pervaded volume in the isotropic phase is <20% of that in the nematic phase).

4.4.3 SGLCP-*b*-PS Structural Length Scales

The scattering patterns for the block copolymers in the nematic phase show a hierarchical structure (**Error! Reference source not found.**) that does not conform to standard form factors for a core-shell micelle with spherical, cylindrical, or ellipsoid cores. This is due to the fact that these models assume a uniform corona thickness in all directions and cannot account for a corona that is anisotropic but with an orientation perpendicular to that of the core. In the absence of an applicable model, it is common to use model-independent scattering functions that allow the approximate length scales of scattering features to be determined without any further information about the underlying structure. We apply this approach to the sector averaged scattering patterns of nematic solutions for sectors parallel and perpendicular to the director.

The scattering corresponding to the shorter axis of the corresponding homopolymer SGLCP (parallel to the director for end-on polymers and perpendicular to the director for side-on polymers) only contains a single feature in the accessible range of q ; we extract a length scale associated with this feature using a Guinier function at low q and approximate the homopolymer-like scattering at high q using Porod function ($I(q) \sim q^{-1}$) [23]. The resulting values of this “Guinier radius” increase with PS block length: in

the end-on type SGLCP-b-PS this apparent Guinier radius (parallel to the director) increases from approximately 20nm for PS400 and PS550 to approximately 30nm for PS800 and PS1150, and in the side-on type SGLCP-b-PS (apparent Guinier radius perpendicular to the director), from approximately 15nm to 35nm (Table 4.6). These apparent radii agree with the half the diameter observed in unstained TEM (Table 4.5). Therefore, we interpret these as these apparent Guinier radii as those of the larger dimension of the PS core.

The orthogonal sector averages appear to have two features, but data at even lower values of q (outside the accessible range in these experiments) would be needed to extract an overall size. It is, nevertheless, possible to determine the length scale of the intermediate q ($0.01\text{\AA}^{-1} \leq q \leq 0.03\text{\AA}^{-1}$) scattering feature. Because of the superposition of real-space scattering features in this region of q it is not possible to adequately describe the scattering by a single model. In such situations it is a reasonable first approximation to linearly superimpose the scattering intensity of multiple form factors, and this approach has been used for a variety of systems with hierarchical structures[42, 43] and is similar in concept to the Beaucage fitting approach[44]. Thus two models were combined, a Guinier-Porod model for the structure and a Lorentzian correlation length model to account for scattering contribution of the intra-chain correlation. The following function was fit to the more complicated scattering:

$$I(q) = D e^{-\frac{1}{3}q^2 R_g^2} + B \quad \text{for } q \leq q_1 \quad (4.4)$$

$$I(q) = \frac{A}{q^n} + \frac{C}{1 + (q\xi)^m} + B \quad \text{for } q > q_1 \quad (4.5)$$

Here the parameters A, C, and D are the scaling factors of the Porod, Lorentzian and Guinier functions, respectively, and B is the incoherent background contribution which was set to a very low value, as most of the background scattering was accounted for by the subtraction of solvent scattering from the data. The Guinier term (equation 4.4) reproduces the plateau part of the hump ($0.01\text{\AA}^{-1} \leq q \leq 0.03\text{\AA}^{-1}$) and is matched at $q=q_1$ to the Porod and Lorentzian scattering (equation 4.5). In this case the Porod term has an exponent $n \sim 4$ corresponding to surface fractal scattering, most probably from the core-corona interface. The Lorentzian term describes the scattering for a polymer chain at high q where the ξ is the correlation length and the power $m=1/\nu$ is the scaling exponent of the chain, in this case corresponding to a polymer in good solvent. The values of n and m were found to be very similar for all molecular weights of both end-on and side-on polymers and were fixed to the physically reasonable values of $n=4$ and $m=2$ in order to reduce the number of floating parameters. The resulting apparent radii again increase with PS block length: in the end-on type SGLCP-b-PS this apparent Guinier radius (perpendicular to the director) increases from approximately 10nm for PS400 and PS550 to approximately 14nm for PS800 and PS1150, and in the side-on type SGLCP-b-PS (apparent Guinier radius perpendicular to the director), from approximately 10nm to 16nm (Table 4.6). These values are small enough that they could be spanned by the PS blocks and we believe they correspond to the thinner dimension of the PS core.

Table 4.6: R_g from SANS for SGLCP-*b*-PS diblocks in nematic LC.

Polymer	R_g parallel (nm)	R_g perpendicular (nm)
CB1250-PS400	21.1	9.4
CB1050-PS550	18.0	9.8
CB1100-PS800	31.9	13.4
CB900-PS1150	27.4	15.8
BB1250-PS400	8.3	14.8
BB1050-PS550	10.7	18.3
BB1100-PS800	15.9	41.5
BB900-PS1150	15.8	32.0

Linear fits were obtained for the sector averaged intensity parallel to the director in end-on polymers (**Error! Reference source not found.**, left side, open red circles) in the region $(0.005\text{\AA}^{-1} < q < 0.008\text{\AA}^{-1})$ which also satisfies the condition that $qR_g < 1.2$ needed for the Guinier approximation. For the side-on polymers, the sector perpendicular to the director (**Error! Reference source not found.**, right side, filled blue squares) showed a good plateau for BB1250-PS400 and BB1050-PS550 but had fewer points available for BB1100-PS800 and BB900-PS1150, although a good linear fit was nevertheless obtained. The combined model described earlier provided a good fit to the perpendicular sector of the end-on polymers (**Error! Reference source not found.**, left side, filled blue squares) and the parallel sector of the side-on polymers (**Error! Reference source not found.**, right side, open red circles) for $q > 0.01\text{\AA}^{-1}$. The pair of dimensions obtained from the Guinier fits for all of the block copolymers is consistent with our interpretation of the data as showing an anisotropic micelle core.

4.4.4 Development of Toy Models to Test Plausibility of Interpretations for Scattering Patterns

Given what we know about SGLCP coils in solution and ordinary coil-coil block copolymer self-assembly, we developed the proposed structures in Figure 4.10; here we test their plausibility. This was done by developing a method to calculate the scattering corresponding to the sectors parallel and perpendicular to the director for a number of proposed structures and then comparing the resulting patterns qualitatively to the observed data. For example, we could test whether the schematic model could capture the fact that crossovers occur for I_{par} and I_{perp} for the longest PS but not for PS400 or PS550 (**Error! Reference source not found.**).

The starting point for this calculation was the fundamental equation that describes elastic neutron scattering from an arbitrary set of N scattering centers with the i^{th} scatterer having scattering length density (SLD) b_i and position \mathbf{r}_i [24], which give scattered intensity $I(\mathbf{q})$ at wave vector \mathbf{q} :

$$I(\mathbf{q}) \sim \frac{d\theta}{d\Omega} = \sum_{i=1}^N \sum_{j=1}^N b_i b_j \langle e^{i\mathbf{q} \cdot (\mathbf{r}_i - \mathbf{r}_j)} \rangle \quad (4.6)$$

This equation is general for any system that is unperturbed by the neutron interaction and in which the scattering is purely elastic. The resulting intensity has both real and imaginary components but simple manipulations show that for any arbitrary set of position vectors the imaginary component will always be zero, so the equation can be rewritten as:

$$I(\mathbf{q}) \sim \frac{d\theta}{d\Omega} = \sum_{i=1}^N \sum_{j=1}^N b_i b_j \langle \cos(\mathbf{q} \cdot (\mathbf{r}_i - \mathbf{r}_j)) \rangle \quad (4.7)$$

This form will always produce a real result for the intensity and is easily solved using elementary functions given a set of position vectors and their corresponding SLDs. The primary limitation is the number of scatterers used in the model system as the inherent computational scaling is $O(N^2)$. Two approaches were used to generate sets of \mathbf{r}_i that describe the hierarchically anisotropic micelles that are formed by SGLCP-*b*-PS self-assembly while keeping N to a value compatible with calculations on current personal computers ($N < 10^6$).

The first toy model approach was to generate the shapes of the core and corona of the micelle on a lattice. The lattice consisted of a 2D grid of M points on each side spaced Δx apart with each point having an associated vector \mathbf{r}_i and SLD b_i . Calculations were done in units of the lattice spacing with each vector \mathbf{r}_i having the lattice coordinates as its components. The SLD was chosen to represent the density of scatterers in that region of the lattice. The structure consisted of two nested ellipses with the inner having its long axis oriented orthogonal to that of the outer with the dimensions of each specified by R_{par} and R_{perp} , parallel and perpendicular to the nematic director. The scattering was calculated along the parallel and perpendicular directions using Equation 4.7.

The scattering predicted for one such structure is shown in Figure 4.11 with a cartoon of the structure inset. For this particular model the following parameters were used: $\Delta x = 1\text{nm}$, $M=150$, $R_{\text{par,core}} = 22\text{nm}$, $R_{\text{perp,core}} = 11\text{nm}$, $R_{\text{par,corona}} = 46\text{nm}$, $R_{\text{perp,corona}} = 64\text{nm}$, $b_{\text{core}} = 8$, and $b_{\text{corona}} = 1$. The size of the core was estimated from the data for CB900-PS1150 with the corona consisting of SGLCP coils surrounding the core. The

SLD values were chosen to be consistent with the estimated 80% polymer in the core and 10% polymer in the corona. The calculation of the scattering intensity took approximately 30 minutes to calculate on an Intel i7 computer.

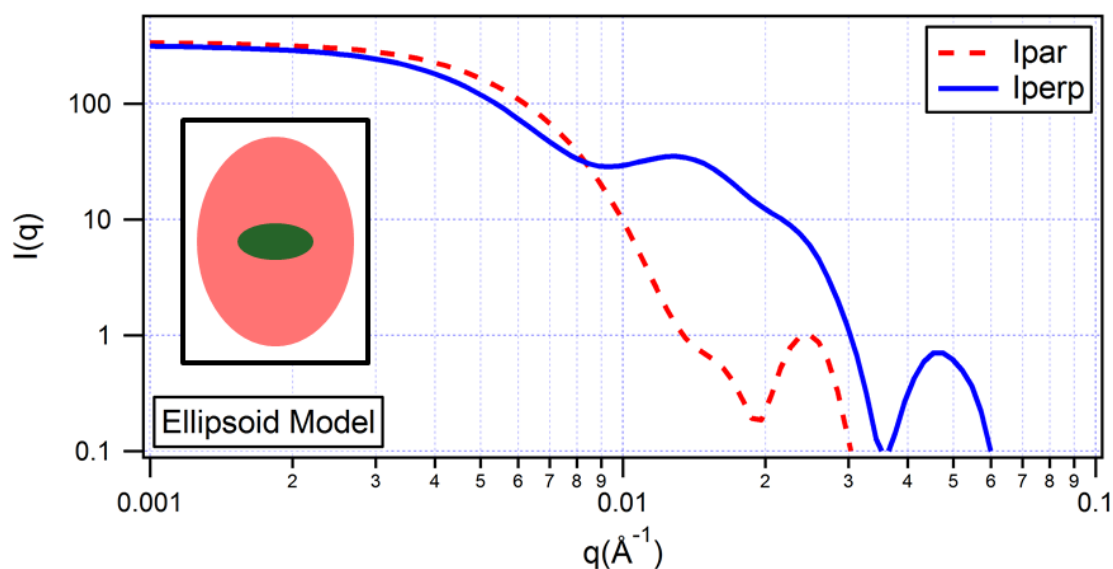


Figure 4.11: Scattering pattern from ellipsoid model. The dashed red line is the scattering parallel to the nematic director while the blue solid line is the scattering perpendicular to the director. The inset on the left side of the graph is a cartoon of the structure used to generate the scattering.

The second approach incorporated much more molecular level detail into the toy model representation. The structure was built up of scattering points representing the polymer segments with each polystyrene segment having an SLD of $b_i = 1$ and each SGLCP segment having an SLD of $b_i = 3$ to represent the larger size of the side-group. The overall structure was constructed by placing individual polymer coils representing the SGLCP around a central region representing the polystyrene core. A schematic of the structure is inset in (Figure 4.12). Each SGLCP coil was generated using a 3D, lattice-free random walk with the segment length (0.5nm) and the number of segments (900) corresponding to CB900-PS1150. Excluded volume was included by rejecting configurations in which segments crossed. The anisotropy and orientation of an SGLCP

was included by making steps parallel to the director more probable to occur and adjusting the probability until the aspect ratio of the resulting walk was approximately equal to that of an end-on SGLCP homopolymer (~ 1.6). For the core, another random walk was started at the end of the SGLCP coil with higher density achieved by ignoring the excluded volume and reducing the length of the segments until the density was similar to the 80% polymer that was estimated for the core.

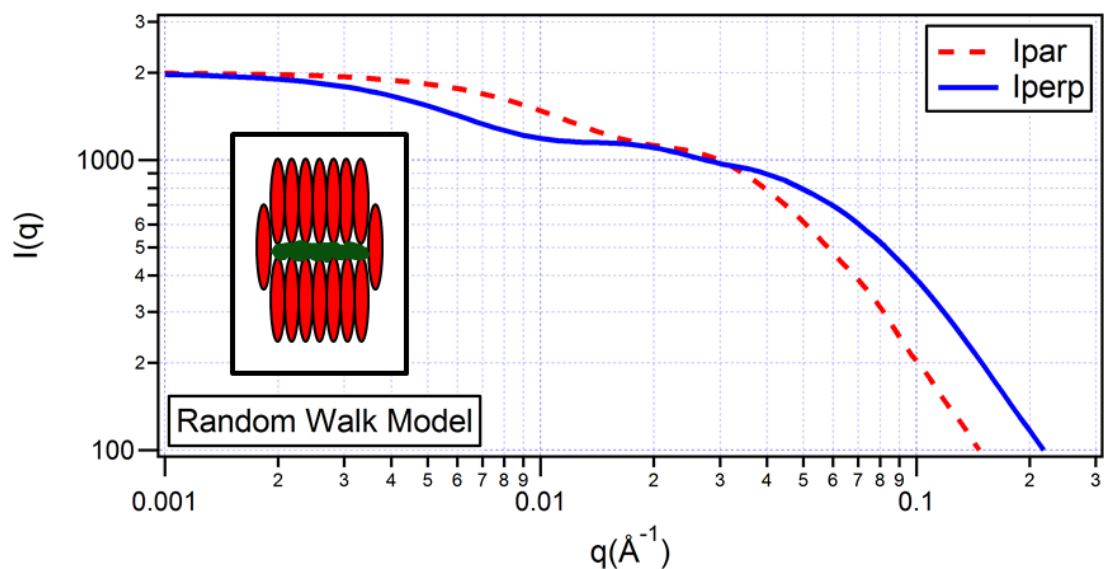


Figure 4.12: Scattering pattern from random walk model. The dashed red line is the scattering parallel to the nematic director while the blue solid line is the scattering perpendicular to the director. The inset on the left side of the graph is a cartoon of the structure used to generate the scattering.

The predicted scattering from one such structure is shown in Figure 4.12. This structure was based on CB900-PS1150 and consisted of 23 polymer coils, with the SGLCP corona coils having their centers positioned around the central core coils, resulting in an anisotropic micelle structure. In order to take into account the ensemble averaging of a real system several replicates of the structure were generated. Each replicate had independently generated random walks for each of the polymer coils, with the starting points of the walk fixed in order to maintain the micelle structure. Scattering

was calculated for each of the replicates using Equation 4.7 and then all of the scattering patterns were averaged. The scattering calculation were much slower for this model due to the greater number of scatterers used, and the same computer used for the first model took several days to calculate the scattering pattern shown in Figure 4.12.

Both approaches qualitatively reproduce some of the features seen in the scattering curves for CB900-PS1150 (Figure 4.9). Both the ellipse (Figure 4.11) and the random walk (Figure 4.12) models show low- q plateaus in the scattering both parallel and perpendicular to the director. For both models I_{par} is higher at the lowest accessible q and plateaus earlier, corresponding to an overall micelle structure with the long axis oriented perpendicular to the director. Both show an intermediate plateau in I_{perp} , in accord with the experimental scattering data. For the ellipse model (Figure 4.11), the scattering at higher q values is dominated by the beat patterns, resulting from the discrete lattice structure and sharp boundaries between the inner and outer scattering features. For the random walk model (Figure 4.12) the scattering shows a smooth power law dependence for $q > 0.08 \text{ \AA}^{-1}$ with the slope consistent with a polymer in good solvent.

Although many of the features of experimental scattering are reproduced by the toy models, there are some discrepancies. In the scattering for both models, the two intensities I_{par} and I_{perp} cross only once, having a low- q region with $I_{\text{par}} > I_{\text{perp}}$ and a high- q region with $I_{\text{par}} < I_{\text{perp}}$. In the experimental data (Figure 4.9) the curves cross twice with $I_{\text{par}} > I_{\text{perp}}$ at both high- q and low- q and an intermediate region $0.01 \text{ \AA}^{-1} < q < 0.02 \text{ \AA}^{-1}$ in which $I_{\text{par}} < I_{\text{perp}}$. The locations and intensities of the experimentally determined scattering are also not quantitatively reproduced by either of the toy models.

Although neither toy model quantitatively reproduced the scattering data, they both capture some of the unique features of the scattering by SGLCP-*b*-PS block copolymers in aligned 5CB. We are optimistic that further refinement of the toy model and further sampling of the structure space will enable more quantitative agreement between the model and the experimental data. Work on the refinement of the toy models is ongoing and should provide greater insight into the size and conformation of hierarchically structured anisotropic micelles.

4.5 Conclusions

Dilute Solution Scattering has revealed a very complex self-assembled structure for SGLCP-*b*-PS block copolymers in nematic 5CB. The selective solvent quality of the nematic 5CB drives the polymers to self-assemble into micelles with polystyrene rich cores and 5CB rich coronas. SANS patterns for aligned solutions of both CB (end-on) and BB(side-on) SGLCP-*b*-PS in nematic 5CB(Figure 4.5, Figure 4.9), show mutually orthogonal anisotropies. This indicates that the PS-rich cores adopt an anisotropic shape that gives greater area normal to the long axis (axes) of the SGLCP's spontaneous anisotropy.

The similarities between the CB and BB micelles were stronger than expected, given the striking difference between the conformations and orientations of the corresponding SGLCP homopolymers. We expected that the prolate BB blocks would tend to drive an oblate shaped core and the mildly oblate CB blocks would decorate the sides of a prolate core. So, we were surprised when the results (mid-*q* SANS + TEM) indicated that the size and shape of the PS-rich cores are similar for both the CB and BB

homologues derived from the same prepolymer (having identical PS content). The trends appear to be similar for both families of SGLCP, as it appears that increasing PS block length causes the aggregation number and the concentration of PS in the core to increase.

We believe that the similarity in structure is a consequence of the fact that the free energy trade-offs governing the size, shape and composition of the PS-rich core are predominantly dictated by the polystyrene block. The penalty for stretching the PS-blocks may be the limiting factor for the size of the minor radius of the core, with the major radii dependent on the aggregation number, in turn dictated by the configurational entropy of the system as a whole (favoring a larger number of micelles with a smaller aggregation number). Although the corona chains have dramatically different spontaneous anisotropy, both CB and BB polymer micelles appear to have oblate cores. In hindsight, an oblate ellipsoid is preferred over a prolate one for both CB and BB, because an oblate perturbation from a spherical core requires a smaller increase in core-corona interface for a given increase in area normal to the SGLCP's long axis(es).

To the best of our knowledge there are no previously published scattering functions $I(\mathbf{q})$ that capture the mutually orthogonal anisotropies observed in the scattering data. In order to verify the plausibility of our proposed structures, we developed toy models that predict scattering from micellar objects with mutually orthogonal anisotropies of the core and corona. The predicted scattering patterns show many of the same qualitative features as the experimental data. Work is ongoing to refine the models and obtain more quantitative structural information from the scattering data.

References

1. Collings, P.J., *Liquid crystals: nature's delicate phase of matter*. 2002: Princeton University Press.
2. Schadt, M. and W. Helfrich, *Voltage-Dependent Optical Activity of a Twisted Nematic Liquid Crystal*. Applied Physics Letters, 1971. **18**: p. 127.
3. De Gennes, P. and J. Prost, *The Physics of Liquid Crystals (International Series of Monographs on Physics, 83)*, 1993, Oxford Science Publications, Oxford.
4. Donald, A.M., A.H. Windle, and S. Hanna, *Liquid crystalline polymers*. 2006: Cambridge University Press.
5. Mattoussi, H. and R. Ober, *Conformation of comblike liquid-crystalline macromolecules*. Macromolecules, 1990. **23**(6): p. 1809-1816.
6. Moussa, F., et al., *Conformational anisotropy of liquid crystalline side chain polymers: a small angle neutron scattering study*. Journal de Physique, 1987. **48**(7): p. 1079-1083.
7. Kempe, M.D., J.A. Kornfield, and J. Lal, *Chain anisotropy of side-group liquid crystalline polymers in nematic solvents*. Macromolecules, 2004. **37**(23): p. 8730-8738.
8. Carri, G.A. and M. Muthukumar, *Configurations of liquid crystalline polymers in nematic solvents*. The Journal of chemical physics, 1998. **109**: p. 1117.
9. Hardouin, F., et al., *Small angle neutron scattering experiments on "side-on fixed" liquid crystal polysiloxanes*. Journal de Physique II, 1992. **2**(3): p. 271-278.
10. Wang, R. and Z.-G. Wang, *Theory of side-chain liquid crystal polymers: Bulk behavior and chain conformation*. Macromolecules, 2010. **43**(23): p. 10096-10106.
11. Lecommandoux, S., et al., *Are nematic side-on polymers totally extended? A SANS study*. Liquid crystals, 1997. **22**(5): p. 549-555.
12. Bates, F.S. and G. Fredrickson, *Block copolymers-designer soft materials*. Phys. Today. February 1999, 32, 2000. **38**.
13. Rubinstein, M. and R.H. Colby, *Polymer physics*. 2003, Oxford ; New York: Oxford University Press. xi, 440 p.
14. Hamley, I., et al., *Micellar ordering in concentrated solutions of di-and triblock copolymers in a slightly selective solvent*. Macromolecules, 1998. **31**(4): p. 1188-1196.
15. Lai, C., W.B. Russel, and R.A. Register, *Phase behavior of styrene-isoprene diblock copolymers in strongly selective solvents*. Macromolecules, 2002. **35**(3): p. 841-849.
16. Lodge, T.P., et al., *Phase behavior of block copolymers in a neutral solvent*. Macromolecules, 2003. **36**(3): p. 816-822.
17. Lodge, T.P., B. Pudil, and K.J. Hanley, *The full phase behavior for block copolymers in solvents of varying selectivity*. Macromolecules, 2002. **35**(12): p. 4707-4717.
18. Svensson, M., P. Alexandridis, and P. Linse, *Phase behavior and microstructure in binary block copolymer/selective solvent systems: Experiments and theory*. Macromolecules, 1999. **32**(3): p. 637-645.
19. Hori, H., O. Urakawa, and K. Adachi, *Dielectric relaxation in phase-segregated mixtures of polystyrene and liquid crystal 5CB*. Macromolecules, 2004. **37**(4): p. 1583-1590.
20. Scruggs, N.R., J.A. Kornfield, and J. Lal, *Using the "Switchable" Quality of Liquid Crystal Solvents To Mediate Segregation between Coil and Liquid Crystalline Polymers*. Macromolecules, 2006. **39**(11): p. 3921-3926.
21. Scruggs, N.R., et al., *Self-Assembly of Coil/Liquid-Crystalline Diblock Copolymers in a Liquid Crystal Solvent*. Macromolecules, 2008. **42**(1): p. 299-307.
22. Scruggs, N.R., *Coupling polymer thermodynamics and viscoelasticity to liquid crystalline order: self-assembly and relaxation dynamics of block copolymers in a nematic solvent*, 2007, California Institute of Technology.

23. Roe, R.-J. and R. Roe, *Methods of X-ray and neutron scattering in polymer science*. Vol. 130. 2000: Oxford University Press New York.
24. Higgins, J.S. and H. Benoît, *Polymers and neutron scattering*. 1994: Clarendon Press Oxford.
25. Wu, S.-T., et al., *Perdeuterated cyanobiphenyl liquid crystals for infrared applications*. Journal of applied physics, 2002. **92**(12): p. 7146-7148.
26. Zhuang, B. and Z.-G. Wang, *Anomalous Concentration Effects on Phase Behavior and Nematic Order in Mixtures of Side-Chain Liquid Crystal Polymers and Low-Molecular-Weight Liquid Crystals*. Macromolecules, 2012. **45**(15): p. 6220-6229.
27. Verduzco, R., *Self-assembled liquid crystal polymer gels*, 2007, California Institute of Technology.
28. Kempe, M.D., *Rheology and dynamics of side-group liquid crystalline polymers in nematic solvents*, 2004, California Institute of Technology.
29. Schmatz, W., et al., *Neutron small-angle scattering: experimental techniques and applications*. Journal of Applied Crystallography, 1974. **7**(2): p. 96-116.
30. Schneider, C.A., W.S. Rasband, and K.W. Eliceiri, *NIH Image to ImageJ: 25 years of image analysis*. Nat Methods, 2012. **9**(7): p. 671-675.
31. Ziegler, J. and N. Nichols, *Optimum settings for automatic controllers*. trans. ASME, 1942. **64**(11).
32. Glinka, C., et al., *The 30 m small-angle neutron scattering instruments at the National Institute of Standards and Technology*. Journal of applied crystallography, 1998. **31**(3): p. 430-445.
33. Kline, S.R., *Reduction and analysis of SANS and USANS data using IGOR Pro*. Journal of applied crystallography, 2006. **39**(6): p. 895-900.
34. Hammouda, B., D. Ho, and S. Kline, *SANS from poly (ethylene oxide)/water systems*. Macromolecules, 2002. **35**(22): p. 8578-8585.
35. Hammouda, B., D.L. Ho, and S. Kline, *Insight into clustering in poly (ethylene oxide) solutions*. Macromolecules, 2004. **37**(18): p. 6932-6937.
36. Pereira, F.V., A.A. Merlo, and N.P. da Silveira, *Behaviour of mesogenic side group polyacrylates in dilute and semidilute regime*. polymer, 2002. **43**(14): p. 3901-3908.
37. Viertler, K., et al., *Macromolecular anisotropic association in isotropic solutions of a liquid crystal side chain polymer*. Macromolecular Chemistry and Physics, 2001. **202**(16): p. 3174-3179.
38. Zhao, Y., et al., *Conformation of comb-like liquid crystal polymers in isotropic solution probed by small-angle neutron scattering*. Journal of Polymer Science Part B: Polymer Physics, 2006. **44**(17): p. 2412-2424.
39. Hammouda, B., *SANS from homogeneous polymer mixtures: a unified overview*, in *Polymer Characteristics*. 1993, Springer. p. 87-133.
40. Park, S.Y., et al., *Self-Assembly of dPS-Liquid Crystalline Diblock Copolymer in a Nematic Liquid Crystal Solvent*. Macromolecules, 2012. **45**(15): p. 6168-6175.
41. Fetters, L., et al., *Connection between polymer molecular weight, density, chain dimensions, and melt viscoelastic properties*. Macromolecules, 1994. **27**(17): p. 4639-4647.
42. Hule, R.A., et al., *Correlations between structure, material properties and bioproperties in self-assembled β -hairpin peptide hydrogels*. Faraday discussions, 2008. **139**: p. 251-264.
43. Hule, R.A., et al., *Dependence of self-assembled peptide hydrogel network structure on local fibril nanostructure*. Macromolecules, 2009. **42**(18): p. 7137-7145.
44. Beaucage, G., *Approximations leading to a unified exponential/power-law approach to small-angle scattering*. Journal of Applied Crystallography, 1995. **28**(6): p. 717-728.

Chapter 5

Self-Assembly of Complementary Telechelic Polymers in Various Solvents: A Small Angle Neutron Scattering Study

The synthetic methodology for the polymers discussed in this chapter was developed by Dr. Jeremy Wei during his time in the Kornfield. The polymers were synthesized by Dr. Jeremy Wei and Boyu Li between January and April of 2013. Boyu Li assisted with the SANS experiments performed at Oak Ridge National Laboratory.

5.1 Introduction

High molecular weight (M_w) polymers can have dramatic effects on the rheological properties of a fluid, even at low concentrations, such as reducing the drag in turbulent flow and suppressing misting. Drag reduction is the significant decrease in frictional losses under turbulent flow conditions such as pumping. The effect can be achieved by the addition of small quantities (as low as 0.02ppm[1]) of long chain polymers ($M_w > 10^3$ kg/mol) to a fluid. This has been used successfully to increase flow and reduce energy usage in the pumping of crude oil through pipelines[2]. The mechanism of the drag reduction is not completely understood but is thought to be related to an increase in elongational viscosity[3] due to the stretching of the polymer chains and the suppression of turbulent velocity fluctuations through elastic absorption and dissipation of the turbulence energy[4]. The addition of small amounts of polymer has also been used to control the spray atomization behavior of liquids in inkjet printing and similar applications. Fluid drop size is dependent on the behavior of the added polymer in elongational flow, observed in the formation of fluid jets and their subsequent break up.

The performance of polymers as anti-misting agents has been correlated to the increase of the extensional viscosity of the fluid[5], with the stretching polymer chains resisting extensional deformation. The drag reduction and mist suppression performance of a polymer is dependent on its M_w , with longer chains being more effective at the same concentration[6].

Reducing the flammability of aviation fuel is a key application of mist control polymers and has been the driver of this branch of research in the Kornfield laboratory. In this application the polymer concentration must be kept very low in order to be compatible with the operation of jet turbines. Linear polyisobutylene (PIB) of 5000 - 10000 kg/mol has been shown to be highly effective at suppressing the flammability of sprays of Jet-A (kerosene base commercial jet fuel) at concentrations as low as 50ppm[7]. Unfortunately, chains with $M_w > 10^3$ kg/mol undergo shear degradation in turbulent flows[8], with average M_w dropping along the length of a pipe during pumping[9]. Effective use of such polymers would require them to be added to the fuel right before use, an impractical solution.

Associative polymers (polymers that are able to form reversible non-covalent bonds between chains) provide a solution to the problem of shear degradation. The non-covalent bonds are broken in the turbulent flow during pumping, but are able to reform afterwards. Individual chains must be short enough to resist shear degradation ($M_w < 10^3$ kg/mol) and able to self-assemble into supramolecules (structures with high effective M_w composed of multiple polymer chains) with $M_w \geq 5 \times 10^3$ kg/mol to provide the desired mist-suppression effect. Ideally, a high fraction of the individual chains would become part of supramolecules, keeping overall polymer concentration low.

Linear polymer chains with hydrogen bonding functional groups (e.g. carboxylic acids) grafted randomly along the backbone were extensively studied as candidates for this application[7, 10]. The most promising early candidate was FM-9 (a proprietary polymer), which was studied extensively[11] but suffered from significant solubility problems in fuel due to the acrylic acid and methacrylate constituents of its backbone as well as the high (~5mol%) acid content. Early efforts in the Kornfield laboratory to improve on FM-9 focused on associative polymers with a similar molecular design (linear polymer backbone with randomly grafted carboxylic acid groups)[12]. These polymers were synthesized by the thiol-ene modification of polybutadiene[13], conferring precise control of the percentage of acid functionalization (equal to the 1,2 content of the polybutadiene pre-polymer) and good solubility in linear, cyclic, and aromatic hydrocarbons[14] of which Jet-A is composed[15].

The polybutadiene based, randomly grafted, self-associating polymers were shown to reversibly aggregate in solution, but did not have the desired mist-control effect[12]. It was concluded that chain collapse (due to intrachain pairing of associating groups) led to compact conformations that were not effective in mist control[12]. Attempts were made to overcome the problem of chain collapse through the use of complementary pair-wise associating groups consisting of a hydrogen donor (carboxylic acid) and a hydrogen acceptor (tertiary amine). These “charge assisted” hydrogen bonds are directional and significantly stronger than those between pairs of carboxylic acids[16]. A series of polybutadienes with tertiary amines grafted randomly along the backbone were prepared using the same thiol-ene approach used for the carboxylic acid polymers[13]. It was found that mixtures of the acid and amine functionalized polymers

aggregated into large clusters and had greater shear viscosity in solution than either the unmodified polybutadiene or the acid functionalized polymers alone[17]. Problematically, they were actually less effective in mist suppression than unmodified polybutadiene[17] due to the compact conformation of the supramolecules.

The failure of randomly grafted associating polymers inspired Dr. Ameri David to develop a statistical theory for the association of randomly functionalized and end-functionalized associating polymers in solution[18]. This theoretical work led to the conclusion that chain collapse was inherent to randomly grafted associating polymers and a new design was proposed, using telechelic (di-end-functional) polymers with associating groups clustered at both chain ends. The molecular design examined by the theory was a complementary associating system with each molecule having either A or B end groups which associate one-to-one and only with their complement (i.e. A to B). Theoretical predictions suggested that an equimolar mixture of A-A and B-B chains having $M_w \geq 500 \text{ kg/mol}$ and an A to B binding energy of $16kT$ could achieve a sufficient population of ultra-high molecular weight supramolecules to have significant mist suppression effects[18]. At the time, the synthesis of hydrocarbon soluble telechelic polymers of sufficient molecular weight had not been achieved.

Extensive work by Jeremy Wei led to the development of a synthetic method for polymers that meet the criteria proposed by the theory[19]. Refining earlier work on the Ring opening metathesis polymerization of cyclooctadiene with a telechelic chain transfer agent[20] has allowed for the synthesis of quantitatively end-functionalized polymers with previously unachievable $M_w \geq 400 \text{ kg/mol}$ [19] (structure shown in Figure 5.3). The procedure allows for the synthesis of polymers with matched backbone lengths

capped on both ends with dendritic structures having the desired number (1-8) of functional groups (ester, carboxylic acid, or tertiary amine base) at each end.

Solutions of less than 1wt% of self-associating acid terminated polymers in Jet-A showed enhanced shear viscosity and improved mist suppression when compared to their ester counterparts. Mixtures of the acid and base polymers had even higher shear viscosity[19] indicative of the formation of larger supramolecules. Ester terminated polymers serve as the negative control, not participating in any hydrogen bonding. Carboxylic acid terminated polymers are self-associating, forming ordinary hydrogen bonds[16]. Mixtures of complementary acid and base polymers are able to form stronger associations by charge assisted hydrogen bonding, with the pKa difference between the carboxylic acid and tertiary amine leading to much greater hydrogen bond energy[21]. Rheological and mist control studies to determine the optimal molecular parameters are ongoing.

The structure of the supramolecules formed in solution is critical to the performance of associating polymers as mist control agents. Self-associating (acid functionalized) polymers can reversibly form a variety of structures in solution (Figure 5.1). Theoretical work has predicted that these consist of a mixture of loops and “flower-like micelles” (small associated core surrounded by loose, solvated corona) of varying aggregation number[22, 23]. Some of the chains have ends that are parts of different micelles, serving as “bridges” between them.

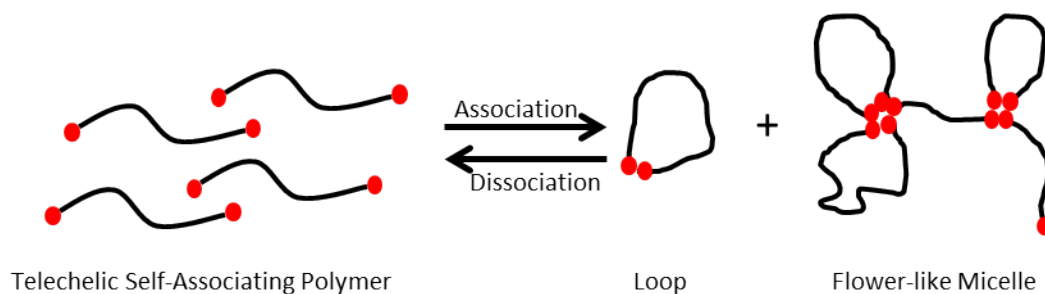


Figure 5.1: Schematic illustration of self-association between acid functionalized telechelic polymers. The individual chain-ends reversibly bind to other chain ends, resulting in a variety of structures with varying aggregation numbers.

Mixing two kinds of telechelic polymer chains (acid ended and base ended) allows for the formation of stronger, charge assisted hydrogen bonds between complementary polymer end groups (Figure 5.2). The significantly more energetically favorable pairwise associations will dominate the self-association between acid-groups and result in the formation of primarily linear and cyclic species.

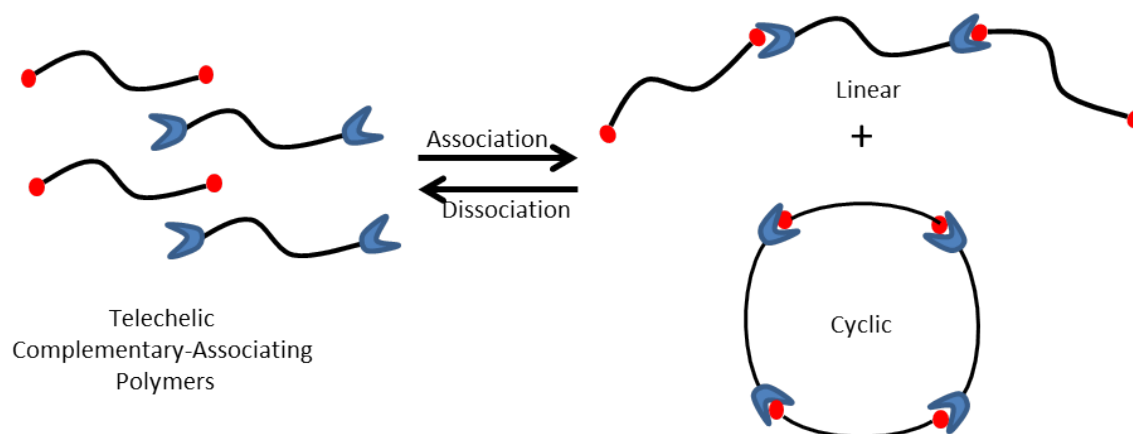


Figure 5.2: Schematic illustration of association between telechelic polymers functionalized with complementary functionalities (red circles and blue sockets). Taking the red circles to be acid groups, we also expect to see some of the structures shown in Figure 5.1.

For complementary associating polymers, theory predicts that increasing the molecular weight of the individual polymer chains favors the formation of linear

supramolecules[18]. Theoretical predictions for the extensional viscosity suggest that both linear and cyclic species will have a greater contribution to the extensional viscosity than the flower-like micelles formed by self-associating telechelics[24]. This is due to the fact that it is the overall length of the supramolecule that is vital, with the loops and “flower petals” in Figure 5.1 contributing minimally.

Experimental studies on solutions of telechelic associating polymers have focused on self-associating polymers with one of two molecular architectures: triblock copolymers (with a soluble center block and solvophobic end blocks)[24-28] and halato-telechelic polymers (having ionic groups at the end of a nonpolar chain, resulting in strong, nonspecific interactions)[29, 30]. Small angle neutron scattering has been used to study the supramolecular structures formed by telechelic triblocks with hydrophilic center blocks (PNIPAM[23] and PEG[31]) end capped by hydrophobic blocks. These were observed to form loose, flower-like micelles in dilute aqueous solution and form transient networks at higher concentrations.

To the best of our knowledge no studies have been conducted on long ($M_w > 100k$) telechelic polybutadienes with hydrogen bonding end groups in hydrocarbon solvents and there have been no reports on complementary associating telechelic polymers. Thus the actual nature of the supramolecules that these polymers form in solution is as of yet unknown. In the present study we report the results of the first SANS study of pairwise complementary associating long telechelic polymers in hydrocarbon solvents.

A homologous series of polymers with ester, acid or base end groups and polybutadiene backbones with M_w ranging from 76kg/mol to 430kg/mol[19] were examined. Since the primary targeted application is the suppression of misting in aviation

fuel, we studied low concentrations (<1wt%) of polymer in hydrocarbon solvents. Neutron scattering experiments require the use of deuterated solvents to achieve contrast and since deuterated Jet-A is not available, we use a range of deuterated single component solvents (cyclohexane, dodecane, and toluene) that are constituents of Jet-A[15]. Studies were also conducted in tetrahydrofuran which interferes with hydrogen bonds and reduces the association strength, easing the comparison between very strongly associating end-groups.

We provide neutron scattering evidence of large supramolecular structures formed by complementary associating polymers in several hydrocarbon solvents. It is determined that there is a significant difference between the aggregation in aliphatic and aromatic solvents. Using the sizes determined by light and neutron scattering we obtain accurate estimates for the overlap concentrations in a variety of solvents, which is lower than was initially estimated. Finally, a method is developed to estimate the aggregation number of the supramolecules even above the overlap concentration. The data in this study proves that SANS can be used to study very dilute solutions (<0.1wt%) of telechelic polymers in hydrocarbon solvents and paves the way for the systematic development of a relationship between the chemical architecture and supramolecular structure of pairwise complementary associating telechelic polymers.

5.2 Experimental

5.2.1 Materials

Deuterated solvents used for SANS experiments (dodecane-d₂₄, cyclohexane-d₁₂, toluene-d₈ and tetrahydrofuran-d₈) were purchased from Cambridge Isotope

Laboratories. Cylindrical quartz “banjo” cells used in scattering experiments were purchased from Hellma Analytics.

Polymers used for the experiments were end-functionalized model polybutadienes (Figure 5.3).

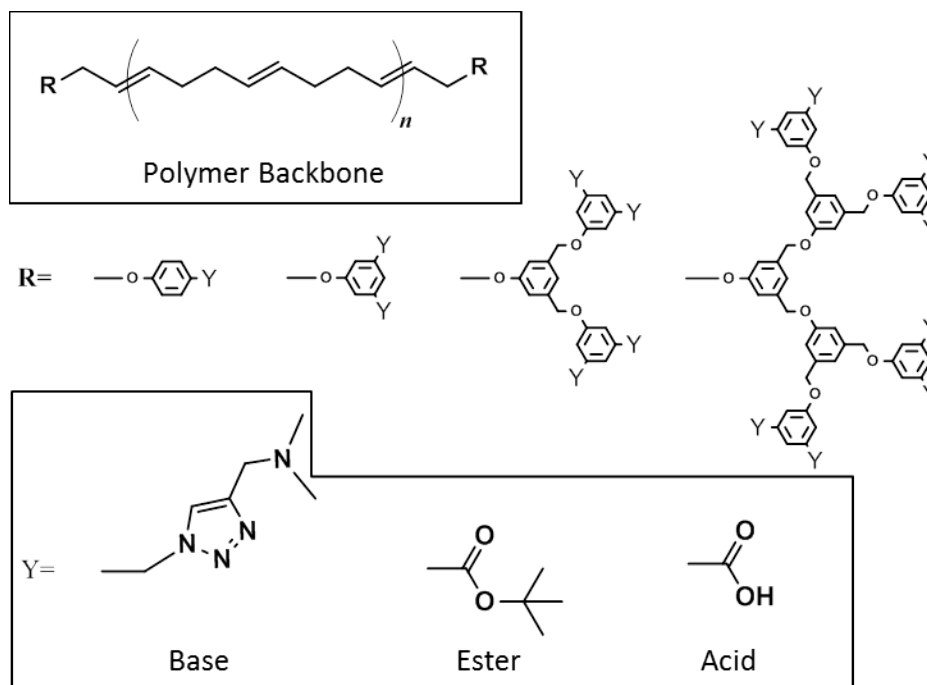


Figure 5.3: Structure of Telechelic Polymers. The upper box shows the polymer backbone with dendritic groups (middle) attached at both ends. For a given polymer, all of the Y groups on the dendritic end groups consist of one type of associating group from the bottom box.

The synthetic details are described in the PhD thesis of Jeremy Wei[19]. The polymers have dendritic end-group structure, allowing for different numbers of functionalities (1, 2, 4 or 8). The active end groups were either carboxylic acid donors or tertiary amine acceptors with a protected ester form of the carboxylic acid serving as the non-associative control. The amine and acid end-groups are able to form charge assisted hydrogen bonding pairs[16] with their opposite members (Figure 5.4).

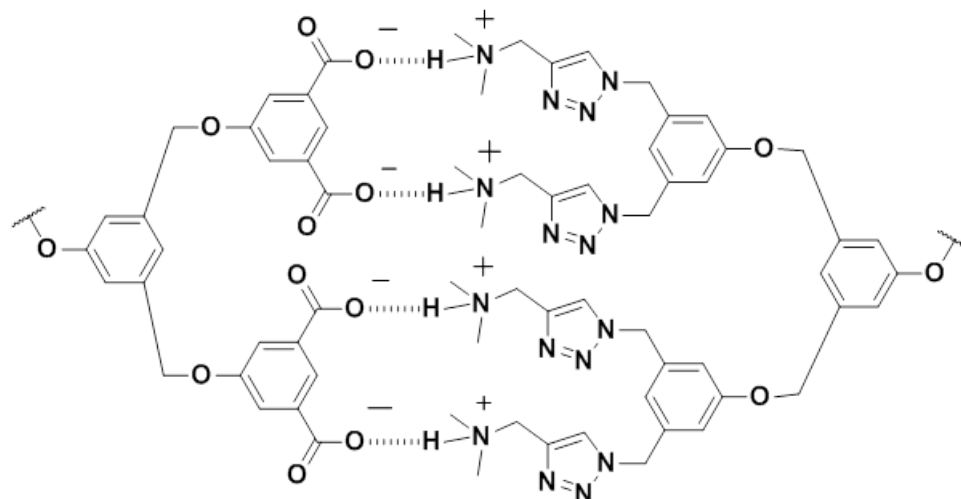


Figure 5.4: Schematic of hydrogen bonding interaction between a Tetra Acid end-group and a Tetra Amine end-group. This consists of four charge-assisted hydrogen bonds.

A series of polymers with a range of molecular weights and end-group types (Table 5.1) were used in our experiments.

Table 5.1: Characteristics of associating polymers from MALLS/GPC.

Polymer Name	End Group Type	Stickers (#/end)	Mw (kg/mol)	PDI
diTetraEster-100kPB	t-Bu Ester	0	76	1.8
diTetraAcid-100kPB	Acid	4	76	1.8
diTetraEster-200kPB	t-Bu Ester	0	230	1.5
diMonoAcid-200kPB	Acid	1	226	1.4
diTetraAcid-200kPB	Acid	4	230	1.5
diOctoAcid-200kPB	Acid	8	207	1.4
diTetraEster-300kPB	t-Bu Ester	0	303	1.4
diTetraAcid-300kPB	Acid	4	303	1.4
diTetraBase-300kPB	Amine	4	293	1.5
diTetraEster-400kPB	t-Bu Ester	0	430	1.5
diTetraAcid-400kPB	Acid	4	430	1.5
diTetraBase-400kPB	Amine	4	425	1.5

The naming of the polymers consists of describing the end-group type followed by the molecular weight of the polybutadiene backbone rounded to the nearest

100kg/mol. For example diTetraAcid-100kPB has four carboxylic acid functionalities at each end of the polymer and an approximately 100kg/mol molecular weight of the backbone.

5.2.2 MALLS/GPC

Polymer absolute molecular weight[32] and polydispersity (PDI) were obtained using Gel Permeation Chromatography with a Wyatt DAWN EOS multi angle laser light scattering detector in series with a Waters 410 differential refractometer. Separation was achieved using four Agilent PLgel columns connected in series (pore sizes 10^3 , 10^4 , 10^5 , and 10^6 Å) with degassed THF at 0.9mL/min as the mobile phase. Samples were prepared at 5mg/mL concentration in THF and filtered through a 0.45µm PTFE membrane syringe filter immediately before injection. Data was analyzed using Wyatt Astra Software (v5.3.4) with the Berry method[33, 34] used to obtain M_w and R_g .

5.2.3 Making Sample Solutions

Sample solutions for SANS were made using perdeuterated solvents (dodecane-d26, cyclohexane-d12, tetrahydrofuran-d8, and toluene-d8). Solutions of ester and base polymers were prepared by weighing out polymer on a Mettler precision balance (± 0.01 mg) into new glass scintillation vials with PTFE lined caps and adding the appropriate amount of solvent using a precision syringe ($\pm 1\%$). These were placed on a wrist action shaker at room temperature overnight. Sample solutions of acid polymers in Tetrahydrofuran (THF) were prepared in an identical manner. For solutions of acid polymers in dodecane, toluene, and cyclohexane, the polymer was weighed out into a new scintillation vial with septum cap and a stirbar was added. The vial was degassed by

pumping down to ~ 100 mTorr and refilling with argon three times. Previously degassed solvent was then added to the vial using syringe transfer. The vial was stirred overnight at 60°C , immersing the vial in an oil bath on a magnetic stir/heat plate (IKA RCT). The oxygen-free conditions prevent degradation of the polymer at elevated temperature. Mixed solutions of acid and base polymers were prepared by combining equal volumes of base polymer solutions and acid polymer solution in a new vial and subsequently placing the mixture on a wrist action shaker for at least 1 hour.

5.2.4 Small Angle Neutron Scattering at NIST and ORNL

Small Angle Neutron Scattering experiments were conducted at the National Institute of Standards and Technology (NIST) on beamline NG-3[35] and at Oak Ridge National Laboratory (ORNL) on beamline CG-2[36, 37] at the High Flux Isotope Reactor (HFIR). Samples were placed in Hellma quartz cylindrical cells with 2mm path length used at NIST (120-QS-2) and 5m path length used at ORNL (120-QS-5). Temperature was controlled by a recirculating water bath at NIST and by Peltier at ORNL. All scattering experiments were conducted at 25°C . 2D scattering patterns were taken for each sample using three detector distances (1.3 – 13m at NIST and 0.3 – 18.5m at ORNL) and associated configurations (see sections 3.2.4 and 3.2.5) with refractive lenses[38] used at NIST to extend the q -range. The overall scattering vector ranges were ($0.0015 < q(\text{\AA}^{-1}) < 0.4$) at NIST and ($0.002 < q(\text{\AA}^{-1}) < 0.8$) at ORNL, with the effective limits for a given sample determined by the signal to noise ratio.

The 2D scattering patterns were corrected for electronic noise, neutron background, detector sensitivity, and empty cell scattering. They were then normalized by the incident neutron flux and radially averaged resulting in absolute intensity $I(q)$.

Patterns for the three detector distances were combined using Igor PRO macros developed by Steve Kline[39] that were also used for subsequent processing and analysis. The solvent background scattering was subtracted from the data as described in section 3.2.4.

Data was analyzed using two scattering functions $I(q)$: the polymer excluded volume function[40] used for polymers with non-gaussian fractal scaling and the Beaucage function[41, 42] used for generalized fractal objects like particles and aggregates. The polymer excluded volume function has the form

$$I(q) = \frac{1}{\nu U^{1/2\nu}} \gamma\left(\frac{1}{2\nu}, U\right) - \frac{1}{\nu U^{1/\nu}} \gamma\left(\frac{1}{\nu}, U\right) \quad (5.1)$$

where $\gamma(x,U)$ is the incomplete gamma function and U is given by

$$U = \frac{1}{6} q^2 R_g^2 (2\nu + 1)(2\nu + 2) \quad (5.2)$$

and the parameters R_g and ν are the radius of gyration and the mass fractal scaling of the polymer coil.

The Beaucage function is an empirical function combining Guinier and Porod scattering[43] with the form

$$I(q) = Bkgd + G \exp\left(-\frac{q^2 R_g^2}{3}\right) + \frac{B \left[\operatorname{erf}\left(\frac{q R_g}{\sqrt{6}}\right) \right]^{3P}}{q^P} \quad (5.3)$$

where R_g is the radius of gyration of the scattering feature and P is the scattering exponent in the power law region with G and B being empirical scaling parameters.

5.3 Results

5.3.1 Solvent and Concentration Effects in Complementary Association

Small Angle Neutron Scattering patterns were acquired at NIST for 0.5wt% solutions of 400kPB polymers in dodecane (an alkane) and toluene (an aromatic), both components of Jet-A[15]. The four polymer samples were diTetraEster-400kPB, diTetraAcid-400kPB, diTetraBase-400kPB, and 1:1 mixture of diTetraAcid-400kPB and diTetraBase-400kPB. The eight radially averaged scattering curves are shown in Figure 5.5.

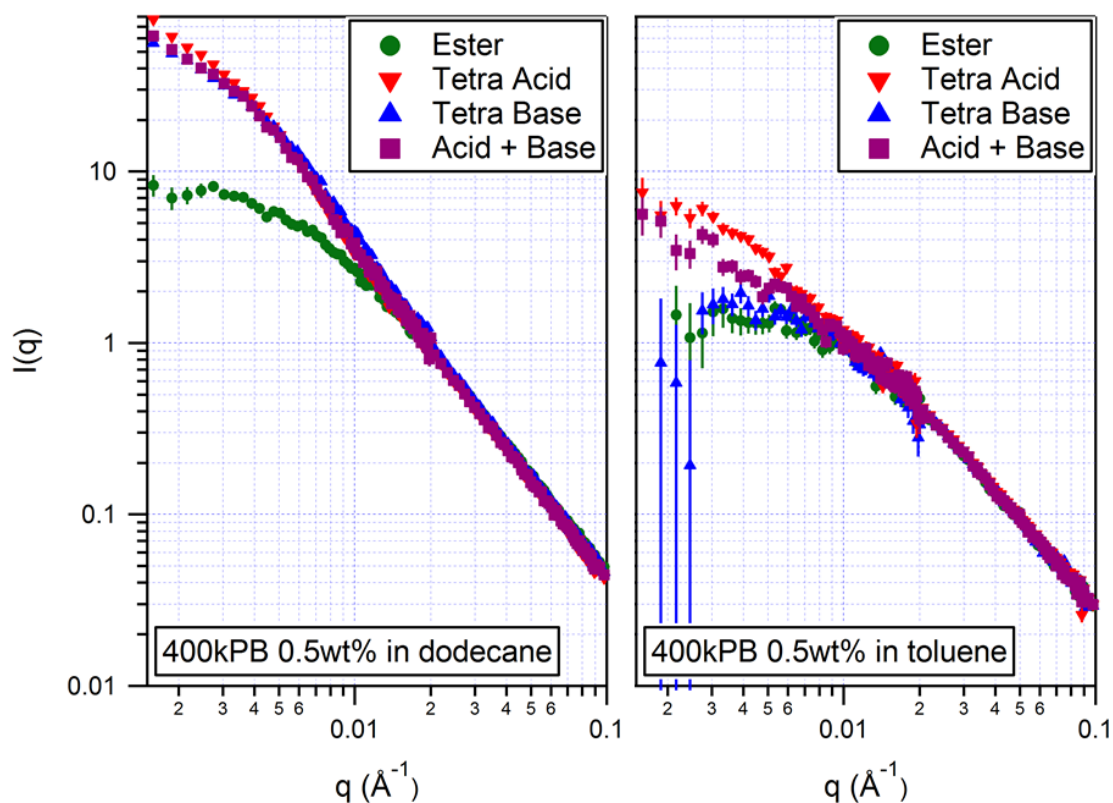


Figure 5.5: Radially averaged scattering patterns for polymers with 400kPB backbones in dodecane (left) and toluene (right) taken at NIST.

All of the scattering intensities follow a power law dependence $I(q) \sim q^{-m}$ for $q > 0.02 \text{ \AA}^{-1}$ with the scattering independent of the end-group type. This region of q space

corresponds to length scales on the order of 10nm or less and therefore the internal structure of the polymer coils. The power law scattering[43] corresponds to the mass fractal behavior of the polymer chains[44] $R_g \sim M_w^{\nu}$, where $\nu=1/m$ is the scaling exponent. In dodecane ν is 0.5 and in toluene ν is 0.6, consistent with theta and good solvent conditions respectively[44]. This result confirms that the conformation of the polymer chain at small and intermediate length scales is unperturbed by the presence of associating end-groups.

At lower q values the scattering curves split, with the scattering for the ester polymer reaching a plateau (q independent scattering) corresponding to the length scale of the entire structure[43]. In toluene the scattering for the base polymer is almost indistinguishable from that of the ester polymer, while the acid polymer and the acid/base mixture have higher intensity and no clearly delineated plateau region. In dodecane all of the scattering curves other than that corresponding to the ester have greatly enhanced low q intensity and no clearly delineated plateau region. The lack of a plateau region indicates that the size of the supramolecule is outside the range of the instrument. The polymer excluded volume function (section 5.2.6) was used to fit the scattering data for ester and base polymers and obtain radii of gyration (Table 5.2).

Table 5.2: Radii of gyration from polymer excluded volume fitting of scattering data for ester and base polymers in Figure 5.5.

Solvent	Rg (nm)	
	Ester	Tetra Base
Dodecane	21	64
Toluene	14	15

The R_g values in toluene are indistinguishable within the experimental uncertainty ($\pm 5\%$) while in dodecane the R_g determined for the base polymer is three times larger than that of the ester polymer. It should be noted that due to the lack of a clear plateau region in scattering from diTertBase-400kPB in dodecane, the measured R_g corresponds to a lower bound. From the scattering data it is clearly evident that all except the ester polymer associate into supramolecules in dodecane and that in toluene the self-association between base polymers is absent. The R_g values for diTertEster-400kPB in dodecane (21nm) and toluene (14nm) are smaller than reported in the literature for polybutadiene in good (35nm) and theta (25nm) solvents[45]. This indicates that the solutions were in the semidilute regime, with the dodecane samples being closer to dilute.

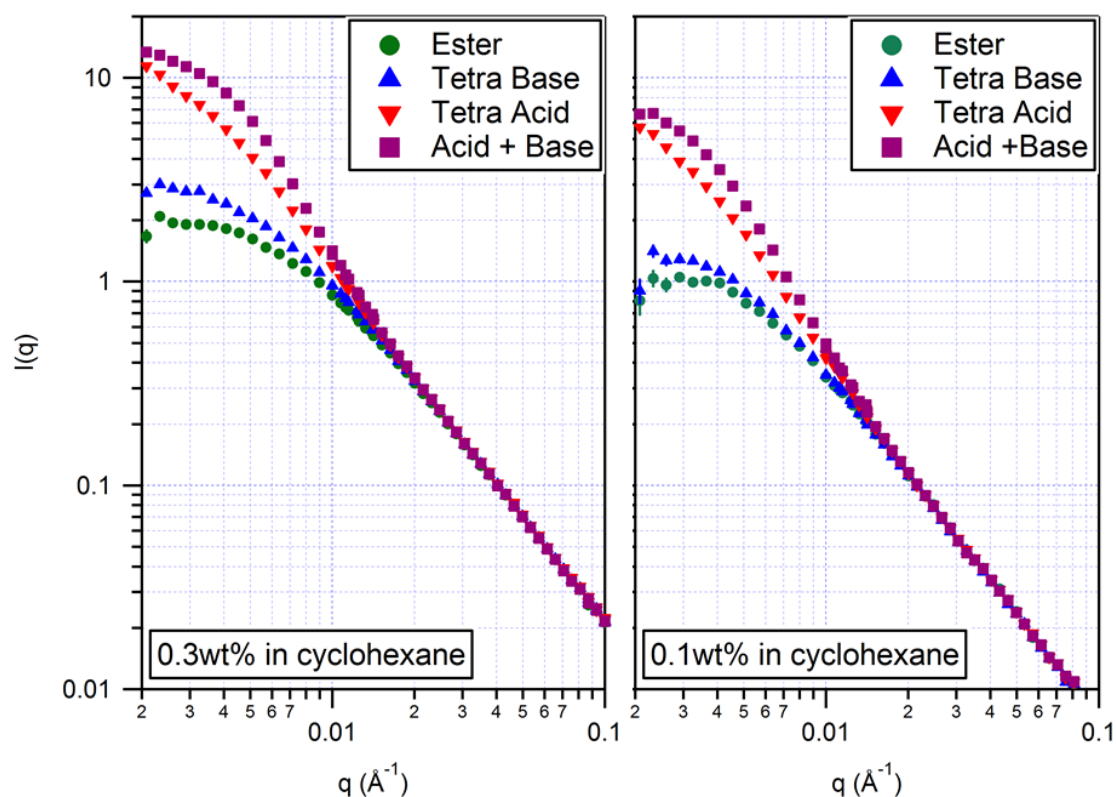


Figure 5.6: Radially averaged scattering patterns for polymers with 300kPB backbones in cyclohexane at 0.1wt% (right) and 0.3wt% (left) acquired at ORNL. Error bars are shown for all data points, falling within the symbol for most of the data shown.

Further SANS experiments were conducted at ORNL, this time using lower concentrations and a shorter backbone. Four polymer samples (diTertEster-300kPB, diTertBase-300kPB, diTertAcid-300kPB and a 1:1 mix of acid and base) were examined as 0.3wt% and 0.1wt% solutions in cyclohexane (Figure 5.6). Cyclohexane (another component of Jet-A[15]) was chosen for being an alkane, a good solvent for the polybutadiene backbone and readily available in deuterated form.

The scattering curves are qualitatively similar to those in Figure 5.5. The curves for all polymers overlap at high- q with power law scattering corresponding to good solvent scaling ($\nu=0.6$) as expected for cyclohexane[45]. The curves at 0.1wt% and 0.3wt% are very similar, showing plateaus for the ester and base polymers with the base polymer scattering plateauing at lower q (consistent with a larger size). No plateaus are observed for the acid polymer or the acid/base mixture. Interestingly, a “hump” is seen in the scattering for the mixed sample indicative of a scattering feature at $0.002\text{\AA}^{-1} < q < 0.01\text{\AA}^{-1}$ corresponding to additional structure with length scale on the order of 10nm. The scattering intensities for the acid polymer at both concentrations and for the acid/base mixture at 0.3wt% appear to still be increasing at the lowest available q , indicating the presence of supramolecular structures with sizes beyond the range of the instrument. The scattering from ester and base polymers was fitted with the polymer excluded volume function and the R_g values are reported in Table 5.3.

Table 5.3: Radii of gyration from polymer excluded volume fitting of SANS for ester and base polymers in Figure 5.6.

Conc	R _g (nm)	
	Ester	Tetra Base
0.1 wt%	28	36
0.3wt%	21	27

The R_g for the ester polymer is larger in the 0.1wt% solution, clearly indicating that the 3wt% solution is semi-dilute. The R_g for the ester polymer at 0.1wt% in cyclohexane is 28nm, which is equal to the infinite dilution R_g for a polybutadiene of 300kg/mol[45] confirming that the solution is dilute. The R_g values are larger for the base polymer at both concentrations and the ratio of size between base and ester are equal with the base 30% larger.

5.3.2 Association of Acid Polymers in THF

All of the scattering curves for acid polymers in hydrocarbon solvents (dodecane, toluene, and cyclohexane) had high low q intensity and no plateau at low q. Thus it was concluded that the self-association of acid polymers was sufficiently strong to result in supramolecules too large to be measured by SANS at all concentrations with both 300kPB and 400kPB backbones. In order to examine the self-association of acid functionalized polymers experiments were conducted in THF. The oxygen in THF is able to disrupt hydrogen bonding, reducing the strength of association and allowing the trends in the self-association of acid polymers to be studied using SANS.

Before beginning SANS experiments, the dilute solution R_g values for the ester polymers in THF were measured by light scattering. Using the MALLS/GPC online measurement technique described in Chapter 3, it was possible to obtain R_g(M_w) for a

broad range of molecular weights with just two polymers (diTertEster-300kPB and diTertEster-400kPB). The data is plotted in Figure 5.7.

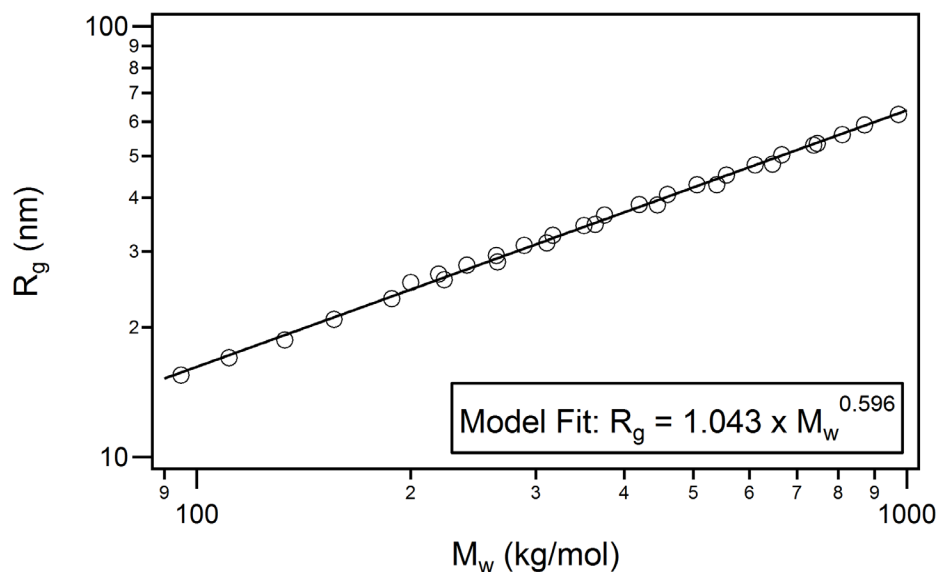


Figure 5.7: R_g as a function of molecular weight for polybutadiene in THF. Data (open circles) obtained from MALLS/GPC of diTetraEster-300kPB and diTetraEster-400kPB obtained as described in section 3.2.2. The solid line is a power law fit to the data with the result inset. The R^2 value is 0.998.

The resulting $R_g(M_w)$ shows simple power law behavior for the available range of $90 \leq M_w(\text{kg/mol}) \leq 1000$ appearing linear on the log-log plot. The linear fit is exceptionally good ($R^2 = 0.998$) and the resulting equation can be used to estimate the free radius of gyration in THF for all polymers used.

SANS patterns were obtained at ORNL for a series of backbone molecular weights of both diTetraAcid and diTetraEster polymers at 0.1wt% in THF. The resulting scattering curves are shown in Figure 5.8 for ester (left) and acid (right).

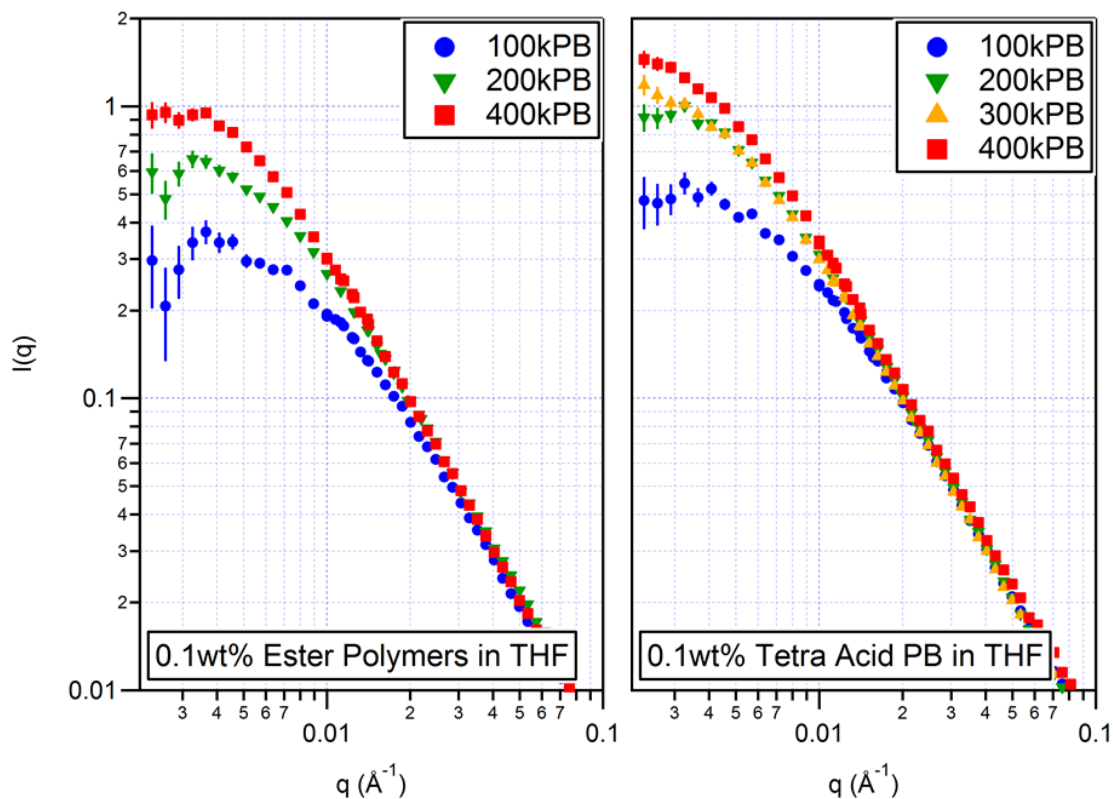


Figure 5.8: Radially averaged SANS patterns for 0.1wt% solutions of diTetraEster(left) and diTetraAcid(right) in THF taken at ORNL. Backbone molecular weights are varied from 100kPB to 400kPB.

All of the scattering curves overlap for $q > 0.03 \text{ \AA}^{-1}$ where the scattering has a power law dependence with $\nu = 0.6$ consistent with the scaling exponent from Figure 5.7. At lower q , the scattering curves reach plateaus of q -independent scattering. Curves for polymers with shorter backbones plateau earlier and have lower plateau intensity, consistent with their smaller size. The acid polymers have a systematically higher intensity at low q than their ester counterparts. This is consistent with larger sizes resulting from self-assembly into supramolecules.

Table 5.4: Radii of gyration from polymer excluded volume fitting of SANS (Figure 5.8) for varied molecular weights of ester and tetra acid polymers at 0.1wt% in THF.

End Group	R _g (nm)			
	100kPB	200kPB	300kPB	400kPB
Ester	15	23	-	32
Tetra Acid	18	29	32	39

The quantitative results confirm the presence of association by the systematic increase in apparent R_g going from the ester polymer to the corresponding acid polymer (Table 5.4). The R_g value for diTertEster-100kPB is approximately equal to that determined by light scattering (Figure 5.10), while those for the longer backbone polymers are smaller, indicating that only the shortest backbone polymer is in the dilute regime at 0.1wt% in THF.

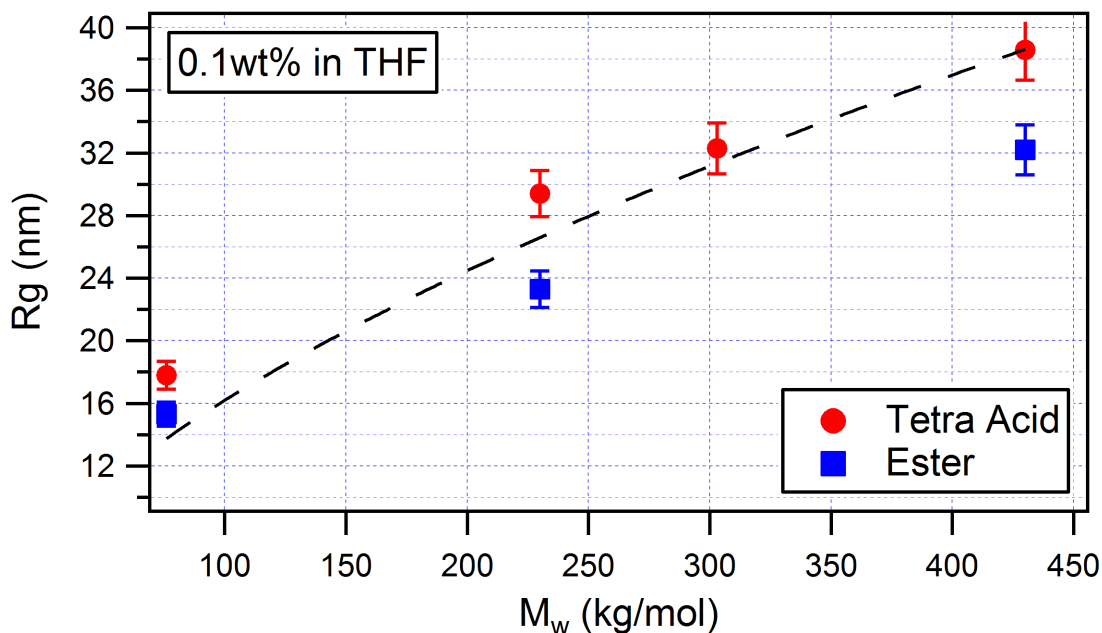


Figure 5.9: Radii of gyration as a function of backbone molecular weight for diTetraEster and diTetraAcid polymers at 0.1wt% in THF. The data points are obtained by fitting the polymer excluded volume function to the scattering curves in Figure 5.8. The dashed line is the model R_g(M_w) relationship obtained by fitting a power law to the MALLS data in Figure 5.7.

SANS patterns were obtained at ORNL for a series of 200kPB backbone polymers at 0.1wt% in THF, varying the number of acid groups at the polymer ends. The four polymers studied were diMonoAcid-200kPB (1 sticker at each end), diTetraAcid (4 stickers at each end), diOctaAcid (8 stickers at each end), and diTetraEster (0 stickers). The resulting radially averaged scattering patterns are shown in Figure 5.10.

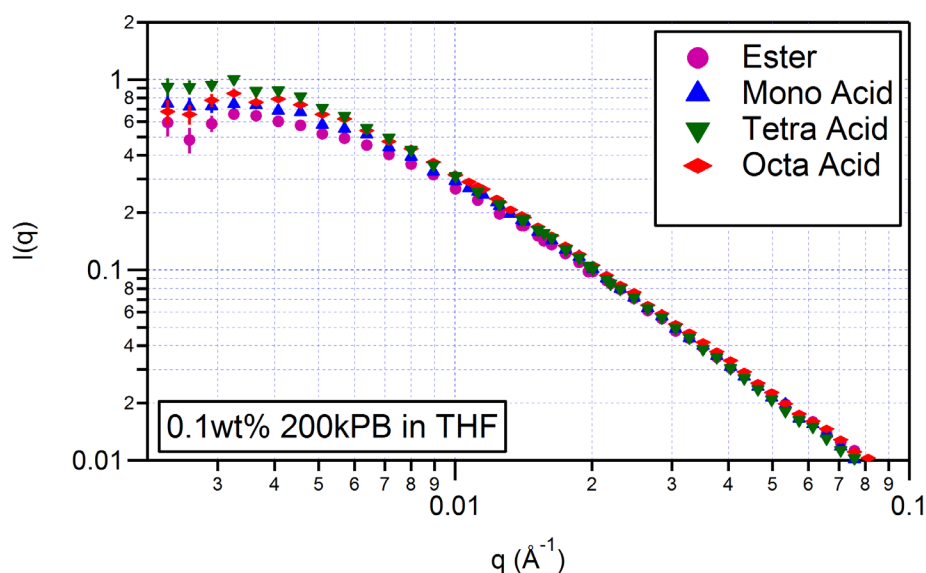


Figure 5.10: Radially averaged SANS patterns (taken at ORNL) for 0.1wt% 200kPB polymers in THF. The number of acid groups at each chain end is varied from zero to eight.

The strength of association can be estimated by the low q intensity (corresponding to aggregation number). By this measure it is evident that the strength of association goes as: Ester < Mono < Octa < Tetra. This is confirmed by the R_g values (Table 5.5).

Table 5.5: Radii of gyration from polymer excluded volume fit to SANS patterns (Figure 5.10) of 200kPB backbone polymers with varied number of acid groups at 0.1wt% in THF.

End Group	Ester	Mono Acid	Tetra Acid	Octo Acid
# stickers	0	1	4	8
R_g (nm)	23	23	29	26

The R_g values follow a similar trend with Ester~Mono<Octa<Tetra. The scattering data indicates that diTetraAcid is the optimum configuration for maximizing aggregation. Whether this extends to the behavior in hydrocarbon solvents remains to be determined.

5.4 Discussion

5.4.1 Qualitative Trends in SANS

The scattering intensity for a solution of particles, polymer coils, or supramolecules becomes independent of q at very low q values with asymptotic intensity $I(q_0)$ [43]. This I_0 is proportional to the concentration and the mass of the objects, with the value of q_0 inversely proportional to the overall size. For some of the SANS patterns presented in this work, there is plateau at low q and I_0 is known. For SANS patterns such as those for diTetraBase-400kPB, diTetraAcid-400kPB, and their mixture in dodecane (Figure 5.5, left), the intensity is still increasing at the lowest q and thus I_0 cannot be determined. We can, however, make some qualitative observations based on the value and slope of $I(q)$ at the lowest available q .

Considering the samples in dodecane we observe that the acid polymer has both the highest intensity and the steepest slope at low q , with the base obviously beginning to plateau and the mixture falling between the two pure component results. From this we can conclude that it is likely that diTetraAcid-400kPB forms the largest supramolecules in dodecane followed by the complementary mixture, with diTetraBase-400kPB forming the smallest supramolecules. Rheological studies of the same polymers in Jet-A showed that the complementary acid/base mixture has the highest viscosity followed by the acid polymer with base having the lowest viscosity[19]. The discrepancy may be due to the topology of the supramolecules formed by the different modes of association. Although

the self-associating diTetraAcid-400kPB appears to form the largest aggregates, these aggregates may consist of more clusters and flowerlike micelles and less linear components that result from the complementary association between diTetraAcid-400kPB and diTetraBase-400kPB. This difference in the relative population of supramolecules is consistent with theoretical predictions[18] and with the observed rheological trend (long linear structures contribute more to the viscosity).

Similar analysis of SANS patterns for 300kPB backbone polymers in cyclohexane (Figure 5.6) reveals the same trend of sizes. Although the intensity at lowest available q is highest for the mixture, the slope corresponding to $I(q)$ for diTetraAcid-300kPB is significantly steeper. We hypothesize that the intensity for the mixed sample is driven up in the available q -range by the presence of supramolecules of a moderate size with a plateau likely to occur at q values only moderately smaller than those available. In contrast, $I(q)$ for the self-associating acid polymer shows a steadily rising intensity that is likely to overtake the intensity of the mixture sample and plateau at a lower q_0 with higher I_0 . In cyclohexane diTertBase-300kPB shows much weaker association than diTertAcid-300kPB and has a plateau that is within the experimental range.

Based on the scattering data we conclude it is likely that the self-association of polymers with acid end-groups leads to larger supramolecular structures than complementary association of acid and base terminated polymers. However, the viscosity of the mixed samples is higher than that of the acid alone, suggesting that the supramolecules formed by complementary association are more expanded (with higher fraction of linear structures) than those formed by self-association. Confirmation of these

hypotheses will require further experiments (with greater instrumental range) to determine the actual sizes of supramolecular structures.

5.4.2 Estimation of Overlap Concentrations and Supramolecule Size

In order to put the SANS results in context, it is useful to determine whether a particular sample was above the overlap concentration. For a sample of volume V , the overlap concentration[44] is defined by the condition $V = V_{coil} \times N_{coils}$ where the subscripted properties refer to individual polymer coils. The overlap concentration C^* can be obtained from the expression:

$$C^*(wt\%) = \frac{m_{polymer}}{V \times \rho_{solvent}} = \frac{M_w \times 10^4}{V_{coil} \times N_A \times \rho_{solvent}} = \frac{M_w \times 10^4}{(4\pi/3)R_{e-e}^3 \times N_A \times \rho_{solvent}} \quad (5.4)$$

Where $m_{polymer}$ is the mass of polymer in the sample, $\rho_{solvent}$ is the solvent density, M_w is the molecular weight of the polymer, N_A is Avogadro's number, and R_{e-e} is the end-to-end distance of the polymer chain. While the end-to-end distance is not a directly measurable quantity, it can be estimated from the R_g using the relationship $R_{e-e} = \sqrt{3}R_g$ derived for an ideal polymer chain[44]. Taking the units of $\rho_{solvent}$ (g/mL), M_w (kg/mol) and R_g (nm) as well as the values of relevant constants into account, results in the following approximate expression:

$$C^*(wt\%) \cong 7.629 \frac{M_w}{R_g^3 \times \rho_{solvent}} \quad (5.5)$$

For polybutadiene in THF we can get the R_g using our experimental results (Figure 5.7) and for polybutadiene in cyclohexane, data is available in the literature[45]. R_g data in dodecane was not readily available, but results for dioxane[45], another theta solvent, can

be used as an estimate. Plugging this data into equation 5.5 for the molecular weights used gives the estimates shown in Table 5.6.

Table 5.6: Estimated overlap concentrations for PB in various deuterated solvents.

Polymer Backbone	Overlap Concentration (wt%)		
	cyclohexane	THF	dodecane
100kPB	0.37	0.23	0.59
200kPB	0.15	0.10	0.34
300kPB	0.12	0.08	0.30
400kPB	0.09	0.06	0.25

The estimated overlap concentrations confirm that diTertEster-300kPB is below the C^* in cyclohexane at 0.1wt%, but above it at 0.3wt%. All but the shortest backbone polymers are above the overlap concentration in THF at 0.1wt% and at 0.5wt% the 400kPB polymers tested in dodecane and toluene are definitely in the semi-dilute regime. C^* is inversely proportional to molecular weight and association into supramolecules can result in a dilute sample of individual chains moving into the semi-dilute regime. This effect makes determining the size of the supramolecules at experimentally accessible concentrations difficult. It is also not immediately obvious how to determine whether an observed R_g for an associating sample (e.g. diTertBase-300kPB at 0.1wt% in cyclohexane) is consistent with being in the semi-dilute regime.

Observing that the high q power law scattering is independent of the end-groups, we can reasonably assume that the scaling $R_g \sim M_w^{\nu}$ for the supramolecules is similar to that of their component polymers. Using this relationship, the M_w corresponding to the observed R_g can be calculated and equation 5.5 used to determine whether the sample is dilute ($C < C^*$). Subsequently we can estimate the approximate molecular weight of the

sample (corresponding to the average aggregation number N_{agg}). It is necessary to mention that this molecular weight ($M_{average}$) is not the molecular weight of the supramolecules but rather the average of all of the species present in solution, including the unassociated polymer chains. For samples determined to be in the dilute regime we can use the simple power law relationship to determine $M_{average}$. For those above C^* we can use the fact that the observed R_g (referred to as R_{SANS}) has the same relationship to the center-to-center distance between the coils as the actual R_g does to R_{e-e} , although it encompasses only part of the supramolecule. This assumes that the scaling for the supramolecules is the same as that for a linear polymer. Since they can be more compact this sets a lower bound on $M_{average}$ consistent with our data. The expression for this value can be derived by rearranging equation 5.5 into the form:

$$M_{average} \geq \frac{C \times R_{SANS}^3 \times \rho_{solvent}}{7.629} \quad (5.6)$$

Subsequently the average aggregation number for the system can be estimated by the formula: $N_{agg} = M_{average}/M_w$, where M_w is the molecular weight of the individual polymer chains. Testing this calculation for the ester samples returned $N_{agg} = 1$ confirming the validity of the approximations.

For the diTertAcid polymers at 0.1wt% in THF (Table 5.4) $N_{agg}=1.4$ for 100kPB, 200kPB and 300kPB. For 400kPB the aggregation number is larger with $N_{agg}=1.8$. The increase in aggregation with backbone molecular weight at a given concentration can be explained by the fact that the larger molecular weight polymer is further into the semi-dilute regime, with more overlap between the polymer coils increasing the likelihood of

associating groups from different coils finding each other. It is unclear why the aggregation numbers for all three shorter backbones are indistinguishable. It is possible that diTertAcid-400k represents an outlier and that the aggregation number does not depend strongly on M_w . It is also possible that this is a consequence of a change in balance between cyclic and linear supramolecules. The formation of linear supramolecules was theoretically determined to be favored by increasing M_w [18] and linear supramolecules are less compact with larger R_g . Thus the higher estimated N_{agg} could be a consequence of difference in topology rather than degree of association.

The trend in N_{agg} with the number of associating acid groups is also quite puzzling. Estimating N_{agg} from the results in Table 5.5 for the samples showing association it is observed that the aggregation number for diOctoAcid-200kPB ($N_{agg}=1.1$) is smaller than for diTetraAcid-200kPB ($N_{agg}=1.4$). Given the very strong association expected for the OctoAcid end-groups (8 hydrogen bonds) it is surprising that the aggregation number is lower than that of TetraAcid. We hypothesize that the poor solubility of the end-groups in THF, along with their strong association, leads to very compact aggregates, although further experiments are needed to test this hypothesis.

For samples in cyclohexane, it was possible to calculate N_{agg} for diTetraBase-300kPB at both 0.1wt% and 0.3wt% (Table 5.3). The supramolecules in samples with diTertAcid-300kPB were too large for R_g to be determined. As expected the aggregation number at 0.3wt% ($N_{agg}=2.1$) was larger than that at 0.1wt% ($N_{agg}=1.8$). The increase in association with concentration is in accord with theoretical predictions[18] for telechelic polymer association, although there is insufficient data for quantitative comparison.

5.4.3 Excess Scattering Due to Complementary Association

SANS patterns for a mixture of diTertAcid-300kPB and diTertBase-300kPB in cyclohexane (Figure 5.6) have “excess” scattering in the range $0.002\text{\AA}^{-1} < q < 0.02\text{\AA}^{-1}$, defined as the residual scattering from the mixed samples that remains after the average of scattering from the single component diTertAcid-300kPB and diTertBase-300kPB samples is subtracted. In other words it is the extra scattering due to pairwise association that is not present in the single component samples. This was calculated for both the 0.1wt% and 0.3wt% series of scattering patterns in Figure 5.6 and the resulting excess scattering is shown in Figure 5.11.

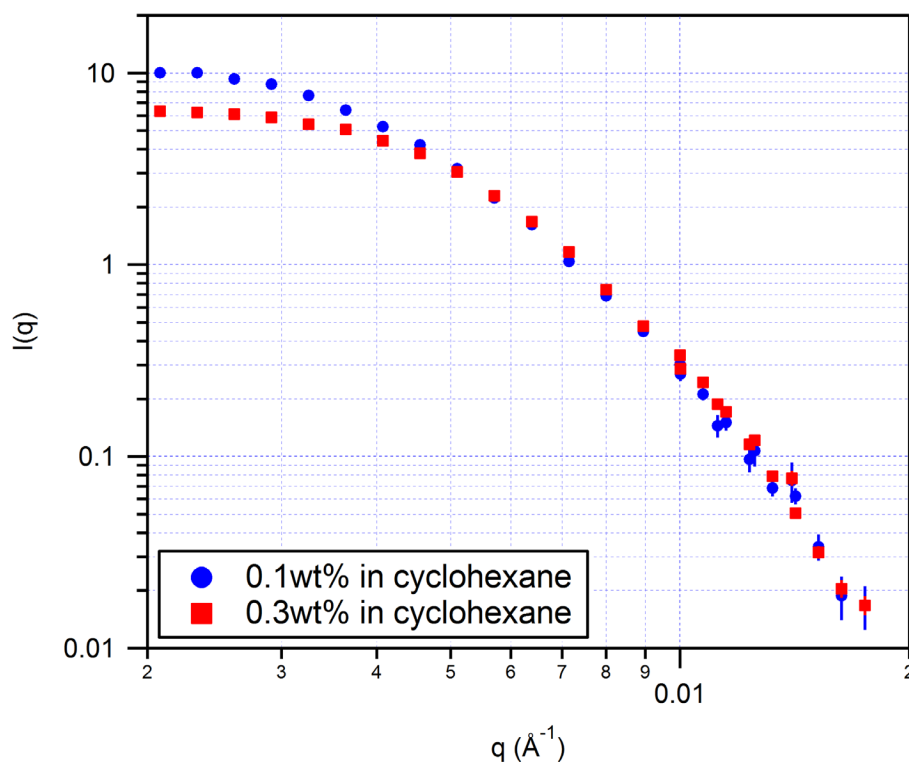


Figure 5.11: Excess scattering for mixture of diTetraAcid-300kPB and diTetraBase-300kPB in cyclohexane at 0.1wt% and 0.3wt%. This is calculated by averaging the scattering from the diTetraAcid-300kPB and diTetraBase-300kPB individually and subtracting the result from the scattering of the mixture. The intensity for the 0.1wt% solution is naturally lower due to the concentration and this multiplied by 3 to compensate.

The excess scattering has a plateau at low q and the intensity drops off very rapidly at higher q with approximate power law scaling $I(q) \sim q^{-5}$. At higher q the scattering for the mixed sample becomes indistinguishable from that of the individual components with no excess remaining. The shape of the scattering curve for the excess scattering is consistent with that of a generalized fractal object and scattering of this type has often been fit with the Beaucage empirical scattering function[41, 42]. Performing this fit we obtain R_g of 43nm and 35nm for the 0.1wt% and 0.3wt% solutions, respectively. Using the approach developed in the previous section we calculate aggregation numbers of 3.0 and 5.0 for the 0.1wt% and 0.3wt% solutions, respectively. The integer values obtained by this method are suggestive, although verifying the physical meaning of the aggregation numbers will require further work. We do believe that this approach enables the direct characterization of supramolecules formed by complementary association of telechelic polymers in organic solvent.

5.5 Conclusions and Suggested Future Experiments

Using SANS, we have successfully observed the formation of supramolecules in dilute and semi-dilute solutions of both self and complementary associating telechelic polymers. These studies were conducted in a variety of hydrocarbon solvents (dodecane, toluene, and cyclohexane) that are all constituents of Jet-A aviation fuel. It was observed that the choice of solvent has a significant effect on associative behavior with toluene (an aromatic solvent) disrupting the associative behavior of diTetraBase-400kPB. SANS in THF allowed the supramolecules formed by the self-association of acid ended polymers to be studied by reducing the strength of association and reducing the size of the resulting

supramolecules. In all scattering experiments, satisfactory signal-to-noise ratios were achieved at concentrations as low as 0.1wt%.

$R_g(M_w)$ was determined for the diTetraEster polymers in THF, which showed simple power law behavior. This information was used along with published $R_g(M_w)$ for polybutadiene in various solvents to estimate the overlap concentration C^* for the polymer and solvent combinations used in this work. Comparing the isolated coil R_g values to those determined by SANS confirmed the validity of the C^* calculations. A relationship was derived between the observed radius (R_{SANS}) and M_w for solutions above the overlap concentration, allowing for the aggregation number to be estimated.

N_{agg} for supramolecules formed by the complementary association of diTetraAcid-300kPB and diTetraBase-300kPB was calculated in cyclohexane both above and below the overlap concentration for the individual polymer chains. This was found to increase with the concentration, in agreement with theoretical predictions. The aggregation numbers in cyclohexane were found to be 3.0 and 5.0 for 0.1wt% and 0.3wt% polymer concentration respectively. Future work is needed to confirm the validity of the assumptions made in estimating N_{agg} but the method appears promising.

The studies reported in this chapter have laid the foundation for a series of planned experiments to explore the complementary associative behavior of long linear telechelic polymers. Given the limitations of available SANS instrumentation it was determined that the backbone lengths used in this study (driven by the application in mist control) led to supramolecules that were mostly too large to be directly measured. In order to get around this limitation a series of materials with TetraAcid and TetraBase end-groups will be synthesized with much shorter backbones (25-100k/mol). The

resulting decrease in the size of supramolecules with equal N_{agg} should allow for more systematic study of associative behavior. In order to compare the results from experiments using different backbone lengths, the concentration will be adjusted to be at the same relative ratio to C^* , using the equations derived to determine $C^*(M_w)$. Since the concentration corresponding to the same degree of overlap will be higher, this should also reduce the acquisition time, improving utilization of SANS beamtime.

Rheological experiments in pure hydrocarbon solvents (dodecane, toluene, cyclohexane, etc...) will be conducted in order to establish the connection between the supramolecular structure and the rheological properties. Using a mixture of linear, cyclic, and aromatic hydrocarbons should allow the trends observed in Jet-A to be replicated, creating an effective Jet-A analog. The resulting solvent mixture will be prepared in deuterated form and used for SANS experiments, studying the supramolecules formed in application relevant conditions. Detailed understanding of the dependence of supramolecular self-assembly on the structural properties of the constituent molecules and its correlation with rheological effects will enable more targeted design of polymer additives for mist control applications.

References

1. Oliver, D. and S. Bakhtiyarov, *Drag reduction in exceptionally dilute polymer solutions*. Journal of Non-Newtonian Fluid Mechanics, 1983. **12**(1): p. 113-118.
2. Burger, E., W. Munk, and H. Wahl, *Flow increase in the Trans Alaska Pipeline through use of a polymeric drag-reducing additive*. Journal of Petroleum Technology, 1982. **34**(2): p. 377-386.
3. Lumley, J., *Drag reduction in turbulent flow by polymer additives*. Journal of Polymer Science: Macromolecular Reviews, 1973. **7**(1): p. 263-290.
4. Ptasinski, P., et al., *Turbulent channel flow near maximum drag reduction: simulations, experiments and mechanisms*. Journal of Fluid Mechanics, 2003. **490**(1): p. 251-291.
5. Anna, S.L. and G.H. McKinley, *Elasto-capillary thinning and breakup of model elastic liquids*. Journal of Rheology, 2001. **45**: p. 115.

6. Liaw, G.C., J.L. Zakin, and G.K. Patterson, *Effects of molecular characteristics of polymers on drag reduction*. AIChE Journal, 1971. **17**(2): p. 391-397.
7. Chao, K., et al., *Antimisting action of polymeric additives in jet fuels*. AIChE journal, 1984. **30**(1): p. 111-120.
8. Ram, A. and A. Kadim, *Shear degradation of polymer solutions*. Journal of Applied Polymer Science, 1970. **14**(8): p. 2145-2156.
9. Brostow, W., *Drag reduction and mechanical degradation in polymer solutions in flow*. Polymer, 1983. **24**(5): p. 631-638.
10. Schulz, D. and J. Bock, *Synthesis and fluid properties of associating polymer systems*. Journal of Macromolecular Science—Chemistry, 1991. **28**(11-12): p. 1235-1243.
11. Peng, S. and R. Landel, *Rheological behavior of FM-9 solutions and correlation with flammability test results and interpretations*. Journal of Non-Newtonian Fluid Mechanics, 1983. **12**(1): p. 95-111.
12. David, R.A., et al., *Effects of pairwise, self-associating functional side groups on polymer solubility, solution viscosity, and mist control*. Macromolecules, 2009. **42**(4): p. 1380-1391.
13. David, R.A. and J.A. Kornfield, *Facile, efficient routes to diverse protected thiols and to their deprotection and addition to create functional polymers by thiol-ene coupling*. Macromolecules, 2008. **41**(4): p. 1151-1161.
14. Alessi, P., et al., *Solvent-polymer interactions in polybutadienes*. Macromolecules, 1993. **26**(23): p. 6175-6179.
15. Smith, B.L. and T.J. Bruno, *Application of a composition-explicit distillation curve metrology to mixtures of Jet-A and S-8*. Journal of Propulsion and Power, 2008. **24**(3): p. 618-623.
16. Gilli, G.G.a.P., *The Nature of the Hydrogen Bond: Outline of a Comprehensive Hydrogen Bond Theory*. 2009: Oxford University Press.
17. David, R., M.-H. Wei, and J.A. Kornfield, *Effects of pairwise, donor-acceptor functional groups on polymer solubility, solution viscosity and mist control*. Polymer, 2009. **50**(26): p. 6323-6330.
18. David, R.L.A., *Associative polymers as antimisting agents and other functional materials via thiol-ene coupling*, 2008, California Institute of Technology.
19. Wei, M.-H., *Synthesis and Potency of Long End-Associative Polymers for Mist Control*, 2013, California Institute of Technology.
20. Morita, T., et al., *A ring-opening metathesis polymerization (ROMP) approach to carboxyl- and amino-terminated telechelic poly (butadiene) s*. Macromolecules, 2000. **33**(17): p. 6621-6623.
21. Gilli, P., et al., *Predicting Hydrogen-Bond Strengths from Acid-Base Molecular Properties. The p K a Slide Rule: Toward the Solution of a Long-Lasting Problem*. Accounts of chemical research, 2008. **42**(1): p. 33-44.
22. Ermoshkin, A. and I. Erukhimovich, *Towards a statistical theory of associating telechelics: Equilibrium molecular structural distribution and one-cluster static scattering*. The Journal of chemical physics, 1999. **110**: p. 1781.
23. Koga, T., et al., *Theoretical modeling of associated structures in aqueous solutions of hydrophobically modified telechelic PNIPAM based on a neutron scattering study*. Macromolecules, 2008. **41**(23): p. 9413-9422.
24. Tripathi, A., K.C. Tam, and G.H. McKinley, *Rheology and dynamics of associative polymers in shear and extension: theory and experiments*. Macromolecules, 2006. **39**(5): p. 1981-1999.
25. Annable, T., et al., *The rheology of solutions of associating polymers: comparison of experimental behavior with transient network theory*. Journal of Rheology, 1993. **37**: p. 695.

26. Berret, J.-F., et al., *Nonlinear rheology of telechelic polymer networks*. Journal of Rheology, 2001. **45**: p. 477.
27. Hough, L. and H. Ou-Yang, *Viscoelasticity of aqueous telechelic poly (ethylene oxide) solutions: Relaxation and structure*. Physical Review E, 2006. **73**(3): p. 031802.
28. Meng, X.-X. and W.B. Russel, *Structure and size of spherical micelles of telechelic polymers*. Macromolecules, 2005. **38**(2): p. 593-600.
29. Bodycomb, J. and M. Hara, *Aggregation behavior of halato-telechelic ionomers in a low-polarity solvent*. Polymer Bulletin, 1988. **20**(5): p. 493-498.
30. Broze, G., R. Jerome, and P. Teyssie, *Halato-telechelic polymers. 4. Synthesis and dilute-solution behavior*. Macromolecules, 1982. **15**(3): p. 920-927.
31. Serero, Y., et al., *Associating polymers: from "flowers" to transient networks*. Physical review letters, 1998. **81**(25): p. 5584.
32. Wyatt, P.J., *Light scattering and the absolute characterization of macromolecules*. Analytica chimica acta, 1993. **272**(1): p. 1-40.
33. Andersson, M., B. Wittgren, and K.-G. Wahlund, *Accuracy in Multiangle Light Scattering Measurements for Molar Mass and Radius Estimations. Model Calculations and Experiments*. Analytical Chemistry, 2003. **75**(16): p. 4279-4291.
34. Berry, G., *Thermodynamic and Conformational Properties of Polystyrene. I. Light-Scattering Studies on Dilute Solutions of Linear Polystyrenes*. The Journal of Chemical Physics, 1966. **44**: p. 4550.
35. Glinka, C., et al., *The 30 m small-angle neutron scattering instruments at the National Institute of Standards and Technology*. Journal of applied crystallography, 1998. **31**(3): p. 430-445.
36. Berry, K.D., et al., *Characterization of the neutron detector upgrade to the GP-SANS and Bio-SANS instruments at HFIR*. Nuclear Instruments and Methods in Physics Research Section A: Accelerators, Spectrometers, Detectors and Associated Equipment, 2012. **693**(0): p. 179-185.
37. Wignall, G.D., et al., *The 40 m general purpose small-angle neutron scattering instrument at Oak Ridge National Laboratory*. Journal of Applied Crystallography, 2012. **45**(5): p. 990-998.
38. Choi, S.-M., et al., *Focusing cold neutrons with multiple biconcave lenses for small-angle neutron scattering*. Journal of applied crystallography, 2000. **33**(3): p. 793-796.
39. Kline, S.R., *Reduction and analysis of SANS and USANS data using IGOR Pro*. Journal of applied crystallography, 2006. **39**(6): p. 895-900.
40. Hammouda, B., *SANS from homogeneous polymer mixtures: a unified overview*, in *Polymer Characteristics*. 1993, Springer. p. 87-133.
41. Beaucage, G., *Approximations leading to a unified exponential/power-law approach to small-angle scattering*. Journal of Applied Crystallography, 1995. **28**(6): p. 717-728.
42. Beaucage, G., *Small-angle scattering from polymeric mass fractals of arbitrary mass-fractal dimension*. Journal of Applied Crystallography, 1996. **29**(2): p. 134-146.
43. Higgins, J.S. and H. Benoît, *Polymers and neutron scattering*. 1994: Clarendon Press Oxford.
44. Rubinstein, M. and R.H. Colby, *Polymer physics*. 2003, Oxford ; New York: Oxford University Press. xi, 440 p.
45. Fetters, L., et al., *Molecular weight dependence of hydrodynamic and thermodynamic properties for well-defined linear polymers in solution*. Journal of physical and chemical reference data, 1994. **23**(4): p. 619-640.

Appendix A

Theoretical Modeling of the Nucleation of Adhesion and Particle Envelopment in a Bio-mimetic Membrane

A.1 Introduction

Many biological processes that are of interest to researchers have stages mediated by interactions at the cellular membrane. Viral budding, an essential step in the infection cycle, requires the viral capsid to adhere to the cell membrane and open a channel in order to leave the cell. In order to exchange materials such as proteins and signaling molecules with other cells in its vicinity a cell must allow for endocytosis, a process by which a particle is engulfed at the membrane, to take place. These interactions are quite complicated and involve a host of processes occurring on a varying set of length and time scales and taking the form of both passive physical relaxations and actively mediated events. Of particular interest is the adhesion process that precedes any interaction between a cell and a particle, bringing the two objects within range of more sophisticated interactions. The study of cell adhesion is an area of active research in both the experimental[1] and theoretical arenas[2]. In particular the interaction of a cell with its local environment and the manipulation of these interactions through surface modification is the subject of ongoing investigation[3]. Additionally a whole host of biomimetic systems used for applications such as drug delivery and the manufacture of organic molecules rely on membrane surface adhesion.

Cellular membranes are composed of amphiphilic lipid molecules that come to-

gether in a thermodynamically driven self assembly process as well as various proteins that decorate the membrane and establish gates that regulate chemical exchange between the cell and its environment[4]. The physical and chemical properties of the membrane vary both spatially and temporally, requiring knowledge of the exact protein and lipid composition and arrangement for a complete description of the properties. The complexity of such a system makes it difficult to analyze theoretically and generally doesn't lend itself to exact analytic solutions. However, close agreement with experimental results has been achieved through the use of a simplified model, treating the membrane as a homogeneous self-assembled lipid bilayer vesicle. The static behavior of such vesicles in solution has been analyzed theoretically and experimentally and they have been found to possess a non-trivial shape space phase diagram with many locally stable free energy minima[5]. The thermodynamic aspects of vesicles undergoing adhesion interactions[6] and under the influence of pulling forces[7] have also been studied and reported. In general vesicles have proven to be a very rich system in spite of their simplicity and are useful for obtaining insight into the behavior of more sophisticated biological systems.

Recently, experiments performed on polymeric vesicles (polymersomes) demonstrated a time delay before the onset of the energetically favorable adhesion interaction[8, 9]. We hypothesize that this time delay is due to the adhesion proceeding by nucleation driven barrier crossing. Vesicles are self-assembled systems that undergo constant thermally driven fluctuations as energy is exchanged between the vesicle and its surrounding. The fluctuations in the energy of the system are manifested in the transient appearance of non equilibrium membrane shapes that explore the configuration space around the equilibrium arrangement and provide the mechanism by which the vesicle may cross barriers in

the free energy landscape between local minima. Since the energy of fluctuations is approximately Boltzmann distributed, the likelihood of such an event and therefore the rate at which it typically occurs would be proportional to the exponent of the negative magnitude of the barrier height. The existence of a free energy barrier to the adhesion process explains the time delay experimentally observed by Nam and Santore, and we believe that this barrier is due to the deformation that the membrane must undergo in order to wrap around the particle. This deformation has an associated energy penalty caused by the elastic nature of the membrane resisting deformation from its initial state. Such barriers and resulting time delays were theoretically shown to exist for a flat membrane undergoing a transition between the two wells of a phenomenological potential[10].

The purpose of the current work is to understand the impact of membrane deformation and the adhesion energy upon the free energy barriers present in the interaction between a vesicle membrane and a spherical particle. The proposed model for membrane adhesion indicates that a possible mechanism for the process is the nucleation of a deformed adhered state that spreads until an equilibrium wrapping extent is reached. Analysis of the free energy landscape indicates the existence of a locally stable point in the wrapping process, the location and depth of the minimum being determined by the adhesive strength and applied tension. The transition between these two states requires the crossing of a barrier, the magnitude of which would determine the natural timescale of the associated process.

By adopting a simple reductionist model of the membrane and particle system we have been able to study the nature of the meta-stable free energy minima present in the system and to analyze the necessary conditions for their existence. We have been able to quantify the barriers for both the adhesion and dehesion processes and to study their depen-

dence upon the binding strength and the tension applied to the membrane. Additionally, we have studied the influence of the separation between the membrane and the particle and showed that the barrier to adhesion grows rapidly with increasing separation while the dehesion barrier decreases leading to the existence of a critical separation beyond which the unsticking of the membrane is spontaneous.

We have also studied the effect that a pulling force applied to the particle has upon the process. These results show that increasing the pulling force diminishes the barrier to dehesion until at a critical value the barrier shrinks to zero and the membrane detachment becomes spontaneous.

A.2 Model and Methods

A.2.1 Description of the system

The primary focus of our study was understanding the interplay between the elastic nature of a lipid membrane and the specific adhesive interactions that occur on the surface. Since our emphasis was not on quantitative predictions of biological experiments, but on the fundamental scaling relationships between the relevant quantities, we chose to study a model system that would embody the behavior of interest without being unmanageably complex. The interaction between a cell and a typical particle involves a variety of length scales with typical cell diameters being on the order of $10\mu\text{m}$ and the range of the hydrogen bonding between ligands and receptors being on the order of nanometers. The typical colloid particle that such a membrane might interact with provides an intermediate length scale, the radius of the particle R_s . It is this length scale that corresponds to the extent of

deformation of the membrane upon adhesion, and both the surface contact energy and the elastic energy scale with it, making it the natural length scale for the interaction.

Two processes that involve a membrane interacting with a particle are viral budding and endocytosis, both active areas of research in biological physics[11, 12]. In both of the aforementioned processes R_s is much smaller than the radius of the cell, which would appear from the perspective of the particle to be nearly flat, allowing us to treat the membrane as being planar and of infinite extent (or connected to a reservoir of lipids). Since the particle is a sphere and there is no other object in the system that would break the symmetry, we treat the membrane as being axisymmetric. The adhesion interaction between the two objects was taken to be the typical specific ligand-receptor binding the strength of which depends on the nature of the ligands and receptors, the length of their attaching tethers, their surface density and the nature of the surface itself[13, 14]. The range of such interactions can be as short as 7nm[22], which is much smaller than the typical particle size for most relevant applications. In order to remove another degree of freedom and associated empirical parameter thereby increasing the generality of the calculation, we treat the limiting case where the range is zero. The adhesion interaction was taken to be a perfectly reversible contact potential characterized by energy per unit area w . A schematic drawing of the system is shown in figure A.1.

For the purposes of calculating the free energy, the membrane was taken to be an axisymmetric embedded 2D surface and the Monge representation[15] was used, allowing the system to be specified by a function $z(r)$, corresponding to the height of the membrane surface at a given radial position. The radial origin of the coordinate system was located at the centerline of the sphere to simplify the representation. The relative positions of the

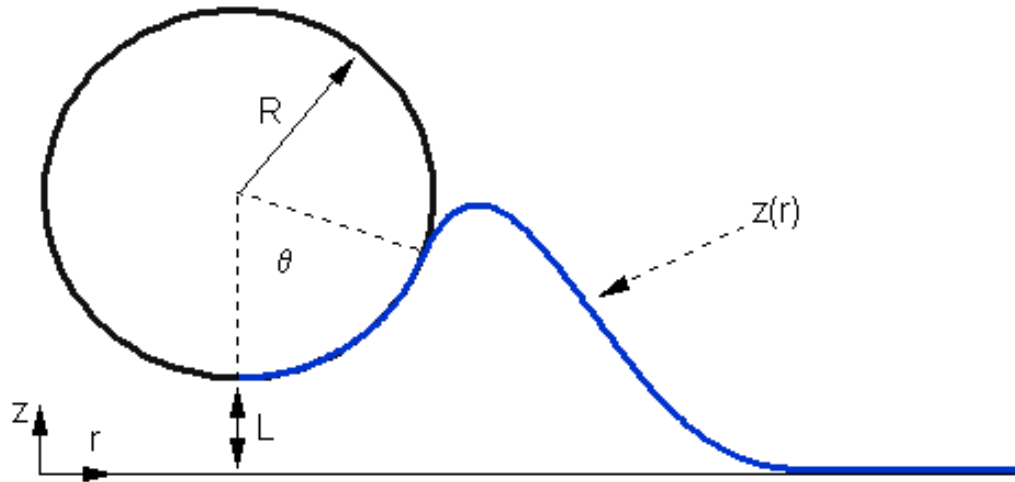


Figure A.1: Schematic of the system. It consists of a spherical particle of radius R_s separated from an initially flat axisymmetric membrane by a distance L . The membrane wraps around the particle starting at the most proximal point and extending up to a wrapping angle θ . The membrane profile is represented by a single valued function $z(r)$ that returns the membrane height at any given radial position.

particle and the membrane were characterized by a gap L , defined as the distance from the lowest point of the particle to the vertical position of the initially flat membrane ($z = 0$). This distance represents the minimum amplitude of distortion that the membrane must undergo in order to come into contact with the particle. The extent of adhesion was represented fully by an angle θ with the portion of the membrane from $r = 0$ to $r = R_s \sin \theta$ following the particle contour and the rest of the membrane remaining free. The cases where the wrapping angle is zero were treated by specifying the vertical position of the centerpoint of the membrane Z_m . Any accessible state of the membrane and particle system is uniquely determined by the function $z(r)$, the angle θ and the gap L (or the height of the membrane center Z_m). The free energy was calculated using the Helfrich curvature elasticity energy functional[16] that has been shown to be a reasonable representation of the free energy of a

vesicle membrane. The free energy is a functional of the local membrane height integrated over the surface of the membrane as shown in Equations 1 and 2. We evaluated this integral in two parts: the bound portion that follows the particle and has a surface contact energy contribution and the free portion which has only elastic contributions.

$$F(L, z(r), \theta) = \int_0^{R_m} \sigma + \frac{1}{2}\kappa(H - H_0)^2 + \bar{\kappa}K - w(r)dA \quad (1)$$

$$w(r < R^*) = w \quad \text{and} \quad w(r \geq R^*) = 0 \quad (2)$$

In Equation 1, H is the mean curvature and H_0 is the spontaneous bilayer curvature arising from the difference in the number of molecules in the inner and outer layers. This would be $\frac{1}{R_v}$ for a spherical vesicle of radius R_v and zero for a flat membrane where the layers are identical. The mean curvature H is defined as $H \equiv \nabla \cdot \hat{n}$ and has a simple form in the axisymmetric Monge representation as shown in Equation 3.

$$2H = \frac{\frac{d^2z}{dr^2}}{\left[1 + \left(\frac{dz}{dr}\right)^2\right]^{3/2}} + \frac{\frac{dz}{dr}}{\left[1 + \left(\frac{dz}{dr}\right)^2\right]^{1/2}} \quad (3)$$

K is the Gaussian curvature, which by the Gauss-Bonnet theorem depends only on the topological genus of a shape[17]. The deformations of the membrane are taken to occur in the elastic regime in which the membrane cannot tear and since no holes are created, the genus and therefore the Gaussian curvature are invariant throughout our studies. Since we are interested only in the relative values of the free energy, which is only ever defined relative to a reference state, for different configurations we can eliminate the additive con-

stant term in the free energy by setting $\bar{\kappa} = 0$. Since both the spontaneous and Gaussian curvature were shown to be invariant we can drop the relevant terms from the free energy, simplifying the expression.

The free energy functional contains several parameters that must be specified. These include: σ the tension conjugate to membrane surface area and corresponding to the chemical potential of a lipid reservoir, κ the bending rigidity of the membrane, and w the surface adhesion energy per unit area between the membrane and the particle. The natural energy scale for studying the system is the bending rigidity κ , a quantity that represents the energy of deformation, and the natural length scale is the sphere radius R_s . In order to simplify the calculations and make the results as general as possible, we scale our system by introducing the dimensionless variables: $\tilde{F} \equiv \frac{F}{\kappa}$, $\tilde{r} \equiv \frac{r}{R_s}$, $\tilde{z}(r) \equiv \frac{z(r)}{R_s}$, $\tilde{L} \equiv \frac{L}{R_s}$, $\tilde{\sigma} \equiv \frac{\sigma R_s^2}{\kappa}$, $\tilde{w} \equiv \frac{\sigma R_s^2}{w}$. In order to make things simpler we will drop the tilde from the scaled quantities and refer to them exclusively throughout the rest of the paper. Using these variables and our knowledge of the curvature at the surface of a sphere, the overall free energy for the system may be written in the simplified forms of Equations: 4,5 with the total free energy $F_{total} = F_{bound} + F_{free}$.

$$F_{bound}(L, z(r), \theta) = 2\pi \left[\sigma - w + \frac{1}{2} \right] \left(1 - \sqrt{1 - R_{bound}^2} \right) \quad (4)$$

$$F_{free}(L, z(r), \theta) = \int_{R_\infty}^{R_{bound}} dr 2\pi r \sqrt{1 + \left(\frac{dz}{dr} \right)^2} \left[\sigma + \frac{1}{2} H^2 \right] \quad (5)$$

The bound portion of the membrane follows the sphere surface and may be integrated over explicitly while the free portion depends on the membrane profile $z(r)$. The

transition between these two regimes occurs at $r = R_{bound}$ where $R_{bound} \equiv \sin \theta$ is the r coordinate of the highest point on the sphere that is wrapped by the membrane. In order to determine the membrane profile for a given set of parameters the free energy functional must be optimized with respect to the profile in order to obtain the stable or metastable membrane configurations. To evaluate the integral for the free portion, the membrane was taken to have a large but finite extent and the integration was carried out to this limit at which the membrane was taken to be asymptotically flat. The free energy functional of Equation 1 was further simplified by the use of the fact that the natural relaxation of the membrane is very fast as compared to the the time scale of the adhesion process and $\tau_{membrane} \ll \tau_{experiment}$. This implies that the interaction proceeds along the equilibrium path in shape space, with the membrane taking on the shape of minimal elastic free energy corresponding to the appropriate value of the reaction coordinate. This allows us to eliminate the membrane profile function from the functional, assuming that the system relaxes rapidly into a profile that minimizes the free energy. We then write the free energy as $F(L, \theta)$, a potentially multivalued (to account for multiple local minima) function of the sphere height and wrapping angle only. This free energy function and therefore the behavior of the system depends on parameters that correspond to easily adjusted experimental conditions. The tension can be varied in a micropipette aspiration experiment through the application of the appropriate suction force. The surface energy of adhesion can be adjusted by changing the ligand and receptor type and surface density. The overall surface interaction can be fine-tuned in a more sophisticated manner through the use of various tether lengths and mobilities of ligands and receptors as well as the introduction of polymeric surface proteins[14]. In order to do this however, we would be forced to adopt a

surface adhesion potential of a finite range and inherently more complicated character.

Another phenomenon of interest is that in which the particle is being pulled away from the membrane. This can be a model for a particle in a hydrodynamic flow or possibly for an active macroscale interaction. Pulling on the particle changes the free energy landscape and therefore the stability and lifetime of the wrapped membrane state. A force also impacts the barriers to transition between the shifted local minima and may in fact eliminate the meta-stable configuration. The effects of a pulling force may be incorporated into the free energy functional through the use of a Legendre transform with respect to the conjugate pair (L, f) and the introduction of a work term into the free energy. In essence this serves to transform the free energy from one that corresponds to a constant separation L to a conjugate one that corresponds to a constant force f shown in Equation 6.

$$G(L, z(r), \theta) = F(L, z(r), \theta) - zf \quad (6)$$

The introduction of a pulling force leads the membrane to deform and also changes the equilibrium bound state. A balance between the elastic and pulling forces leads to the existence of a unique equilibrium position z^* at which the new free energy is at a minimum and corresponding to the bound state defined by Equation 7.

$$\frac{\partial F(L, z(r), \theta)}{\partial z} = f \quad (7)$$

Unlike the force free situation, the bound state is never globally stable for any nonzero force. This is due to the presence of an infinitely deep overall energy minimum at infinite separation between the membrane and particle. While the divergence of the free

energy is unrealistic, it is reasonable to suppose that the acting range of whatever applies the force is greater than the range of membrane interactions and beyond the membrane elastic limit. Given sufficient time, the thermal fluctuation present in the system will lead to crossing of the barrier between the local minimum and the infinitely separated state and the membrane will detach from the particle. This will result in a relaxation of the membrane to its initial configuration and a rapid acceleration of the particle. The time required for this process to occur spontaneously defines the stability of the adhesion and decreases monotonically with increasing magnitude of the force.

A.2.2 Calculations

In order to study the membrane particle system at equilibrium, the stable membrane shape must be determined at a given extent of wrapping. We calculated these by minimizing the free energy functional of the free portion of the membrane (Eq 5) with respect to the shape as represented by a discrete function $z(r)$ represented by a vector \mathbf{z} . This was accomplished through numerical multivariate optimization using several well known algorithms[18][19]. The membrane profiles that corresponded to free energy minima in shape space were considered to be the values returned by the function $F(L, \theta)$ and were determined uniquely by the membrane-particle separation L , wrapping angle, and the imposed tension. It should be noted that the adhesion energy has no effect upon the free portion of the membrane at a given extent of wrapping. It affects the absolute stability of that wrapping angle and shifts the free energies of all shapes corresponding to the given θ by a constant value.

The adhesion process requires going from an initially flat membrane at a specified

distance L from the particle to a portion of the membrane wrapping around the particle with the portion of the membrane $r \rightarrow R_m$ remaining unperturbed. A natural reaction coordinate for this process is the extent of wrapping[20], in this case represented by the angle θ . The free energy space along the path was sampled by optimization of the shape function at progressively increasing values of the extent of wrapping mapping out the function $F(L, \theta)$. The membrane shape function obtained at a given angle was used as the initial guess for the subsequent angle, ensuring rapid convergence of the minimization algorithm and a smooth progression of membrane profiles.

The resulting free energy functions showed a non-monotonic dependence on the wrapping angle for separations below a critical value L^* . While there is always at least a meta-stable minimum at the unperturbed flat membrane state corresponding to $\theta = 0$, for separations that are less than L^* , there is also a stable, bound state with an extent of wrapping that is greater than zero. As the separation is increased past this point this configuration becomes meta-stable before vanishing at a sufficiently high value L^{**} . Because the system is undergoing constant thermal fluctuations, it can reversibly transition between the stable and meta-stable states. In order for this to occur, the system must proceed along a path with higher energy through a region of unfavorable extents of wrapping. In this region the membrane deformation dominates the favorable contribution of the adhesion and leads to a local maximum in the free energy. In order to undergo adhesion, the membrane must nucleate a distorted shape that corresponds to the extent of wrapping at this intermediate maximum. The extent of distortion required for this and therefore the free energy difference between this and initial state corresponds to a barrier for the process.

Figure A.2 shows a typical free energy curve for a system with local minima. Illus-

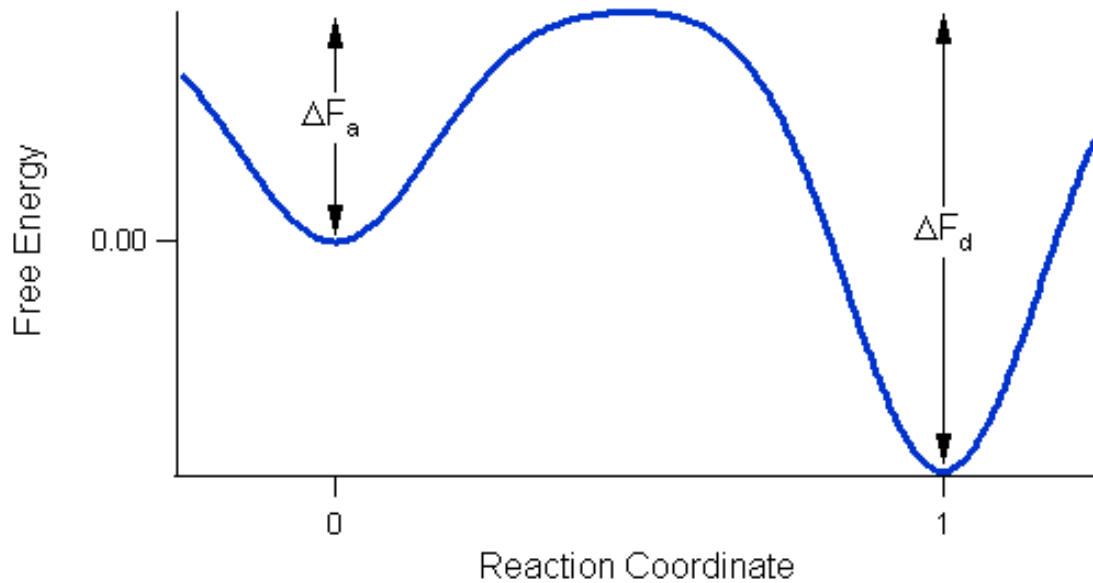


Figure A.2: Sketch of the free energy as a function of reaction extent for a process having two local minima along the reaction coordinate. In the system to be considered the initial metastable minimum at $R = 0$ represents the flat membrane, not contacting the particle. The global minimum is the equilibrium state in which the membrane wraps the particle to an equilibrium extent θ^* . In order to undergo the transition $r = 0 \rightarrow r = 1$ (adhesion process) a free energy of ΔF_a must be overcome. For the reverse (dehesion) process, a barrier of ΔF_d must be crossed. The relative stability of the two states depends on the value of L and the system parameters σ and w .

trated in this schematic are the essential features for a system that undergoes a transition between two states driven by thermal fluctuations. This diagram is remarkably similar to the free energy of a chemical reaction plotted with respect to the reaction coordinate, and it is this similarity that leads to the use of reaction terminology in describing the adhesion process taking the extent to which the membrane has wrapped the particle as the reaction coordinate. The system shown has both a globally stable minimum and a locally stable one separated in one-dimensional reaction coordinate space by a local energy maximum corresponding to a barrier. Assuming a properly defined reaction coordinate, the system is constrained to move continuously along the path shown and thus must go through the high energy state corresponding to the barrier. The differences in energy between the minima

and the unstable transition configuration correspond to the amount of energy that the system must acquire from the background by thermal fluctuations in order to undergo the process of adhesion or dehesion. Assuming that the system behaves thermodynamically, and using as a basis the Arrhenius model of reaction kinetics as well as the Bell[21] model, the time constants for such processes may be considered to scale exponentially with the barrier height. From this relationship, the thermodynamic information may be used to obtain some measure of insight into the expected dynamics of the process.

For a particle with a nonzero applied force, the appropriate free energy is the force explicit one G , but otherwise the methods of calculation of the free energy for a given system configuration are identical to the force free case. The overall free energy functional is changed by the addition of a force as is the path by which adhesion or dehesion proceeds. In the case of a system that is held at a chosen separation L the force is implicit and any given membrane configuration corresponds to a particular value of the force that would have to be exerted on the particle in order to keep the system in static equilibrium. Choosing a specific value of the force uniquely determines the equilibrium value of L , making it unreasonable to consider multiple values of the separation for a given force. Thus for a constant pulling force, the adhesion process takes place over a range of particle membrane separations. Assuming that the time scale of membrane relaxation τ_m is significantly less than that of the particle motion τ_p , we can consider the membrane to be at its equilibrium extent of wrapping for all separations L . This allows us to consider the free energy $G(L)$ with L being the natural reaction coordinate for the interaction. From this function, the relative free energies of the local minima and the height of the barrier can be obtained.

A.3 Results and Discussion

A.3.1 Equilibrium Free Energy and the Membrane-Particle Separation

In order to study the nature of the free energy landscape of the system, a phase diagram was constructed for a single set of values for the tension and adhesion energy taken to be consistent with reasonable experimental values. The data for the phase diagram was obtained by the minimization of the free energy functional with respect to the shape of the membrane for a range of membrane particle separations L . The resulting local free energy minima traces are shown in figure A.3.

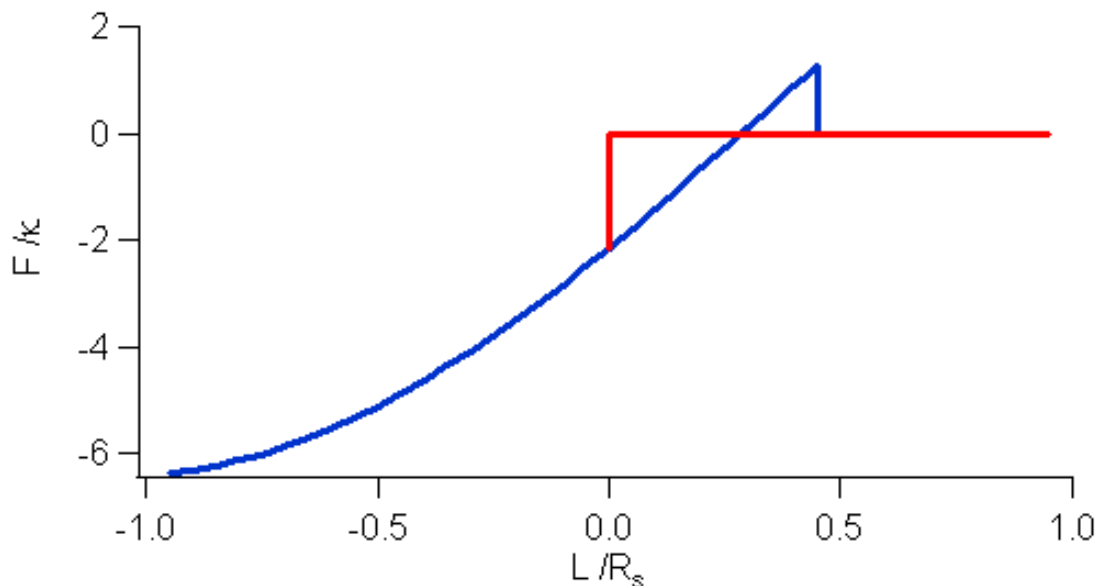


Figure A.3: Minimum free energy F as a function of the separation between the membrane and particle (L) at $\sigma = 3$ and $w = 5$. When $L > 0$ and $L \leq .45$ the flat membrane configuration (red) and the wrapped state (blue) are both local minima of the free energy functional. When L becomes zero the particle is below the initial position of the membrane and only the wrapped state is sensible. At separations greater than .45 the effect of the tension is too great for the surface binding energy to stabilize the wrapped state. In the intermediate region it is possible for the system to transition between the two configurations by thermally crossing the barriers ΔF_a (from flat to bound) or ΔF_d (from bound to flat). Upon further separation of the membrane and particle, the dehesion process becomes spontaneous and the adhesion impossible.

The phase diagram shows that for a range of separations that depends on the particular values of the system parameters (in this case $0 < L \leq 1.45$) there is more than one local minimum in the free energy. These local minima correspond to meta-stable configurations of the system with the two states having different extents of wrapping, with one generally corresponding to the initially flat membrane configuration and the other to a state at an equilibrium extent of wrapping. It is in this range of separations that interaction between the membrane and the particle is possible but is not certain. In this coexistence region both the flat and the wrapped configuration of the membrane are locally thermodynamically stable and the system may be found in either configuration, transitioning between the two by thermally driven barrier crossing. The region of coexistence is limited by the particle penetrating the membrane centerline at zero separation and therefore eliminating the possibility of a locally stable unbound membrane configuration. At high separations the coexistence region is limited by the fact that too great a membrane distortion is necessary to reach the particle. In this case the elastic contribution dominates the adhesive at all wrapping extents and the local minimum corresponding to a wrapped state vanishes. The separation L at which this occurs may be considered to be a critical value for interaction L^* , which may be thought of as the distance to which a particle must be brought from infinite separation in order to make an adhesive interaction possible. From figure A.3 it can be seen that the free energy of the bound state grows nearly linearly with increasing separation, with the absolute value of the energy of the wrapped state being lowered by bringing the membrane and particle closer together. This is true in this case because the particular values chosen for σ and w favor a finite extent of wrapping θ^* and the positive elastic contribution to the free energy is minimized by bringing the particle down until the membrane centerline is

close to the point at which the membrane separates from the sphere at the particular extent of wrapping. In a system with no external forces and in which the particle were allowed to move freely this would be the globally stable state to which the system would evolve. Since the goal of the current work is to understand the behavior of the membrane during transitions, our focus is states that are away from the global stationary point.

A.3.2 Effects of Tension and Contact Energy

Both the functional shape and the absolute value of the free energy functional are dependent upon the imposed tension and the surface contact energy. Since the evolution of the membrane shape and the wrapping angle are presumed to be sufficiently fast for the membrane to be at its equilibrium shape and extent of wrapping, we are interested in the function $F(L)$, a form of the free energy that has been minimized over both $\mathbf{z}(r)$ and θ . The equilibrium free energy of the wrapped state and the wrapping angle corresponding to this configuration, as well as their dependence upon w and σ , are shown in figure A.4. While the plots show a single value function, this is only a single branch of the phase diagram for any separation $L > 0$. In the case where the particle has not penetrated the membrane centerline, the state in which the membrane is flat and unattached to the particle is a local minimum of the free energy and is in fact the value to which the free energy curves are normalized. Thus the point at which the free energy curve crosses zero is also the transition from the regime where the wrapped state is favored to that where the separated configuration is favored.

It can be seen in figure A.4a that the increase in free energy is nearly linear with the separation L , growing with increasing separation until at a critical value L^* , the bound state

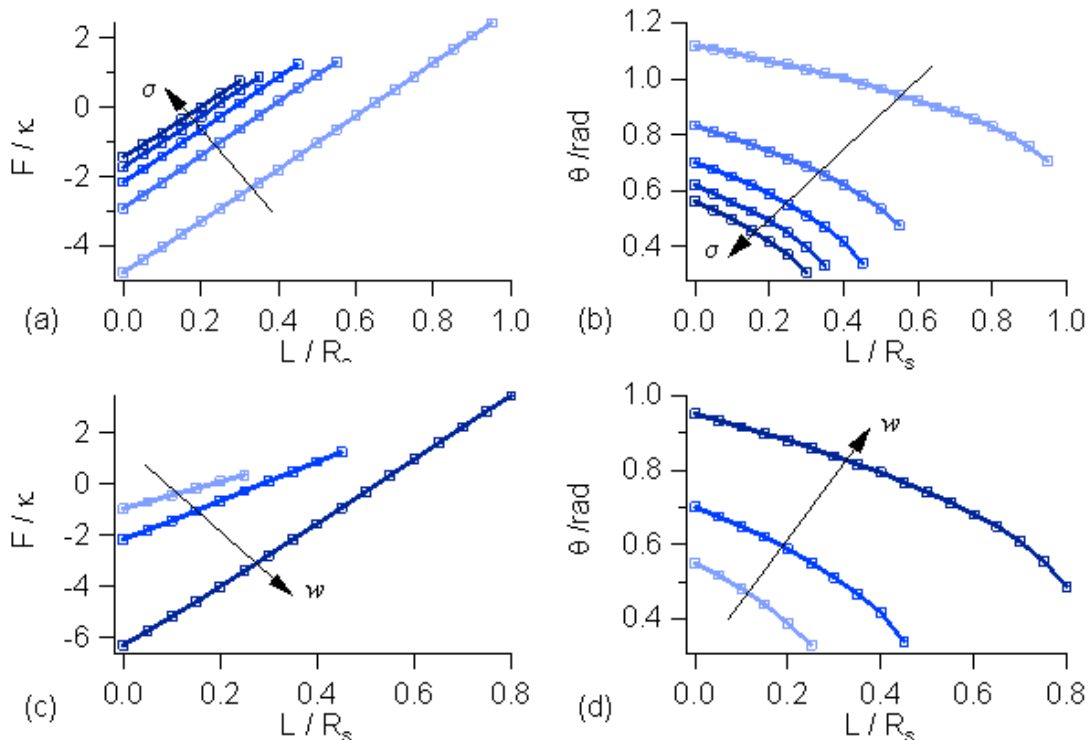


Figure A.4: Free energy, F , of the locally stable wrapped state and the corresponding wrapping angle θ for varying values of σ (a,b) and w (c,d). The curves in a and b correspond to $\sigma = 1, 3, 5$ with darker lines corresponding to increasing values of the tension. The curves in c and d correspond to $w = 4, 5, 7$ with darker lines corresponding to increasing values of the adhesion energy. The curves representing lower tensions and/or stronger surface binding extend into higher values of L because the bound state is stabilized for greater separations. Increasing the tension raises the free energy of the system in a linear fashion across the range of L while the surface energy has a more complicated effect, increasing the slope of the F vs L curve for stronger surface adhesions.

loses its local stability. Increasing the tension, effectively making the membrane a stronger spring, tends to destabilize the bound state and raise the free energy at a given separation.

This is because the bound state requires distortion of the membrane, the magnitude of which scales with L and increased tension increases the associated cost. The increased tension also reduces the equilibrium wrapping angle for any given separation, as can be seen from figure A.4b. It should also be noted from the plots that the curves extend into higher values of L for lower tensions, an effect that is due to the decrease of L^* with increasing tension.

Increasing the strength of the adhesion by raising the magnitude of the surface contact energy w naturally favors the wrapped membrane configuration and increases the equilibrium wrapping angle that is sustained at any given value of the separation L as shown in figure A.4d. The free energy F is generally reduced by increasing w , thereby making the adhesion more favorable. Figure A.4c also shows that L^* is increased allowing more distorted membrane configurations to be sustained, and also that $F(L)$ remains roughly linear at all tested values of w .

The overall free energy function is an interplay between the contributions of the elastic membrane distortions and the surface energy of adhesion. The two contributions favor decreased wrapping angle and allowed separations and increased ones respectively. Also it may be seen that while changing the tension seems to shift the free energy curve up or down in energy without changing the slope, increasing the adhesion energy makes the dependence of the free energy on the separation more dramatic. Figure A.4 illustrates the interplay between the two parameters and the fact that they allow tuning of the overall interaction as well as manipulation of the region in which the separated and the bound state can coexist.

Throughout the coexistence region the free energy landscape of the particle membrane system has two local minima. One of these corresponds to the initial configuration where the membrane is flat and not contacting the particle, and the other is a state where the membrane is wrapped partially around the particle with a portion of its surface undergoing an adhesive interaction. At any particular value of the separation and the system parameters one of these states is the global and the other merely a local minimum. The system is able to go between the two minima and will do so continuously when it is undergoing

thermal fluctuations from contact with a reservoir at ambient temperature. The determining factors as to what fraction of the time the system spends in a particular state are the relative rates of transition to and from a given state, which in this simple binary system are directly correlated. Kinetic equations may be formulated to describe both the likelihood of finding the system in a particular state and the rate at which transitions occur. Using the Arrhenius argument and assuming that the excited states are Boltzmann distributed as was discussed in Section A.3.2, the rates may be related to the height of the free energy barrier for the transition process. These barriers were calculated both for the forward “adhesion” process of going from the flat to the wrapped state and the backward or “dehesion” process. These are shown in figure A.5 for the same range of w and σ values as were used in figure A.4.

The range of separations for which coexistence of the two states is possible is increased by increasing the surface energy of adhesion and decreased by increasing tension accounting for the different lengths of the plots in figure A.5, which all terminate at L^* . Beyond this effect, the barrier to adhesion seems to be almost entirely unaffected by changing the strength of adhesion as shown in figure A.5c. This is a sensible result that supports the idea that most of this barrier is due to the elastic penalty of distorting the membrane sufficiently for contact with the particle to occur. This is further supported by figure A.5a where increasing tension is correlated with increasing barriers to adhesion. This effect is also more pronounced at greater separations where more distortion is required for contact to occur.

The barrier to the reverse process, dehesion, shows a more pronounced dependence on both parameters as can be seen in figure A.5b,d. In this case increasing the tension makes the dehesion barrier higher, while increasing the strength of adhesion lowers it. This

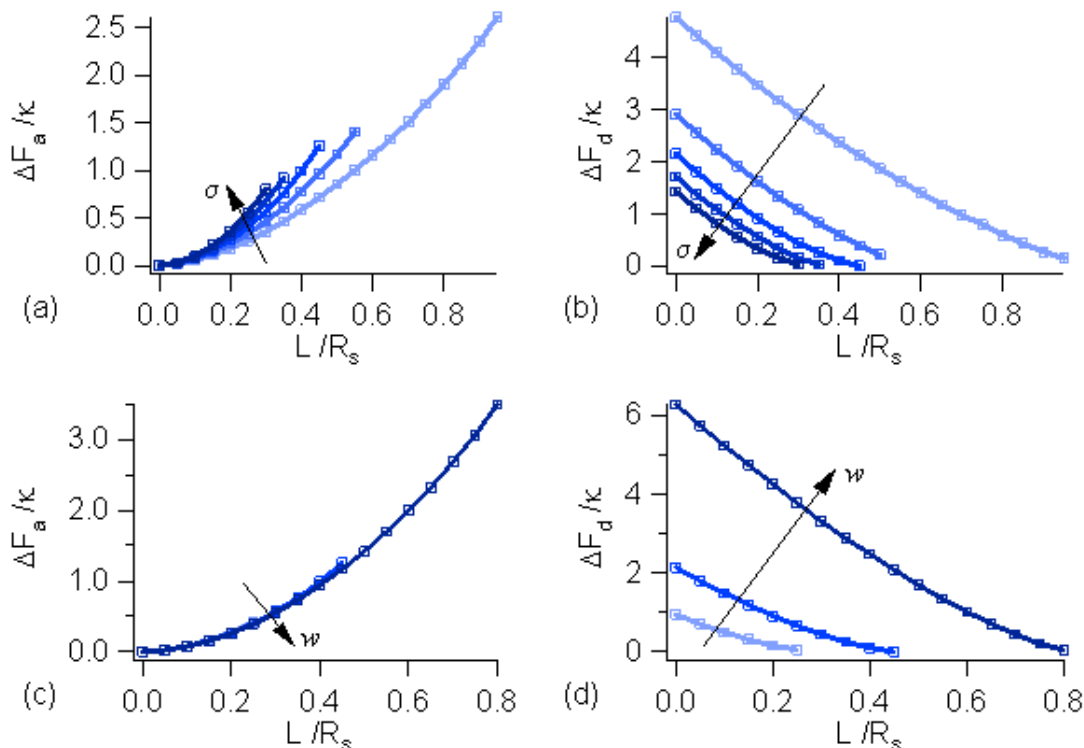


Figure A.5: Barriers to the adhesion (ΔF_a) and dehesion (ΔF_d) processes as a function of the separation L for varying values of σ (a,b) and w (c,d). The curves in a and b correspond to $\sigma = 1, 3, 5$ with darker lines corresponding to increasing values of the tension. The curves in c and d correspond to $w = 4, 5, 7$ with darker lines corresponding to increasing values of the adhesion energy. The curves representing lower tensions and/or stronger surface binding extend into higher values of L because the bound state is stabilized for greater separations. The curves in (a) overlap at small values of L .

is due to the fact that the dehesion process requires the system to go through an unfavorable state that occurs at a wrapping angle that is much less than the equilibrium value. The free energy of this state is raised by reducing the area of contact with the particle and is reduced by the fact that less membrane distortion is necessary to sustain a state that engulfs the particle to a lesser degree. The effect of the loss of contact area is proportional to the magnitude of the adhesive energy, while the energy contribution due to the reduction of distortion is proportional to the imposed tension.

These results show that the barriers to the adhesion and dehesion processes and

therefore the rates depend on the values of w and σ . Since the dependence of the forward and backward rates have very different dependencies on the two parameters, it may be possible to isolate their effects and to use experimental data about the transition rates to obtain information about the properties of a membrane. In particular one could obtain information about the tension by measuring the change in the rate of adhesion and then use this knowledge to isolate the effect of the adhesion strength on the rate of dehesion in order to obtain information about this quantity. It can also be seen that generally the barrier to adhesion grows monotonically with increasing separation L while the barrier to dehesion has the opposite behavior.

A.3.3 The Force Explicit Formulation

For all of the previous results, the particle was assumed to be stationary with respect to the centerline. Throughout the adhesion or dehesion process, the separation L was treated as a constant and the wrapping angle θ was taken to be the relevant reaction coordinate. This results in a free energy analogous to the Helmholtz with the extensive size of the system being fixed. Since the membrane exerts a force on the particle that depends on its position and the membrane configuration, an equal but opposite force must be exerted on the particle in order to have it experience a zero net force. Thus in order to maintain the position of the particle a force must be exerted on it.

This same system may be analyzed from different perspective by considering the force that is conjugate to the separation and performing a Legendre transform on the free energy F in order to transform it into the force explicit G as shown in Section A.2.1. This changes the nature of the dehesion process that we are studying, by having it occur

at a constant force rather than a constant separation. Generally the explicit addition of a force favors the adhesion of the particle as the free energy will always be decreased as the separation is increased. The dependence of the two free energies on the membrane configuration are identical and once the overall free energy landscape is mapped out in either representation, the other may be obtained through a straightforward mathematical operation on the resulting functional.

In general increasing the value of the applied force favors adhesion and reduces the barrier to membrane particle detachment. While one could speak of the barrier to adhesion in the constant force representation, this barrier would always be infinite and as such is not sensible. The force may not be increased to arbitrarily high values. Just as there was a critical value of L above which the bound state was no longer a stationary point, there is also a value of the force f above which a bound state cannot exist for any finite length of time and adhesion is spontaneous. The behavior of the function G at an equilibrium extent of wrapping for a range of force values is shown in figure A.6.

As can be seen in figure A.6, one of the minima occurs at a value of the separation that is significantly less than zero. This corresponds to a state where the particle has been enveloped by the membrane and is below the original centerline of the unperturbed membrane. The value of L at which this occurs is determined by the particular values of w and σ . In order to compare the various values of the pulling force in a simple way, this was chosen to be the zero reference point for the work contribution to the free energy (i.e. the $z = 0$ point in equation 7) and making the value of the free energy in this configuration the same for all values of the applied force.

Increasing the force makes extended conformations progressively more favorable

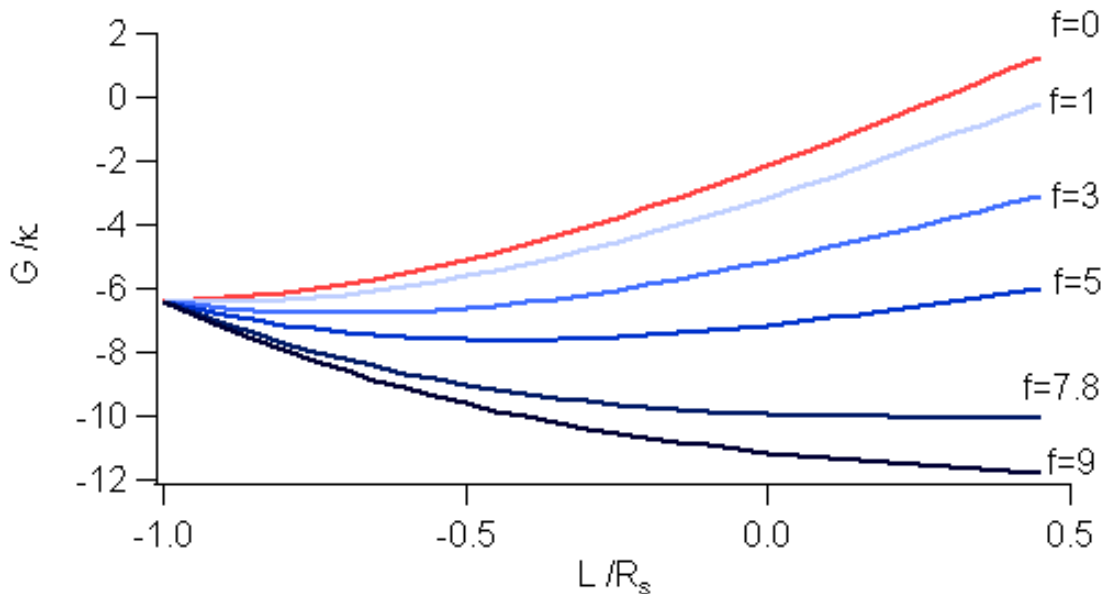


Figure A.6: The force explicit free energy G as a function of L for $\sigma = 3$ and $w = 5$. This is a representative set of parameters from the middle of the range of values sampled. While the particular values of parameters would change the character of the individual curves, the trend of reduced free energy barriers with increased pulling force is general. The darker lines represent a stronger applied force as indicated by labels at the right hand side of the traces. All of the curves have a minimum at a finite value of the separation L for all values of the force less than a critical value ($f \approx 7.8$) with greater forces leading to the vanishing of the barrier and therefore spontaneous dehesion.

by counterbalancing the elastic contribution of the membrane. Thus as the force reaches a critical value $f^* \approx 7.8$ the free energy function becomes monotonic, with increasing L making the dehesion spontaneous. The dehesion process in the constant force case is one in which the particle moves away from the membrane centerline, causing the membrane to stretch. With a sufficiently large force this is always favorable, but the process can only proceed to a point. Once $L > L^*$ for a given set of parameter values, the bound state would no longer be locally stable and the membrane would detach from the particle, which would then speed off to infinite separation. In the contact potential model this corresponds to a cusp in $F(L)$, a point past which the free energy drops discontinuously to a state where the membrane and particle are separated. In a system with a finite range potential function there

would be a maximum rather than a cusp with the bound state becoming locally unstable for increasing values of the separation.

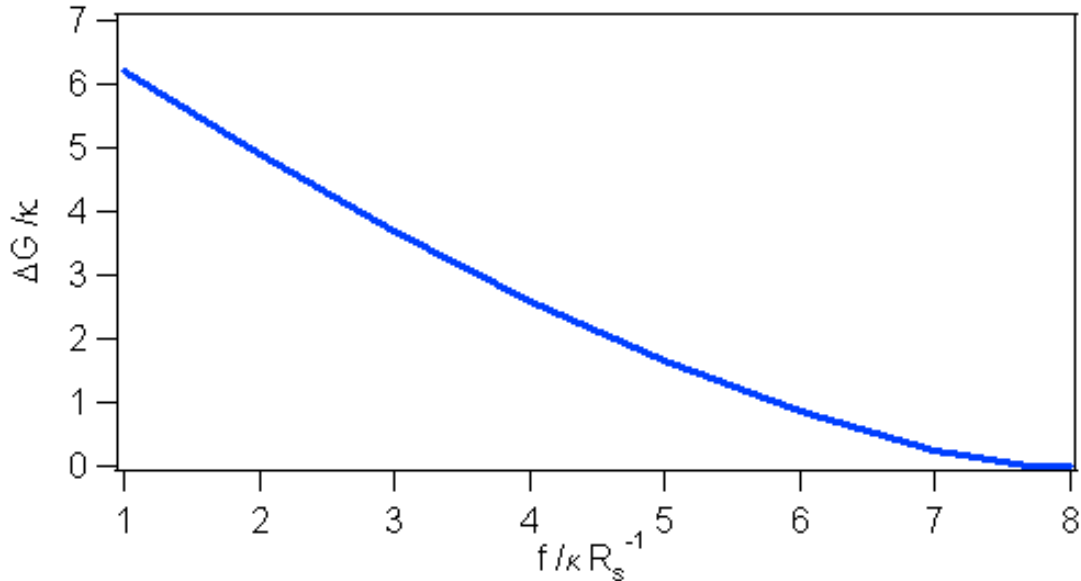


Figure A.7: This figure shows the barrier to the dehesion of the membrane from the particle in the force explicit free energy ΔG as a function of the applied force f for $\sigma = 3$ and $w = 5$. The barrier height decreases with increasing force and vanishes at a critical value of $\approx 7.8 \frac{k}{R_s}$. This plot shows the effect that the introduction of a force has on the system and clearly demonstrates the existence of a critical force value corresponding to the maximum force that may be sustained by the membrane particle adhesion.

The barrier to the dehesion process under constant force follows a very predictable trend of decreasing with greater pulling force. This trend is shown in figure A.7 and appears to be a faster than linear approach to $\Delta G = 0$ as f approaches the critical value f^* . The constant force results can be combined with the dependence of the free energy F on σ and w that were seen in figures A.4 and A.5 as the changes to the constant separation free energy translate very simply to changes to G . This represents a different scenario from that modeled by the constant separation formulation. In this case, rather than a situation where the particle is held at a fixed distance from the membrane in a rigid assembly, a particle can be attached to a calibrated spring, allowing another independent measurement that could

be used to elucidate the membrane properties.

A.4 Conclusions

By analyzing the free energy space of a model membrane and particle system we have been able to elucidate some of the essential dependencies of the adhesion process on system parameters. We have observed the existence of barriers to the transition from the bound to the unbound state and vice versa. These barriers have been shown to depend primarily on the tension imposed upon the membrane and to be generally independent of the strength of the adhesion interaction. The surface adhesion energy has a large impact upon the height of the barrier to dehesion and also the energy landscape at higher extents of wrapping.

The differing importance of these system parameters on the forward and backward progress allows them to control the overall system kinetics by altering the rates at which the system transitions between its locally stable states. Comparing the adhesion and dehesion time scales would allow for the membrane elasticity and the surface interaction potential to be determined given the appropriate experimental data.

The introduction of a force pulling on the particle leads to a lowering of the dehesion barrier and increases the rate of detachment. The process of dehesion occurring at a constant force has the particle follow a reaction path that involves it becoming progressively more distant from the membrane with the thermal fluctuations leading to fluctuations in particle position. The introduction of a force does not affect the ultimate level of deformation that the membrane may sustain and thus the distance at which the separation occurs is also the critical separation for the force free system. It does generally favor more sepa-

rated states by counterbalancing the elastic energy with work done by the force in moving the particle. Above a critical value of the force the process becomes spontaneous and detachment occurs with no time delay.

References

- [1] E.A. Cavalcanti-Adam, T. Volberg, A. Micoulet, H. Kessler, B. Geiger, J.P. Spatz, *Biophysical Journal* **92**, (2007) 2964-2974.
- [2] R. Lipowsky, U. Seifert, *Langmuir* **7**, (1991) 1867-1873.
- [3] M.M. Stevens, J.H. George, *Science* **310**, (2005) 1135-1138.
- [4] H.F. Lodish, *Molecular Cell Biology. 5th ed.* (W.H. Freeman and Company, New York 2003)
- [5] U. Seifert, *Advances in Physics* **46**, (1997) 13-137
- [6] U. Seifert, R. Lipowsky, *Physical Review A* **42**, (1990) 4768-4771
- [7] A.S. Smith, E. Sackmann, U. Seifert, *Europhysics Letters* **64**, (2003) 281-287
- [8] J. Nam, M.M. Santore, *Langmuir* **23**, (2007) 7216-7224
- [9] J. Nam, M.M. Santore, *Langmuir* **23**, (2007) 10650-10660
- [10] C.Z. Zhang, Z.G. Wang, *Physical Review E* **77**, (2008) 021906
- [11] S. Tzlil, M. Deserno, W.M. Deserno, A. Ben-Shaul, *Biophysical Journal* **86**, (2004) 2037-2048

- [12] H.J. Gao,W.D. Shi,L.B. Freund, Proceedings of the National Academy of Sciences of the United States of America **102**, (2005) 9469-9474
- [13] J.I. Martin,C.Z. Zhang,Z.G. Wang, Journal of Polymer Science Part B-Polymer Physics **44**, (2006) 2621-2637
- [14] C.Z. Zhang,Z.G. Wang, Langmuir **23**, (2007) 13024-13039
- [15] S.A. Safran, *Statistical thermodynamics of surfaces,interfaces and membranes* (Addison-Wesley Publishing, Reading Massachussets 1994)
- [16] W. Helfrich,Z Naturforsch C. **28**, (1973) 693-703
- [17] E. Kreyszig, *Differential geometry* (Dover Publications, New York 1991)
- [18] J.A. Nelder,R. Mead, Computer Journal **7**, (1965) 308-313
- [19] E. Bitzek,P. Koskinen,F. Gahler,M. Moseler,P. Gumbsch, Physical Review Letters **97**, (2006) 170201
- [20] M. Deserno, Physical review E **69**, (2004) 031903
- [21] G.I. Bell, Science **200**, (1978) 618-627
- [22] E.A. Evans,D.A. Calderwood, Science **316**, (2007) 1148-1153
- [23] R. Merkel,P. Nassoy,A. Leung,K. Ritchie,E. Evans, Nature **397**, (1999) 50-53